EPFL

Thèse n° 10 232

Supercell Thunderstorms in the Alpine Region - From Weather Radar Observations to Idealized Modeling

Présentée le 23 mars 2023

Faculté de l'environnement naturel, architectural et construit
Laboratoire de télédétection environnementale
Programme doctoral en génie civil et environnement

pour l'obtention du grade de Docteur ès Sciences

par

Monika FELDMANN

Acceptée sur proposition du jury

Prof. J. Schmale, présidente du jury
Prof. A. Berne, Dr M. Gabella, directeurs de thèse
Prof. M. Kumjian, rapporteur
Prof. K. Schröer, rapporteuse
Prof. C. Schär, rapporteur

École polytechnique fédérale de Lausanne

2023

“There is peace even in the storm”
— Vincent van Gogh, *The Letters of Vincent van Gogh*

Monika Feldmann, April 2021, repainting of the "Starry Night" by Vincent van Gogh

Acknowledgements

I sincerely thank my advisors, Prof. Alexis Berne and Dr. Marco Gabella, for the opportunity to pursue this exciting research project in an enticing collaboration between research and operations. Their unwavering support over the years made it possible to pursue many research ideas and also transfer the results into operational use. Their guidance has not only helped me grow professionally, but also personally and I greatly value all of the feedback, advice and encouragement they gave me throughout this PhD journey.

From the very beginning international collaborations were a part of this project. I thank Prof. Curtis N. James for the great collaborative effort to improve the existing dealiasing algorithm at MeteoSwiss.
I am also very grateful to the EPFL EDCE mobility grant and NCAR's advanced study program for financially supporting a prolonged stay at NCAR. I am very thankful to Dr. Richard Rotunno for hosting my visit, introducing me to idealized modeling and continuing our collaboration beyond the stay.

I also thank my jury members Prof. Matthew Kumjian, Prof. Katharina Schröer and Prof. Christoph Schär for taking the time to read and evaluate this work, as well as their valuable feedback and the interesting discussions during the private defense. In particular I thank Prof. Julia Schmale for chairing and moderating the exam.

This project would not have been possible without the support of colleagues and friends. My heartfelt gratitude goes to LTE for all the great times we enjoyed together, ranging from winter days and movie nights over radar deployments to valuable discussions about our projects. I thank Anne-Claire Billault-Roux, Dr. Rebecca Gugerli, Dr. Alfonso Ferrone, Dr. Josué Gehring, Gionata Ghiggi, Adrien Liernur and Dr. Étienne Vignon, as well as practically-LTE-members Lucile Ricard and Paraskevi Georgakaki for their support, contributions and friendship during this time.

I also deeply thank my colleagues at MeteoSwiss for in-depth scientific discussions, insights into operational use and many great conversations in the sun on Locarno-Monti's terrace. In particular I would like to thank Dr. Urs Germann for his scientific advice and support in pushing the algorithms towards operational implementation. Special thanks as well to Marco

Boscacci, for his assistance in setting up two new products in the pre-operational test chain. Many thanks to Dr. Alessandro Hering, Dr. Ulrich Hamann, Dr. Luca Nisi, Dr. Luca Panziera and Dr. Lionel Peyraud for their insights on thunderstorms, Dr. Daniele Nerini and Dr. Daniel Wolfensberger for their technical support, as well as Nathalie Rombeek, Francesco Zanetta, Dr. Lea Beusch, Dr. Loris Foresti and Dr. Jussi Leinonen for being great colleagues and friends.

This collaboration between EPFL and MeteoSwiss offered me the opportunity to work in both a research- and an applications-oriented environment. Splitting the PhD journey into two years in Lausanne and two years in Locarno was a very enriching experience also on a personal level, allowing me to learn and improve on languages and feel at home in both places.

In spite of the brevity of the visit, I greatly enjoyed my stay at NCAR and cherish the colleagues I met there. The exchange with the scientists, PostDocs and other visiting PhD students was very enriching and also led to great friendships. In particular I would like to thank Dr. George Bryan for his advice and expertise, Dr. Morris Weisman, Julia Kukulies and Dr. Anna del Moral.

I also profoundly thank my parents Sabine and Dr. Burkhard Feldmann, as well as my siblings Christiane and Matthias Feldmann for their continuous encouragement and wholehearted support of my ambitions. I am also very grateful to my friends Joel Zeder, Dr. Ray Harran, Prof. Tom Beucler, Stefanie Stanke, Alexandra Kisch, Roxanne Dörge, Julia Isler, Dr. Richard Zhang and Dr. Raphael Rousseau-Rizzi for always taking time for me and staying close in spite of the long distance.

Locarno, February 18, 2023 Monika Feldmann

Abstract

The high-impact nature and increasing occurrence of severe weather phenomena pushes forward research on their occurrence and improving our understanding thereof. Supercell thunderstorms are the focus of much severe convective research, as they represent one of the most hazardous convective storm types. The behavior of supercell thunderstorms in complex terrain is still poorly understood. In Switzerland there are no previous comprehensive studies concerning supercells, in contrast to hailstorms, which have been studied more extensively. The Swiss radar network offers high-quality observations with a dense spatio-temporal coverage that provides a good foundation for convective studies.

This thesis establishes a general understanding of supercell characteristics for the Alpine region. By employing automatic detection in radar data, a large set of events provides the basis for observational analyses. These inform modeling scenarios that aim to achieve an understanding of the underlying meteorological phenomena in complex terrain.

This first entails improving the processing of Doppler velocity data from the Swiss operational radar network and implementing a systematic detection and tracking algorithm for rotation in convection to identify supercells. Making use of the radar data archive, a catalog of past events is generated, allowing for a description of the overall frequency, spatial distribution and temporal occurrence patterns. Revealing frequency clusters in both the Northern and Southern Prealpine regions, analyses into topographic influence show a detrimental effect of increasing altitude on rotation strength in supercells. To gain contextual understanding, a comprehensive comparison against severe rain- and hailstorms indicates that the detected supercells represent the most intense fraction of observed thunderstorms. Additionally, the frequency clusters in the Prealpine areas prevail across the different convective classes. Supercells particularly cluster in the proximity of the lakes in the Southern Prealpine valleys. The decreasing peak intensity with increasing topographic complexity is also found across these types of severe convection. By setting up idealized scenarios in a numerical model, we investigate the effects of slopes, valleys and lakes as moisture sources on supercell development and intensification. Especially valleys with a lake are able to sustain supercellular development in initial conditions, where they no longer develop in the absence of topography.

Abstract

The comprehensive assessment of supercell behavior and the comparison to other, more studied, types of severe convection, provide a fundamental description of supercell characteristics in the Alpine region. The modeling experiments help understand the meteorological drivers behind the topography-influenced frequency and intensity distribution of supercells. As systematic supercell observation in mountainous regions is rare, this constitutes an important contribution to research on severe convection in complex topography.

Zusammenfassung

Die großen Auswirkungen und das zunehmende Auftreten von Unwetterphänomenen treiben die Forschung zu deren Vorkommen und zur Verbesserung unseres Verständnisses voran. Superzellengewitter stehen im Fokus der Forschung zu schweren konvektiven Unwettern, da sie eine der gefährlichsten konvektiven Gewitterarten darstellen. Über das Verhalten von Superzellengewittern in komplexem Gelände ist noch wenig bekannt. In der Schweiz gibt es bisher keine umfassenden Studien über Superzellen, im Gegensatz zu Hagelstürmen, die ausgiebiger erforscht wurden. Das Schweizer Radarnetz bietet qualitativ hochwertige Beobachtungen mit einer dichten räumlichen und zeitlichen Auflösung, die eine gute Grundlage für konvektive Studien bieten.

Diese Arbeit schafft ein allgemeines Verständnis für die Eigenschaften von Superzellen im Alpenraum. Der Einsatz von automatischen Detektionsalgorithmen in Radardaten liefert eine große Anzahl von Ereignissen, diese liefern die Grundlage für Beobachtungsanalysen. Die daraus gewonnenen Erkenntnisse sind die Augangsbasis für Modellierungsszenarien, die darauf abzielen, ein Verständnis der zugrunde liegenden meteorologischen Phänomene in komplexem Gelände zu erlangen.

Dazu wird zunächst die Verarbeitung von Doppler-Geschwindigkeitsdaten aus dem Schweizer Radarnetzwerk verbessert und ein systematischer Detektions- und Trackingalgorithmus für Rotation in Konvektion implementiert, um Superzellen zu identifizieren. Unter Verwendung des Radardatenarchivs wird ein Katalog vergangener Ereignisse erstellt, der eine Beschreibung der Gesamthäufigkeit, der räumlichen Verteilung und der zeitlichen Muster des Auftretens ermöglicht. Die Analyse des topografischen Einflusses zeigt, dass sich zunehmende Höhe nachteilig auf die Rotationsstärke von Superzellen auswirkt und Häufigkeitscluster sowohl in den nördlichen als auch in den südlichen Voralpenregionen auftreten. Um ein kontextuelles Verständnis zu erlangen, zeigt ein umfassender Vergleich mit schweren Regen- und Hagelstürmen, dass die entdeckten Superzellen zu den stärksten beobachteten Gewittern gehören. Darüber hinaus überwiegen die Häufigkeitscluster in den Voralpengebieten in den verschiedenen Gewitterkategorien. Superzellen treten vor allem in der Nähe der Seen in den südlichen Voralpentälern auf. Die abnehmende Spitzenintensität mit zunehmender topographischer Komplexität findet sich auch bei allen schweren Unwetterkategorien.

Zusammenfassung

Durch die Erstellung idealisierter Szenarien in einem numerischen Modell untersuchen wir die Auswirkungen von Steigungen, Tälern und Seen als Feuchtigkeitsquellen auf die Entwicklung und Intensivierung von Superzellen. Insbesondere Täler mit einem See sind in der Lage, die Weiterentwicklung von Superzellen unter anfänglichen Bedingungen aufrechtzuerhalten, in denen sie sich in Abwesenheit von Topographie nicht mehr entwickeln.
Die umfassende Bewertung des Verhaltens von Superzellen und der Vergleich mit anderen, besser untersuchten Arten von schwerer Konvektion liefern eine grundlegende Beschreibung der Eigenschaften von Superzellen im Alpenraum. Die Modellierungsexperimente helfen, die meteorologischen Triebkräfte hinter der von der Topographie beeinflussten Häufigkeits- und Intensitätsverteilung von Superzellen zu verstehen. Da systematische Superzellenbeobachtungen in Gebirgsregionen selten sind, ist dies ein wichtiger Beitrag zur Erforschung tiefer Konvektion in komplexer Topographie.

Preface

LTE has a close collaboration with MeteoSwiss, in particular with the Radar, Satellites and Nowcasting Group in Locarno, led by Dr. Urs Germann. This collaboration generated fruitful projects, combining academic, scientific and more operationally oriented objectives, that led to methodological developments and operational products relevant for the services provided by MeteoSwiss to the Swiss society.

Mesocyclones are a key feature of supercells, potentially associated with intense rain, large hail or severe wind gusts. Despite being a damaging severe weather phenomenon, supercells were poorly documented and thought to be rare in Switzerland. The idea to use the operational radar network to identify mesocyclones and study supercells in Switzerland was first proposed by Urs, and Dr. Marco Gabella and myself were immediately convinced. We had the project, we needed the person to achieve it!

Right after the interview, we were sure to have in Monika the right person to undertake the difficult work and achieve those ambitious goals. She joined the team and brought her expertise in severe weather and convective phenomena, that we did not have. Monika started her PhD journey by working on the de-aliasing of radar velocity fields, a quite technical topic, that led (thanks to the light side of the force) to the R2D2 algorithm that can now be used operationally. She continued by taking advantage of the multiyear archive of operational radar data at MeteoSwiss to quantitatively characterize the occurrence of mesocyclones (and supercells) in Switzerland, which appear more frequently than initially thought, as well as to study the distinctive features between the different types of convective storms (intense rain- or hailstorms, supercells). She finally took up the challenge of using a numerical model to investigate the influence of complex terrain and lakes on the evolution of supercells, a so far unexplored question. All those results constitute a remarkable achievement and a valuable contribution to the community.

Monika covered an impressive breadth of topics during her PhD, demonstrating that she deepened but also broadened her expertise. I would like to highlight the fact that Monika not only made original academic contributions, but also developed tools that are used operationally, with hence a rather direct societal impact. It was a real pleasure to work with Monika all along those four years as she is a nice person, a true team player (the famous Weather Club!), and I learned a lot working with her. Overall, I feel privileged to have supervised Monika during her PhD work, and I wish her nothing but success!

Lausanne, February 18, 2023 Prof. Alexis Berne

Contents

List of Symbols

The following table lists the most important symbols used throughout the thesis.

Symbol	Units	Description
ζ	[s^{-1}]	z-vorticity
η	[s^{-1}]	y-vorticity
Θ	[K]	Potential temperature
Θ_e	[K]	Equivalent potential temperature
λ	[cm]	Radar wavelength
ξ	[s^{-1}]	x-vorticity
φ	[rad]	Phase
φ_{az}	[°]	Azimuth angle
$\vec{\omega}$	[s^{-1}]	Vorticity
A	[km^2]	Area
ACC	[mm h^{-1}]	Hourly precipitation accumulation
b	[m s^{-1}]	Threshold for buffer areas in dealiasing
c	[m s^{-1}]	Speed of light
$CAPE$	[J kg^{-1}]	Convective available potential energy
CIN	[J kg^{-1}]	Convective inhibition
D	[m s^{-1}]	Maximum absolute velocity difference
D_{av}	[m s^{-1}]	Average maximum absolute velocity difference
ET	[km]	Echotop height (usually for a certain reflectivity level)
h	[m] or [km]	Height
i	[#]	Number of dealiasing iterations
iRR	[mm h^{-1}]	Instantaneous precipitation rate
LTG	[$\frac{\#}{tA}$]	Lightning rate
$MESHS$	[cm]	Maximum expected severe hail size
POH	[%]	Probability of hail
n	[ ]	Average refractive index of air
PRF	[s^{-1}]	Pulse repetition frequency
QI	[0-1]	Radar quality index
r	[m] or [km]	Range distance
R	[mm h^{-1}]	Precipitation rate

$RANK$	[0-40]	Thunderstorm severity rank
T	[°C]	Temperature
t	[s] or [min]	Time
u	[m s^{-1}]	Velocity in x-direction
v_{DOP}	[m s^{-1}]	Doppler velocity
v_{NYQ}	[m s^{-1}]	Nyquist velocity
V	[0-20]	Radar visibility
v	[m s^{-1}] or [km h^{-1}]	Velocity in general
v	[m s^{-1}]	Velocity in y-direction
VIL	[kg m^{-2}]	Vertically integrated liquid
w	[m s^{-1}]	Velocity in z-direction
x	[m] or [km]	Cartesian coordinate
y	[m] or [km]	Cartesian coordinate
z	[m] or [km]	Cartesian coordinate
Z	[dBz] or [mm^6 m^{-3}]	Radar reflectivity factor

List of Acronyms

Abbreviation / Acronym	Description
4DD	4 Dimensional Dealiasing
ASL	Above sea level
CAPE	Convective available potential energy
CI	Convective initiation
CIN	Convective inhibition
COSMO	Consortium for Small-scale MOdeling
DSD	Drop size distribution
E	East
EPFL	Ecole Polytechnique Fédérale de Lausanne
GWT	GrossWetterTypes
HS	Hailstorm
IQR	Interquartile range
LLSD	Linear least squares derivative
LTE	Laboratoire de Télédétection Environnementale
M-DaTing	Mesocyclone Detection and Tracking
MESHS	Maximum expected severe hail size
MIL	Milano
N	North
NWP	Numerical weather prediction
OR	Ordinary thunderstorm
PAY	Payerne
POH	Probability of hail
PPI	Plan position indicator
PRF	Pulse repetition frequency
R2D2	Region-based Recursive Doppler Dealiasing
RS	Rainstorm
S	South
SC	Supercell
SHS	Severe hailstorm
SRS	Severe rainstorm
T-DaTing	Thunderstorm Detection and Tracking

T0	Center of thunderstorm life cycle
TRT	Thunderstorm radar tracking
VAD	Velocity azimuth display
W	West

1 Introduction and Background

1.1 Motivation

Supercell thunderstorms are one of the most costly weather hazards worldwide (Hoeppe, 2016). With their capability to bring strong windgusts, severe precipitation, large hail and tornadoes, they have a significant impact on society, infrastructure and livelihoods. These significant impacts have lead to extensive research efforts targeting the high-occurrence areas of the Great Plains and the Southeast of the United States. Field campaigns (NSSL, 2019, 2021; Garcia de Jesus, 2019), analyses of operational data networks and modelling studies (Weisman and Klemp, 1982; Davies-Jones, 2015; Kumjian et al., 2021) aim to improve our understanding of supercells in these areas. Particularly tornado formation and evolution is a key focus of ongoing research. The occurrence and processes behind large hail have recently gained more traction (Kumjian et al., 2021; Gutierrez and Kumjian, 2021; Murillo and Homeyer, 2019; Murillo et al., 2021). With hail occurring more frequently and affecting larger areas, it has a larger societal impact than tornadoes do.

In mountainous regions, supercells remain poorly observed, understudied and we hence lack an understanding of if and how they behave differently from supercell thunderstorms over flat terrain. As a result, studies aimed at analyzing supercell behavior over complex terrain have recently increased, with field campaigns targeting mountain areas in South America and Europe (Varble et al., 2021; Lombardo and Kumjian, 2022; Nesbitt et al., 2021; Serafin et al., 2020) and modeling studies investigating severe convection in the Himalayas (Kukulies et al., 2021). Since systematic observations are limited and challenging in complex orography, studies utilizing large sets of operational observations are not prevalent. In modelling studies, terrain has become a more frequent factor of investigation, with a few studies targeting the influence of terrain features on supercell evolution (Scheffknecht et al., 2017; Ćurić et al., 2007; Markowski and Dotzek, 2011; Katona and Markowski, 2021). A number of case studies highlight the importance of improving our understanding of supercells in orography, but often fail to yield systematic results that can transfer to larger storm samples or other regions (Bluestein, 2000; Peyraud, 2013; Avolio et al., 2020; Grazioli et al., 2019).

The Swiss radar network covers a large portion of the Alpine region (Germann et al., 2022). With it being tailored to providing high-quality measurements in complex terrain, we use the operational radar data to establish a general understanding of supercell occurrence in the observed area. These observational results help inform idealized modelling experiments, that identify the underlying meteorological processes.

1.2 Meteorological Background

1.2.1 Supercell Thunderstorms

The following introduction to supercell thunderstorms is based on Markowski and Richardson (2010); Houze (2014); Lohmann et al. (2016) and the sources within.
Supercell thunderstorms are the most severe type of a single thunderstorm cell. Their high degree of organization allows for long lifetimes and they are prone to producing heavy precipitation, strong wind gusts, large hail and tornadoes. Supercell thunderstorms commonly develop in environments with large amounts of convective available potential energy (CAPE) and a high degree of vertical wind shear, which presents a reservoir of horizontal vorticity.

Vorticity

Vorticity is defined as the curl of the 3-D velocity field, as shown in Eq. 1.1. Eq. 1.2 shows its three components separately, corresponding to the x- (ξ), y- (η) and z-components (ζ) of vorticity.

$$\vec{\omega} = \nabla \times \vec{v} \tag{1.1}$$

$$(a)\ \xi = \frac{\partial w}{\partial y} - \frac{\partial v}{\partial z}\ ;\ (b)\ \eta = \frac{\partial u}{\partial z} - \frac{\partial w}{\partial x}\ ;\ (c)\ \zeta = \frac{\partial v}{\partial x} - \frac{\partial u}{\partial y} \tag{1.2}$$

For supercell thunderstorms, the evolution of vertical vorticity is of particular importance. Its change in time (see Eq. 1.3) is defined by stretching of existing vertical vorticity (blue), tilting of horizontal vorticity through an updraft (red) and mixing (green).

$$\frac{d\zeta}{dt} = \zeta\frac{\partial w}{\partial z} + \eta\frac{\partial w}{\partial y} + \xi\frac{\partial w}{\partial x} + F_\zeta \tag{1.3}$$

The vertical wind shear results in an environmental background level of horizontal vorticity. After convective initiation (CI) the resulting updraft tilts the horizontal vorticity into the vertical, which results in a rotation on the horizontal plane, as is illustrated in Fig. 1.1. Initially this produces both a cyclonically and anticyclonically rotating component in the forming updraft.

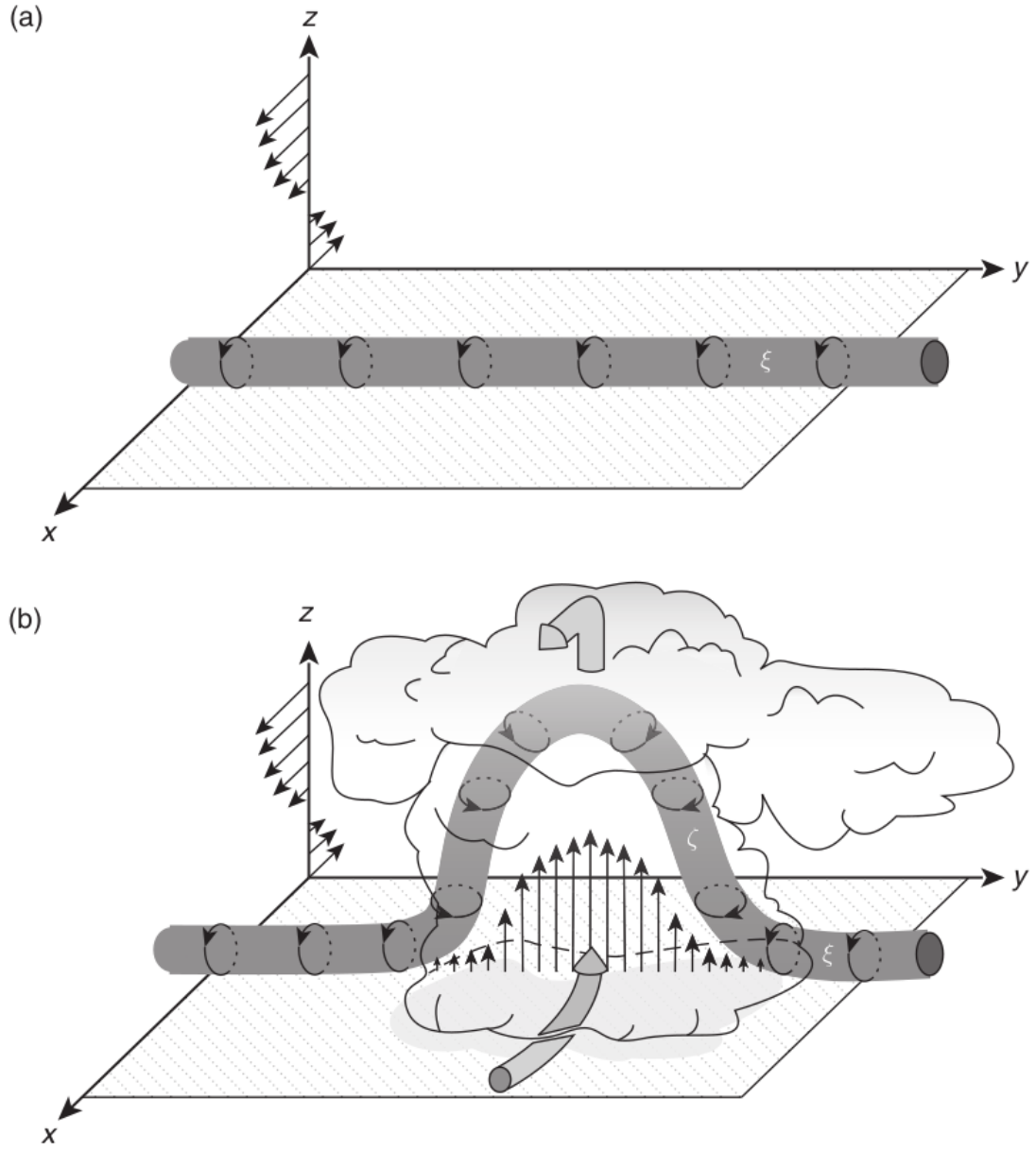

Figure 1.1: Conversion of horizontal vorticity η into vertical vorticity ζ in a thunderstorm in the presence of vertical wind shear $\frac{du}{dz}$ indicated by the horizontal arrows. (a) The creation η of by $\frac{du}{dz}$, (b) The creation of ζ by the superposition of an updraft of a convective cloud on a horizontal vorticity tube. The large mid-gray arrows show the in- and outflow, the vertical arrows denote the updrafts. The arrow loops around the gray tubes indicate the vorticity. Figure adapted from Klemp (1987). Lohmann et al. (2016), reproduced with permission of the licensor through PLSclear. As the use of ξ and η for x- and y-vorticity is inconsistent in literature, this caption has been adapted to match the definition in this thesis.

The rotating updraft is one of the key features in a supercell and is called the mesocyclone. With high updraft velocities, supercells extend up to the tropopause and partially beyond with the overshooting top. The ascending air cools and begins forming precipitation. At the tropopause the majority of the rising air spreads horizontally, with a distinct storm-top divergence signature. The subsequent outflow out of the thunderstorm occurs through the forward and rear flank downdrafts, which are separated from the warm inflow air. The developing gust front at each outflow produces additional vorticity through baroclinicity, which gets advected back into the storm via the inflow. The separation of the inflow from the outflow and the advection of vorticity back into the storm enable the long lifetime of supercell thunderstorms, as long as the overall environment remains favorable. With the precipitation occurring in the downdraft areas surrounding the updraft, the mesocyclone itself is an area of relatively low precipitation intensity below. The rotation of the mesocyclone however wraps the precipitation of the rear flank around itself, resulting in the typical hook-shape of the end of the storm. Figure 1.2 shows the typical structure of a supercell from the side, Fig. 1.3 provides an overview from the top, highlighting the typical hook-echo shape.

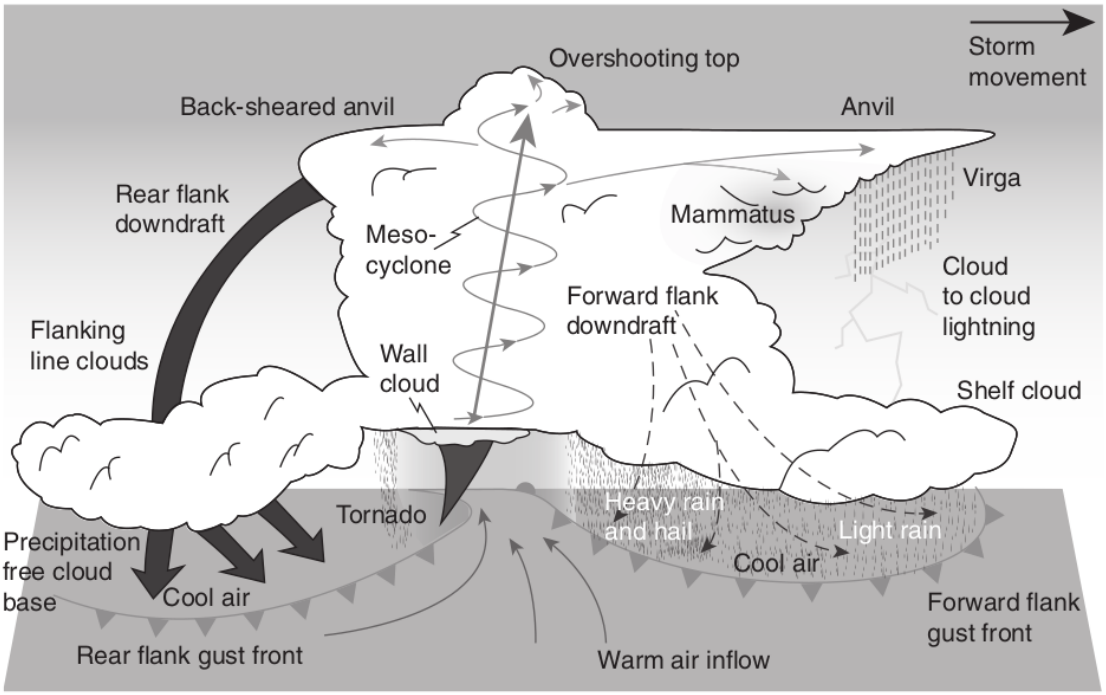

Figure 1.2: Schematic of the main features, including the updraft and downdrafts and surface air flow, associated with a tornado-breeding supercell thunderstorm. Lohmann et al. (2016), reproduced with permission of the licensor through PLSclear

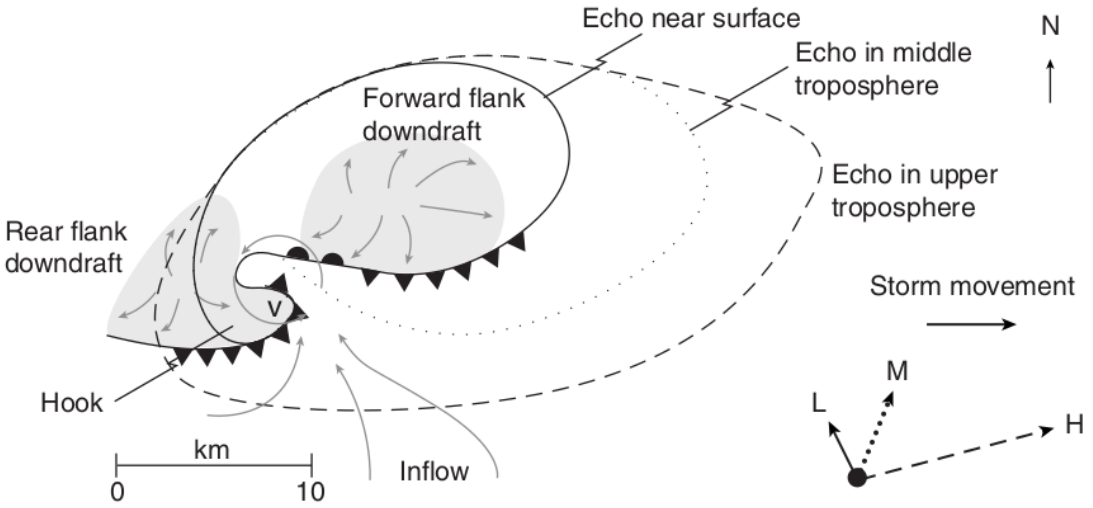

Figure 1.3: Schematic diagram showing horizontal sections of the precipitation radar echoes at three different levels of a supercell storm. Environmental winds relative to the storm at low, medium and high levels of the troposphere are represented by the three vectors low (L), middle (M) and high (H). The tornado is represented by a V (vault). Lohmann et al. (2016), reproduced with permission of the licensor through PLSclear

The initial rotating updraft contains a cyclonic and anticyclonic component. In the initial phases of storm development, a downdraft forms in between these opposing rotation pairs as precipitation forms. This results in a split of the updraft into two separate entities, a cyclonic and an anticyclonic one. The split of storms is also observed in non-precipitating modeling experiments, but is accelerated by the formation of precipitation. Each rotation results in a surface pressure perturbation that deviates the mean storm motion from the steering flow aloft. The cyclonic rotation is displaced to the right of the mean flow, whereas the anticyclonic rotation is displaced to the left. This opposing motion results in a split of the thunderstorm, with two separating storms. If the background shear profile has a directional component (e.g. clockwise), it will be more favorable for one of the storms (in this case the right-mover). In a unidirectional sheared environment, both cells will be mirrors of one another.

Supercells are known to produce large hail. Hail formation is largely dependent on the size and strength of the updraft, as well as the rotation within. Hail growth primarily takes place while the particle is suspended within the updraft. Most hail trajectories transcend through the updraft until they get ejected into the downdraft areas, as shown in Fig. 1.4. Hail trajectory studies have shown that this usually occurs during a single trajectory, where hailstones encounter wet and dry growth regions in different sections of the updraft (Kumjian and Lombardo, 2020). Hence, the updraft area is key for hail size. Moderate updraft velocities are more favorable than very high velocities, as the additional turbulence in very strong updrafts tends to eject hailstones sooner and the residence time is reduced due to the higher updraft velocities. The primary areas for hailfall in a supercell are in the rear- and forward flank downdrafts, close to

the mesocyclone. These mirror the areas of most intense precipitation. A strong updraft allows a large volume of warm, moist air from the low levels to be transported upwards in a short amount of time. Hence, the resulting amount of condensed moisture and finally precipitation rates are very high.

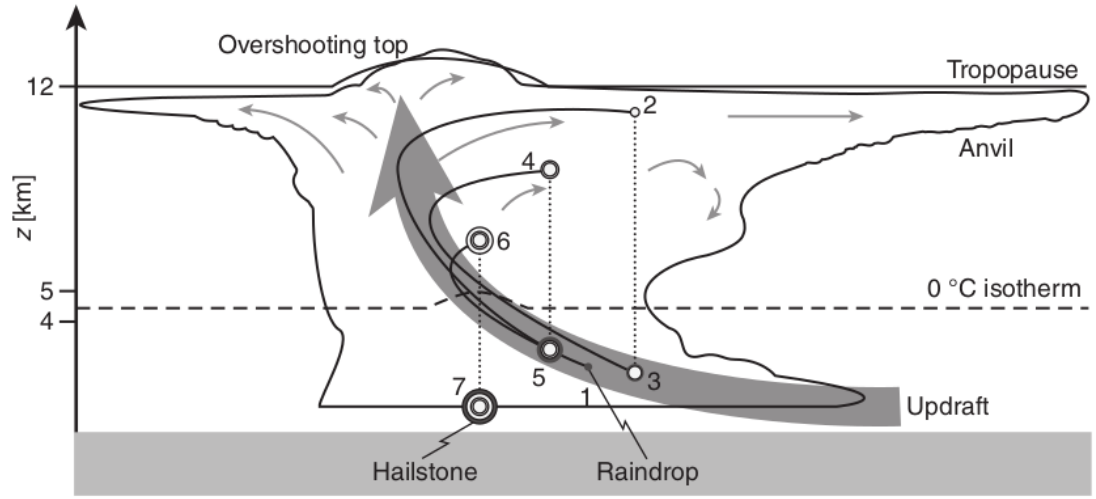

Figure 1.4: Schematic of hailstone formation. Black circles denote wet growth and white circles dry growth. Upward directed motions of the hailstone are denoted by solid lines and downward motions by dotted lines. Lohmann et al. (2016), reproduced with permission of the licensor through PLSclear; recent studies suggest a single growth trajectory without recycling (Kumjian and Lombardo, 2020) and circular trajectories to be rare (Kumjian et al., 2021)

The prevalence of both frozen and liquid particles in the updraft of a supercell is also responsible for the high lightning rates of these storms. The friction in between liquid and frozen particles causes a separation of charges that leads to subsequent discharges in lightning. The rotation of the mesocyclone additionally enhances the friction. The largest fraction of lightning occurs within the cloud (intra-cloud, IC). The majority of cloud-to-ground (CG) strikes are due to negative discharge and originate from the bottom towards the ground. CG positive discharges are the smallest fraction of lightning strikes and occur from the cloud top, these strikes can cover significantly larger distances and strike at far distances from the storm.

The majority of supercell research focuses on the Great Plains in the USA. This area harbors the highest number of archetypal supercells, occurring in high-shear and high CAPE environments. To provide some background on Europe and the Alpine region, the following two sections target severe convection in general, as specific supercell studies are not as common.

1.2.2 Severe Thunderstorms in Europe

Convective hazards present some of the costliest natural hazards in Europe, therefore an extensive amount of research has targeted severe thunderstorms in Europe (Hoeppe, 2016). Since meteorological observation networks in Europe are managed nationally, the heterogeneous data coverage and structure present a challenge in attempting studies covering the entire European continent (Punge and Kunz, 2016). Hence, a lot of studies are rather of a regional nature, focusing on single countries.
Most studies on supercells in Europe focus on single case studies (Scheffknecht et al., 2017; Peyraud, 2013; Avolio et al., 2020). We here concentrate on studies with a larger scope, to present a general understanding of severe thunderstorm behavior.
In Germany, supercells have been observed using a radar-based mesocyclone detection algorithm (Hengstebeck et al., 2018). The majority of them produce significant hail - and vice versa, the majority of ground-reported, significant hailstorms, also contain a mesocyclone (Wapler et al., 2016; Wapler, 2017, 2021). The mesocyclone tends to precede the onset of hail. The mesocyclone forms during the development of the updraft, while hail tends to grow in a more mature storm. Supercell thunderstorms tend to occur in weather regimes of Southwesterly flow, when warm, moist air from the Mediterranean Sea is advected towards Central Europe (Wapler and James, 2014; Mohr et al., 2020). More generally, southwesterly flow situations are known to produce wide-spread severe weather outbreaks in Central Europe ranging from France and Northern Italy over Switzerland to Germany. These are related to ground-based observations of flash flooding, severe hail and wind gusts (Mohr et al., 2020).
More comprehensive analyses over Europe make use of combined storm report databases (Mohr et al., 2020; Taszarek et al., 2019) and investigate storm environments as proxies (Taszarek, 2019; Taszarek et al., 2020, 2021a,b). Overall, past observations indicate an increase in the frequency and severity of convective hazards in Europe (Taszarek et al., 2020). Moreover, the increasing frequency of storm-favorable environments is detectable in reanalysis data and continues in future climate scenarios (Taszarek, 2019; Taszarek et al., 2021b). With severe convection expected to increase with warming in Europe, a better understanding is key for adaptation and prevention. This clear and spatially homogeneous trend is at odds with the trends found in the United States, where a spatio-temporal shift of the peak convective areas is projected.

1.2.3 Convection in the Alpine Region

The complexity of mountainous terrain has a considerable influence on the initiation and the development of convection, making this an area of active and relevant research. In addition, the terrain introduces additional difficulties in observing and modelling thunderstorms appropriately.
CI is facilitated over ridges, due to differential heating over complex orography and resulting valley circulations. Consequently, in particular the Prealpine areas show high levels of convective activity. The inner Alps are more separated from the meteorological patterns around and tend to be drier. In addition, the high altitude reduces the potential for high CAPE values. Several observational climatologies from radar, satellite and lightning data show overall reduced convective activity in the inner Alps, most notably so for severe convection (Nisi et al., 2018; Punge et al., 2017; Enno et al., 2020; Manzato et al., 2022).
Studies in Switzerland have largely focused on hail (Nisi et al., 2016, 2018, 2020; Trefalt et al., 2018; Kopp et al., 2022; Barras et al., 2021, 2019; Schemm et al., 2016). The Northern and Southern Prealps emerge as hail hotspots, with a pronounced diurnal cycle that shows an activity maximum in the late afternoon. However, the storms occurring during the low-activity times at night and in the morning tend to be among the most-durable and largest. The importance of the SW flow situation also applies here, though additionally Westerly flow produces a large number of hailstorms.
A case study detailing the progression of a tornado-producing supercell in 2005 (Peyraud, 2013) also highlights the importance of SW flow, in a large-scale constellation called the Spanish plume (Morris, 1986). Tornadoes are rare in Switzerland, with on average less than one occurring per year, but their intensity can vary substantially (Sturmarchiv Schweiz, 2021). The Spanish plume in particular holds a high potential for severe weather, as it introduces an elevated mixed layer of dry and hot continental tropical air at mid-levels over a moist and warm maritime tropical Mediterranean boundary layer. This superposition of airmasses essentially caps and delays convective initiation until later in the day and allows the instability of the airmass to release explosively once the convective inhibition is overcome via surface heating or large-scale airmass lift and cooling. This combination produces exceptionally favorable convective environments.
A field experiment targeting hailstorms in Switzerland provided first insights into supercell occurrence in Switzerland. "Grossversuch IV" took place from 1975-1982 and covered a radius of 60 km in the Northern Prealps. By analyzing the storm tracks and reflectivity structure, an equal fraction of left- and right-mover storms were found, indicating no systematic environmental preference for the sense of rotation (Houze et al., 1993).

1.3 Weather Radar Background

1.3.1 Weather Radar Principles

The principles of weather radars are explained in detail in Fabry (2015); Ryzhkov and Zrnic (2019). We here provide a brief introduction to the subject, for more detailed information the reader is referred to the aforementioned works.
Radio detection and ranging (radar) is a remote sensing technique that makes use of electromagnetic waves. These are emitted from the antenna and the power and phase of the return are measured. The return consists of the reflection and scattering of the electromagnetic waves from particles within their path. The emission takes place in a series of short pulses. The time in between the emission and the recorded return allows to infer the distance of the target. The time in between two pulses, or pulse repetition frequency (PRF) hence determines the maximum unambiguous range for targets. In radar meteorology, it is mostly desired to have small precipitation targets compared to the radar wavelength, such that scattering is well characterized by the Rayleigh approximation. The usual weather radar wavelength hence exceeds the size of most precipitation particles, with common wavelengths being S-band (8-15 cm), C-band (4-8 cm) and X-band (2.5-4 cm). The return of undesired targets is called clutter. The definition of clutter depends on the use of a radar; in meteorology returns from the ground, aircraft, insects and birds are considered clutter.
Polarimetric radars use two waves, polarized at 90° of one another. Comparing the properties of both waves provides information about the size and shape of the measured particles. We here mainly use the single polarization variables horizontal reflectivity and Doppler velocity, which are explained in more detail below.

Reflectivity Factor

The radar reflectivity factor is the target variable that is determined as a ratio of emitted and returned power with respect to the targeted volume. It depends on the emitted power, wavelength, range of target volume, size of the scatterers and their dielectric component, among other factors. The formula below establishes the relationship between emitted and returned power, and reflectivity.

$$P_r = \frac{1.22^2 0.55^2 \pi^7 c}{1024 log_e(2)} \frac{P_t \tau D_a^2}{\lambda^4} \frac{T(0,r)^2}{r^2} |K|^2 Z \,, \tag{1.4}$$

where c is the speed of light, P_t the transmitted power, D_a^2 the antenna diameter, λ the wavelength, τ the pulse duration, T the transmittance along the atmospheric path, r the range to the sampling volume, $|K|^2$ the dielectric constant of the scatterers and Z the reflectivity. The gray section denotes constants, radar related parameters are green, path specific variables red and properties of the target blue. As the dielectric constant of liquid water and ice differ and the phase of the scatterers is unknown, the dielectric constant is assumed to be that of liquid water. Eq. 1.4 can then be used to obtain the equivalent reflectivity factor Z_e.

The reflectivity factor of a volume filled with spherical water drops in the Rayleigh scattering regime can also be described as a function of its size distribution:

$$Z = \int_0^\infty N(D) D^6 dD \,, \tag{1.5}$$

where N is the number concentration of particles and D their diameter. Since reflectivity scales with scatterer size to the sixth power, the largest particles present in the measured volume dominate the reflectivity. Reflectivity is commonly used to estimate precipitation rate on the ground. The precipitation rate R stemming from the drop size distribution (DSD) is defined as follows:

$$R = \frac{\pi}{6} \int_0^\infty N(D) D^3 w_r(D) dD \,, \tag{1.6}$$

where w_r is the fall speed of the hydrometeors. The corresponding reflectivity - rain rate relationship (also called Z-R relationship) usually takes the form:

$$Z = aR^b \tag{1.7}$$

The frequently used empirical fits of Gunn and Kinzer (1949); Joss and Waldvogel (1967) found values of a=300 and b=1.5, whereas in Switzerland a=316 and b=1.5 are used (Joss et al., 1998). While remote sensing only offers an indirect measurement and hence may be considered less precise than in-situ measurements, the data coverage is spatially continuous, offering a better coverage in space and time than, for instance, rain gauges.

Doppler Velocity and Dealiasing

Doppler velocity (v_{DOP})is the reflectivity-weighted average radial velocity of the scatterers in the target volume with respect to the radar. It is obtained by measuring the phase difference in between the separate electromagnetic pulses.

$$\Delta\varphi = -\frac{4\pi n}{\lambda} \frac{v_{DOP}}{PRF} \tag{1.8}$$

The direct velocity estimate is limited to an interval called the Nyquist interval (I_{NYQ}), which is bounded by $\pm v_{NYQ}$ (Nyquist velocity). This represents the velocities, which lead to a phase shift of less than 360° in between two pulses. The Nyquist velocity is given by

$$v_{NYQ} = \frac{\lambda}{4n} PRF \tag{1.9}$$

It therefore depends on both the wavelength and the PRF. Outside of this interval, the phase shift will be reprojected onto the range of 0-360°, hence leading to aliasing, also called folding. De-aliasing is subsequently the procedure of reconstructing the full velocity field. This is often done by obtaining a first guess about the flow direction and magnitude and using spatio-temporal continuity constraints to shift areas by +- I_{NYQ} and obtain a physically consistent velocity field. The smaller v_{NYQ} is, the more challenging the problem becomes, as physical

velocity differences can approach or even exceed v_{NYQ}.

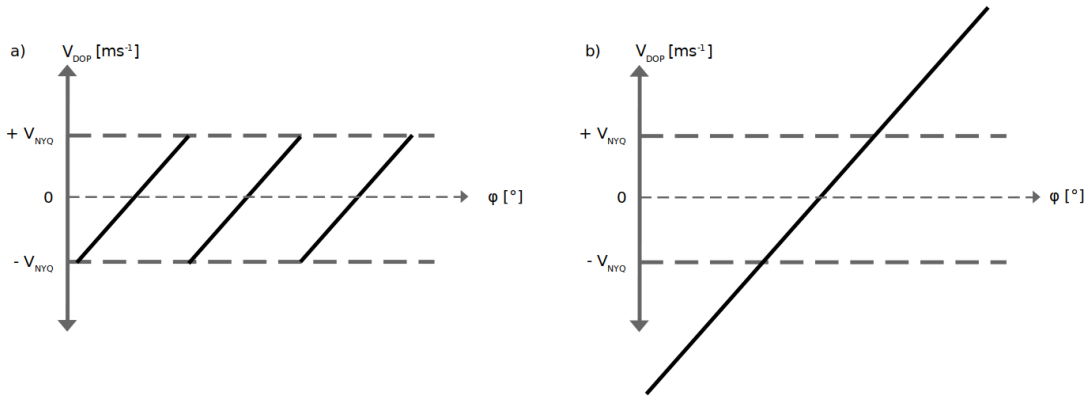

Figure 1.5: Schematic of (a) aliased and (b) de-aliased Doppler velocity along azimuth angle φ_{az}

Larger v_{NYQ} can be achieved by either a longer wavelength, or a higher PRF. The PRF, however, inversely correlates with the maximum unambiguous range, leading to the Nyquist dilemma:

$$r_{max} = \frac{c}{2nPRF} \tag{1.10}$$

With a given radar that has a prescribed wavelength, an increase in Nyquist velocity is at the expense of a decrease in maximum unambiguous range.
With Doppler velocity being a radial measurement and only providing the velocity component of scatterers towards the radar, it only provides partial information about the absolute velocity of scatterers. Fig. 1.6 shows how a linear wind field of 20 m s^{-1} presents from the view of a Doppler radar.

The components directly towards or away from the radar are measured at their full extent. In all other portions of the wind field, only the fraction pointed towards the radar is retrieved. In case of flow perpendicular to the radar beam, no velocity is measured at all. This results in an area of zero velocity, called the zero-isodop. In a linear flow situation the mean wind direction is orthogonal to the zero-isodop.
If close enough to one another, multiple radars can be combined in a multi-Doppler analysis to retrieve the full velocity field with u, v and w components. The derivatives of the radial velocity field also provide useful meteorological information. The azimuthal derivative approximates rotation on the plane of the elevation angle. Assuming a horizontal elevation and a symmetrical rotation, vertical vorticity can be derived with the following relationship:

$$\zeta_{DOP} = 2 \cdot \frac{dv_{DOP}}{d\varphi} \tag{1.11}$$

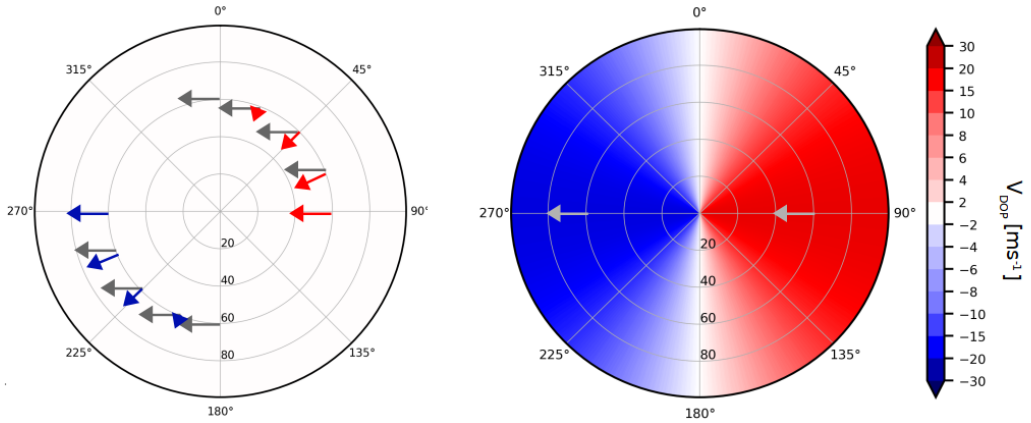

Figure 1.6: Schematic of a linear velocity field projected into radial winds, grey arrows denote velocity vectors, red arrows radial components towards the radar, blue arrows radial component away from the radar.

The assumption of axisymmetry determines the vorticity of the components lateral to the radar to be equal to those measured in radial direction. Conversely, the radial derivative corresponds to divergence on the plane of the elevation. Assuming a horizontal plane, horizontal divergence corresponds to the following:

$$div_{DOP} = \frac{dv_{DOP}}{dr} \tag{1.12}$$

Since divergence phenomena are not generally axisymmetric, we do not assume the component lateral to the radar here.

1.3.2 Swiss Operational Weather Radar Network

In this thesis we focus on exploiting the data of the Swiss operational weather radar network Rad4Alp, which is operated by MeteoSwiss (Germann et al., 2022). It consists in five polarimetric C-band radars that are situated at altitudes ranging from 900 to 3000 m above sea level (ASL). The overlap in between the radars ensures a high coverage in both the Swiss plains and above the Alps, where high-altitude terrain complicates radar observations. The radars are situated on the peaks of Albis, La Dôle, Monte Lema, Pointe de la Plaine Morte and Weissfluh, which reduces beam blockage in their close proximity.

They operate with a synchronized and static scan strategy that consists in 20 elevation angles from $-0.2°$ to $40°$. This corresponds to maximum unambiguous ranges between 246 km and 27 km, while the corresponding Nyquist velocity spans 8.25 $m\,s^{-1}$ to 20.63 $m\,s^{-1}$. The full volume is completed every 5 min. The scan is carried out in an interleaved manner, with a partial volume update of 10 elevations every 2.5 min. One partial volume operates with slightly higher PRFs, resulting in increased Nyquist velocities. The scan strategy is listed in Table 1.1.

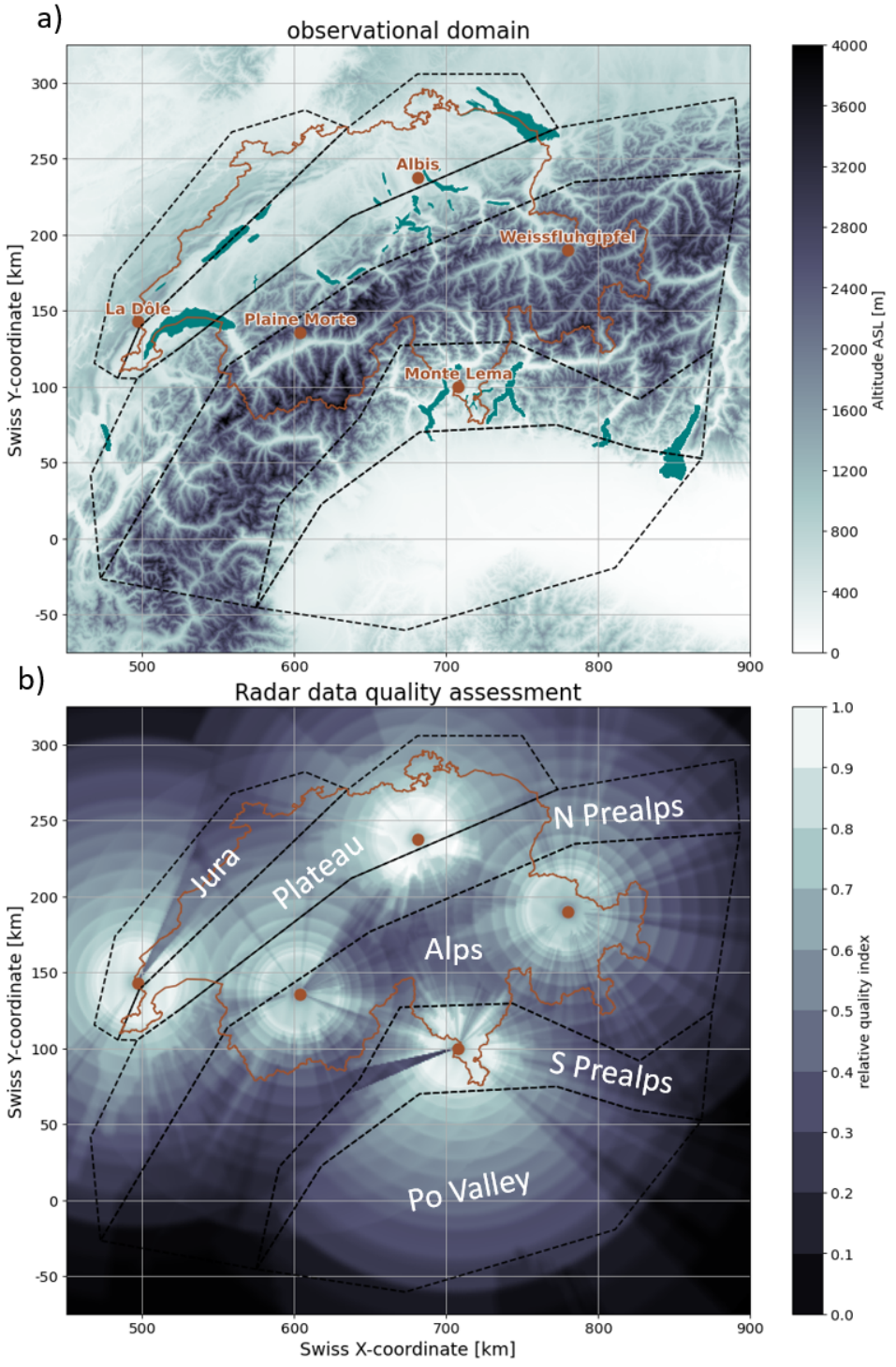

Figure 1.7: (a) Topographic map of the Swiss radar domain including radar locations; (b) relative quality map of Swiss radar network

Elevation angle [°]	r_{max} [km]	v_{NYQ} [m s^{-1}]	PRF [s^{-1}]	order [ ]
-0.2	246	8.25	600	5
0.4	210	9.625	700	15
1	246	8.25	600	4
1.6	162	12.375	900	14
2.5	183	11	800	3
3.5	162	12.375	900	13
4.5	146	13.75	1000	2
5.5	162	12.375	900	12
6.5	140	13.75	1000	1
7.5	121	16.5	1200	11
8.5	111	16.5	1200	10
9.5	100	16.5	1200	20
11	87	16.5	1200	9
13	75	20.625	1500	19
16	62	20.625	1500	8
20	50	20.625	1500	18
25	41	20.625	1500	7
30	34	20.625	1500	17
35	30	20.625	1500	6
40	27	20.625	1500	16

Table 1.1: MeteoSwiss scan strategy

The data are stored at 1° azimuthal and 500 m range resolution. The high temporal resolution for the full volume necessitates a high rotation rate, which limits the number of pulses per azimuth degree. To ensure high reliability and a good signal-to-noise ratio, the scan strategy operates with a single PRF per elevation. In an international context, the Nyquist velocities are considered to be very low and pose a challenging dealiasing problem. However, the long unambiguous ranges particularly at low elevations ensure a good coverage of the complex orography in the Alps. Multiple radars observe the area from different perspectives, so a beam blockage of one radar is generally covered by a scan of a different radar at a longer distance. The long ranges also provide observations far into the neighboring countries, providing timely information of approaching precipitation systems. The high temporal resolution is crucial for the observation of rapidly evolving orographic and convective precipitation.

Radar Data Processing

For a single radar, horizontal reflectivity, Doppler velocity and all polarimetric variables are available on a polar grid. All variables are provided after clutter removal. To combine the information from all available radars, a Cartesian mosaic is computed for certain variables. The Cartesian mosaic has a 1 x 1 km^2 horizontal resolution and spans an area of 640 x 710 km^2, extending well beyond the borders of Switzerland. The polar horizontal reflectivity data is interpolated into the Cartesian grid and a column maximum is applied, reducing it to a 2-D Cartesian data set. This Cartesian reflectivity product is used for e.g. thunderstorm tracking. The polar horizontal reflectivity is also the primary driver of the radar-derived precipitation estimate. By applying a vertical weighting scheme to the polar reflectivity data (Gabella et al., 2017), the following Z-R relationship is applied to compute the rain rate at MeteoSwiss (Joss et al., 1998):

$$Z = 316R^{1.5} \tag{1.13}$$

The rain rate is also provided as a 2-D Cartesian data set every 5 min (Gabella et al., 2017; Germann et al., 2022).
Additional reflectivity-derived metrics, such as echotop height (ET, highest altitude of a certain reflectivity threshold) and vertically integrated liquid (VIL, column estimate of all liquid) are additionally computed on the Cartesian grid.

1.3.3 Thunderstorm Tracking

Thunderstorm tracking algorithms aim to identify convective cells and track their evolution over time. They are most commonly used with weather radar data, but also operate on satellite or lightning data, and are often also able to process numerical model output data to identify and track convection in models. MeteoSwiss' operational algorithm thunderstorm radar tracking (TRT, Hering et al., 2004) employs object detection techniques in the 2-D max. reflectivity data. A multi-threshold approach is used to identify the high-reflectivity cores of convective cells. The cell area is then grown outwards until it meets all minimum requirements for a thunderstorm cell with constraints on cell size and a variable lower reflectivity threshold that sets the cell boundary around the most relevant area for each case. This outward growing approach also separates convective cores that are within a congruent high-reflectivity area, as long as the reflectivity in between them dips sufficiently low. For tracking in time, each cell is advected with its average past motion of three time steps and matched to the new detections in the next time step. With sufficient overlap, cells are determined to be the same and added to a cohesive cell track. In storm splits and mergers, the respective smaller cell is considered to be newly generated or decayed.
TRT also extracts characteristic variables within the cell contour for each time step, providing a tabular data set for each identified thunderstorm with its track and radar-observed intensity evolution. The spatio-temporal resolution is determined by the 1x1 km^2 and 5 min resolution of the input data.

1.3.4 Mesocyclone Detection

To identify supercells in radar data, mesocyclone detection algorithms have been used for several decades (Stumpf et al., 1998). They aim to detect the rotation in the supercell updraft, namely the mesocyclone (Kumjian and Ryzhkov, 2008). This involves the identification of a vertically consistent and temporally persistent rotation within a convective cell. Commonly, this is performed by using dealiased Doppler velocity data of the closest radar. The azimuthal shear field provides the necessary information to find anomalous areas and compute vorticity (see Eq. 1.11) and rotation metrics for these. Identified areas per elevation can then be assembled vertically into a 3-D object and tracked in time (Stumpf et al., 1998; Hengstebeck et al., 2018).
Due to the prevalence of cyclonic supercells in many areas, these algorithms are often confined to only detecting cyclonic rotation. In Switzerland, past research indicates a prominent fraction of anticyclonic cells, (Houze et al., 1993) indicating a necessity to detect both senses of rotation.
Mesocyclone detection is sensitive to the quality of the Doppler velocity data, particularly to persisting aliasing (Xu and Nai, 2017). With remaining folds, the azimuthal derivative contains sharp, pixelated anomalies on the order of the Nyquist interval. As dealiasing algorithms often employ vertical and temporal consistency as well (James and Houze, 2001; Feldmann et al., 2020), dealiasing errors have the potential to erroneously trigger a mesocyclone detection, if not handled with care.

1.3.5 Radar-based Hail Detection

The vertical structure of reflectivity is often used to determine the presence of hail and estimate its size. Approaches including polarimetric variables are also becoming more common. We here focus on the operational products probability of hail (POH, Waldvogel et al., 1979; Foote et al., 2005; Betschart and Hering, 2012) and maximum expected severe hail size (MESHS, Betschart and Hering, 2012). POH represents a relationship between the altitude of the highest 45 dBz radar echo (ET45) and the melting level, as computed by the numerical weather prediction model COSMO-1 (Consortium for Small Scale Modelling, 2018). As it represents a probability, POH ranges from 0-100 % and only refers to the presence, not the size of hail. MESHS on the other hand estimates the maximum size of severe hail, starting from 2 cm maximum dimension. Here, the relationship consists in the distance between the highest 50 dBz radar echo (ET50) and the model-derived melting level, following the Treloar nomogram (Treloar, 1998).
Particularly the estimation of hail size from radar data remains challenging, even when exploiting polarimetric variables. This stems from a lack of observations of hail size distributions, hence our ability to accurately determine the size distribution from radar measurements is strongly limited. Especially at C-band, hailstones often reach sizes that cause resonance scattering effects, transitioning from the Rayleigh scattering regime into the Mie scattering regime (Ryzhkov and Zrnic, 2019). Here, the returned power no longer increases with size, but

rather oscillates, further complicating the problem. In addition, C-band beams are attenuated more easily, which leads to hail-induced beam shielding, in extreme cases.
In this context we largely use POH and MESHS in combination to determine the overall presence of hail. We additionally use MESHS to separate small from large hail and obtain relative size tendencies.

Figure 1.8 shows a case example of thunderstorm tracking and hail detection at MeteoSwiss from June 28, 2022. TRT presents the observer with information on cell location and size (location and size of ellipses), severity (ellipse color), projected motion (arrows), future affected areas (shaded ellipses) and the past track (orange line). In this case we see a splitting supercell (a), where subsequently the right mover intensifies strongly (b, c) and produces a prolonged hail swath along the Southern Prealps (e, f) before weakening upon moving into the main Alpine ridge and finally decaying at the border to Austria (d). The left-mover's track leads immediately into the high-altitude mountains of Valais, which prevent further intensification (b).

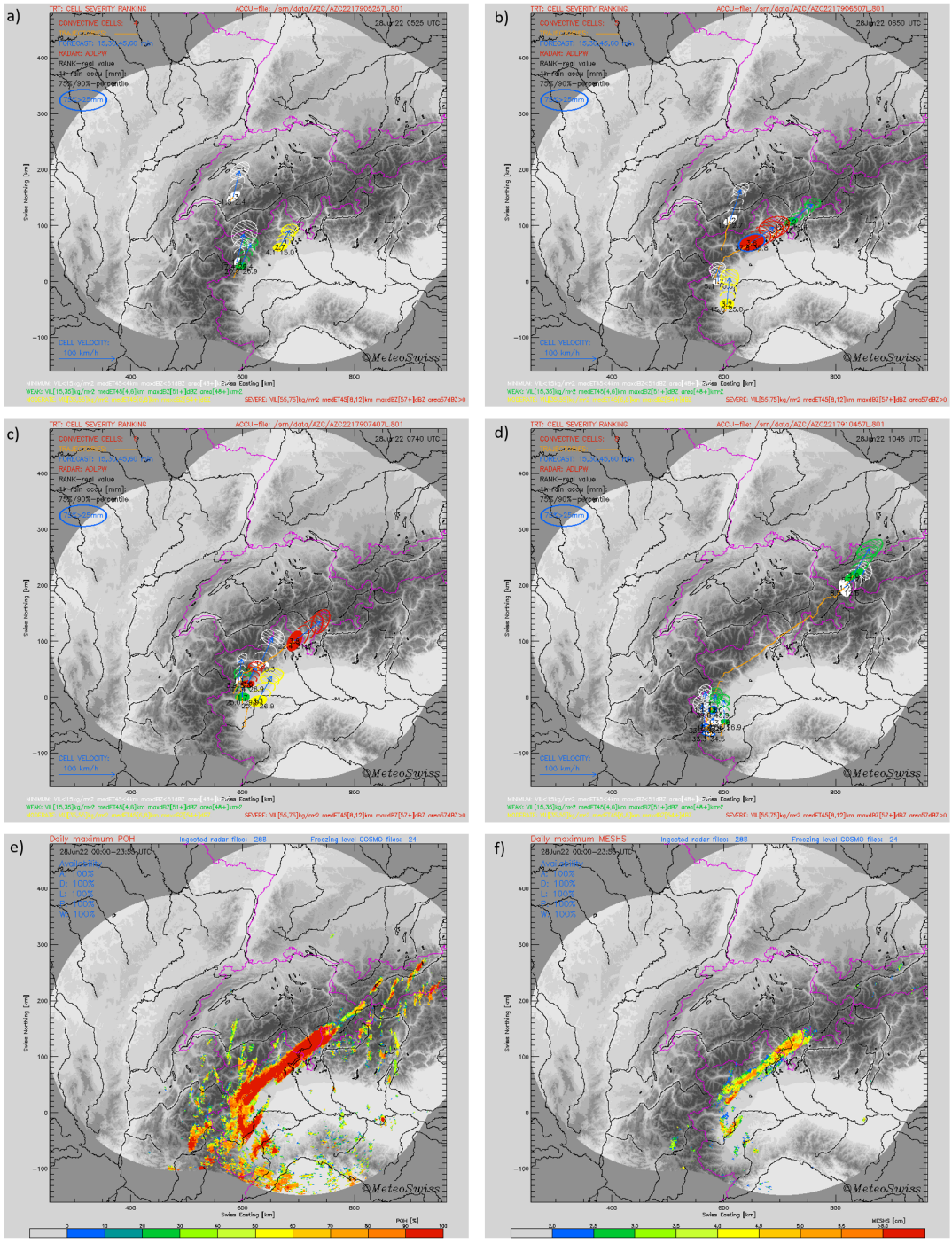

Figure 1.8: Example of thunderstorm tracking at MeteoSwiss: a)-d) result of TRT, severity rank of detected thunderstorms depicted in colored ellipses, projected movement indicated with arrows and shaded ellipses, e) daily integrated max. POH, f) daily integrated max. MESHS; example of June 28 2022: a) splitting storm in northwestern Italy (green and white ellipses), b) left-mover decaying in Valais, right-mover intensified to supercell, moving towards Ticino, c) peak intensity of right-mover over Locarno, d) right-mover decays in Grisons, total track indicated with orange line; ©MeteoSwiss

1.4 Outline

As outlined above, the effects of topography on supercell thunderstorms are poorly understood. A large fraction of research focuses on the Great Plains of the United States, where the terrain is predominantly flat. Emerging research undertaken over the Appalachians and in South America over the Sierras de Cordoba allows a better understanding of the influence of topography on storm environments, convective initiation and upscale growth. Due to the observational challenges in complex terrain, systematic data sets of supercells in mountainous regions are rare and often confined to field campaigns. In Switzerland we have the advantage of a dense, high-quality radar network in both one of Europe's most active convective regions and within considerable orographic complexity including steep topography ranging from low to very high altitudes. This presents one with the unique opportunity to investigate convective behavior over a range of topographically diverse sub-regions within the same observation network.
The main questions we aim to answer during this thesis can be summarized as follows:

- Can we systematically detect supercell thunderstorms using the operational radar data?
- How often do supercell thunderstorms occur in the Swiss domain? Where and when do they occur preferentially?
- Are there clear dependencies on the underlying topography?
- How do supercells compare to other types of severe convection?
- How does topography influence the evolution of supercells?

Supercell thunderstorms are largely unexplored in Switzerland and we here aim to establish a general understanding of supercell occurrence and behavior within the observational domain of the Swiss radar network. Exploiting the high quality of spatially and temporally dense observations, we assess the spatial and temporal patterns in supercell occurrence over a multi-year period. In the complex terrain of the Swiss Alps the influence of topography is a key factor for severe convection. The systematic observations allow us to identify patterns related to orographic complexity and to compare them to other types of severe convection. Based on the findings from observational analyses, idealized modeling helps us establish an understanding of the processes driving the topographic effects.
Our main objectives are summarized by the following points:

- Systematic supercell tracking
- Characterization of supercell frequency and spatio-temporal occurrence
- Identification of topographic influence
- Comparison with other types of severe convection

- Understanding of processes leading to orographic impact

To pursue these scientific questions, we seek to develop a robust Doppler velocity processing chain to reliably detect supercell thunderstorms in the Swiss radar network. This first involves revising the existing dealiasing algorithm 4DD (James and Houze, 2001), which is described in chapter 2. The new algorithm must work within the operational constraints of processing a full volume well below the update time and yield high-quality results, particularly in convective situations. Subsequently, in chapter 3, existing mesocyclone detection techniques are combined and tailored to the specifics of the application within the Alpine region. In addition, we evaluate the spatial heterogeneity of the observational quality to avoid spurious artifacts in our results. With this basis, chapter 4 establishes a multi-year database to assess the spatial and temporal patterns of supercell occurrence in the observed domain, covering the spatial occurrence patterns, diurnal cycle, dependency on synoptic weather and influence of complex terrain. In chapter 5, we additionally establish a comparison with other types of better-understood convective storms, to provide context for this new storm classification. This comparison highlights spatial frequency patterns in contrast with intensity patterns. The spatial patterns are clearly influenced by the orographic complexity. To improve our understanding of the underlying meteorological processes, in chapter 6 we derive simplified, idealized modeling scenarios to investigate topographic, surface-related and environmental factors that drive the observed patterns. This allows us to develop a conceptual model that demonstrates key processes responsible for supercell frequency clusters in Prealpine lake valleys. Chapter 7 then summarizes the results and provides perspectives for future work.

2 R2D2: A Region-Based Recursive Doppler Dealiasing Algorithm for Operational Weather Radar

This chapter is based on the postprint version of the published article “Feldmann, M., James, C. N., Boscacci, M., Leuenberger, D., Gabella, M., Germann, U., Wolfensberger, D., & Berne, A. (2020). R2D2: A Region-Based Recursive Doppler Dealiasing Algorithm for Operational Weather Radar, Journal of Atmospheric and Oceanic Technology, 37(12), 2341-2356". The dealiasing algorithm was developed by both Monika Feldmann and Prof. Curtis N. James. Prof. Curtis N. James implemented the code, while Monika Feldmann derived and set up the performance assessment utilizing model data. Marco Boscacci assisted with the implementation of the code and ensured transferability to MeteoSwiss's operational chain. Dr. Daniel Leuenberger provided the high-resolution model data used for performance assessment. Dr. Daniel Wolfensberger previously developed the radar operator used for performance evaluation and adapted it for the purpose of aliasing velocity fields. Dr. Marco Gabella, Dr. Urs Germann and Prof. Alexis Berne organized the project and supervised the progress.

This chapter discusses the development and evaluation of a novel dealiasing algorithm for the processing of the Swiss operational Doppler velocity data. This first step ensures a sufficient quality of Doppler velocity data to use it for mesocyclone detection. In addition, the improvement of the Doppler velocity data brings the potential of further velocity-related product development at MeteoSwiss.

2.1 Introduction

2.1.1 Doppler Radar Challenges in Complex Terrain

Doppler velocity measurements are a useful weather monitoring tool, as they provide near real-time information about the inner dynamics of meteorological phenomena. The identification of strong gate-to-gate velocity shears in azimuth (corresponding to rotation), or in range (corresponding to divergence), can provide key information about meteorological hazards such as turbulence, severity of convection, frontal activity and wind gusts. For nowcasting applications and weather warnings, as well as data assimilation, the correct retrieval of Doppler velocity measurements is essential.

As the Doppler velocity corresponds to the measured phase shift between the incident and reflected signal, ambiguous measurements occur if the shift exceeds 2π. This phenomenon is called aliasing. The maximum unambiguous velocity, or Nyquist velocity, $\pm v_{NYQ}$, increases with increasing pulse repetition frequency (PRF) and thus results in a trade off with maximum unambiguous range.

Since Doppler velocity measurements provide a valuable tool in analyzing the dynamical evolution of precipitation systems and can aid in assessing potential hazards in weather situations, a high-quality reconstruction of the true velocity field is essential. The process of removing the velocity folds, or aliases, is called dealiasing.

In mountainous terrain, the Doppler dilemma presents an additional challenge. With beam blockage from terrain significantly reducing the observable terrain, a long unambiguous range from multiple radars can help ensure more accurate measurements, by covering the same area from different directions and angles (Germann et al., 2016a). Moreover, the rapid, dynamic nature of mountain meteorology calls for a frequent volume update to adequately monitor evolving precipitation fields (Germann et al., 2016a). In this study, we focus on the operational radar network of MeteoSwiss Rad4Alp (Germann et al., 2015, 2016c) that is tailored to Alpine precipitation monitoring. With long ranges, particularly at low elevations, and a rapid volume update over 20 elevations it is well-suited to the operational requirements of precipitation, thunderstorm and hail nowcasting. Due to limited observable range and construction constraints in an Alpine environment, the network consists in 5 polarimetric C-band radars.

These decisions result in an overall low Nyquist velocity, which introduces a particularly challenging situation for handling Doppler velocity measurements. Problems arise when turbulence, shears or rotational patterns commonly present in the airflow around the Alps are not well resolved by the Nyquist velocity.

2.1.2 Existing Dealiasing Methods

The main feature of many dealiasing algorithms is 2-D spatial continuity within each elevation scan (He et al., 2011; Witt and Brown, 2009; Zhang and Wang, 2006; Eilts and Smith, 1990). Here, each gate is inspected with respect to its velocity difference with its neighbors, to detect and resolve aliasing. This also increases the dependency of dealiasing decisions on single gates. Helmus and Collis (2016), Xu et al. (2011) and Wüest et al. (2000) reduce the importance of single gates by relying on larger areas of information for dealiasing decisions. A regional approach is also taken by Yuan et al. (2020), where areas of contiguous data coverage are first identified and then further split along velocity folds into regions. Each region is assigned a single dealiasing solution, thus also avoiding issues from single gates. A mixture of regional and spatial dealiasing is pursued by Louf et al. (2020). The main dealiasing approach is similar to spatial dealiasing and solves gate by gate, however it draws on a larger, predefined region around each gate to obtain a solution.
When Doppler velocity cells are disconnected from each other by regions with no echoes, it is often advantageous to utilize supplemental information about the velocity field during the dealiasing process. To estimate the general velocity direction and magnitude above a radar, the velocity azimuth display (VAD) is a method that assumes a horizontally uniform velocity field and provides an estimated vertical profile of horizontal velocity (Germann, 1999). At constant altitude, all available radar measurements are fitted to a sine curve with azimuth to estimate velocity magnitude and bearing from the phase and amplitude of the sine curve.
While different methods exist to derive a VAD (Germann, 1999; Tabary et al., 2001; Xu et al., 2010), several dealiasing approaches rely on the VAD as additional wind information to aide dealiasing (He et al., 2011; Xu et al., 2011; Witt and Brown, 2009; Wüest et al., 2000; Eilts and Smith, 1990). The VAD provides useful information to initialize dealiasing, however it does not represent spatial heterogeneity and requires sufficient data coverage around the radar in order to create a representative velocity profile. Therefore a VAD is inadequate for initializing dealiasing when spatial heterogeneity of the velocity field and/or high shear exist in the radial velocity field. Zhang and Wang (2006) and also Louf et al. (2020) propose to identify the primary wind direction without additional wind information, by initializing close to the zero isodop. This can be problematic in cases, when wind velocities exceed multiples of the Nyquist interval, thus leading to the occurrence of several zero isodops. James and Houze (2001) proposed the use of 4-D data continuity, leveraging the vertical and temporal dimensions available in operational Doppler data streams, to improve dealiasing in the presence of shear or heterogeneity. Yuan et al. (2020) use local reference points from the current sweep, or from the sweeps above and from a previous radar sweep if necessary, to determine the general flow. Thus, Yuan et al. (2020) have also extended dealiasing from 2-D to 4-D continuity constraints. Louf et al. (2020) utilize 4-D continuity within their error detection procedure. Lim and Sun (2010) showed that using the product of assimilated Doppler velocities into a numerical weather prediction (NWP) model yields a substantially better approximation of the velocity field, retaining spatial heterogeneity. Xu et al. (2013) also make use of hourly model-predicted winds to improve velocity estimates for isolated areas at far ranges.

The preceding techniques do not specifically target problematic dealiasing phenomena, such as supercellular mesocyclones or tropical cyclones, though some recent studies have focused on targeting these specifically, such as Xu and Nai (2017) for mesocyclones and Jiang and Xu (2016) and Chang et al. (2019) for tropical cyclones. These situations are both characterized by strong vortex winds that pose difficult dealiasing problems due to the curvature of the velocity field and high shear. These latter studies propose fitting vortex models to the radius and magnitude of the rotational velocity maxima and re-initializing dealiasing with the fitted vortex model.
Recent work has shown an aliasing-robust implementation of the integrated velocity-azimuth process (IVAP) (Liang et al., 2019). This method effectively provides localized reference winds and thus aides local turbulence phenomena, however is computationally quite demanding.

Since 2005, MeteoSwiss has implemented 4-Dimensional Dealiasing (4DD, James and Houze 2001) as its operational dealiasing algorithm. 4DD specializes in solving dealiasing problems with low Nyquist velocities, as mentioned above, by applying 4-D continuity constraints from the previous time step, the elevation above, and in 2-D space within the targeted elevation. If there is insufficient information in the sweeps before and above, it relies on the VAD (Tabary et al., 2001) as a last resort to initialize dealiasing. The particular challenge with low Nyquist velocities is the occurrence of multiple folds. This can make it difficult to identify the correct zero isodop without additional information.
4DD initializes dealiasing in single velocity gates that have a high level of agreement with the according gate in the sweep before and above. From there, the algorithm spreads, applying 2-D continuity constraints. This procedure is repeated until the majority of the data has been reconstructed. Remaining data segments are targeted with a windowing technique, where a larger spatial window is used to estimate the correct Nyquist interval of remaining, uncorrected areas.
Particularly in stratiform precipitation situations, where the data coverage is high and velocities are more homogeneous, 4DD provides very reliable results. Stratiform events constitute the majority of precipitation situations in Switzerland, especially during the cold season.
However, in convective situations with low Nyquist velocity, when the data coverage is more fragmented and strong gate-to-gate shears and turbulence abound, 4DD exhibits some performance issues. If dealiasing erroneously initializes in a noisy gate, the error propagates in space via the 2-D spatial dealiasing technique and feeds into the sweeps below and the next time steps due to the vertical and temporal continuity constraints. The same issue occurs in the case of unresolved wind shear from one gate to the next. Spatial dealiasing can assign the wrong Nyquist interval in these situations, resulting in a spreading error. Additionally, the VAD method has issues in low data coverage, as it reconstructs velocity magnitude and direction from measurements at constant altitude around the radar. As the VAD assumes spatial homogeneity of the wind field, it is also less representative in heterogeneous, turbulent situations, as commonly found in convection. The complex wind field often observed in the Alps, especially in the presence of deep convection, further complicates the dealiasing

problem.
Therefore, we focus this study on developing a technique that reduces the importance of single gates on dealiasing decisions and mitigates error propagation horizontally, but also vertically and in time.
This paper describes the development of a novel dealiasing algorithm targeted at these challenging circumstances. Section 2.2 introduces the data that were used for algorithm development and testing. Section 2.3 describes the design of the new algorithm, called Region-based Recursive Doppler Dealiasing (R2D2). In section 2.4, the results of a comparison between R2D2 and its predecessor 4DD are presented. Finally, section 2.5 concludes the evaluation of R2D2.

2.2 Data

2.2.1 Radar Network of Switzerland

This dealiasing approach aims to improve over the current operational algorithm of Switzerland's operational radar network. The radar network of MeteoSwiss consists of five polarimetric C-band radars (Germann et al., 2016b; Bundesamt für Meteorologie und Klimatologie MeteoSchweiz, 2018). Their altitudes range from 900 m to 3000 m above sea level, which ensures a good coverage of the Swiss plains and above the Alps. They are located on the peaks of Albis, La Dôle, Monte Lema, Pointe de la Plaine Morte and Weissfluh (see Fig. 2.1). A more detailed description of the operational scan strategy is given in section 1.3.2. The Doppler velocity fields operationally available are processed with 4DD, as described in section 2.1.2, using each corresponding VAD as an environmental wind estimate.

Velocity Azimuth Display

VADs for all five radars are operationally produced every five minutes. The implemented algorithm follows Tabary et al. (2001) and is briefly described in the following section.
The VAD utilizes the sinusoidal behavior of a Doppler velocity field at constant range. By merging all available velocity measurements at constant altitude from the two highest elevation scans, the VAD algorithm reconstructs a vertical profile of horizontal wind above the radar. First the VAD algorithm is also faced with aliased velocity gates. To solve this, the azimuthal derivative of the radial wind is computed. As the derivative of the radial wind has sinusoidal behavior, a sine curve is fitted to the derivative as a first estimate of the VAD wind vector. Thereafter, this first estimate is used to dealias all velocity gates. Then, a second sine curve is fitted to the dealiased velocity gates. Phase and amplitude of this sine curve yield the VAD wind vector, if sufficient data are available. The elevations at 35° and 40° represent and area of approximately 22 km around each radar. Fitting a sine-curve assumes a horizontally uniform velocity field within this region. Low data coverage and turbulent situations compromise the quality of the vertical profile.

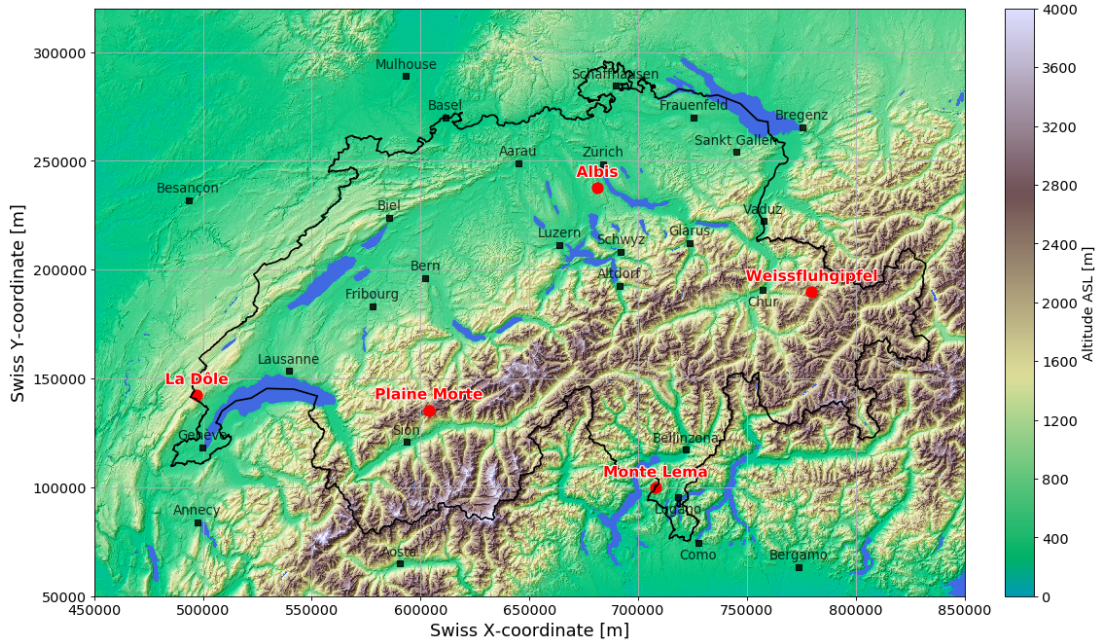

Figure 2.1: Elevation Map of the Western Alps with the 5 radar sites (marked in red) of the dual-polarization operational Swiss weather radar network (Rad4Alp). Major cities are indicated in black.

2.2.2 COSMO-1 Numerical Weather Prediction Model

COSMO-1 is the operational, high-resolution NWP model of MeteoSwiss with a horizontal mesh size of 1.1 km (de Morsier et al., 2012). It provides a high-resolution 3-D wind field over the Swiss radar domain and is used here as an alternative source of environmental wind information.

As a non-hydrostatic, convection-permitting model it also partially resolves the internal dynamics of convective systems. To reproduce the observed wind field as closely as possible, COSMO-1 is used in analysis mode, where it assimilates observations from radiosondes, surface weather stations, wind profilers, aircrafts and surface precipitation estimates from the five Swiss C-Band radars. The boundary conditions are provided by the European Centre for Medium Range Forecasts (ECMWF) global model. To match the temporal resolution of the radar data, the output frequency is set to 5 minutes.

2.2.3 Forward Polarimetric Radar Operator

A forward polarimetric radar operator, as introduced in Wolfensberger and Berne (2018), allows us to transform COSMO-1 output into the perspective of a radar. The radar operator is configured to mimic the Swiss operational scan strategy, replicating the maximum range, Nyquist velocity and elevation angles at the five radar locations. It additionally accounts for terrain blockage.
Our main interest is the creation of a simulated Doppler velocity field for testing the performance of dealiasing algorithms. With the possibility to change the Nyquist velocity easily, the COSMO-1 data is processed once with the operationally implemented Nyquist velocity and once without any Nyquist constraint. This allows the computation of a ground truth, to which the folded velocity field and different dealiasing results can be compared.

2.2.4 Analyzed Case Studies

The analyzed data expands over six case studies representing different meteorological situations. With the focus being on improving the dealiasing performance in convective situations, four of them represent different convective cases, while the other two represent stratiform situations. The selected cases present challenging dealiased situations due to the presence of high wind speeds, low data coverage and high wind shear. Table 2.1 provides an overview of the case studies.
All case studies provide at least three hours of data for the analysis, with sufficient previous data to allow for algorithm start-up. Overall, 372 time steps are analyzed, resulting in 7440 elevation scans.

Table 2.1: Case studies

Date	observing radar	event
2 Aug 2017	Albis radar	supercellular convection
11 Jun 2018	La Dôle radar	multicellular convection
15 Jun 2019	La Dôle radar	mesoscale convective system
11 Aug 2019	Pointe de la Plaine Morte radar	supercellular convection
7 Mar 2019	Weissfluhgipfel radar	cold front passage with high winds
19 Oct 2019	Monte Lema radar	cold front passage with collapsing Foehn situation

2.3 Region-based Recursive Doppler Dealiasing (R2D2)

2.3.1 First Guess Field

Instead of ingesting the radar's VAD as additional environmental wind information, we replace it with NWP data. For this purpose we use COSMO-1 analysis' 5 minute output of the 3-D wind field. To avoid errors stemming from convective features, such as thunderstorm inflow, gust fronts or mesocyclones, that may be misplaced in space and time, the field is smoothed with a 20 km convolution kernel. Dynamical convective features generally have a size smaller than 10 km (Markowski and Richardson, 2010). By applying the convolution to the wind field, the general flow and spatial heterogeneity are conserved, while strongly reducing the influence of convective features.
To derive a first guess of the wind field from the radars' perspective, the wind field is transformed to a radial wind field for each radar using a purely trigonometric approach. The radial wind field is extracted at all 20 elevations. This COSMO-derived radial wind estimate for each elevation replaces the VAD in our tests.
The first-guess field is only used if there are no other data sources available. Its intention is to provide the general direction and magnitude of the flow and its spatial distribution, not small-scale dynamic features.

2.3.2 Dealiasing Procedure

Considering the existing algorithms described in section 2.1.2, our main criteria for a novel algorithm can be summarized as follows:

1. Apply a regional approach to reduce importance of single gates.
2. Utilize 4-D continuity to reduce dependency on environmental winds.
3. Mitigate error propagation.
4. Supplement dealiasing using 3-D velocity information.
5. Ensure reliability and efficiency for operational implementation.

Following James and Houze (2001) R2D2 best operates on a continuous data stream, where the algorithm can leverage 4-D constraints. In each volume, it starts at the highest elevation where the Nyquist velocity is typically larger and where Doppler velocity data are generally less noisy, then proceeds downward to the more difficult low-elevation sweeps. Within each sweep, it follows a 9-step procedure, as shown in Fig. 2.2.

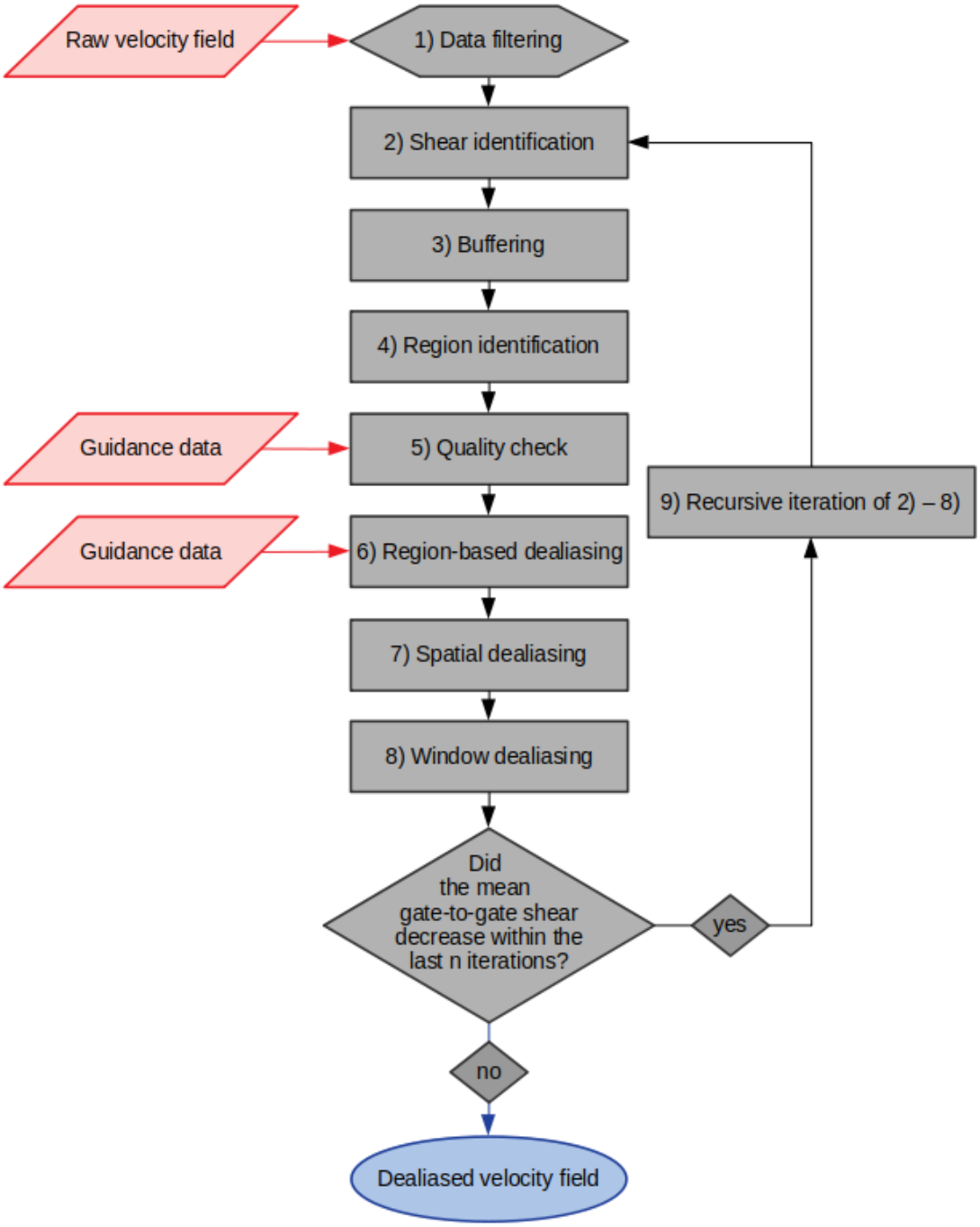

Figure 2.2: Flowchart of algorithm steps within R2D2, red corresponds to input data, gray to algorithm step and blue to output data

Data filtering - Step 1

Prior to dealiasing, the operational clutter detection algorithm of MeteoSwiss is applied. It makes use of criteria on reflectivity, Doppler spectrum and velocity, signal fluctuations, differential phase shift and reflectivity, copolar correlation coefficient and dynamic and static clutter maps to identify non-meteorological echoes. Clutter cancellation is done individually for each 83 m gate, the highest possible radial resolution, which is an important aspect in complex terrain (MeteoSwiss, 2020; Germann and Joss, 2004). Faced with the challenge of retaining as much data as possible, while dealing with considerable terrain contamination in the main and side lobes of the radar beams, the resulting Doppler velocity field still contains noise and residual clutter.
Therefore, in the first step, the raw radial velocity data are filtered to minimize the influence of noise, which can introduce errors during dealiasing. The algorithm first deletes all small, isolated echoes or speckles in each sweep that occupy an area equivalent to or less than 10 connected gates at a range of 100 km from the radar, and whose velocity values are close to zero. Experience has shown that these small regions generally contain noise and would otherwise lead to problems during the windowing procedure (see step 8). In addition, the user may opt to apply a Bergen and Albers filter (Bergen and Albers, 1988), to remove problematic gates on the edges of larger data regions, or apply a reflectivity threshold that discards all gates below a certain value. Finally, the user has the ability to remove terrain clutter. If the radar's visibility (Gabella et al., 2017) decreases with range along a radial, or drops below a user-defined threshold, the surrounding gates may be discarded as shadowed regions, respectively. The filtering process seeks to improve the quality of the raw velocity data and increase the likelihood of success in a simple and efficient manner, though too much deletion (especially of terrain shadowed regions) can create discontinuities in the data and make dealiasing more challenging.

Anomalous Shear Identification and Buffering - Steps 2 and 3

Before initializing dealiasing, the maximum value of the absolute difference D of each velocity gate to its up to eight neighbors is computed. All gates where the maximum difference exceeds a primary threshold b are flagged as high-shear gates. All gates within a 5x5 range of the initially identified gate are also flagged. These buffer zones covering high-shear areas and their vicinity are excluded from the initial dealiasing attempts. They are deemed to be difficult to dealias, as they either contain a velocity fold or high wind shear. The size of 5x5 gates aims to include small regions of unresolved shear lying close to detectable shear, without making the zones so large that they cover excessive amounts of data.
The conceptual schematic in Fig. 2.3 exemplifies this procedure. Figure 2.3a shows the initial velocity field that contains a turbulent region on the left and a velocity fold at the bottom right. Figure 2.3b depicts the maximum gate-to-gate difference in any direction from each gate, which strongly highlights the fold, but also the area of turbulence. Figures 2.3c and d then show the resulting buffered areas in gray, overlaid on the velocity and maximum difference

field, respectively. Here, a threshold of 8 m s^{-1} was used, which corresponds to $0.8 \cdot v_{NYQ}$.

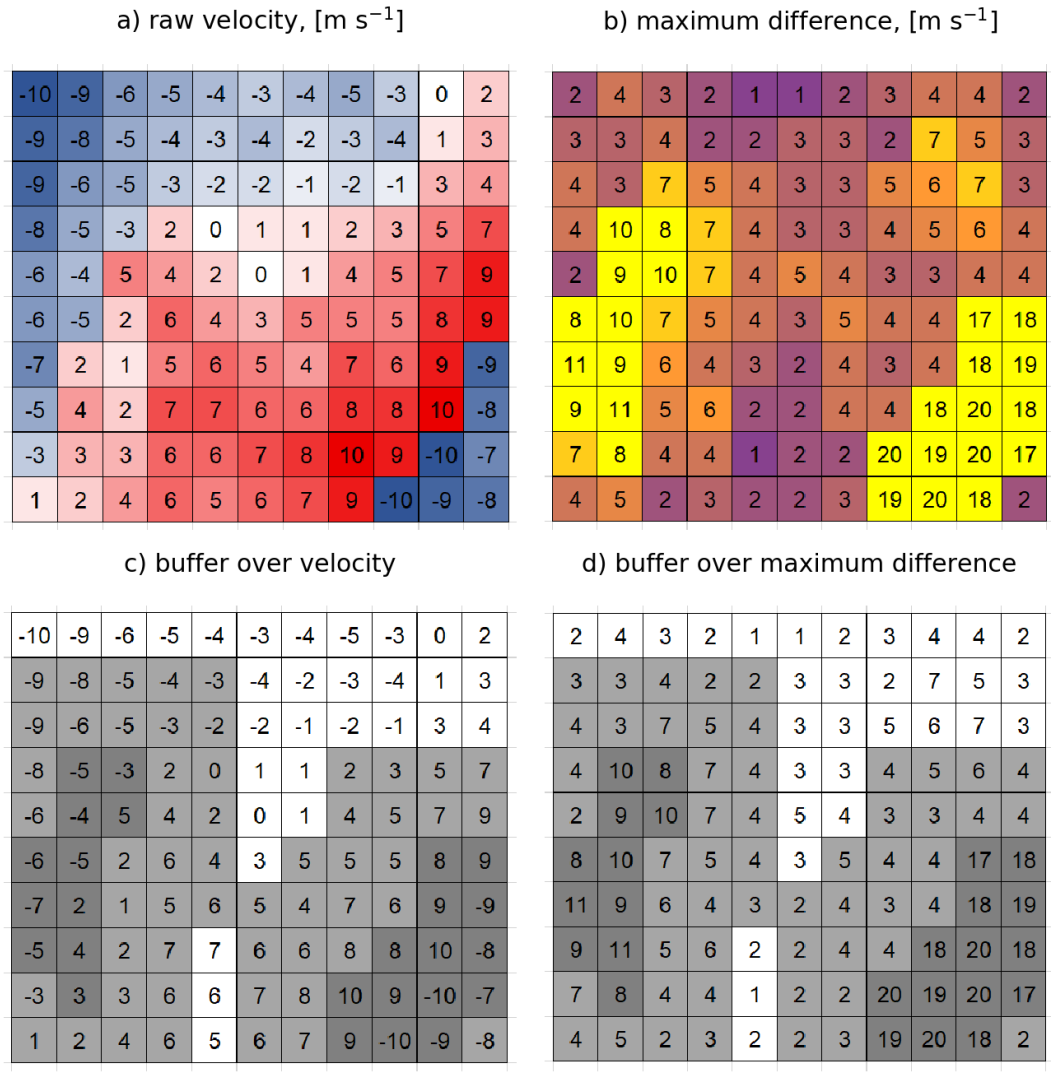

Figure 2.3: Conceptual schematic of buffering procedure of R2D2; Top left: v_{DOP} in m s^{-1}, $v_{NYQ} = 10$ m s^{-1}; Top right: maximum difference D in m s^{-1}, threshold $b = 0.8 \cdot v_{NYQ} = 8$ m s^{-1}; Bottom images: v_{DOP} and D with gates, where $D >= b$, in dark gray shading and the resulting 5x5 buffer in light gray shading

Low-shear Regions and Quality Check - Steps 4 and 5

After the buffer zones have been flagged, it is assumed that the remaining regions do not contain any folds or high shear. Each congruent region is referenced with an ID and assigned to the same Nyquist interval. Figure 2.4 illustrates a modelled example of this procedure. Figure 2.4a shows the folded velocity as produced by the radar operator, noting that by Swiss convention positive radial velocity means inbound motion. Figure 2.4b depicts the maximum

difference field. The resulting buffer zones, derived by the same procedure as in Fig. 2.3, are shown in dark blue in Fig. 2.4c. All contiguous white regions are assigned an individual ID for the subsequent dealiasing procedure.
As we are dealing with very small Nyquist velocities, there remains the possibility of an extended region of unresolved shear, a hidden fold, where the difference to the neighboring gates actually exceeds the Nyquist velocity, inside the identified regions. To prevent this from happening, a quality check is implemented. Each region is compared to the corresponding gates in the sweep above, the sweep before and the first guess field. These three fields provide the guidance information for each region. If the standard deviation of the difference between all gates in a region and its guidance data exceeds a certain threshold g, it is likely that there still remains a fold in the region, or its guidance data. In this case, the region is also flagged as a buffer zone to avoid introducing or propagating a large error. By comparing each region to the guidance, the algorithm makes use of 4-D continuity information available in the velocity field. As the elevations are relatively close to each other and are updated every five minutes, in most cases they correspond to the velocity field of the current elevation very well.

Dealiasing - Steps 6 - 8

The remaining regions are then assigned into their respective Nyquist intervals. To obtain the correct Nyquist interval, each region as a whole is compared to the corresponding gates in the sweep above and in the previous time step. In the first iteration, if both of these data are missing in more than 90 % of the gates, the first guess field is used as an added constraint. In subsequent iterations, all guidance information is used. For each guidance region, the average difference to the current region is computed and the Nyquist interval of least absolute difference is assigned. If the Nyquist interval matches for all available guidance information, the region is dealiased. If there is disagreement, the region is flagged as a buffer zone and reserved for spatial dealiasing.
After all regions have been dealiased in this manner, spatial dealiasing corrects the buffer zones. Spatial dealiasing follows the procedure of James and Houze (2001), except that it is only used within these buffer regions in order to confine potential errors to smaller areas. Gates adjoining dealiased gates are corrected by shifting them by a number of Nyquist intervals to result in a velocity difference smaller than a certain threshold s to the dealiased neighbors. This procedure is repeated in different scanning directions up to n times, with iteratively relaxing thresholds s_n. This allows regions with small velocity differences to be dealiased first and strong shear zones are targeted last. This approach mitigates error propagation from high shear areas. By applying spatial dealiasing only within buffer zones, the dependency on single gates is limited to the buffer zones. Errors resulting from noisy or high-shear gates will thus also be confined to the buffer zones. Propagation of errors is avoided by surrounding buffered gates with the previously dealiased regions.

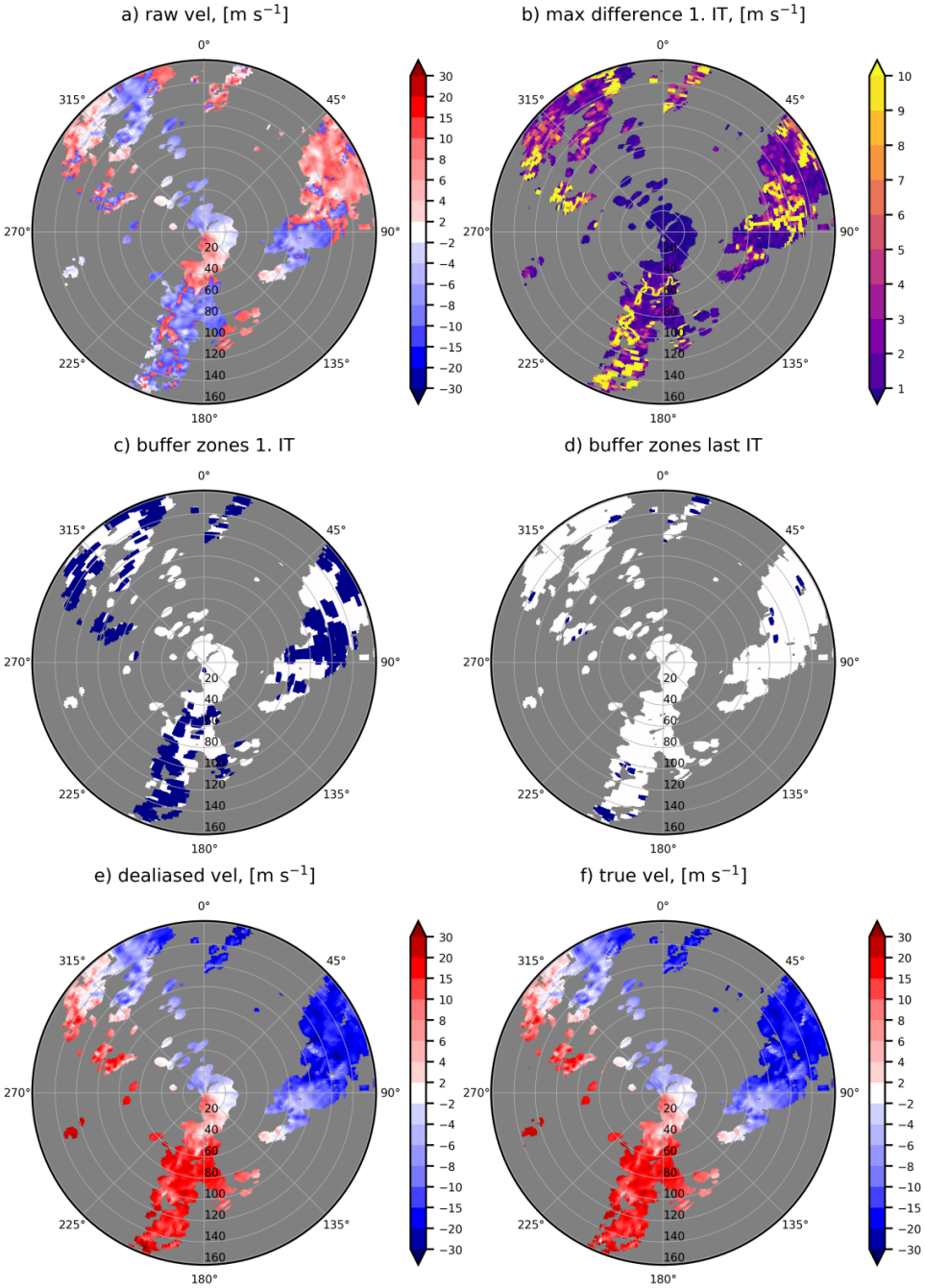

Figure 2.4: Region identification of R2D2, modelled data; $v_{NYQ} = 9.6\,\mathrm{m\,s^{-1}}$, $b = 0.8 \cdot v_{NYQ} = 7.7\,\mathrm{m\,s^{-1}}$: modelled folded velocity, maximum difference D, buffer zones (blue) of first and last (3rd) iteration, dealiased velocity and modelled true velocity

Remaining data that have not been corrected by spatial dealiasing are then targeted by windowing as in James and Houze (2001), where a larger spatial window, i.e. 10x10 gates, is used to estimate the Nyquist interval from neighboring dealiased data. This routine allows isolated cells that did not qualify as regions to be dealiased adequately as well.

Recursive Iteration - Step 9

After completing a first attempt at dealiasing an elevation sweep, the algorithm recursively iterates again through steps 2-8. On the second attempt, most folds have already been removed, which results in larger regions and less buffer zones. This can be seen in Fig. 2.4d, which shows the identified buffer zones of the last iteration before yielding the dealiasing result. The folds have been effectively removed with remaining buffer zones predominantly covering high shear regions. With larger regions, more guidance data is available to assign the correct Nyquist interval, which yields a more robust result. By reducing the number of folds included in buffer zones and thus shrinking their size, the dependency on spatial dealiasing is further reduced.
For each iteration, the average of the maximum absolute difference field D, D_{av}, is computed. As long as D_{av} decreases within a certain number of iterations i, the procedure is repeated, until a minimum value is reached and no further optimization can be found within i iterations. Consequently, in Fig. 2.4, R2D2 performs 5 iterations with the optimum being reached after 3 iterations. Fig. 2.4d and e show the buffer zones and dealiasing result of the third iteration. As a comparison, Fig. 2.4f shows the true velocity field, as initially modelled in COSMO-1 and obtained by the radar operator.

2.3.3 Specific properties of R2D2

Whereas spatial dealiasing (James and Houze, 2001; He et al., 2011; Witt and Brown, 2009; Zhang and Wang, 2006; Eilts and Smith, 1990) and region-based dealiasing (Yuan et al., 2020; Xu et al., 2011; Wüest et al., 2000) are known concepts and commonly employed, they are usually not used in combination. A recent exception to this is presented by Louf et al. (2020), where multiple spatial dealiasing approaches are combined with using a larger reference region than only immediately neighboring gates, similar to the windowing procedure.
We effectively combine both approaches, exploiting their respective strengths. Region-based dealiasing is a powerful method where there is little turbulence or shear present and data coverage is widespread. Dealiasing entire regions at the same time is also computationally more efficient than spatial dealiasing, reserving computing resources where they are needed most. Spatial dealiasing targets high-shear zones beginning from the areas with lower shear and with strict continuity constraints, then slowly relaxing the constraints and progressing to the higher shear areas.
The buffering procedure serves as a method of identifying areas where spatial dealiasing outperforms region-based dealiasing. Moreover, our recursive region-identifying procedure minimizes the number of folds finally targeted by spatial dealiasing, allowing the regions to

grow and merge together. This leaves predominantly high-shear regions to spatial dealiasing, while large, continuous velocity regions are solved by region-based dealiasing. Iteratively minimizing the average maximum difference D_{av} by repeating the dealiasing procedure simplifies the dealiasing problem from one iteration to the next, yielding a more optimal dealiasing outcome.
Initializing dealiasing by utilizing the sweep above and before constrains data continuity in the vertical and in time (James and Houze, 2001). Only in cases where there is insufficient information from spatio-temporal continuity, is a reference first-guess field used. This approach effectively mitigates errors in isolated cells or new cells that appear in a sequence of volumes. In combination, these properties of R2D2 effectively target the challenge posed by small Nyquist velocities in turbulent, sheared, and high-velocity situations, as well as the challenge of data discontinuity in convective events and mountainous terrain.

2.3.4 Technical Implementation

This algorithm was developed within the operational framework of MeteoSwiss's existing operational chain. It leverages code from 4DD (James and Houze, 2001), the previous operational algorithm. The algorithm is programmed in C, which allows it to process full-volume scans in near real-time (<20 s on the full MeteoSwiss radar volume, depending on the data coverage and complexity of the dealiasing problem). While this is considerably slower than the previous implementation of 4DD (~ 3 s on the full MeteoSwiss radar volume), the improvements are considerable and results are still delivered within a timely manner. Within the operational framework, R2D2 depends on secondary algorithms, such as the clutter removal algorithm and the VAD algorithm and in its current form cannot be isolated from the operational chain. However, in general, the dealiasing procedure is applicable to any Doppler radar that yields a regular data stream of PPIs at constant elevations.

2.4 Results

2.4.1 Error Analysis

To quantify the performance differences of several dealiasing algorithm versions, we utilize the data produced by the COSMO forward radar operator (Wolfensberger and Berne, 2018) to work in a controlled framework. A similar approach was applied in Altube et al. (2017) to quantify improvements in velocity processing.
The main advantage of utilizing simulated data here is the availability of the true wind field and the ability to process a large number of time steps. Whereas manual error assessment has been often used in past studies (e.g., James and Houze, 2001), it does not guarantee the correct unfolding of the aliased velocity field, especially in turbulent situations. It also strongly constrains the number of elevations that can be processed.

As COSMO-1's resolution is restricted to 1.1 km, it cannot represent very localized shear phenomena and produces a smoother field than is generally observed in reality. Moreover, it does not contain the noise generally present in radar measurements. To add noise to the field and increase the likelihood of small-scale shear, Gaussian noise with a standard deviation of $1\,\mathrm{m\,s^{-1}}$ is added to the aliased radar operator data.
When adding the environmental wind information derived from COSMO-1 in this framework, the wind naturally matches better than in reality. Even considering that the first guess field is smoothed and the radar operator has added noise, the agreement is disproportionally high. Together with the shortcoming of smoothness of the wind field, the statistics computed here are to be evaluated qualitatively. Additional checks are performed on the observed radar data of the same cases to confirm the performance obtained within the radar operator framework. To quantify the performance, the percentage of erroneous gates in relation to all valid gates containing data, is computed. Empty gates are disregarded, as well as deleted gates. Data deletion only occurs in noise suppression and is not a result of dealiasing failure.

2.4.2 R2D2 Evaluation Using COSMO-1 Simulated Radar Data

Since recursion requires more computation time, especially in challenging dealiasing situations, the algorithm is also evaluated without iterations, hereafter Region-based Doppler Dealiasing (RD2). Figure 2.5 shows the performance of the different dealiasing algorithms for each evaluated meteorological event. The percentage of erroneous gates among all valid gates is shown. Whereas the overall percentage is low (<2%), it is nonetheless desirable to reduce this percentage since errors tend to happen where correct dealiasing is needed most. Our experience has shown that difficult dealiasing situations with both high velocities and large gate-to-gate shear values are of meteorological interest. As evident in Fig. 2.5, among the cases there is consistent improvement from 4DD using the VAD to R2D2 using COSMO-1. In all cases, R2D2 with COSMO-1 yields the lowest error percentage. Additionally, there is a significant improvement in all algorithm versions when using COSMO-1 data as reference velocity. Especially when utilizing COSMO-1, RD2 routinely performs worse than 4DD and R2D2. This shows that the iterative process is a requirement to arrive at R2D2's high performance values and justifies the additional computational expense. Where 4DD processes a volume in ~ 3 s, RD2 requires ~ 5 s. The iterations cause R2D2 to need $10-20$ s of computation time per volume.

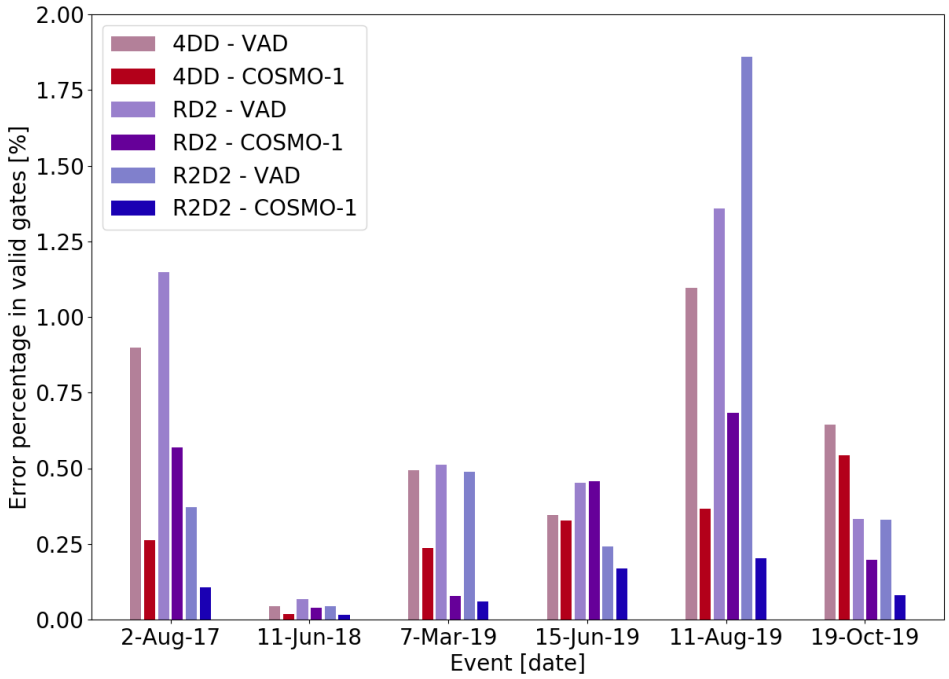

Figure 2.5: Error statistics for different dealiasing versions, separated by evaluated event: percentage of erroneous gates within all valid gates of a case study, computed on modelled data

When using the VAD, the case of 11 Aug 2019 actually shows a decrease in performance from 4DD to RD2 to R2D2. This stems from both RD2 and R2D2 requiring robust guidance information over larger areas. The case study is from the Pointe de la Plaine Morte radar, which is situated at ~ 3000 m ASL. At these high altitudes there is only sparse data coverage, particularly in the higher sweeps. Additionally, the case analyzed shows supercellular convection with scattered precipitation cells. The compounding effect of sparse data coverage in low elevations and a lack of data from higher elevations leads to very unreliable VAD estimates. This in turn can lead to mistakes when assigning the Nyquist interval to regions. In RD2, this leads to a fraction of regions being dealiased erroneously. However, in R2D2, the iterative procedure propagates these errors to larger contiguous regions due to a lack of better guidance data. When using COSMO-1, we can see that this issue does not occur, emphasizing the importance of supplemental wind information in situations of sparse data coverage.
The quantitative error analysis shows that using COSMO-1 to provide environmental wind information and applying our region-based, recursive dealiasing approach both contribute to substantial improvements in dealiasing accuracy. Across all analyzed cases, COSMO-1 reduces the number of erroneous gates by ~ 50%. Moreover, adding the switch from 4DD to R2D2 further reduces the number of erroneous gates by ~ 50%, yielding a final improvement over all cases of ~ 75%.

The improvements of COSMO-1 and R2D2 are cumulative, as they target different sources of errors in dealiasing. The use of COSMO-1 targets initialization issues in isolated cells at far ranges. The VAD does not represent these areas very well, as it assumes spatial homogeneity, which can lead to large regions being dealiased incorrectly, even in R2D2. Additionally, it requires a high data coverage to produce robust results, which is generally not the case when dealing with isolated cells. Especially with cells first entering the radar range, there is also no previously dealiased sweep to derive information from. COSMO-1 represents the general flow well enough to initialize these cells in the correct Nyquist interval, resulting in the significant improvement seen here.
R2D2 targets several different issues. The region-based approach reduces the influence of single gates, basing dealiasing decisions on a larger consensus. By checking the deviations from the general decision within each region, an additional error-check is introduced to avoid large spatial extents of errors. The iterative approach additionally reduces dealiasing errors in regions, as the regions start merging with increasing iterations, as velocity folds are removed. Larger regions are more robust, as they can be verified with more guidance data. By mitigating spatial dealiasing to small buffer zones, the potential to spread errors this way is also strongly reduced. This allows a stronger relaxation of thresholds for spatial dealiasing, which facilitates retrieving the correct velocity values in situations when the gate-to-gate shear is on the order of the Nyquist velocity.
The convective weather situations benefit most from the improvements in the R2D2 scheme. Localized turbulence is targeted more specifically and error propagation is strongly reduced. COSMO-1 equally aids stratiform and convective situations, as it plays a crucial role in correctly initializing dealiasing of data appearing at the outer ranges of the radars.

2.4.3 R2D2 on Operational Radar Data

To verify the general trends observed in the radar operator framework, the same case studies are processed with operational radar data. Here, we can inspect the performance of R2D2 on noisier data that generally contains higher shear values. Additionally, the COSMO-1 data no longer provide a perfect match and we can investigate its benefit over the operational VAD. A visual inspection of the results of the case studies generally confirms the trends observed in the radar operator. R2D2 and COSMO-1 individually contribute to substantial improvements and target different areas of issues, thus yielding the optimal result, when combined. The following examples focus on showcasing the improvement gained from R2D2 over 4DD, as well as the improvement from using COSMO-1 over VAD estimates.
The example shown in Figs. 2.6 and 2.7 illustrates the differences between 4DD and R2D2 in a case with supercellular convection. The velocity data from 2 Aug 2017 at 00:00 UTC and 1.6° elevation are shown. Fig. 2.6a depicts the radar reflectivity and the corresponding raw velocity is illustrated in Fig. 2.6b. Figures 2.6c and 2.6d show the different first guess fields derived from the VAD and COSMO-1. Additionally, Figs. 2.6e and f show the 4-D guidance data from the previous and above elevations, here dealiased with R2D2 using COSMO-1. We can clearly see that the VAD did not perform correctly, due to poor data coverage in the vicinity of the radar.

The radial velocity data over the entire sweep are thus vastly underestimated. Moreover, the VAD cannot be produced for all altitude levels, resulting in large data gaps between available values. These issues can be seen in Fig. 2.6c, as the data are interpolated over large stretches, resulting in large areas of identical information, e.g. from 0 to 70 km range and from 70 to 160 km range. As can be seen in Fig. 2.6d, the first guess field derived from COSMO-1 shows a much smoother data transition, but also generally higher velocity values. It also represents the spatial heterogeneity of a wind field in an orographic environment much better.

Fig. 2.7a shows the results of applying 4DD with the VAD, and Fig. 2.7b shows the results of 4DD with COSMO-1, revealing that there is a large spread of dealiasing error that can be traced back to an area of unresolved shear at 50 km range and 320° azimuth. Without any additional constraints, the error can propagate through spatial dealiasing and negatively affect the subsequent sweeps. Figures. 2.7c and Fig. 2.7d show R2D2's results with the VAD and COSMO-1, respectively. Here, we clearly see the rotational structure of the mesocyclone at 50 km range and 320° azimuth. There are still errors detected (e.g. at 60 km range and 5° azimuth), however they are constrained to much smaller areas. Overall the main dynamical features are retrieved even in this extreme, high-shear environment. Figures 2.7e and f depict the identified buffer zones during the first and last, here third, iteration. The merging of regions over folds, while preserving the buffer zones over sheared areas, is clearly visible. This decrease in separate regions also demonstrates an increase in dealiasing robustness throughout the iterations. The first iteration (Fig. 2.7e) depends on correct dealiasing decisions for many more groups of data, whereas the third iteration (Fig. 2.7f) mainly needs to solve the separate precipitation regions, before filling in the shear zones with spatial dealiasing.

When comparing the results of dealiasing with the VAD versus dealiasing with COSMO-1, it is noticeable that this only affects few areas. Both algorithms rely on the first guess field only as a last resort, reducing the amount of data affected. Nonetheless, we can see that along 45° azimuth, several smaller cells benefit from the use of COSMO-1 and appear to be dealiased correctly in Figs. 2.7b and 2.7d.

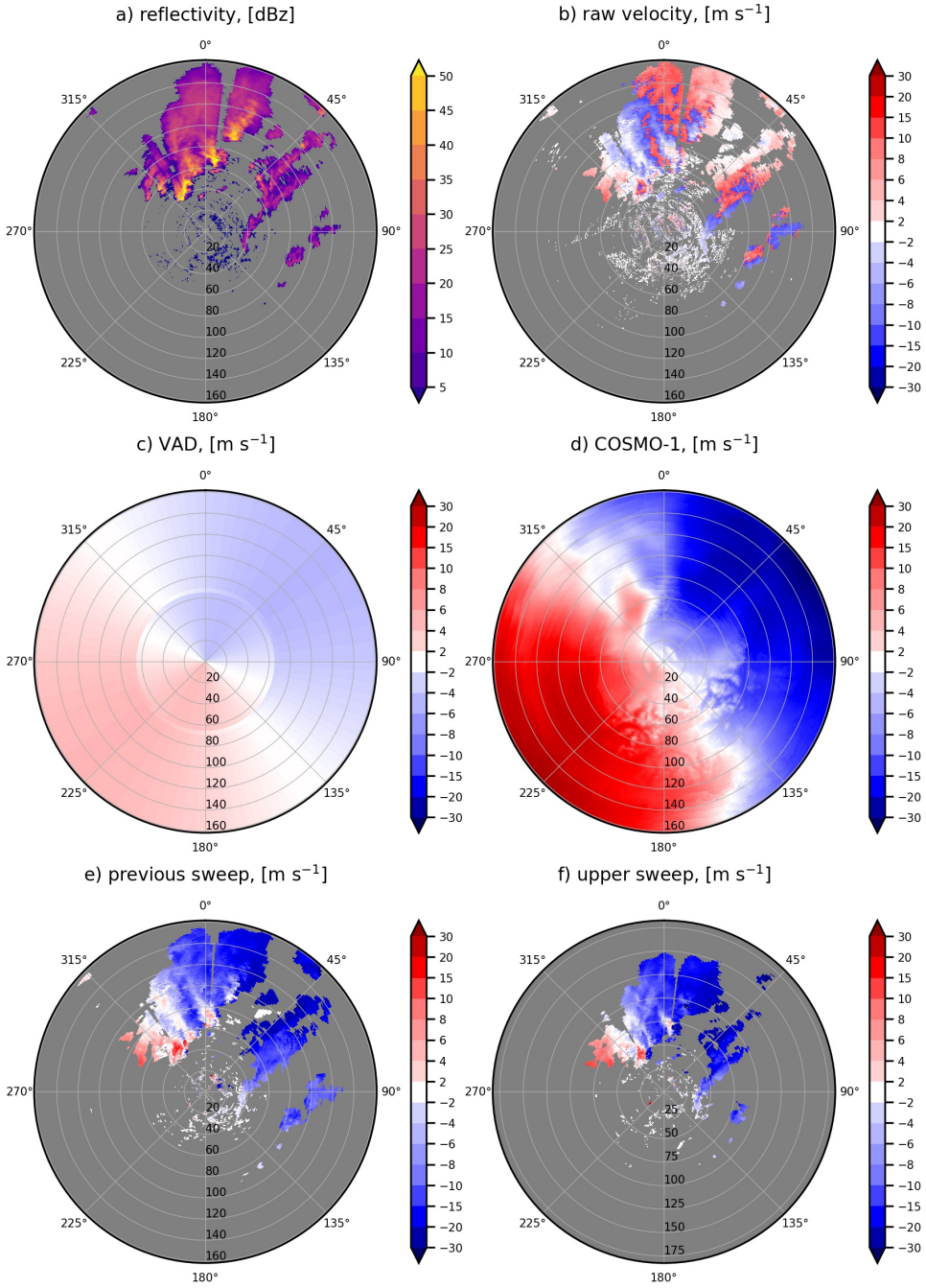

Figure 2.6: Case study 2 Aug 2017, 00:00 UTC, Albis radar, 1.6° elevation, $v_{NYQ} = 12.4\,\mathrm{m\,s^{-1}}$: reflectivity, raw velocity, VAD and COSMO-1 estimates, guidance data from the previous and above dealiased sweeps

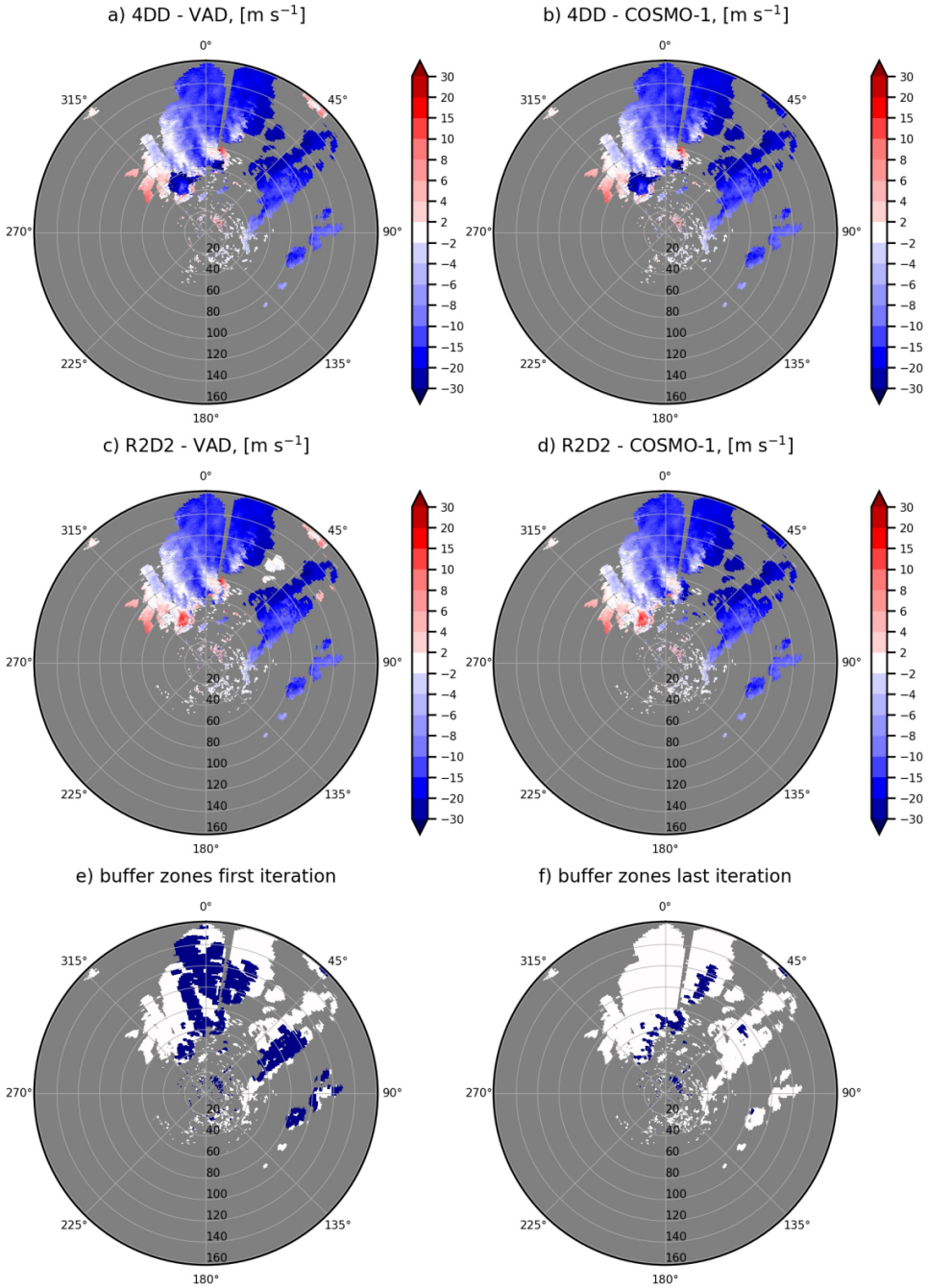

Figure 2.7: Dealiasing example 2 Aug 2017, 00:00 UTC, Albis radar, 1.6° elevation, v_{NYQ} = 12.4 m s^{-1}: dealiasing outcomes of 4DD with the VAD, 4DD with COSMO-1, R2D2 with the VAD and R2D2 with COSMO-1; buffer zones (blue) of first and last (3rd) iteration of R2D2 with COSMO-1

Figs. 2.8 and 2.9 showcase a dealiasing example 11 Jun 2018 at 18:20 UTC and 1.6° elevation. Figures 2.8a and 2.8b depict the radar reflectivity and raw velocity. Figure 2.8c shows the first guess field derived from the VAD, whereas 2.8d is derived from COSMO-1. We can see that the data coverage is again somewhat localized, resulting in difficulties when deriving the VAD. Here, the VAD was only produced at one altitude relevant to this elevation. In Fig. 2.8c, we can see that the limited VAD results in a single estimate of velocity magnitude and direction for all ranges. On the other hand, the first guess field from COSMO-1 (see Fig. 2.8d) provides velocity values that are much higher and spatially heterogeneous. Figures 2.8e and f additionally show the 4-D guidance data obtained from the previous and above elevations. In Figs. 2.9a and 2.9b, the data is dealiased with 4DD using the VAD and COSMO-1. These figure panels clearly illustrate that the use of COSMO-1 data instead of a VAD as supplemental wind information can dramatically improve algorithm performance. COSMO-1 mitigates errors that occur mainly at far ranges, but generally affect large areas and is thus a substantial improvement. Figures 2.9c and 2.9d depict R2D2's performance using the VAD and COSMO-1. In this case, the region-based approach already resolved the major error using the VAD at $100-160$km, $220-260°$. The addition of COSMO-1 further contributes to minor improvements along 45° azimuth. In this case, an isolated convective cell is developing at 60 km range but is not well represented by the VAD, while the COSMO-1 data lead to a reliable interpretation of the Doppler velocity in that location. Figures 2.9e and f also show the progress of region merging between the first and last (third) iteration. Here we can also see that even with the velocity field appearing more homogeneous, there are still velocity shears present that exceed $0.8 \cdot v_{NYQ}$ within neighboring gates. These shear zones remain flagged as buffer zones in the last iteration of R2D2. This shows the challenging nature of dealiasing in the context of low Nyquist velocities.

Our tests also reveal that dealiasing results are often forgiving of misplaced convective cells. When using COSMO data whose valid time had a 3 h offset from the observed radar data, we obtained largely the same dealiasing results, with very few deviations. Since COSMO-1 grids are interpolated and used as a last resort in the dealiasing process, we postulate that obtaining the precise location of deep convection in the model is generally not necessary. Moreover, mesoscale forecast grids, as opposed to accurate mesoscale analyses of convective precipitation, would be more than sufficient and may be the only option for dealiasing in an operational context.

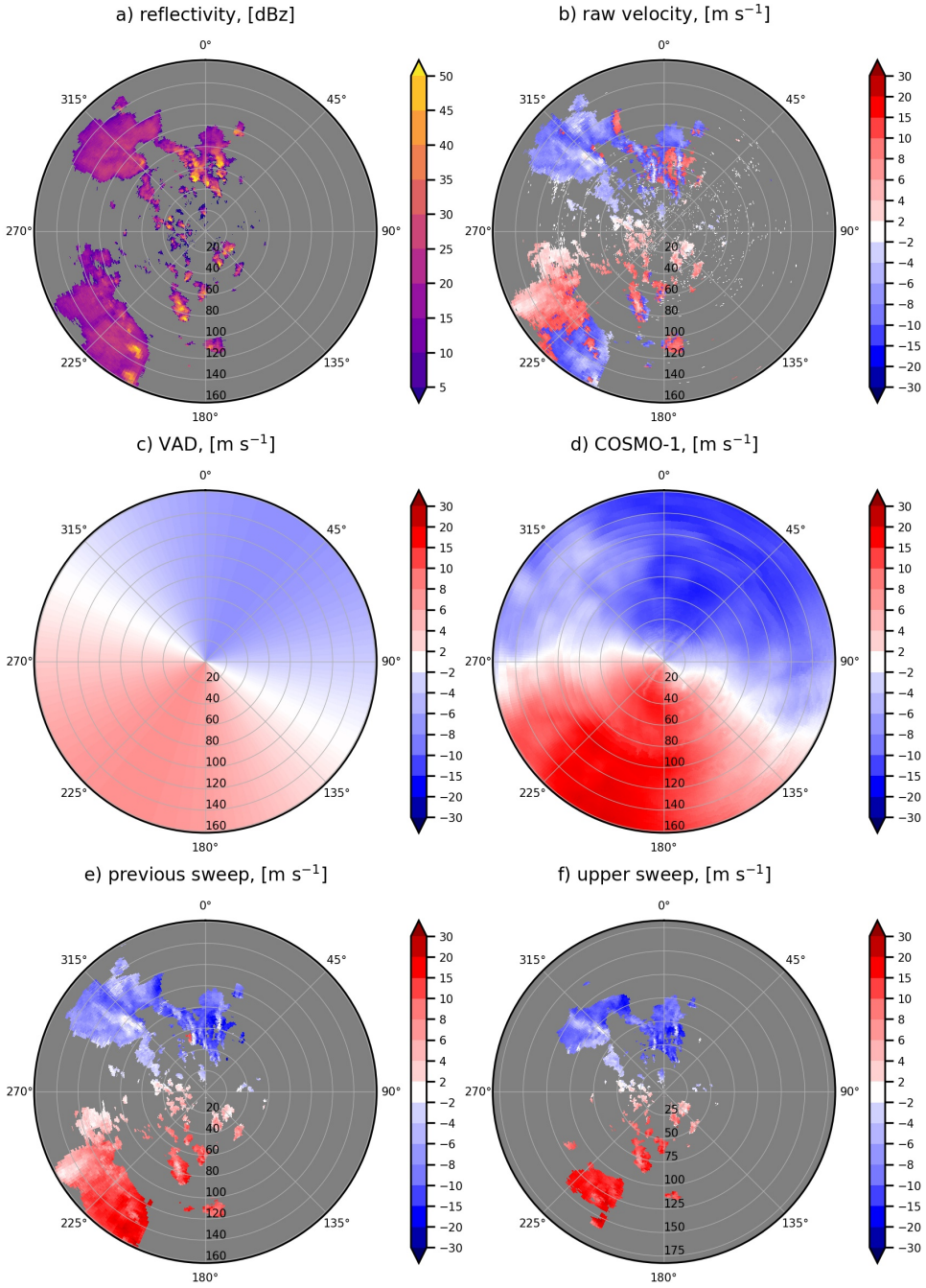

Figure 2.8: Case study 11 Jun 2018, 18:15 UTC, La Dôle radar, 1.6° elevation, $v_{NYQ} = 12.4\,\mathrm{m\,s^{-1}}$: reflectivity, raw velocity, VAD and COSMO-1 estimates, guidance data from the previous and above dealiased sweeps

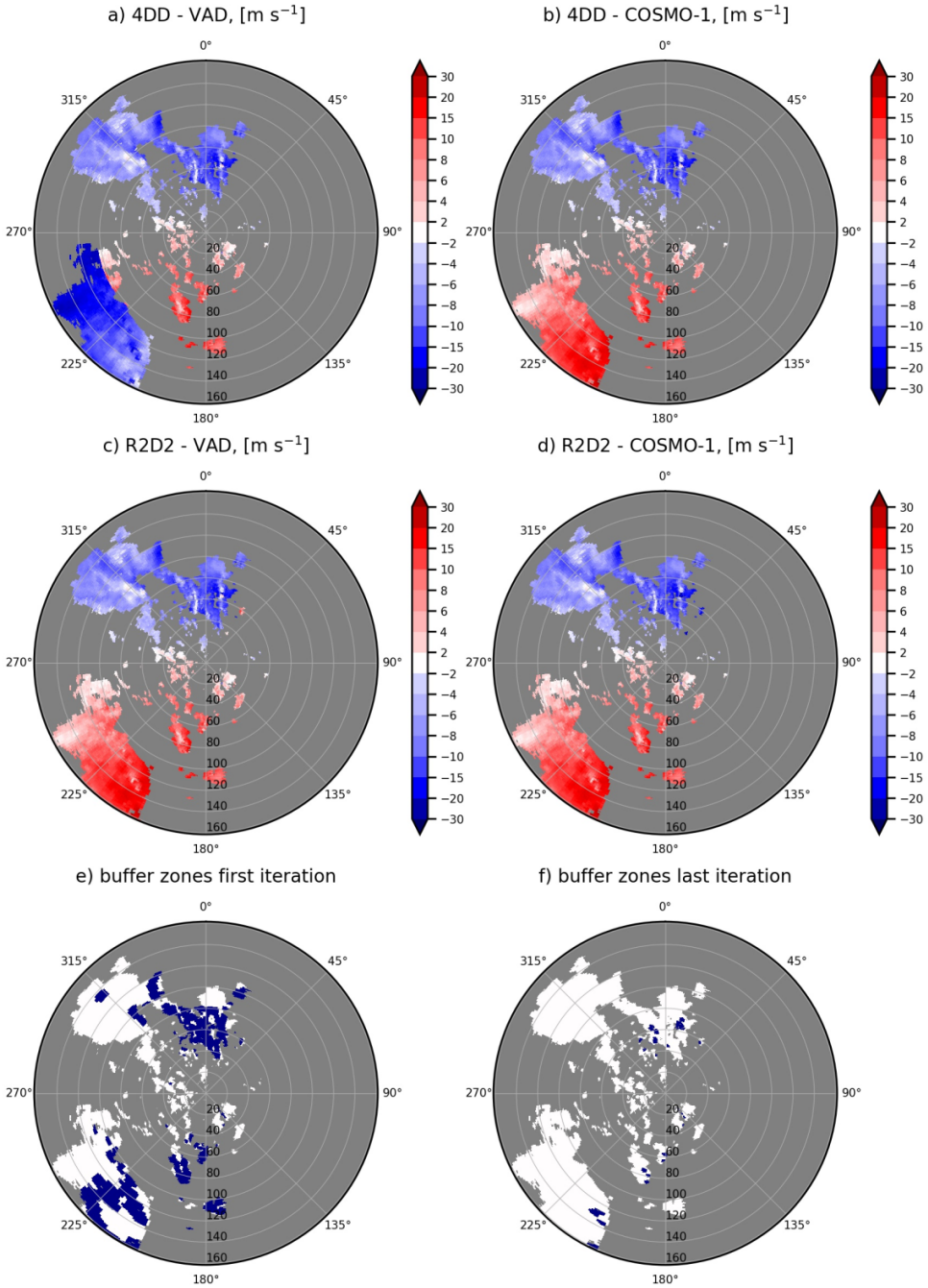

Figure 2.9: Dealiasing example 11 Jun 2018, 18:15 UTC, La Dôle radar, 1.6° elevation, v_{NYQ} = 12.4 m s^{-1}: dealiasing outcomes of 4DD with the VAD, 4DD with COSMO-1, R2D2 with the VAD and R2D2 with COSMO-1; buffer zones (blue) of first and last (3rd) iteration of R2D2 with COSMO-1

2.5 Conclusion

The novel dealiasing algorithm R2D2 adequately achieves our objectives of region-based initialization, 4-D continuity, mitigated error propagation, improved environmental wind estimates and suitability for operational implementation in challenging dealiasing situations. Improved algorithm design and environmental wind estimates contribute to substantial improvements in various meteorological situations over the existing Swiss operational algorithm. The best results are achieved when combining COSMO-1's first guess field with R2D2. The improvements are robust in a variety of convective and stratiform case studies. The most challenging situations occur, however, when the velocity differences between two gates exceed the Nyquist velocity. This often leads to dealiasing errors; however R2D2 contains these errors to small areas.

Our analysis included cases that portrayed different but challenging wind situations, including high-shear environments of supercells and mesoscale convective systems, as well as the high wind speeds and wind direction changes associated with a strong cold front passage. The performance increase of R2D2 is robust across all cases and therefore suitable for a general, operational application. Completing the dealiasing cycle once is a computationally efficient procedure. The iterative approach takes accordingly longer, depending on how many iterations are needed to find the optimum solution. R2D2 requires more processing time than 4DD, especially in challenging situations. Nonetheless, the data can be processed near real-time and the procedure is suitable for operational implementation.

The dealiasing procedure in R2D2 is generally suited for a continuous stream of radar data measured in a succession of PPIs. While it processes data top-down, the measurements can generally proceed in any order, as long as the assumption of data continuity between elevations and time steps are still valid.

3 Convection Detection and Tracking Algorithms

This chapter is based on the appendices of the postprint version of the published article “Feldmann, M., Germann, U., Gabella, M., and Berne, A.: A characterisation of Alpine mesocyclone occurrence, Weather Clim. Dynam., 2, 1225–1244, https://doi.org/10.5194/wcd-2-1225-2021, 2021". The algorithms were developed and tested by Monika Feldmann. Dr. Marco Gabella, Dr. Urs Germann and Prof. Alexis Berne organized the research project and supervised the progress.

This chapter introduces new methods in thunderstorm tracking, mesocyclone detection and radar data quality assessment that are used throughout the following chapters. The development of a new thunderstorm tracking algorithm that is built in a modular way in python allows for a greater deal of flexibility for research applications. This algorithm has been made publicly available and is now used in various research groups. The mesocyclone detection algorithm exploits the improved Doppler velocity data for the identification of significant rotation in severe convection. This algorithm has been added to the real-time processing chain of MeteoSwiss and contributes to the suite of products available to forecasters for severe weather warnings.
Due to the complex topography in the Alpine regions, radar observations are challenging. The quality index presented here aims to provide a summarizing metric that combines several aspects of radar data quality. This provides context for the interpretation of radar-based observations and the identification of potential artifacts.

3.1 Thunderstorm Detection And Tracking (T-DaTing)

3.1.1 Introduction

The thunderstorm detection is based on a dynamic threshold algorithm, which works very similarly to MeteoSwiss's operational Thunderstorm Radar Tracking (TRT) algorithm (Hering et al., 2004). Cells are identified based on thresholds in the Cartesian maximum reflectivity field. Adjoining cells' boundaries are identified by using a watershed algorithm. From one time step to the next, the motion of the cells is estimated by the pySTEPS optical flow (Pulkkinen et al., 2019) approach. Newly identified cells in the next time step with a large spatial overlap to previously advected cells are then matched. A more detailed description of the T-DaTing algorithm can be found in section 3.1. Key differences between TRT and T-DaTing are a fixed minimal detection threshold in T-DaTing, as opposed to the dynamic minimum threshold in TRT and the cell advection with optical flow in T-DaTing versus extrapolating previous motion in TRT.
The Thunderstorm Detection and Tracking (T-DaTing) algorithm utilizes image processing, computer vision and optical flow techniques to identify thunderstorms and track them in time. The 2-D Cartesian maximum reflectivity field of the Swiss operational radar network is used as input. Its spatial resolution is 1 x 1 km^2 and it is generated every 5 minutes. All thresholds are tuned to this input data (Hering et al., 2004), but are adaptable to other data sets. This algorithm has been published as a part of the pySTEPS package (PySteps developers, 2021).

3.1.2 Thunderstorm Detection

The detection of thunderstorms follows a dynamic, multi-threshold approach. The procedure is modeled after MeteoSwiss's operationally running TRT algorithm (Hering et al., 2004). All thresholds are listed in Table 3.1 and stem from Hering et al. (2004).
Utilizing the 2-D maximum reflectivity composite from all five radars, in a first step, all areas below the minimum reflectivity Z_{min} are discarded. All remaining areas need to have a peak reflectivity value exceeding Z_p and be larger than the area A_{min}. We chose a relatively large size limit here, as we are interested in supercellular convection, which generally takes place on larger spatial scales. The next step uses local maxima within the area boundaries to determine whether these should be further split into separate convective cells. To excessive splitting in areas of very high reflectivity values, where there are many extreme local maxima, the data is saturated at the maximum reflectivity Z_{max}. Within these areas exceeding Z_{min}, a local maximum detection algorithm is employed (van der Walt et al., 2014). Maxima within a consecutive area are counted as separate, if the path of least change between them decreases by at least ΔZ. Maxima within 10 km of each other are merged to avoid excessive cell splitting. The remaining maxima are used as anchors for the cells. To separate cells that lie within the same connected area, an inverted watershed algorithm (Beucher and Lantuejoul, 1979; van der Walt et al., 2014) assigns the corresponding areas to each maximum. Thus the boundaries of the inverted watershed algorithm lie along the lowest values of reflectivity in between maxima

that are within the same consecutive area, but have a reflectivity drop of at least ΔZ in between them.
This produces the labeled areas for the identified thunderstorm cells. The detection part of the algorithm can be performed on any length of data and does not require temporal continuity. It yields results very similar to Hering et al. (2004), the main deviations are a larger minimum size and the introduction of the minimum distance between maxima. Additionally contours are slightly larger, as they always extent to the boundary of Z_{min}.

Table 3.1: Thunderstorm detection thresholds.

variable	unit	threshold
min. reflectivity (Z_{min})	dBz	35
max. reflectivity (Z_{max})	dBz	51
min. difference in reflectivity (ΔZ)	dBz	6
peak reflectivity (Z_p)	dBz	$Z_{min} + \Delta Z = 41$
min. area (A_{min})	km^2	50

3.1.3 Thunderstorm Tracking

After detecting the thunderstorm cells, the tracking part of the algorithm estimates the future path of each cell, propagates it and matches it to the detected cells in the next time step.
The movement of the cells is estimated from three consecutive frames of the 2-D input data. The Lucas Kanade optical flow algorithm (Lucas and Takeo, 1981) applied to the current and previous two time steps of the maximum reflectivity field yields the projected movement for the next time step (Pulkkinen et al., 2019). Each cell of the previous time step is propagated according to the results from the optical flow. This is then compared to the identified cells of the current time step. If the overlap between two cells is more than 50 %, they are considered as the same cell and assigned the same ID as before. If there is no overlap to a new cell, the cell track ends and this ID is no longer used. If there is no previous cell matching a new cell, a new ID is generated and thus a new track initiated. If a cell splits, the smaller fraction is considered a new cell and obtains a new ID. In case of merging, the smaller (area) cell is considered decayed, where the track of the larger one continues in the merged cell.
For each step, the x and y coordinates, maximum reflectivity, centroids, area and distance from last detection are recorded.
In a final step the detections from each time step are resorted into the tracks assigned to their IDs. Tracks shorter than three detections are rejected.
The tracking procedure follows the same steps as Hering et al. (2004). However where previously the cell motion from one detection to the next was estimated by the past track of the cell, we extrapolate the motion from one detection to the next utilizing the output of the optical flow algorithm (PySteps developers, 2021; Pulkkinen et al., 2019) applied to the three latest time steps.

3.2 Mesocyclone Detection and Tracking (M-DaTing)

3.2.1 Introduction

Within the contours of identified thunderstorms cells, the mesocyclone detection algorithm becomes active. This algorithm is modeled after the existing approaches of Stumpf et al. (1998) and Hengstebeck et al. (2018), but tailored to the specific requirements of the Swiss radar network. Identifying mesocyclonic rotation in radar data relies on estimating vertical rotation (around a vertical axis) from Doppler velocity data (Stumpf et al., 1998). As Doppler velocity only measures the radial component of the full velocity vector, it denotes the incoming or outgoing velocity of particles with respect to the radar. The azimuthal derivative is an approximation of vertical rotation (Miller et al., 2013) and corresponds to roughly half of the vertical vorticity component (see Sect. 3.2, Eq. 3.2). Areas of consistently high positive or negative azimuthal derivative indicate rotation phenomena. As there is no clear preference in rotation direction in Switzerland (Houze et al., 1993), we retain detections for both directions. At each radar elevation we employ object detection techniques to identify these areas and compute additional rotational metrics such as rotational velocity and vorticity per object (see Sect. 3.2, Eqs. 3.2 and 3.1). All identified objects that meet the detection criteria are grouped within each cell and evaluated for vertical and temporal continuity (Hengstebeck et al., 2018). The definition of a mesocyclone applied here requires a minimum vorticity of 10^{-2} s^{-1} (Hengstebeck et al., 2018), a minimum rotational velocity of 10 m s^{-1} (Stumpf et al., 1998) and a signature depth of 3000 m (Stumpf et al., 1998). All of these criteria linearly decrease towards far ranges to compensate for decreasing spatial resolution (Stumpf et al., 1998), allowing for detections at more than 100 km distance from the radar and compensating for the decreasing spatial resolution. Signatures must persist over at least three detections, each at maximum two time steps apart.
T-DaTing provides the constraints for M-DaTing. The detected thunderstorm areas are used as a mask to filter out data unrelated to convection. Additionally, all rotation detected within a cell is assigned to this cell.

3.2.2 Data Preparation

To filter the relevant data, the detected thunderstorm areas are dilated with a 5 x 5 km^2 kernel. Since mesocyclones can be located outside of the area of largest reflectivity (Kumjian and Ryzhkov, 2008), we consider areas slightly larger than each detected cell. One by one, the algorithm then iterates through the detected cells.
To compute rotation, the dealiased velocity data from all 5 radars and 20 elevations is used. The dealiasing procedure is performed with the novel algorithm R2D2 and COSMO-1 analysis data is used as a first guess. As the velocity data is in polar coordinates, the filter obtained from the Cartesian reflectivity filter is regridded to the polar grid of each radar. Additionally the first 5 km in range from each radar are excluded from processing, due to excessive noise in the data.

For each elevation the azimuthal velocity shear is computed using a centered-difference method. In case of residual velocity folds or dealiasing errors, a quality check is in place. If an area of more than three adjacent pixels exceeds the Nyquist velocity (Fabry, 2015) of the corresponding elevation, the Nyquist interval is added or subtracted to reduce the absolute value of the shear in this area. With Nyquist velocities being quite low (Feldmann et al., 2020), particularly in the lower elevations, the azimuthal shear can physically exceed the Nyquist interval. However, usually this will occur in isolated high-shear gates and not in larger areas. Velocity folds and dealiasing errors however produce contiguous lines of erroneous azimuthal shear and can thus be corrected for in this method. The mesocyclone detection presented here is thus less sensitive to dealiasing errors, as long as the edges of folds can be distinguished from physical shear and the estimation of rotational velocity does not cross a velocity alias.

3.2.3 Rotation Detection

Within each elevation, the convective cells are evaluated iteratively. From the azimuthal shear $\frac{dv}{d\varphi_{az}}$, first pattern vectors are constructed. Consecutive areas of shear exceeding a threshold $\frac{dv}{d\varphi_{az}}$ are conserved, if they exceed 1 km in length and contain at least three gates. All other data is discarded. These pattern vectors are merged over the ranges using 8-bit connectivity. If pattern vectors neighbor each other over a corner, or directly, they are considered one area. These resulting areas are then further evaluated. They each need to exceed a minimum rotational velocity and vorticity threshold Δv (Eq. 3.1) and ζ (Eq. 3.2, see Table 3.2). Additionally, their aspect ratio needs to be less than 1:3, approximating circular objects:

$$\Delta v = \frac{v_{max,inbound} - v_{max,outbound}}{2} \tag{3.1}$$

and

$$\zeta = 2 \cdot \frac{v_{max,inbound} - v_{max,outbound}}{\Delta x}, \tag{3.2}$$

where Δx is the Cartesian distance between the velocity maxima.
All rotation areas identified in this way are collected. For each area the location of the centroids, size, rotational metrics, elevation and thunderstorm ID are recorded. Within one cell, more than one detection is possible per elevation, as rotational signatures can be fragmented. Positive and negative azimuthal shear are evaluated separately, to differentiate cyclonic and anticyclonic rotation signatures.

3.2.4 Vertical Continuity

After processing all elevations of one radar, the detected rotation objects are merged. All objects of one thunderstorm ID are considered to belong together and are stacked vertically, as the storm structure can be slanted and detections can be discontinuous due to residual aliasing in the velocity data. Additionally, the vertical depth of the lowest and highest detection must exceed a certain depth h.

Figure 3.1 shows a schematic overview of the detection process until this point. Figure 3.1 a) shows the process within a radar elevation. First the data is filtered with the contours identified in T-DaTing, here approximated with the dark grey cloud (1.). Then the velocity data (2.) is evaluated. Here green denotes outbound velocity from the radar and red inbound. From the velocity, the azimuthal derivative is derived (3.), which results in anomalies in the derivative around the velocity couplet. Cyclonic anomalies are shown in light red here and anticyclonic anomalies in light green. Within these anomalies the rotational velocity and vorticity are computed and measured against thresholds, here resulting in one final rotation object shown in blue (4.). In Fig. 3.1 b) the aggregation of rotation objects within a thunderstorm contour is shown. Detections (blue ovals) from each elevation (dashed slices) within the contour contribute to the overall vertical structure. To these identified objects the vertical continuity constraints on h are applied. After exceeding all criteria, the objects are summarized as one rotation column (light blue column) for the corresponding convective cell. Also here, anticyclonic and cyclonic signatures are considered separately and must each fulfill all criteria to be recorded and are stored as separate columns.

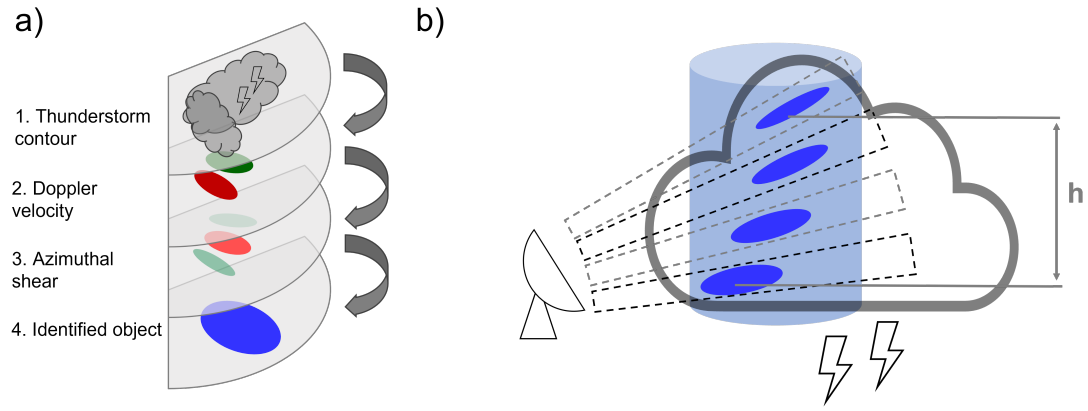

Figure 3.1: Schematic of mesocyclone detection; a) detection of rotation within radar elevations; b) vertical merging of detections within thunderstorm contour.

In chapter 4 the vertical continuity check is applied to all detections of a single radar, before merging the detections of multiple radars. With continuous algorithm improvement, both the operational version of M-DaTing and chapter 5 apply the vertical continuity check to the detections of all radars, merging them beforehand. This improves continuous detectability of supercells in between radars.

3.2.5 Range Dependent Thresholds

All detection criteria are range dependent thresholds T (Stumpf et al., 1998). The thresholds are most strict at a range of 20 km at T_m and decrease outwards until 100 km to T_o, from where they remain stationary. Within 20 km they decrease towards the radar to T_i. The decrease of the thresholds with range compensates for the reduction in resolution in the data. Within 20 km, the decreased thresholds aim to allow for detections in the noisy shear data at small azimuthal distances. The following table depicts the values chosen in the algorithm here.

Table 3.2: Mesocyclone detection thresholds following Stumpf et al. (1998) and Hengstebeck et al. (2018).

variable	unit	inner threshold (T_i)	max. threshold (T_m)	outer threshold (T_o)
azimuthal shear ($\frac{dv}{d\varphi_{az}}$)	s^{-1}	$1 \cdot 10^{-3}$	$3 \cdot 10^{-3}$	$1 \cdot 10^{-3}$
rotational velocity (Δv)	$m\,s^{-1}$	6	10	6
vorticity (ζ)	s^{-1}	$6 \cdot 10^{-3}$	10^{-2}	$6 \cdot 10^{-3}$
vertical depth (h)	m	0	3000	1000

The range dependent thresholds help detecting significant rotation in complex observation situations. Due to the complex nature of the Swiss terrain, there is often no visibility of the lower portion of a storm. Additionally, the environmental conditions allowing for supercellular convection in Switzerland generally show a lower vertical shear than e.g. in the US plains. We tuned the thresholds by investigating visually confirmed cases of supercellular convection and range dependent thresholds that relax at very close and far ranges. While this may detect more storms as supercells, that were merely exhibiting significant rotation but otherwise lack the typical storm structure, we avoid missing detections due to observational issues.

3.2.6 Temporal Continuity

Within a valid thunderstorm track, rotation of the same sign must have been detected at least 3 times within 10 minutes of each other. Additionally the rotation track must leave the range of 20 km around a radar. In strong linear wind situations, the geometric nature of the radial velocity produces artificial rotation signatures at opposing sides of the radar that remain stationary. These can produce false detections, but are easily removable considering that thunderstorms generally propagate.

3.3 Relative Quality Index

3.3.1 Introduction

Considering the complexity of radar observations in mountainous terrain, this section introduces a method of estimating observational uncertainties within a radar network. We combine different aspects of the radar network to obtain a qualitative index that represents the relative quality of observations at a given location.
The considered properties are theoretical visibility, minimum and maximum altitude of measurements, spatial resolution and numerical noise stemming from data quantization. These metrics are assessed for each radar and merged onto a Cartesian grid, where the highest quality metric is retained. The metrics are then rescaled between 0 (lowest quality) and 1 (highest quality) and combined into a general quality index. A detailed description of the computation of the quality index is in section 3.3.
This results in a spatial map of the quality index of the radar network. It is a qualitative index and only represents a relative comparison of detection probability, not a quantitative measure of correcting for detection gaps.
While the components contributing to the quality index are based on the full radar network and represent impacts to all radar products, no all observed meteorological phenomena are impacted equally by the limitations. The selection here is tailored to convective phenomena that can reach very high altitudes and require a high spatial resolution. Other combinations of these components lead to differing results, however the overall spatial pattern of the quality index is robust and representative of radar product quality in general.

Figure 3.2 depicts the results of the quality index assessment over the Swiss domain (the influence of each considered property is shown in Fig. 3.3 in section 3.3). The black dots indicate the locations of the 5 radars. With the topography underlain in the background, we can see the clear influence orography has on the quality index. This is primarily a consequence of radar beam blockage, which decreases visibility, particularly at low levels. Two noticeable artifacts are a dip in quality to the Northeast of La Dôle and a similar gap in observations to the West of Lema radar. These artifacts stem from constructions in the vicinity of the radars blocking the visibility. The obstruction of Lema is more recent and does not affect the entire analysis period. The decrease in quality in the main Alpine ridge is caused by beam blockage of terrain.

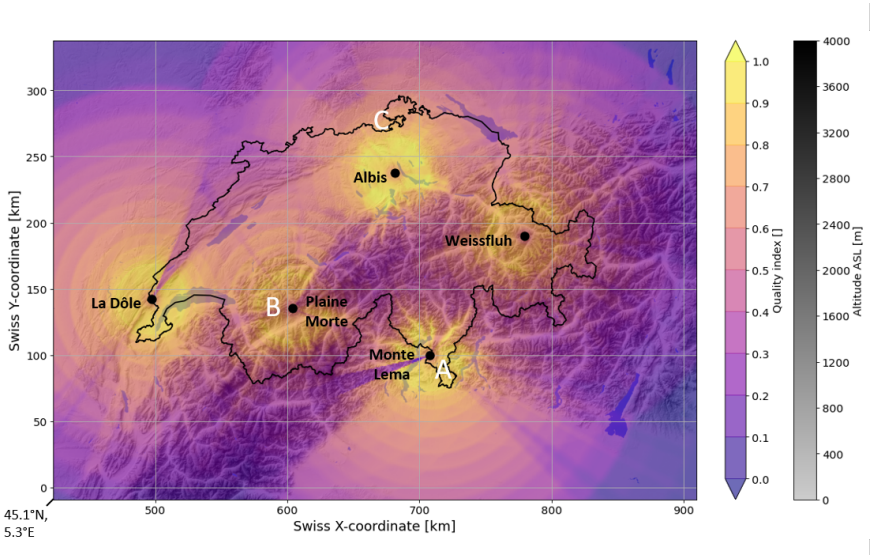

Figure 3.2: Relative quality index for mesocyclone and thunderstorm detection in the Swiss weather radar network depicted over elevation map; case study locations (Figs. 4.2, 4.3 and 4.4) indicated with white letters; radar locations shown with black dots; radar altitudes: Albis - 938 m, La Dôle - 1682 m, Monte Lema - 1626 m, Plaine Morte - 2937 m, Weissfluh - 2840 m.

3.3.2 Components

The relative quality index combines multiple physical constraints of the Swiss radar network and combines them to a single, summarizing quality index. The characteristics we include are: the vertical sum of theoretical visibility V (dimensionless, ranging from 0-1 for each elevation, in total ranging from 0-20), minimum altitude of observation h_{min} [m], maximum altitude of observation h_{max} [m], azimuthal resolution $\Delta\varphi_{az}$ [m] and discretisation in velocity shear ϵ [s^{-1}].

The theoretical visibility corresponds to the unblocked fraction of a radar beam at each location. It is derived combining the effective earth radius model (AMS Glossary of Meteorology, 2012) with a refractive index of 5/4 and a digital elevation model to estimate beam blockage. The vertical sum over all 20 elevations is computed on a 2-D polar grid for each radar. In a similar fashion, the minimum and maximum altitudes of measurements are obtained from the altitude of the lowest and highest radar beam with 100 % visibility, yielding each a 2-D polar grid per radar. The resolution corresponds to the distance of each radar bin to its azimuthal neighbors. As we here work with the azimuthal derivative of Doppler velocity, we additionally introduce the quantization noise. The numeric resolution at which the Doppler velocity is stored introduces a small level of noise. The azimuthal derivative is strongly range-dependent, as it utilizes the azimuthal resolution. In the vicinity of the radars this noise reaches high levels and thus impacts the data quality. We here compute the noise level by dividing the numerical resolution by the azimuthal resolution.

After obtaining the radar-based grids for each variable, these are regridded to a 1 km resolution Cartesian grid, where the highest-quality index at each location of overlap is retained. The

contribution of each variable is shown in Fig. 3.3.

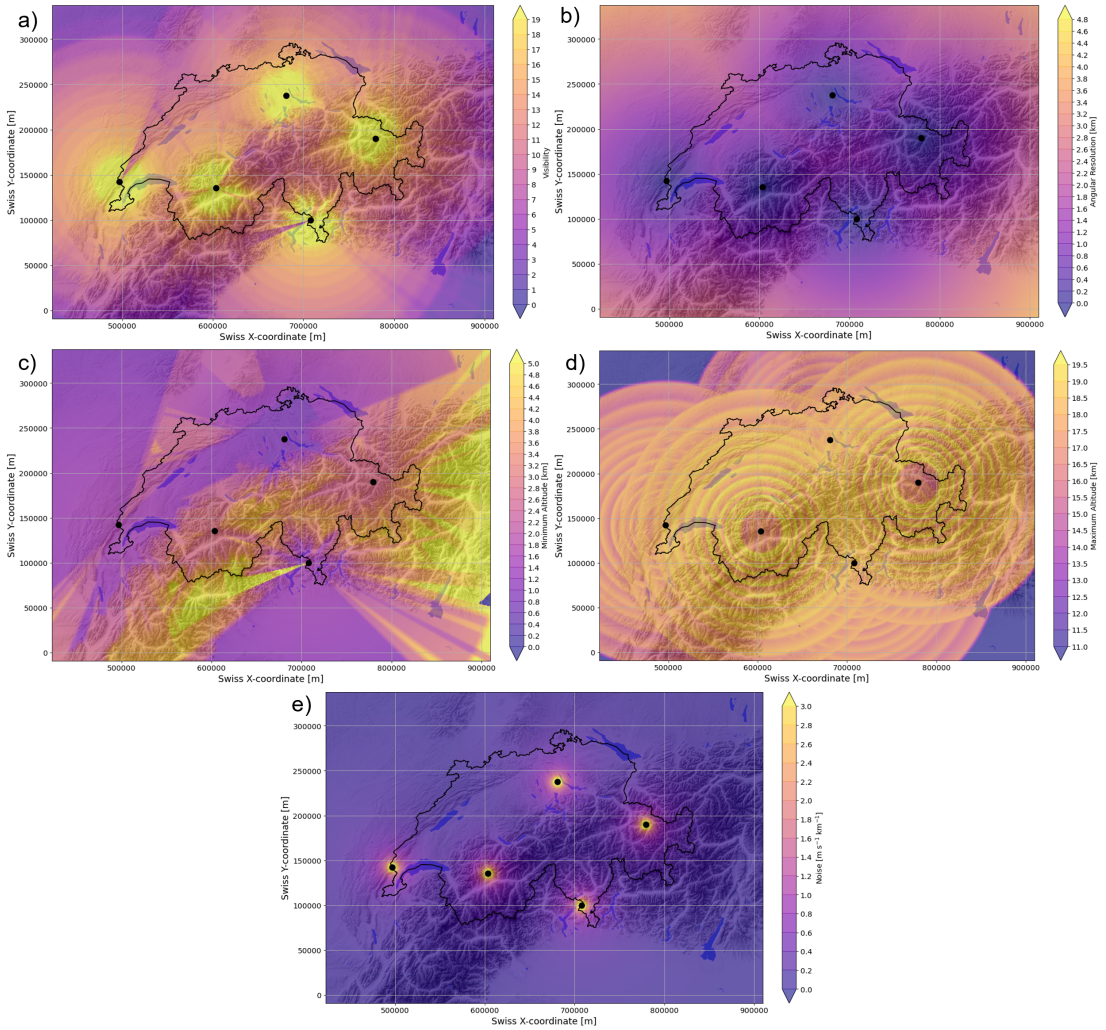

Figure 3.3: Components contributing to the relative quality index for mesocyclone detection in the Swiss radar network; a) vertical sum of visibility; b) azimuthal resolution; c) minimum altitude of observations; d) maximum altitude of observations; e) numerical noise in azimuthal velocity derivative.

To constrain the fields to values that correspond to strong quality degradations, some fields are saturated at threshold values. The minimum altitude field's upper bound is is saturated at 5 km ASL, corresponding to an inability to observe the lower atmosphere. The maximum altitude field's lower bound is saturated at 11 km, indicating a lack of convective top observations. The noise field's upper bound is saturated at $3 \cdot 10^{-3}$ s^{-1}, which is a critical threshold for rotation detection.
Each Cartesian field of a characteristic is then rescaled between 0 and 1, utilizing the highest and lowest values present in the domain, so that 0 represents the lowest quality value and 1 the highest quality value. The normalization for the positively (Eq. 3.3), as well as negatively (Eq. 3.4) correlating variables is given in the following:

$$var_{p\_norm} = \frac{var - var_{min}}{var_{max} - var_{min}} \tag{3.3}$$

and

$$var_{n\_norm} = \frac{var_{max} - var}{var_{max} - var_{min}}. \tag{3.4}$$

Positively correlating variables are visibility and maximum altitude of measurements, where high values correspond to a high quality index. Negatively correlating variables are resolution, minimum altitude of measurements and noise, where a low value corresponds to a high quality index. All characteristics are then combined by the following formula:

$$index = V_{p\_norm} \cdot \frac{(h_{min,p\_norm} + h_{max,n\_norm} + \epsilon_{n\_norm} + \Delta\varphi^2_{az,n\_norm})}{4}$$

As visibility can degrade the quality to zero in absolute terms, it is used as a multiplicative factor. The other variables do not directly influence each other and are thus averaged at equal weights. To account for both horizontal and vertical azimuthal resolution, it is squared.

4 A Characterization of Alpine Mesocyclone Occurrence

This chapter is based on the main text of the postprint version of the published article “Feldmann, M., Germann, U., Gabella, M., and Berne, A.: A characterisation of Alpine mesocyclone occurrence, Weather Clim. Dynam., 2, 1225–1244, https://doi.org/10.5194/wcd-2-1225-2021, 2021". The analyses were performed by Monika Feldmann. Dr. Marco Gabella, Dr. Urs Germann and Prof. Alexis Berne organized the research project and supervised the progress.

This chapter analyses a multi-year data set of mesocyclones based on the newly developed detection algorithm. This presents a first-time comprehensive distribution of significantly rotating convection throughout the Swiss radar domain. The analyses discuss the spatial distribution, corresponding synoptic weather situations, the diurnal cycle, as well as the influence of topography on intensity.

4.1 Introduction

Severe convection in Europe is an increasing weather hazard, that causes significant damage and loss every year (Hoeppe, 2015; Púčik et al., 2019; Kron et al., 2019). Switzerland’s Prealpine areas are known to be one of the most active regions in Europe (Taszarek et al., 2019; Nisi et al., 2018). Supercells are a part of severe convection, the consequential hazards include lightning, downbursts, severe precipitation, hail and tornadoes (Markowski and Richardson, 2010). Thus, they pose a risk to infrastructure, property and lives. Identifying mesocyclone structures in deep, moist convection allows the detection of supercell thunderstorms and a monitoring of their occurrence (Zrnić et al., 1985; Miller et al., 2013).
Supercells and particularly tornadoes have largely been studied in the Great Plains and Southeast of the United States, where the terrain is flat. Many field campaigns have taken place there to obtain in situ and close-range measurements of supercell environments, ranging from early campaigns in the 70s (Bluestein, 1999), the 25-year VORTEX project (NSSL, 2019) and ongoing TORUS campaign (Frew et al., 2020; Garcia de Jesus, 2019). VORTEX-SE (NSSL, 2021) began

covering the beginning of the Appalachian chain, including more complex orography. The observational climatology established in this region is also one of the longest, with mesocyclone detection algorithms having been introduced in the 90s (Zrnić et al., 1985; Stumpf et al., 1998). However, terrain is no obstacle to the initiation of supercells and recent studies have focused more on studying supercells in diverse geographical contexts. The data stemming from the recent RELAMPAGO-CACTI (Varble et al., 2021; Nesbitt et al., 2021) field campaign contains the potential to dissect the role of terrain (here the conjunction of the Andes and the Sierra de Cordoba) in the upscale growth of supercells to mesoscale convective complexes (Mulholland et al., 2019, 2020). However, most studies focus on single cases or a small number of cases, as the amount of data from a field campaign is limited. The ongoing TEAMx project (Serafin et al., 2020) in the Alps specifically targets transport and exchange processes over the mountains, and also contains a section targeting the evolution of convection. All these recent campaigns show the relevance of investigating the nature of severe convection in mountainous areas.

Only very little research in Switzerland has thus far focused on mesocyclones and supercells specifically. Houze et al. (1993) investigated the behavior of severe convection in the Northern Prealps, with 7 years of data from a single-polarization radar. Rotation was inferred from radar reflectivity images. This analysis produced 42 rotating storms during the observation period within the 60 km range of the radar. Only little more right-moving storms occurred than left-moving storms, indicating that there is no strict preference in rotation direction. The study also showed a significant overlap with hailstorms observed during this period.

With hail being a prominent risk factor of severe convection in Switzerland, it is the focus of many recent studies. They range from case studies on hailstorms (Trefalt et al., 2018) over collecting crowd sourced hail reports (Barras et al., 2019) and investigating hail in radar data (Nisi et al., 2016, 2018, 2020) to building a conclusive hail climatology from multiple data sources (NCCS, 2021). Barras et al. (2021) investigates the dynamic conditions leading to hail clusters, as opposed to single hail events, whereas Schemm et al. (2016) analyzes the connection between hail and approaching fronts. The link between lightning jumps and hail occurrence for the purpose of nowcasting has also been investigated (Figueras i Ventura et al., 2019). Particularly Nisi et al. (2018) describes the general occurrence and frequency of hail events in Switzerland, taking into account the effects of the seasonal and diurnal cycle and investigating the influence of the synoptic weather situation. Key takeaways are the importance of weather situations with south-westerly and westerly flow, as well as the dominance of rather large, persistent hailstorms at low convective activity hours of the night.

While tornadoes are rare in Switzerland, they nonetheless occur approximately once per year, as estimated by the Swiss severe weather database (Sturmarchiv Schweiz, 2021). Most tornadoes are very weak and classify as F0 events, but on rare occasions, a more significant event can take place. Both Peyraud (2013) and Grazioli et al. (2019) show case studies of tornadoes in Western Switzerland. Avolio et al. (2020) describe the case of a supercell, that media reported to have a suspected tornado, just beyond the Southern Swiss border.

In Germany, mesocyclone detection has been implemented more recently (Hengstebeck et al., 2018; Wapler et al., 2016). Studies there also show that supercells can occur in all parts of the country, including areas with complex topography, such as the Bavarian Prealps (Wapler et al.,

2016; Wapler, 2017, 2021). The majority of hailstorms have a mesocyclone structure before and during the production of hail, indicating the relevance of detecting mesocyclones for nowcasting purposes. Mirroring the overall behaviour of convection, there is a pronounced seasonal and diurnal cycle, with a large influence of the synoptic weather situation. In comparison with (Nisi et al., 2018), the dominant flow situations initiating severe convection in Germany differ from Switzerland due to the different geographical location. Over Southern, Western and central Europe in general Southwesterly situations can lead to deep, moist convection (Piper et al., 2019; Mohr et al., 2019; Wapler et al., 2016; Morris, 1986), as the advection of moist, warm air from the Mediterranean provides favourable conditions. In addition, other flow situations can be beneficial regionally, depending on the geographic situation (Piper et al., 2019; Nisi et al., 2018; Wapler et al., 2016). Mohr et al. (2020) show the influence of synoptic weather on a series of severe thunderstorms from Southwestern France to Northeastern Germany in June 2018, highlighting the importance of the large-scale flow on widespread severe weather outbreaks including supercells. With the potential of severe convection rising not only globally (Diffenbaugh et al., 2013), but also in central Europe (Rädler et al., 2019; Mohr and Kunz, 2013; Púčik et al., 2017), we have a large incentive to better understand and characterize mesocyclones in the Swiss domain.

Our work focuses on the region covered by the Swiss operational radar network Rad4Alp (Germann et al., 2016b; Bundesamt für Meteorologie und Klimatologie MeteoSchweiz, 2018), which extends over the main Alpine ridge, Prealps, Jura mountains (along the Northeastern border between Switzerland and France, see locations in Nisi et al. (2016), Fig. 1) and parts of the neighboring countries Germany, France, Italy and Austria. The Alps dominate the topography of this area, allowing a study of supercell behavior in complex terrain and high altitude environments. We here establish a systematic detection of mesocyclones in the entire radar domain over 5 years. This allows a first-time characterization of the spatio-temporal distribution of mesocyclones in the Swiss domain and builds the basis for operational automatic mesocyclone detection and nowcasting. Recent improvements in the processing of radar Doppler velocity (Feldmann et al., 2020) now allow the implementation of a robust, radar-data based mesocyclone detection algorithm. The data set established here permits us to investigate the occurrence and evolution of supercells in high altitude, complex terrain. The analysis focuses on identifying spatial patterns, the influence of the synoptic flow and the diurnal cycle.

Our work presented is organized as follows. Section 4.2 describes the data sets used in our analyses. The results are presented and discussed in Sect. 4.3, followed by our conclusion (Sect. 4.4). The previous chapter 3 includes more detailed descriptions of the thunderstorm detection algorithm (3.1), mesocyclone detection algorithm (3.2) and the radar network quality assessment 3.3).

4.2 Data

All data are analyzed for the years 2016-2020, for the months April through October. As the occurrence of supercells in Switzerland was a priori unknown, we consider an extended convective season to ensure an analysis of all significant events. As shown in Barras et al. (2021), this time frame extends beyond the expected seasonal occurrence of severe convection. In this study we largely rely on the operational radar data of the Swiss Rad4Alp network. To pre-process the Doppler velocity data, the numerical weather prediction model COSMO (Consortium for Small Scale Modelling, 2018; de Morsier et al., 2012) provides velocity data as an initialization. We here use COSMO-1 analysis data which is produced operationally by MeteoSwiss at a spatial resolution of 1 km and a temporal resolution of 1 hour, extracted within the Swiss radar domain. The model assimilates data from surface observations, radiosonde and wind profiles, as well as radar data. It is a convection-permitting model that partially resolves convective dynamics. As we use hourly model data to initialize a first-guess for 5 minute radar data, the data is convolved using a 20 km kernel to smooth out smaller scale convective dynamics and retain primarily the larger scale flow (Feldmann et al., 2020).
Additional information is drawn from an operational classification of the general weather situation (Weusthoff, 2011) and a digital elevation model of Switzerland (©swisstopo, 2005; Jarvis et al., 2008). The digital elevation model, which is a merged product from ©swisstopo (2005) and Jarvis et al. (2008), provides elevation data over the Swiss radar domain. It is used to provide topographical context for our analyses and investigate the first-order influences of terrain. To characterize the meteorological and topographical environment of convection, we use a synoptic type weather classification and a digital elevation model. The so-called Gross Wetter Types (GWT) weather classification provides 8 different weather types over Switzerland that are based on the synoptic flow at 500 hPa geopotential height (Weusthoff, 2011). The classes directly correspond to the eight cardinal flow directions.

4.2.1 Operational Radar Network

A detailed description of the operational radar network is given in section 1.3.2.
We use the 2-D Cartesian maximum reflectivity product, as well as the 3-D dealiased Doppler velocity in polar coordinates. Due to relatively low Nyquist velocities in the raw Doppler velocity and complex airflow situations in thunderstorms, the aliased Doppler velocity poses a challenging de-aliasing problem. Therefore, we initialize the Region-based Recursive Doppler Dealiasing (R2D2) algorithm (Feldmann et al., 2020) with a radial wind estimate from COSMO-1 analysis data (Consortium for Small Scale Modelling, 2018) to remove all velocity aliases. During this 5-year period, all 5 radars provide homogeneous data coverage with the same, synchronized scan strategy and COSMO-1 data is available. Prior to 2016 the two high altitude radars were not yet installed and COSMO was operated at a 2 km spatial resolution.

4.3 Mesocyclone Characterization

To reliably detect mesocyclones in an Alpine context, we combine a 2-D thunderstorm detection and tracking algorithm (T-DaTing) with a 3-D mesocyclone detection and tracking algorithm (M-DaTing). The mesocyclone detection activates within the identified thunderstorms. Both algorithms are described in detail in chapter 3. In addition, we take into account the quality of the radar observations with the quality index established in chapter 3. Figure 4.1 depicts the quality index superimposed on the Swiss orography. The quality index ranges from 0 (relatively lowest observational quality) to 1 (relatively highest quality). The locations of the case studies discussed in section 4.3.1 are indicated in letters.

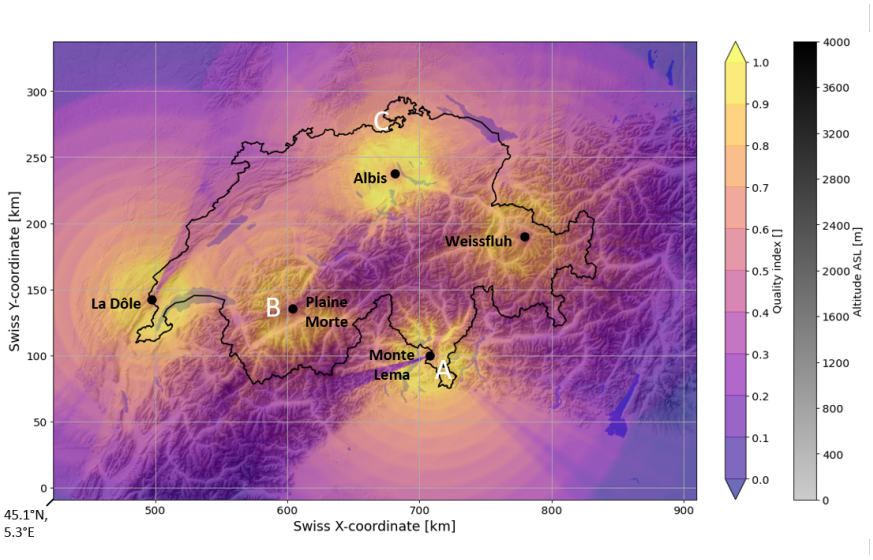

Figure 4.1: Relative quality index for mesocyclone and thunderstorm detection in the Swiss weather radar network depicted over elevation map; case study locations (Figs. 4.2, 4.3 and 4.4) indicated with white letters; radar locations shown with black dots; radar altitudes: Albis - 938 m, La Dôle - 1682 m, Monte Lema - 1626 m, Plaine Morte - 2937 m, Weissfluh - 2840 m.

4.3.1 Case examples

As an introduction to mesocyclonic rotation in an Alpine context, we first show an example case from the Southern Prealps that are very prone to thunder- and hailstorms (Nisi et al., 2018; Schemm et al., 2016). Figure 4.2 shows the radar reflectivity, Doppler velocity and vertically integrated liquid (VIL) measured from Monte Lema radar (marked with A in Fig. 4.1) at 17:30 UTC on August 20th, 2019. In the reflectivity data we can clearly see the location of the convective cell at 10-15 km range and 90-150° azimuth with values exceeding 45 dBz, indicating strong convection. The shape of the area of high reflectivity shows the typical hook-echo, which suggests the presence of prominent rotation (Markowski, 2002; Kumjian and Ryzhkov, 2008). The storm here is observed at an altitude of approximately 2500 m ASL. In the Doppler velocity data, we can see the opposition of inbound (red, following the Swiss

convention of depicting Doppler velocity) and outbound (blue) velocities close to the hook, here presenting anticyclonic rotation (indicated with arrows), confirming the presence of a mesocyclone. While these signatures are quite clear, the rotational velocity is not particularly high in comparison to supercells in other regions (e.g. in the Great Plains, USA), here averaging around 12 m s^{-1}. We can also see that VIL is elevated in the area of highest reflectivity, but not extremely high. This indicates significant precipitation, but not necessarily hail. The proximity to the radar may lead to an underestimation of VIL, as the upper part of the storm is above the highest radar beam. To represent the spatial heterogeneity in Switzerland, two additional case studies from the high Alpine region (marked B in Fig. 4.1) and the Rhine valley (C) are provided as well. They show that supercells in Switzerland exhibit a range of rotational intensities and reflectivity features.

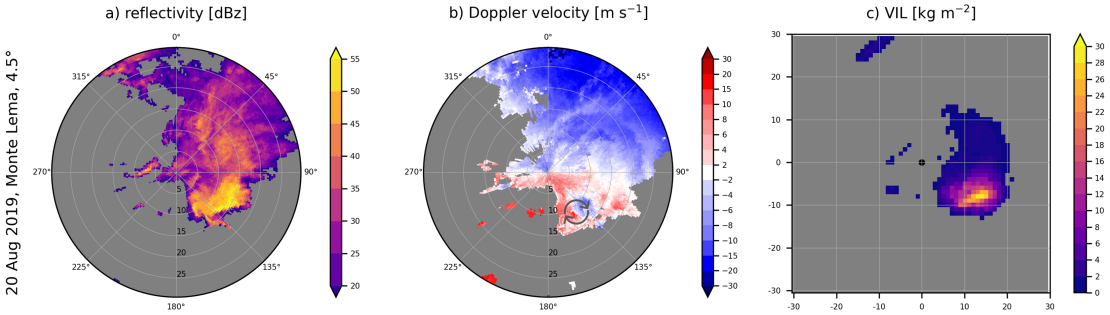

Figure 4.2: Example of supercell in the Southern Prealps; August 20th, 2019 at 17.30 UTC.

Case B, as indicated in the map of Fig. 4.2, is located in the Valais Alps and was observed from Plaine Morte radar. It shows a case in complex, high-altitude terrain, observed at ~ 4800 m ASL. Figure 4.3 shows the supercell at 10-30 km range and 200-240° azimuth, in the Doppler velocity panel the location and direction of rotation is indicated with arrows. The hook shape in the reflectivity is less evident here compared to the event presented in Fig.4.2, but we can see a clear indentation in the high reflectivity values at the location of outgoing (blue) Doppler velocities, showing the perturbation from the rotation. The high values of VIL also indicate the large moisture content in the atmospheric column. This storm was associated with multiple extreme precipitation and wind gust measurements (MeteoSwiss, 2019).

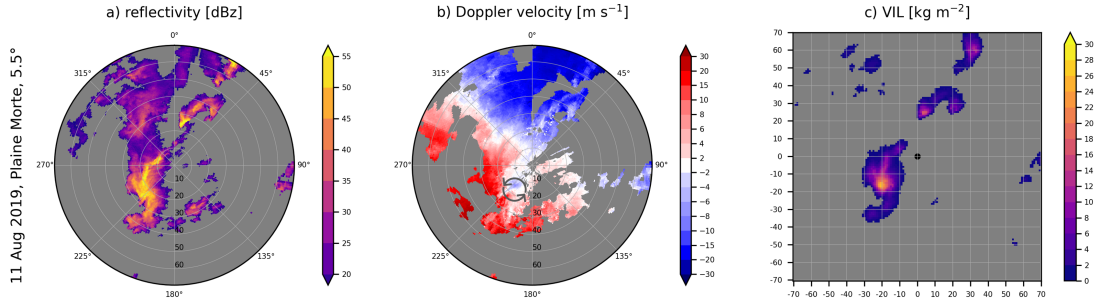

Figure 4.3: Supercell in Valais; August 11, 2019.

The third case (Fig. 4.4) stems from the Rhine valley and comes closest to convection without orography in Switzerland and is shown in the radar imagery at an altitude of approximately 2000 m ASL. Nonetheless the proximity of the Black Forest to the Northwest and Jura in the Southwest indicate that topography is a relevant factor for thunderstorm initiation and development everywhere in Switzerland. The supercell is at a further range than the previous cases (30-50 km, 330-30°), but nonetheless well observed. We can see a clear perturbation in the high reflectivity signature. The rotation in the Doppler velocity fields is quite strong, averaging around 20 m s^{-1}. The main region of the thunderstorm shows high values VIL. This storm was responsible for a new precipitation record in Switzerland (36.1 mm in 10 minutes) at the time (MeteoSwiss, 2017). During the evolution of the storm, the reflectivity data also shows significant attenuation behind the storm core. Probability of hail is also estimated to be close to 100 % throughout large parts of the track, however no hail was reported on the ground, possibly due to the storm taking place at night.

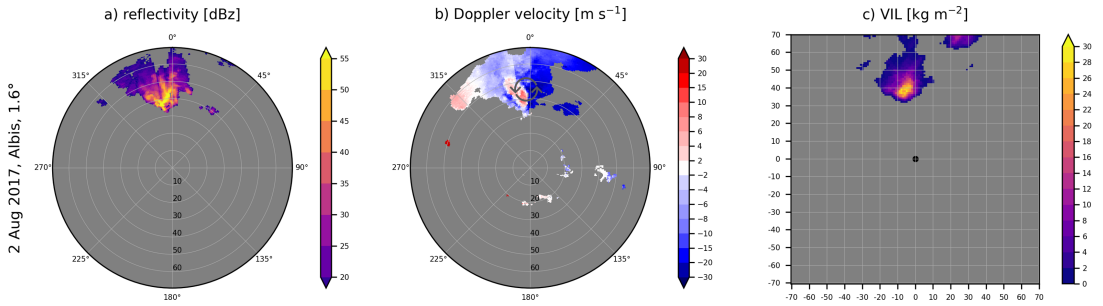

Figure 4.4: Supercell along the Rhine valley; August 2nd, 2017.

4.3.2 Spatial Patterns

From here we will inspect the overall distribution and occurrence of mesocyclonic rotation over the Swiss domain during the 5 analyzed years and compare this to the general occurrence of thunderstorms and the quality of the radar network. Table 4.1 gives an overview of the annual average convective activity.

Table 4.1: Overall annual average occurrence of mesocyclones and thunderstorms during 2016-2020 in the Swiss weather radar network.

	number of detections	number of storm tracks	number of active days
mesocyclones	690	80	22
thunderstorms	203'700	25'200	170

Approximately 10 % of days during the convective season had at least one mesocyclone within the Swiss domain. T-DaTing is configured to detect storms exceeding 50 km^2 to focus on more significant convective systems (see section 3.1). 0.3 % of all detected thunderstorms showed mesocyclonic rotation. Overall the earliest detected mesocyclone was in the last week of April and the latest in the beginning of the last week of October.

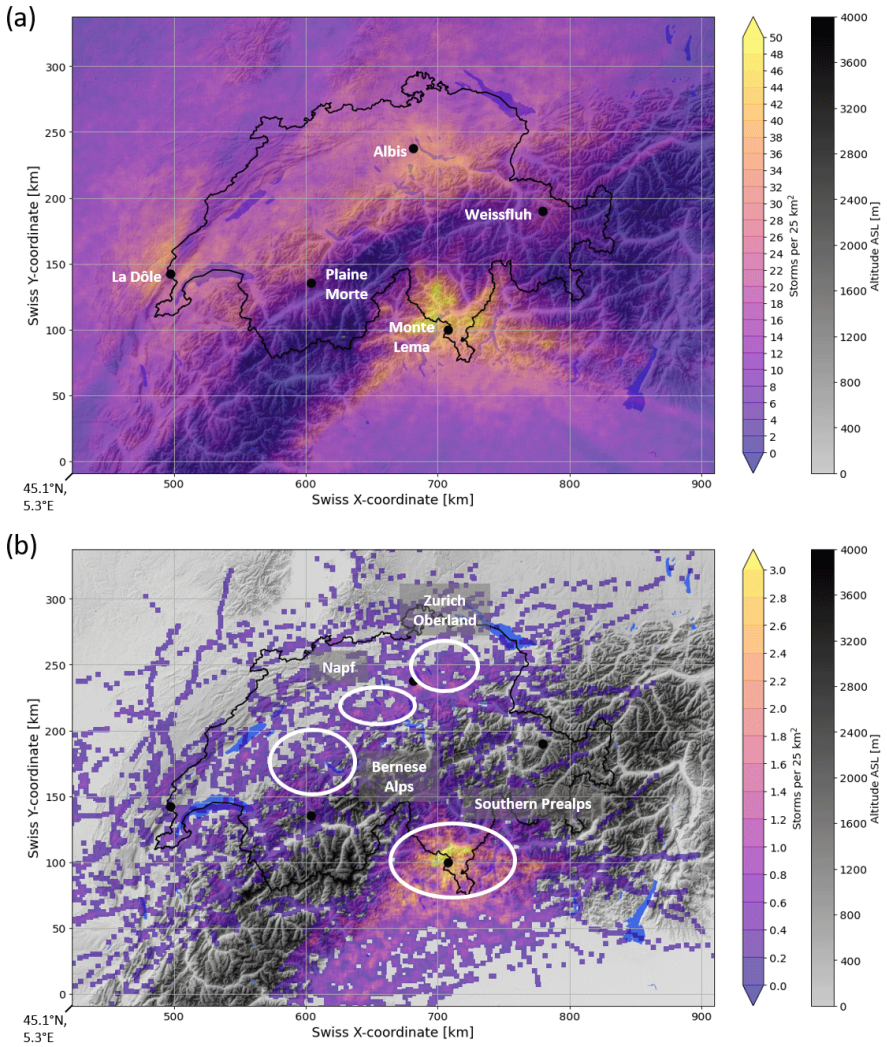

Figure 4.5: Annual average individual detections of a) thunderstorms and b) mesocyclones from 2016-2020 per 25 km^2. Highlighted regions of interest: Zurich Oberland, Napf, Bernese Alps and Southern Prealps.

Figure 4.5 a) shows the annual average spatial distribution and density of the 5-year thunderstorm and mesocyclone analysis. Thunderstorms are clustered in the Prealpine valleys in moderately high topography. In absolute terms the main hot spot is to the South of the Alps in the canton Ticino. The Alps serve as a meteorological divide, separating Northern Switzerland from Mediterranean air masses (MeteoSwiss, 2018). Ticino experiences more

subtropical, Mediterranean conditions than the rest of Switzerland, with generally higher temperatures and frequently high relative humidity (Nisi et al., 2016; MeteoSwiss, 2018). These conditions are more conducive to convective initiation and development. Topography can induce convection through valley wind systems (Linder et al., 1999; Rampanelli et al., 2004; Nisi et al., 2016). Particularly in the afternoon hours, upslope winds cause convergence over ridges and can provide the initial lift needed to overcome convective inhibition. We can also see that the frequency of thunderstorm detections is higher in the vicinity of the radars. If we compare the spatial distribution of thunderstorms to the relative quality map of the Swiss domain, we can clearly see that more thunderstorms are detected in locations where the quality index is high. While we do not establish a quantitative relationship, a lower quality index increases the probability of underestimating thunderstorm occurrence. Nonetheless, the dominant spatial trends of convective preference in the Prealps are meteorologically consistent with orographic convection and can be confirmed with lightning climatologies (Enno et al., 2020; MeteoSwiss, 2016). The clearest deviation from meteorological expectations can be seen to the Northeast and Southwest of the Jura. Beam blockage significantly lowers the capability of La Dôle radar to accurately observe convective events in these areas. While we may underestimate thunderstorm occurrence in the inner Alpine regions, where the quality index is lower, the reduced convective activity here is confirmed by independent lightning climatologies (Enno et al., 2020; MeteoSwiss, 2016). Moreover, the spatial patterns do not significantly change in the vicinity of the Alpine radars Plaine Morte and Weissfluh, where the quality index is higher.

Shifting our focus to the annual average spatial distribution of thunderstorm tracks that contain a mesocyclone in Fig. 4.5 b), we can see a similar spatial pattern. Most mesocyclonic storms occur to the South of the Alps. In the North, they largely occur in Prealpine areas. A small, but relevant hot spot can be seen in the Napf area to the West of Lake Lucerne. Additionally the Bernese Alps and Zurich Oberland are areas of elevated frequency. Both the global maximum in Ticino and the local maxima in the Northern Prealps correspond to hail occurrence maxima (NCCS, 2021; Nisi et al., 2018; Trefalt et al., 2018). Considering that hail is a known severe weather consequence of mesocyclones, this overlap reinforces the robustness of the obtained spatial distribution. We can see a lesser dependence of detections on the quality index. This may be due to the fact, that mesocyclones generally have a large vertical extent and can be detected in multiple consecutive elevation scans, thus being less dependent on accurate measurements in single elevation scans. Range-dependent rotation thresholds compensate for decreasing measurement resolution with range and allow mesocyclones to be detected even beyond a range of 100 km per radar. The most issues can still be noted over the Jura, where the beam blockage of La Dôle radar impacts the first 10 elevation scans. The beam blockage in this area is severe enough, that confirmed cases of mesocyclones are missed in this region. This is illustrated by the case study of a tornado near Neuchatel in Grazioli et al. (2019), in which the data from both a mobile, X-band radar that was tracking this storm cell, and the operational C-band data, are analyzed. The rotation is clearly visible in the X-band data, however from La Dôle radar the rotation is undetectable and the location is at a far range from Albis radar.

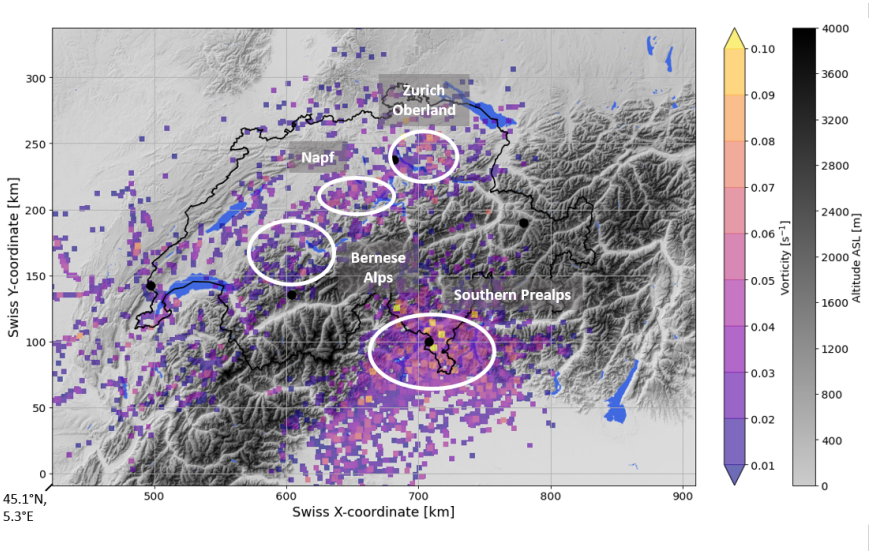

Figure 4.6: Maximum detected vorticity per 25 km^2 during five years (2016-2020).

Figure 4.6 shows the maximum measured vorticity values of all detected mesocyclones. The values range from $0.6 \cdot 10^{-2}s^{-1}$ to $12 \cdot 10^{-2}s^{-1}$, with a mean of $2 \cdot 10^{-2}s^{-1}$. The typical mesocyclone definition (Stumpf et al., 1998) requires a vorticity of $10^{-2}s^{-1}$, showing that the average event is twice as strong and the extremes exceed this value by an order of magnitude. The lower minimum value stems from the use of range-dependent thresholds, where we lower the vorticity requirement with increasing distance to the radars to compensate for decreasing spatial resolution (see section 3.2).
The largest cluster of high vorticity values is located around the Ticino hot spot. But also the Napf area and Zurich Oberland show consistently elevated values of vorticity. This is not the case for the Bernese Alps, where the vorticity values are on the low end of the spectrum and close to the detection threshold. The topography is significantly more complex here, which may impact a storms capability to maintain strong rotation.
The spatial overlap of the strongest rotation concurring with the largest size hail in the Napf region and Southern Ticino established in longer-term hail climatologies (NCCS, 2021) indicates that stronger rotation usually favors larger hail (Allen, 2018; Blair et al., 2017; Witt et al., 2018). However the differences in the Bernese Alps, where we have large hail, but low rotation velocities and Zurich Oberland, where we have high rotation velocities, but smaller hail show that there may also be other factors at play and warrants further investigation. The Bernese Alps have a reduced quality index, due to beam blockage to the Northeast of Plaine Morte radar. This may interfere with the ability to reliably detect and estimate the intensity of vortices. Discrepancies may also be owed to the relatively short duration of the 5 year analysis.

4.3.3 Dependency on Synoptic Weather Situation

The synoptic weather classification Gross Wetter Types (GWT) provides insight in which synoptical flow situations mesocyclones are likely to occur. Figure 4.7 a) shows the complete tracks of all detected mesocyclones (lines) as well as the location of mesocyclone initiation (dots), color coded by the corresponding flow direction. Figure 4.7 b) provides a histogram of the overall occurrence of all weather classes during the analyzed period, in comparison to the histogram focusing on the days with mesocyclone activity. Figure 4.7 c) presents the fraction of days in each weather class that produce a mesocyclone during the analysis period.
Flow from the Southwest is responsible for the majority (55 %) of mesocyclone detections. These situations are generally characterized by air masses originating in the warm, humid Mediterranean area. They hold high amounts of convective available potential energy (CAPE) and moisture, thus presenting favorable conditions for severe convection. In the analyzed time period, approximately 25 % of days with a Southwesterly flow produced at least one mesocyclone (see Fig. 4.7 c). Among others, Mohr et al. (2020) and Wapler and James (2014) show that a Southwesterly flow induces favorable conditions for deep, moist convection in most of central and Western Europe. A particularly potent synoptic constellation is called the "Spanish plume" (Morris, 1986; Peyraud, 2013), where the low-level Southwesterly flow is in the prefrontal zone of an approaching cold front over France, the mid-level flow supplies warm, dry air stemming from the Iberian peninsula and the upper-level flow is Westerly, with cooler, Atlantic air. This leads to high amounts of CAPE in addition to lifting occurring through the approaching front. The vertical change in flow direction provides directional wind shear, which is beneficial for mesocyclone development (Peyraud, 2013). Depending on the altitude of the transition to the Westerly upper-level flow, a fraction of Spanish plume events may also be classified as Westerly flow in the GWT classification. As shown in Schemm et al. (2016), approaching fronts also play an important role in hail formation, particularly in Swiss regions, where hail falls less frequently.
Westerly flow is the second most frequent flow direction during mesocyclones, contributing to a third of all detections, followed by Southerly flow at ~ 10 %. Both have similar characteristics as Southwesterly flow, but less reliably yield the optimal conditions for severe convection (each approximately 12 % of the time, see Fig. 4.7 c). As Fig. 4.7 b) shows, Westerly flow is the most common flow situation in Switzerland (MeteoSwiss, 2018) and rather brings Atlantic air masses to Switzerland. Roughly 10 % of days with Westerly flow produce at least one mesocyclone. Southerly flow is more prevalent to the South of the Alps, but already leads to much less mesocyclone cases. To the North, there are only few cases that are displaced further North, as descending air crossing the Alps does not provide favorable conditions. Other flow directions play a very small role and are only responsible for very few cases (<5 %).
As the track lines in Fig. 4.7 a) indicate, the synoptic flow steers the main direction of storm tracks, while allowing for the deviation of left- and right-mover storms. Histograms of storm direction per weather class cluster in a Gaussian distribution around the direction of synoptic flow (figures not shown). Given the synoptic-scale criteria for the weather classification, the mesoscale flow at the steering level of convection (5000 - 7000 m ASL, Foresti et al., 2018) can

also deviate from the classification.
While Southwesterly flow also plays an important role in hailstorms, it is not the dominant weather class (Nisi et al., 2018). Hailstorms predominantly form in Westerly flow, which is also the most frequent weather class. With hail also occurring much more frequently (Barras et al., 2019; Nisi et al., 2018), it appears that Westerly flow yields conditions that are sufficient for hail production, but not as frequently for mesocyclone formation. Westerly flow also leads to a hail hotspot in the Northern Jura, where the quality of Doppler velocity data is limited and we potentially miss mesocyclones.

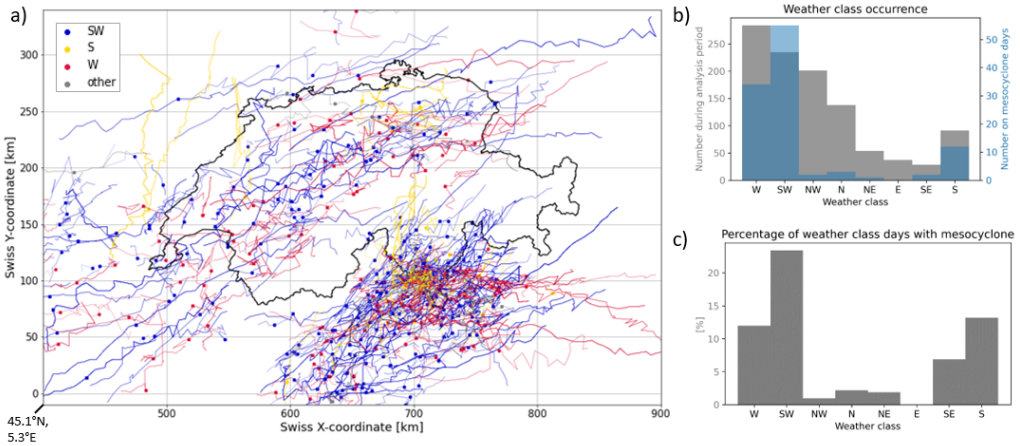

Figure 4.7: a) Spatial dependency of synoptic weather situation based on prevailing flow at 500 hPa, lines show complete tracks of mesocyclones, dots depict mesocyclone initiation; b) histograms of weather class occurrence during entire analysis period and during mesocyclone days; c) Percentage of days per weather class with mesocyclone activity.

4.3.4 Diurnal Cycle

The occurrence of mesocyclones shows a pronounced diurnal cycle that mirrors the cycle of convection in general (see Fig. 4.8 a)). The majority of storms occur in the afternoon and first half of the night, with the peak of formation at 15 UTC. Mesocyclones, however, show a local, smaller peak, during the second half of the night as well (0-4 UTC) and then a minimum in the early morning at 4 UTC. Thunderstorms in general drop to a lower occurrence from 0-10 UTC, but can initiate at all hours of the day. The base frequency at unfavorable hours in the late night and early morning is almost constant.

In comparison to this frequency distribution, there is also a diurnal cycle reflected in cumulated storm area and track length, as shown in Fig. 4.8 b). The storm area refers to the cumulative area over the entire storm track, whereas the track length refers to the overall distance along the path of the storm track. The behavior of the track duration mirrors the

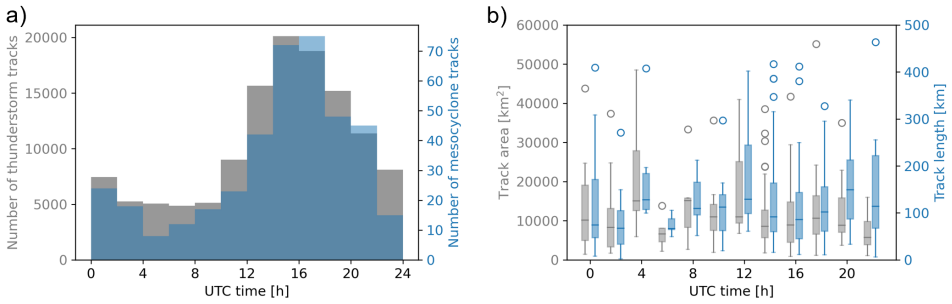

Figure 4.8: Diurnal cycle of convection (a), each 2h bin shows the number of tracks beginning at this time; diurnal cycle of mesocyclone track properties (b), each 2h bin shows the cumulative track area and length of tracks beginning at this time.

track length (not shown here). In contrast to the occurrence histogram, the global peak of both variables is at 12 UTC, before the peak mesocyclone occurrence time in the day. A local peak is additionally found at 4 UTC during the minimum of mesocyclone occurrence. Even though the sample size is very small (<10), this shows parallels to research conducted on hailstorms, where the longest and largest storms also occur outside hours of the convective peak (Nisi et al., 2018). Due to the significant drop in convective activity at this time of day, this indicates a significant overlap between mesocyclones identified here and hailstorms analyzed in Nisi et al. (2018). In spite of the small sample present, this agreement with severe hailstorm behavior also reinforces the notion found in Nisi et al. (2018) that convective storms that initiate during unfavorable hours of the day are more likely to be severe, whereas the most active hours of the day contain a larger fraction of less intense storms. As this hypothesis based on the small sample in the mesocyclone data set is rather speculative, it should be revisited, once longer homogeneous data series are available.

4.3.5 Terrain

Utilizing the data from the digital elevation model, we can see that the majority of rotating storms move uphill during their lifetime. With the majority of storms occurring in Ticino (~ 60 % of mesocyclones are detected from Lema radar) and a Southwesterly flow direction dominating here, many storms follow a Northeasterly path towards the main Alpine ridge (see Fig. 4.7), thus moving uphill. As Fig. 4.9 a) shows, in the South of the Alps, up to an altitude of approximately 1500 m, the storms do not show intensity correlation to the altitude. Beyond that, higher altitude negatively impacts the upper potential of intensity metrics such as rotational velocity and vorticity, here shown by the decreasing trend in the 95th percentile. The same effect can be seen to the North of the Alps, however at a lower altitude. With the storm tracks being more parallel to the Alps (see Fig. 4.7), less storms move uphill and encounter higher altitudes. In both cases the lowering in intensity is mirrored by a lowering in case numbers

with altitude. Similar trends can be observed for vertical extent and maximum reflectivity (not shown). Storms with weak rotation occur throughout the entire domain and dominate the intensity distribution, however with increasing altitude the upper percentiles decrease, indicating a limit to the potential rotational intensity a storm can achieve in this environment. As the number distribution with altitude shows, the majority of storms are detected in lower altitude regions. This concentration in relatively flat areas within the Prealpine region, such as the larger valleys and lakes, is also shown in Fig. 4.5. At high altitudes beyond 1500 m ASL the terrain becomes increasingly complex with steep slopes and rapid altitude changes. We hypothesize that this could impact the low-level dynamics of a supercell, disturbing the generation of vorticity at the outflow boundary and its advection back into the storm in the inflow.

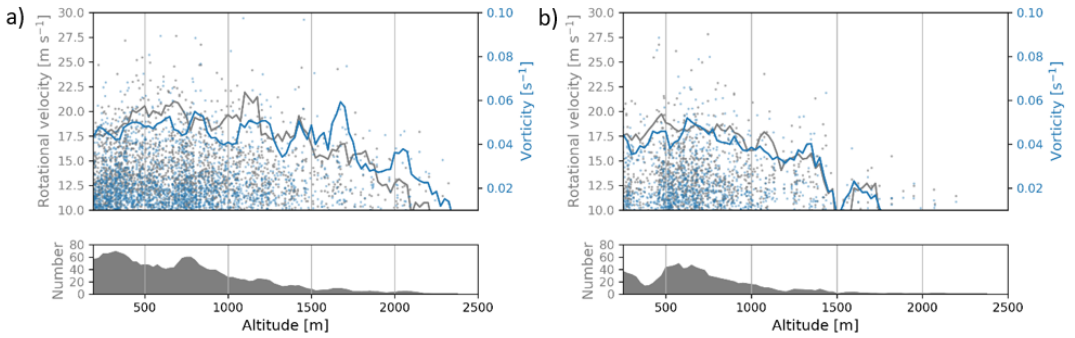

Figure 4.9: Topographical influence on rotational metrics; scatterplot of rotational velocity and vorticity versus altitude. The grey and blue lines indicate the smoothed 95th percentile, the lower graph shows the number of detection per altitude. a) Cases detected by Lema radar (South), b) cases detected by radars Albis and La Dôle (North).

As the quality index also decreases over the main Alpine ridge, the probability of underestimating mesocyclone occurrence here also rises. However, as shown in Enno et al. (2020) and MeteoSwiss (2016), the overall thunderstorm frequency, derived from radar-independent lightning data, also decreases significantly here, indicating that we are observing a true trend and not a limitation of the radar network.
With the majority of storms located in the Prealpine regions, orographic triggers for convective initiation play an important role in Switzerland (Nisi et al., 2016; Linder et al., 1999). The main Alpine ridge poses a strong separation for thunderstorms. With the thunderstorm frequency dropping substantially over the inner Alpine regions in Fig. 4.5 a), we can see that thunderstorm tracks generally do not persist crossing the Alpine ridge. In Fig. 4.5 b) we can see the inner Alpine regions devoid of rotation detections. Additionally, Fig. 4.7 a) shows only one mesocyclone track crossing the Alps, while all other tracks heading towards the main Alpine ridge decay prior. This supports the hypothesis that high altitude mountainous terrain has an inhibiting impact on the rotation dynamics of a thunderstorm.

4.4 Conclusion

The implementation of a radar-based mesocyclone detection algorithm and the analysis of the years 2016-2020 allows a first time assessment of the occurrence of mesocyclones in Switzerland. Around 80 thunderstorms per convective season (April - October) had a mesocyclone, distributed over 22 days per convective season. It is evident that mesocyclones can be detected and tracked in a large portion of the Swiss radar domain. While range is usually a limitation, the maximum detectable range for mesocyclones in the Swiss radar network exceeds 100 km per radar. The accompanying relative quality index map helps interpret, where the mesocyclone detection is impeded by the physical limitations of the radar network. The most pronounced limitations are over the Jura in Northwestern Switzerland and over the inner, main Alpine ridge, as well as at far ranges outside of Switzerland.
The 5 year analysis allows a first assessment of the overall frequency and spatial distribution of mesocyclones in the Swiss domain. The absolute maximum of detections lies in the Southern Prealps. Monte Lema radar, situated in this region, detects approximately 60 % of all mesocyclones, with the other half being distributed rather evenly between the other 4 radars. Smaller, local maxima lie in the Prealpine valleys to the North of the Alps, such as in the Bernese Alps, the Napf region and the Zurich Oberland. This spatial distribution parallels that of hailstorms (NCCS, 2021).
Clear characteristics emerge and show parallels to other features of convection in Switzerland, such as the importance of the synoptic flow and the pronounced diurnal cycle. Southwesterly flow is the most conducive for mesocyclone occurrence, followed by Westerly and Southerly flow. The diurnal cycle of mesocyclone initiation shows a clear peak in the late afternoon hours and a minimum in the early morning hours, mirroring the diurnal cycle of thunderstorms in general. Size metrics such as area and track length however indicate that the few storms occurring during the minimum tend to be larger and last longer. This tendency can also be observed in hailstorms (Nisi et al., 2018), indicating a probable overlap between the two storm populations. The importance of Southwesterly flow to convection in central and Western Europe is also shown in (Wapler and James, 2014) and (Mohr et al., 2020), which highlights the significance of synoptic flow for large regions.
With mesocyclones being rather rare events, longer timelines are necessary to establish robust assessments of interannual variability and seasonal trends. The spatial distribution can also be evaluated more robustly with a longer analysis period, as low-activity regions are currently dominated by the characteristics of single events. Data prior to 2016 was not used in this study, as major changes in the radar network took place at that time.
The spatial distribution of both thunderstorms and mesocyclones shows that terrain has a clear influence on the initiation of convection. Similarly, the inner Alpine regions are devoid of mesocyclones, indicating that steep, high altitude environments have a negative influence on rotational dynamics. Rotational metrics show a negative correlation with increasingly high altitudes as well.
After establishing this first time assessment of mesocyclones in Switzerland, future work is required to clarify the severe weather consequences of mesocyclones in Switzerland and

further investigate the interactions with the complex terrain.

5 Hailstorms and Rainstorms vs. Supercells - A Regional Analysis of Convective Storm Types in the Alpine Region

This chapter is based on the latest revised version of the preprint “Monika Feldmann, Marco Gabella, Alessandro Hering et al. Hailstorms and rainstorms versus supercells - a regional analysis of convective storm types in the Alpine region, 07 June 2022, PREPRINT (Version 1) available at Research Square [https://doi.org/10.21203/rs.3.rs-1666457/v1]", which has been accepted at npj Climate and Atmospheric Science. The analyses were performed by Monika Feldmann. Dr. Alessandro Hering provided valuable insights severe convection in Switzerland as well as expertise in the use of Swiss thunderstorm data. Dr. Marco Gabella and Prof. Alexis Berne organized the research project and supervised the progress.

Since supercells are a new type of classified thunderstorm in the Swiss radar domain, this chapter aims to provide a contextual understanding of how supercells compare to established severe convection. We here compare the life cycle evolution and intensity distribution to severe hail- and rainstorms. This adds relevant information for the operational use of the algorithm, as it provides forecasters with context on how a detected mesocyclone usually evolves and how intense the storms generally become. In addition, this rich data set in severe convective storms spanning multiple topographically diverse regions provides the basis for a more comprehensive topographic analysis.

5.1 Severe Thunderstorms

Severe thunderstorms are one of the most costly natural hazards (Hoeppe, 2016; Púčik et al., 2019; Ward et al., 2020). They can lead to straight line winds, intense rainfall, large hail and even tornadoes (Markowski and Richardson, 2010). These phenomena pose a risk to infrastructure, properties and human life. With the fraction of severe thunderstorms expected to increase with climate change in Europe (Púčik et al., 2017; Rädler et al., 2019; Kron et al., 2019; Raupach et al., 2021a), improved understanding of severe thunderstorms is highly relevant for future risk assessment.

Research on severe thunderstorms often focuses on the single hazards, such as studies on hail (Allen et al., 2016; Martius et al., 2018; Nisi et al., 2018; Allen et al., 2020; NCCS, 2021) or severe rain (Gaál et al., 2014; Panziera et al., 2016; Aregger, 2021; Miglietta and Davolio, 2022). We here aim to take a more comprehensive approach and study multiple aspects of severe convection across diverse topographic regions. To improve short-term warnings, nowcasting hail and precipitation has been a priority in Europe (Panziera et al., 2011; Nisi et al., 2014; Panziera et al., 2016; Wapler et al., 2016; Foresti et al., 2019; Sideris et al., 2020). Key findings have been the integration of orographic enhancement in precipitation nowcasting (Panziera and Germann, 2010; Panziera et al., 2011; Foresti et al., 2019) and considering lightning jumps for hail (Wapler et al., 2016; Nisi et al., 2020).

While severe thunderstorms have been studied for a long time, there is still limited understanding about their behavior in complex terrain. Several studies on hailstorms in Switzerland (Nisi et al., 2016, 2018, 2020; Barras et al., 2021) discuss their occurrence and behavior in the Alpine region. Previous studies on supercell thunderstorms in Switzerland (Houze et al., 1993; Huntrieser et al., 1997; Feldmann et al., 2021) show their overlap with and similarity to severe hailstorms. Analyses in Germany have shown comparisons between mesocyclonic and non-mesocyclonic storms (Wapler et al., 2016; Wapler, 2021) and also discuss the life cycle of hailstorms (Wapler, 2017; Kunz et al., 2020). They show that lightning jumps generally precede the most intense hail in a storm's life cycle, which was also shown for Switzerland in Nisi et al. (2020). In addition in most cases mesocyclonic storms will produce the mesocyclone before or with the onset of hail (Wapler, 2021; Witt et al., 2018; Davies-Jones, 2015). Numerous studies focus on single severe storms in or near complex terrain in Europe (Peyraud, 2013; Barthlott and Kirshbaum, 2013; Manzato et al., 2015; Miglietta et al., 2016, 2017; Scheffknecht et al., 2017; Trefalt et al., 2018; Grazioli et al., 2019; Avolio et al., 2020), in the USA (Soderholm et al., 2014; Milrad et al., 2017; LeBel et al., 2021) and South America (Mulholland et al., 2019; Lombardo and Kumjian, 2022). A broader stance is taken in several studies (Piper et al., 2016; Mohr et al., 2020; Wilhelm et al., 2021), where clusters of severe thunderstorms causing large hail and flash floods in central Europe are analyzed. Studies in Italy investigate the conditions leading to tornadoes throughout the country (Bagaglini et al., 2021), as well as the distribution of lightning in the Northeastern region ranging from the Adriatic coast to the Julian Alps (Feudale and Manzato, 2014). In Austria, a multi-year assessment of severe convection in radar and reanalysis data investigated the dependency of convective organization on atmospheric shear (Kaltenboeck and Steinheimer, 2015). More recent studies in the United States (Katona and

Markowski, 2021) and Argentina (Mulholland et al., 2018) also focus on severe convection in more complex terrain utilizing large, multi-year event sets. In addition, the dependency of storm environments on topography in the Eastern USA is presented in (Katona et al., 2016). A multi-sensor-based climatology for thunderstorms in Europe is provided in Taszarek et al. (2019).
With the United States experiencing some of the most severe convection worldwide, numerous studies focus on this region. The research ranges from investigating hailstorms in remote sensing data (Murillo and Homeyer, 2019) to establishing climatologies of hail (Allen and Tippett, 2015; Murillo et al., 2021), quasi-linear convective systems (Ashley et al., 2019) and mesoscale convective systems (Haberlie and Ashley, 2019), as well as analyzing the changing trends in tornado and hail occurrence (Gensini and Brooks, 2018; Tang et al., 2019).
Utilizing data sets from lightning networks and severe weather reports, a comparison between severe convection climatologies in Europe and the United States was established (Taszarek et al., 2020). Consequently, the differences in regional trends in the past decades were discussed (Taszarek et al., 2021a), with modeled severe convective environments in Europe increasing, while they are decreasing in the United States. A more global stance is taken in Taszarek et al. (2021b), where differences in globally observed convective trends are highlighted.
In this study we provide a comprehensive comparison of severe thunderstorm types, by comparing ordinary thunderstorms to severely precipitating storms, hailstorms and supercellular thunderstorms in the Alpine region. We particularly focus on the behavior of supercell thunderstorms, whose behavior in complex terrain is still poorly understood. The comparison to other, better understood convective storm types provides the necessary context. Each of these storm categories are classified using radar-based metrics and can overlap with each other. We highlight the differences in the life cycles between the severe convective storm types. By dividing the Alpine region into sub-regions of homogeneous topographical complexity, we dissect the different behaviors of severe convection in comparison to the orography. Establishing a thunderstorm classification from the same radar-based data set over different orographic regions allows for a direct comparison of both storm types in general and the differences in the orographic regions. Previous studies usually only allow for a comparison either between storm types in less complex terrain, or highlight the distribution of one storm type in different terrain situations, thus only inferring indirect comparisons.

5.2 Data

This study is based on radar-derived thunderstorm data from the extended convective season running from April to October of the years 2016-2021 in Switzerland. The Swiss radar domain is shown in Fig. 5.1. With five C-band Doppler dual-polarization radars situated at altitudes from 900 m ASL to ~2900 m ASL, the network covers a large portion of the Alps, extending into France, Italy, Austria and Germany, as well as the surrounding Prealpine regions and plains (Germann et al., 2015, 2022). Each radar scans a full volume of 20 elevations every

five minutes. From the 100 polar elevation scans at a resolution of 500 m x 1°, 2-D merged Cartesian products at a 1 km spatial resolution are derived. Consequently, the thunderstorm data set has a spatial resolution of 1 km and a temporal resolution of 5 minutes.
In addition the available radio sounding data from the observational sites in Payerne (Swiss Plateau) and Milano (NW Po Valley) were extracted during the observation period (2491 soundings from Payerne and 2463 from Milano (University of Wyoming, 2022)). The soundings are performed twice per day at 00:00 and 12:00 UTC.
Figure 5.1 a) shows a topographical map of the analyzed region, indicating the radar locations and names. The polygons show the regional split into areas of differing homogeneous topographical complexity. They largely follow the polygons used in Raupach et al. (2021b) and Nisi et al. (2016). Table 5.1 shows an overview of the regions. A relative quality index (QI) for radar data (derived in Feldmann et al. 2021) is shown in Fig. 5.1 b), which ranges from 0 (relatively lowest observational quality in the network) to 1 (relatively highest observational quality). We exclude all areas below 0.3 QI (teal hatched areas) to avoid quality biases in the radar data.

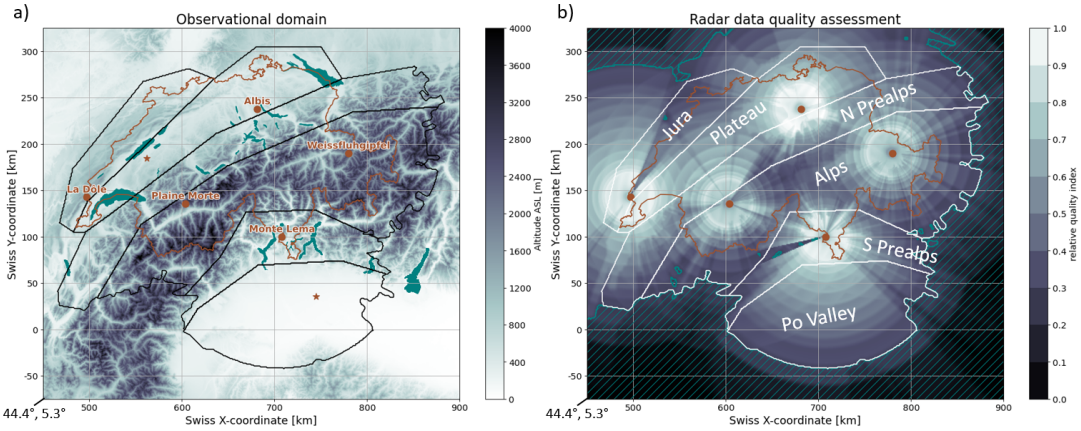

Figure 5.1: a) Radar domain and regional split, underlain with topographical elevation map (Digital elevation model from ©swisstopo (2005) and Jarvis et al. (2008)), as well as site of the five radars in Switzerland (dot) and two sounding sites (stars); b) relative quality index of radar observations for convective phenomena (Feldmann et al., 2021) and regional split with regions' names.

While the Southern and Northern Prealps have similar topographical complexity, their weather regimes differ considerably. The Southern Prealps regularly experience Mediterranean influence and are warmer than the Northern side of the Alps, with more intense precipitation on single days in between prolonged dry spells (Bundesamt für Meteorologie und Klimatologie MeteoSchweiz, 2022; Isotta et al., 2014). They are also one of the most convectively active regions in Europe (Taszarek et al., 2019; Enno et al., 2020; Taszarek et al., 2021a; Manzato et al., 2022). The large Prealpine lakes additionally cause a milder climate than in other North Italian regions and act as a moisture source. The Northern Prealps are more influenced by Central European weather situations, often characterized by Westerly flow (Feldmann et al., 2021; Bundesamt für Meteorologie und Klimatologie MeteoSchweiz, 2022). They are cooler and

have more evenly distributed precipitation in time. While showing lower convective activity than the Southern Prealps, they are however the second most active region in Switzerland and are known for severe hailstorms (Nisi et al., 2018; Feldmann et al., 2021; Bundesamt für Meteorologie und Klimatologie MeteoSchweiz, 2022; NCCS, 2021).
The Jura also presents as a region of moderate terrain complexity, but does not border the high-altitude Alps. Similarly to the Northern Prealps, it is more influenced by Westerly flow. However, as it serves as a geographical divide and shields the Swiss plateau and Northern Prealps, it experiences a larger Mediterranean influence, particularly on its Western flank (Bundesamt für Meteorologie und Klimatologie MeteoSchweiz, 2022). While it is also an area of elevated convective activity (Enno et al., 2020; Manzato et al., 2022), observational limitations have prevented previous studies from analyzing the full breadth of convective hazards in this area (Nisi et al., 2018; Feldmann et al., 2021; NCCS, 2021).
The Central Alps serve as a weather divide for Europe, separating the Mediterranean influence from the moderate, central European weather regimes. The inner Alpine valleys are shielded by the high mountain chains from approaching air masses and are thus drier than the Prealpine valleys (Bundesamt für Meteorologie und Klimatologie MeteoSchweiz, 2022). Generally, high-mountain environments are unfavorable to severe convection, as convective available potential energy (CAPE) is reduced at high altitudes (Taszarek et al., 2020). Convective initiation however is facilitated by reduced convective inhibition (CIN) and updrafts induced by valley wind convergence.
The Po Valley experiences a Mediterranean climate with hot and humid summers. It is the lowest and flattest region analyzed here. The part of the Po Valley covered in this study is reduced to the central northern part that does not border the sea and is thus drier than the coastal areas. The high temperatures and humidity lead to large amounts of CAPE, particularly in situations of cold upper-level air intrusions from the Alps, and thus the region is known for severe convective outbreaks (Taszarek et al., 2019; Avolio et al., 2020). The Swiss plateau is also a rather flat region and experiences a moderate climate with warm summers. The weather is strongly influenced by Westerly flow that often brings cooler, moist air from the Atlantic. The majority of severe convection is associated with Southwesterly flow (Nisi et al., 2018; Feldmann et al., 2021), which advects warmer, humid air from the Mediterranean through the Rhône valley (Peyraud, 2013; Trefalt et al., 2018).

Table 5.1: Description of regions

Region	Topography	Weather regime	Area [km^2]	Mean QI [ ]
Northwestern (NW) Po valley	flat	Mediterranean	17'862	0.47
Southern (S) Prealps	smaller mountain chains	Mediterranean	9'887	0.60
Central Alps (Alps)	high mountain terrain	mixed, Alpine	31'110	0.51
Northern (N) Prealps	smaller mountain chains	Central European	17'764	0.58
Swiss Plateau (Plateau)	hills	Central European	14'347	0.71
Jura	smaller mountain chains	Central European	8'448	0.57

5.2.1 Thunderstorm Data

The data set of thunderstorms contains tracked thunderstorms lasting at least 30 minutes that are identified with unique IDs. For each thunderstorm, several intensity metrics are gathered from the operational radar data (Germann et al., 2022), lightning detection network (Meteorage, 2022; Schulz et al., 2016; Azadifar et al., 2016), radio soundings (University of Wyoming, 2022) and numerical weather prediction model COSMO-1 (Consortium for Small Scale Modelling, 2018). The most relevant storm metrics used for this study are listed in Table 5.2.

Table 5.2: Thunderstorm intensity variables

Acronym	Definition	Unit
A	storm area	km^2
A57dBz	storm area with reflectivity ≥ 57 dBz	km^2
LTG	cloud-to-ground (CG) lightning	$\frac{\#}{5minA}$
RANK	heuristic thunderstorm severity rank (see Eq. 5.3.1)	[unitless, 0-40]
ET45	45 dBz echo top height	km ASL
ACC	radar derived precipitation accumulation in last hour	mm h^{-1}
iRR	radar derived instantaneous precipitation rate	mm h^{-1}
VIL	vertically integrated liquid	kg m^{-2}
Z	Cartesian composite maximum radar reflectivity	dBz
Zmax	maximum Z within A	dBz
MESHS	maximum expected severe hail size	cm
POH	probability of hail	%
v	translational speed	km h^{-1}

As almost all analyzed variables in this study are derived from radar data, we next discuss the correlation of these variables. Fig. 5.2 shows the correlation matrix of all investigated variables, depicting the R-value where it exceeds 0.5. First, we look at all variables used in the RANK computation. The lowest correlation is found with A57dBz (<0.5), whereas all other variables (ET45, Zmax and VIL) correlate strongly with the RANK and, slightly less, with each other. These strongly correlating variables all target the vertical extent of convection, whereas A57dBz concerns the horizontal extent. As the RANK is comprised of mostly components taking into account the vertical extent, the correlation with the horizontal extent is rather low. We use RANK as a summarizing variable for its components.
Next we investigate the variables used for the intensity comparison in the life cycle and regional analyses. Once again A exhibits a very low correlation with all other intensity variables, as well as v and LTG. MESHS shows some correlation with the RANK (0.6) and POH (0.6), as well as VIL (0.7). The correlations here are considerably lower than within the RANK-associated variables. POH shows the largest correlation to other RANK-related variables, but only moderate correlation with iRR (0.7). Considering the low correlation between the Var2 variables, the analyses shown in Fig. 5.5 and 5.7 show distinct properties of the storm populations.

Lastly, we show the variables used for storm classification. A30mm and A50mm depict the contiguous area exceeding 30 mm h^{-1} and 50 mm h^{-1} accumulation, which are the thresholds used for rainstorm classification. A2cm and A4cm show the contiguous area exceeding 2 cm and 4 cm MESHS and are used for hailstorm classification. These are mostly correlated within the hazard category, so it is important to consider that the storm types within the same hazard (e.g. hail) are exclusive of each other. Moreover all MESHS-related variables show higher correlation values between each other.

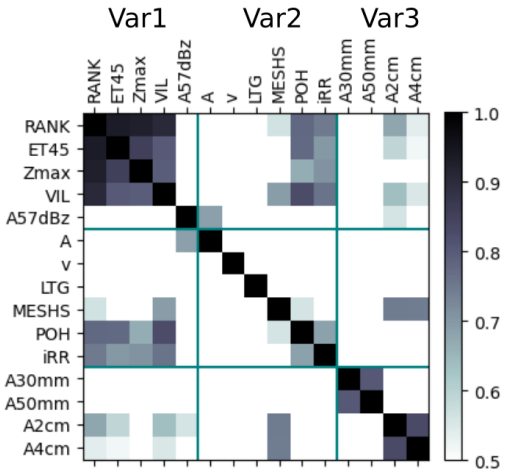

Figure 5.2: Correlation matrix of evaluated metrics, R-value >0.5 shown in colorbar; RANK - A57dBz (Var1): variables used in RANK computation, A - iRR (Var2): intensity variables, A30mm - A4cm (Var3): variables used for storm classification

5.3 Methods

5.3.1 Thunderstorm Detection

All thunderstorms within the Swiss radar domain are identified with the operational thunderstorm radar tracking (TRT) algorithm (Hering et al., 2004). It employs a detection with dynamic thresholds on the 2-D Cartesian maximum reflectivity field that is derived from all five radars. From each time step to the next, detected thunderstorms are advected based on the weighted average motion of the past three detections. New detections with sufficient overlap are matched to the advected past cells to establish a continuous track.
To avoid retaining a spurious number of small cells in this data set, we remove all tracks that last less than 30 minutes, which represents the lower end of a typical thunderstorm life cycle. In addition, thunderstorm detections below a quality index of 0.3 (as in Fig. 5.1 b)) are removed. This only concerns the outer edges of the domain. In regions of low observational quality the observations are skewed towards more severe phenomena, as they are more likely to still be detected.

The TRT algorithm also provides a heuristic severity rank, that summarizes several intensity metrics of a thunderstorm. The intensity variables in eq. 5.3.1 are first categorized using a fuzzy logic weighting scheme for each variable before computing the rank:

$$RANK = \frac{(2 \cdot VIL + 2 \cdot ET45 + Zmax + 2 \cdot A57dBz)}{7} \tag{5.1}$$

(Rank first developed in Hering et al. (2008), most recent version in Figueras i Ventura et al. (2019))

5.3.2 Thunderstorm Classification

The thunderstorms are classified into the categories ordinary (OR), intense rainstorm (RS), severe rainstorm (SRS), hailstorm (HS), severe hailstorm (SHS) and supercell (SC). An overview of the classification criteria is listed in Table 5.3. The two rainstorm and hailstorm classes and the SC overlap considerably. While OR excludes the other classes, the more severe types can overlap and thunderstorms can contribute to multiple categories, e.g. SHS and SC.

RS and SRS are defined by the radar-estimated hourly precipitation accumulation. The instantaneous precipitation rate (iRR) is derived on a 1 km Cartesian grid, as described in Germann et al. (2006); Gabella et al. (2017). In this study we use the radar-derived hourly accumulation of precipitation (ACC). An accumulation exceeding 30 mm in the past hour in at least 3 connected pixels classifies a storm as RS. Accordingly, 50 mm accumulation in the past hour correspond to the SRS classification. By requiring several pixels to exceed the threshold we avoid triggering the threshold through potential residual clutter (Nisi et al., 2020). By using an hourly accumulation instead of an instantaneous precipitation rate, we reduce the risk of hail being mistaken for an intense precipitation event. These thresholds mirror the operational precipitation warning thresholds in thunderstorms of MeteoSwiss (Bundesamt für Meteorologie und Klimatologie MeteoSchweiz, 2021).

To classify HS and SHS we rely on the metrics probability of hail (POH) (Waldvogel et al., 1979; Foote et al., 2005; Betschart and Hering, 2012) and maximum expected severe hail size (MESHS) (Betschart and Hering, 2012; Treloar, 1998). To classify as HS, either POH or MESHS must exceed 80% or 2 cm, respectively in at least 5 contiguous km^2 (Nisi et al., 2018). To classify as SHS, MESHS must exceed 4 cm in at least 5 contiguous km^2 (Nisi et al., 2018). For both classes, one time step fulfilling the hail or severe hail criterion is sufficient to label the entire storm as a HS or SHS. This method of classifying HS and SHS was first established in (Nisi et al., 2016), verified against insurance data and later established as the principal method in the Swiss hail climatology (NCCS, 2021). While radar-based hail detection is challenging and can differ from ground-based methods, it yields a high spatio-temporal coverage that is not achieved with crowd-sourcing (Barras et al., 2019) or hail sensors (Kopp et al., 2022).

SC are classified by a mesocyclone detection algorithm that identifies consistent rotation around a vertical axis from Doppler radar data (Feldmann et al., 2021). This identifies the rotating updraft, that is a core structure of a SC (Kumjian and Ryzhkov, 2008; Markowski and Richardson, 2010). The processing chain here includes dealiasing the Doppler data (Feldmann et al., 2020), computing the azimuthal derivative per radar elevation, identifying areas of elevated azimuthal shear and employing vertical and temporal continuity constraints (Feldmann et al., 2021). The procedure merges measurements from all available radars at a given location to maximize the likelihood of detecting and tracking a mesocyclone. The use of range-dependent thresholds mitigates azimuthal resolution loss with increasing distance. Shallow, low-level mesocyclones may be veiled in areas of low-level beam blockage, persistent mesocyclones with a sufficient vertical extent are reliably detected.

Lastly, OR are separated from more severe types. They are required to have less than 4 contiguous km^2 of either POH >80% or MESHS >2 cm, respectively, to ensure than hail is unlikely. Similarly, at most 2 connected pixels may exceed 30 mm precipitation accumulation. They must also not have a detected mesocyclone. Removing these intermediate strength storms that do neither meet the classification criteria from the OR nor those of HS and RS affects less than 1 % of the data.

The radio soundings are assigned to all thunderstorm classes occurring in the 2h before or 12 h after a sounding. For the soundings in Payerne all thunderstorms in the Jura, Swiss Plateau and N Prealps are considered, for the Milano sounding the thunderstorms of the S Prealps and NW Po Valley. The thunderstorms over the main Alpine ridge are not used in the sounding analysis as the inner Alpine profile does not necessarily correlate with either sounding. This sounding data set is then filtered by thunderstorm category. Soundings assigned to OR contain no other thunderstorm category. Soundings assigned to RS exclude SRS and those assigned to HS exclude SHS. A sensitivity analysis of the use of sounding data is presented in Section 5.4.4.

5.3.3 Region Assignment

The outlines of the regions are shown in Fig. 5.1. As many thunderstorms have tracks crossing multiple regions, entering or leaving the considered domain, it is necessary to anchor points to specific regions. We aim to anchor them with the time steps we are most interested in. An overview of the criteria are shown in Table 5.3. OR are assigned to the region, where they are detected most frequently, weighted by their intensity. This anchors them in the region, where they exhibited the highest intensity for the longest time. All severe types are labeled with the region where they had the most classifications of their storm type (e.g. most detected mesocyclones). Section 5.4.4 contains a sensitivity discussion regarding the region assignment.

5.3.4 Centering the Life Cycle

When comparing life cycles of storm populations, the temporal progression of the storms need to be aligned to a time T0. Per storm type, we center the timeline around the time of highest interest (see Table 5.3). For OR, this is the time of peak intensity. For the more severe storm types, we center T0 around the first classification of the meteorological phenomenon.

Table 5.3: Thunderstorm classification; *contiguous refers to corner-connectivity

Class	Criterion	Region anchor	T0
ordinary (OR)	<4 contiguous* km^2 of POH >80 % or MESHS >2 cm; <3 cont.* km^2 of ACC >30 mm h^{-1}; no mesocyclone	most frequent region weighted by intensity	highest intensity
rainstorm (RS)	≥ 3 contiguous* km^2 of ACC >30 mm h^{-1}	most frequent region during intense rain	intense rain onset
severe rainstorm (SRS)	≥ 3 contiguous* km^2 of ACC >50 mm h^{-1}	most frequent region during severe rain	severe rain onset
hailstorm (HS)	≥ 5 contiguous* km^2 of POH >80 % or MESHS >2 cm	most frequent region during hail	hail onset
severe hailstorm (SHS)	≥ 5 contiguous* km^2 of MESHS >4 cm	most frequent region during severe hail	severe hail onset
supercell (SC)	classified by mesocyclone detection algorithm	most frequent region during mesocyclones	mesocyclone onset

5.4 Results

To get an overview of the frequency of different thunderstorm types, we first investigate their overall occurrence. The following Fig. 5.3 shows the total number of detected storm tracks per category and the overlap of the hazard categories.

The majority of all detected thunderstorms are OR, occurring more than one order of magnitude more frequently than then next most frequent category of RS. RS and SRS occur slightly more frequently than HS or SHS. SC are the least frequent thunderstorm type with 540 detected tracks among 73'688 total analyzed thunderstorm tracks.
When looking at the overlap between RS and SRS, HS and SHS and SC, here shown with a Venn diagram, the majority of SC are also classified as HS or RS. RS and HS also overlap considerably, but there are larger fractions with a single hazard. SRS are not necessarily characterized by other hazardous features. Relatively weak, but stationary thunderstorms can precipitate intensely enough to trigger the rain accumulation threshold. While the majority of all SC are also HS, the inverse is not true. Out of all SHS, only approximately 10 % present with a mesocyclone. This differs from the results of Wapler (2017), where the majority of SHS present with a mesocyclone. So while SHS still occur regularly in the complex topography

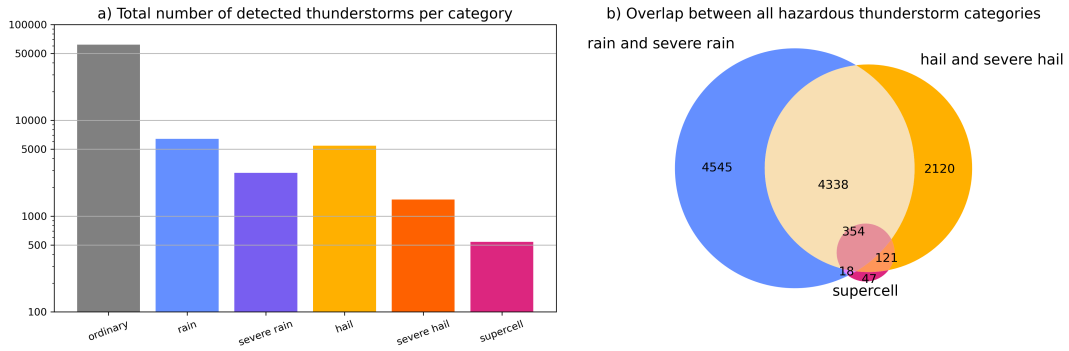

Figure 5.3: a) number of detected storms per category, b) overlap between hazardous thunderstorm categories - rain and severe rain, as well as hail and severe hail are each categorized together, over the entire 6-year data set.

of Switzerland (Nisi et al., 2016; Punge et al., 2017; Nisi et al., 2018, 2020; NCCS, 2021), the conditions of SC are less prevalent and they occur less frequently (Feldmann et al., 2021).

Next, we show the average annual spatial distribution per thunderstorm type in Fig. 5.4. Each thunderstorm detection is depicted with a radius of 5 km, corresponding to a localized storm density. A single storm can contribute to more than one category. Beginning with OR, we can clearly see the climatology and the influence of the radar data quality (see Fig. 5.1b). Particularly, our ability to observe weak thunderstorms of small spatial and vertical extent is impeded in areas of reduced radar visibility. More severe storm types tend to be taller and wider (see Fig. 5.5), leading to more robust detections even in lower quality areas.
The overall pattern shows that the activity maximum for all convective storm types lies in the S Prealps, encroaching onto the NW Po valley (Punge et al., 2017; Nisi et al., 2018; Manzato et al., 2022). The N Prealps and Jura also show elevated activity, but less pronounced than the S Prealps. The Plateau has slightly reduced activity. The lowest overall activity is in the main Alpine ridge. The minimum in convective activity here is confirmed by satellite- and lightning-based climatologies that are independent of the radar network (Enno et al., 2020; Bundesamt für Meteorologie und Klimatologie MeteoSchweiz, 2017; Anderson and Klugmann, 2014; Punge et al., 2017). This suggests that moderately complex terrain is beneficial to the formation of convection, whereas the high Alpine environment is detrimental (Manzato et al., 2022; Punge et al., 2017).

5.4.1 Life Cycles of Different Convective Types

Investigating the life cycles of different convective types allows us to better understand their defining characteristics. By analyzing their behavior before and during their most intense phases, we can gain insight into the processes related to to hazardous weather phenomena.
In Fig. 5.5 we show the 45 minutes prior to the life cycle anchoring point of each storm type, as well as the hour after. This encompasses the expected life time of most convective storms, as

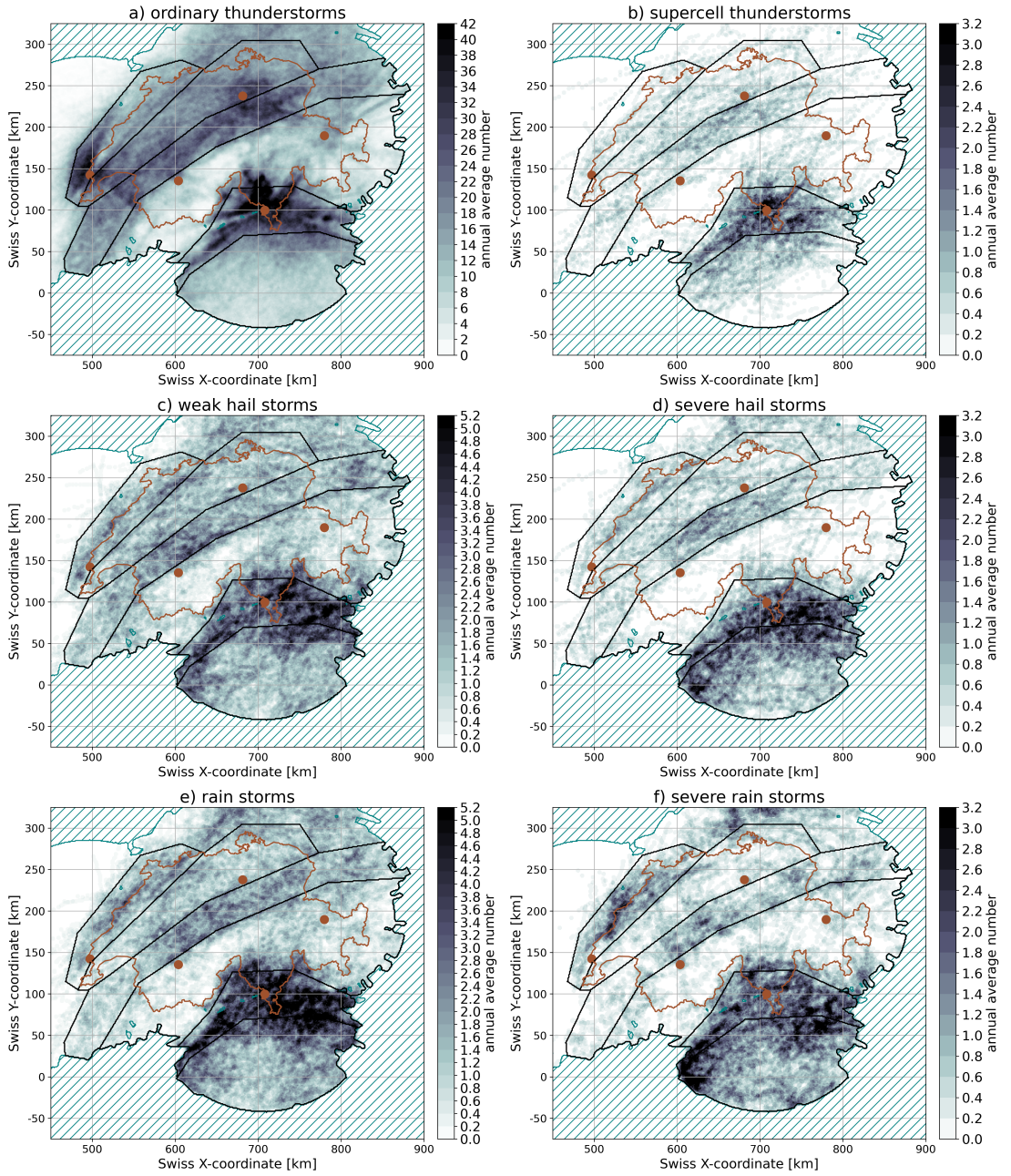

Figure 5.4: Annual average spatial occurrence of each thunderstorm type (2016-2021), grayscale differs across figure panels. The sites of the five radars are also indicated, as well as the regional polygon boundaries.

well as the usual useful time frame of less than an hour for thunderstorm nowcasting purposes. If we observe distinct behavior leading up to the anchor, this variable may have predictive and thus nowcasting properties. We show the evolution of the median, as well as the 25th and 75th quantiles (shaded areas) for each convective storm type. We focus on the variables severity rank [unitless] (see eq. 5.3.1), area [km^2], translational speed [km h^{-1}], CG lightning strikes [$\frac{\#}{5minA}$], MESHS [cm] and iRR [mm h^{-1}]. The translational speed (computed from the distance of a thunderstorm's centroids in between time steps) is considered an environmental variable, as it is determined by the storm's environment (Zöbisch, 2020), whereas the others are storm-internal intensity variables.

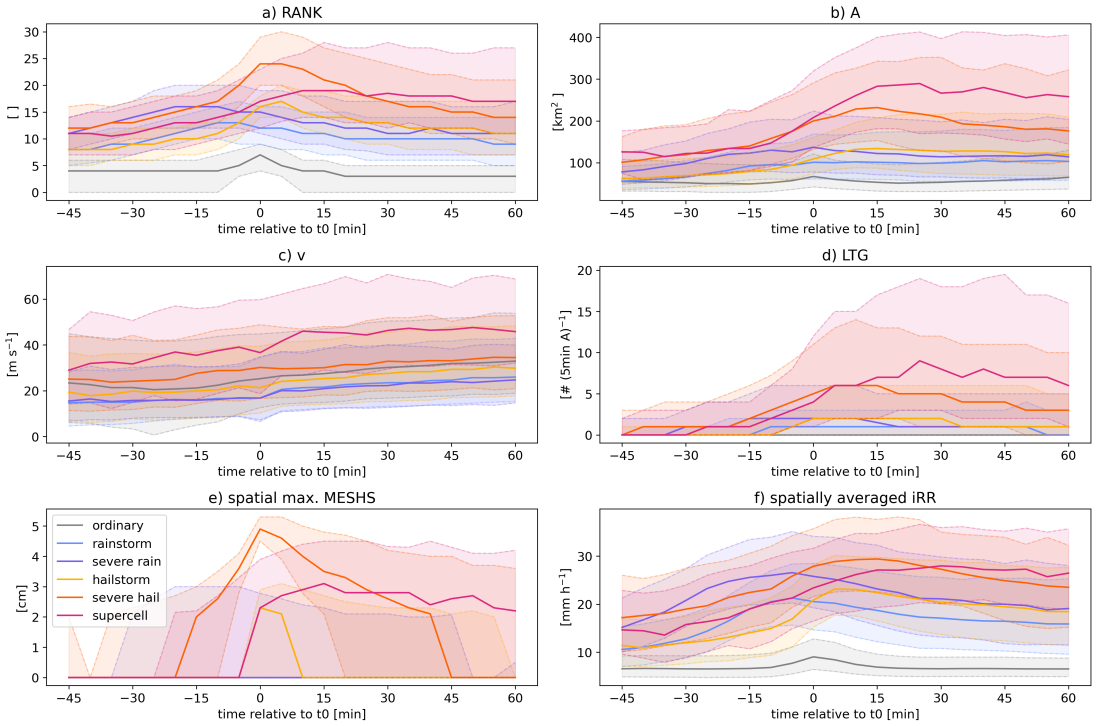

Figure 5.5: Evolution of six variables during the 45 min leading up to and 60 min after the center of the life cycle of each storm type, the solid line depicts the median, while the shaded area represents the range of the 25th and 75th percentile

Overall we can see that both SHS and SC show the highest values in RANK, A, LTG, MESHS and iRR and longest lasting peaks during their life cycles. Most life cycle curves peak shortly before or at the life cycle anchor for all variables, apart from translational speed.
As determined by the definition of T0, OR peak in intensity at T0. Overall they have a lower intensity than all other storm types, but an intermediate translational speed.
In comparison, rain and SRS show slower translational speeds. The importance of stationary storms to heavy convective precipitation events has been analyzed in more detail in Aregger (2021). Precipitation accumulation is driven by two factors, precipitation rate and precipitation duration. The more stationary a storm is, the longer it will precipitate over a given area, increasing the likelihood of exceeding the accumulation threshold. As they are classified by

hourly precipitation accumulation, the processes in the hour preceding T0 are very important. We can see that the intensity variable peaks (most notably iRR) lie in the 30 minutes before T0, with a higher, broader and slightly earlier peak for SRS.
The life cycles of HS and SHS are quite similar in terms of the overall tendencies, but SHS experience higher and more prolonged intensity peaks. As the definition of both storm types, as well as T0, is closely tied to MESHS, the sharp jump at T0 is expected. We clearly see the higher, 4 cm criterion, for the SHS in comparison to the lower, 2 cm criterion, of HS. Figueras i Ventura et al. (2019) highlights the importance of the presence of rimed particles for lightning production. With riming contributing to the growth stages of HS, rimed particles are abundant. We can see a clear increase in lightning activity in HS and SHS, which is only further exceeded by SC. As also shown in Nisi et al. (2020), the lightning frequency increases before T0 and peaks within the 15 minutes afterwards. The increase in overall severity rank, storm area, lightning rate and iRR is only shortly before T0 (Nisi et al., 2020). The larger area and lightning flash rates last for a longer amount of time, whereas the peaks in severity rank, MESHS and iRR are quite narrow.
SC show the overall highest peaks for A, v and LTG. With SC requiring highly sheared flow environments and also inducing motion with their internal dynamics, it is unsurprising to see the highest v here. Wapler (2021) also shows higher v and LTG for mesocyclonic storms in comparison to non-mesocyclonic storms in general. SC are also known to have a large spatial extent in comparison to other single storm types (Markowski and Richardson, 2010). The peaks in the intensity-related variables tend to be broader than for HS and occur after T0. This shows that, as previously established in other regions, SC in our observational domain also tend to have a longer time period of peak intensity and the onset of rotation precedes the most intense phase, making it a potential nowcasting predictor for SC intensification.
The increase in translational speed over the life cycle of all storm types is notable. While the trend is small enough to lie within the quartiles, it is persistent across all types and thus covers groups of vastly different sample sizes, indicating a physical phenomenon. A similar trend was found in Zöbisch (2020). The translational speed of most convective storms is induced by the steering flow in the mid-troposphere (Foresti et al., 2019). During convective initiation the storm is mainly influenced by ground flow, which is generally rather low. Only once the storm extent reaches the mid-troposphere the stronger steering flow can begin to influence the storm motion. The longer the storm experiences the influence, the more it is accelerated.

As the onset of rotation tends to precede storm intensification, we investigate the relationship with hail in more detail. Fig. 5.6 a) shows the evolution of max. MESHS and POH within the cell contours throughout the life cycle of a SC thunderstorm, with the onset of rotation occurring at T0. The sharp increase of MESHS at and after T0 indicates that already falling hail tends to intensify after the detection of rotation. POH also increases with T0 and remains elevated for approximately an hour after.
The most relevant phase for hail in a SC is during the first 30 minutes after the first detection of a mesocyclone. The mesocyclone detection preceding or coinciding with the onset of hail

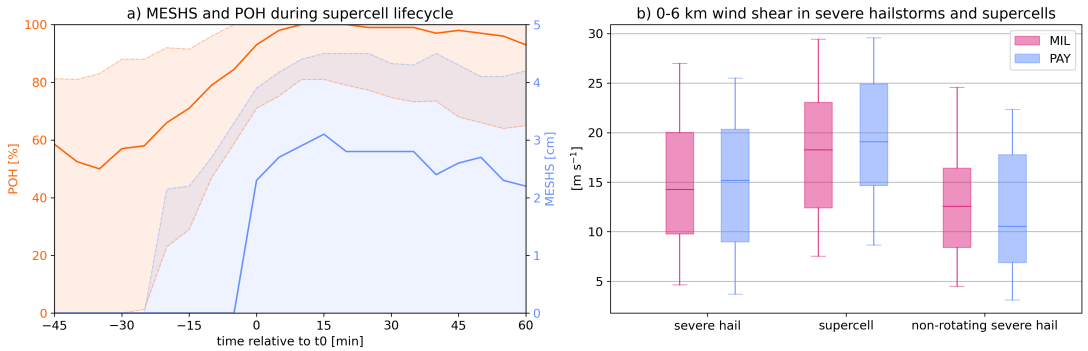

Figure 5.6: Evaluating temporal relationship between mesocyclone onset and hail:a) behavior of POH and MESHS during SC life cycle; b) deep layer bulk shear from radiosoundings in Milano (MIL) and Payerne (PAY)

in most cases was also found in Wapler (2017), where 8 years of hailstorms were investigated in the German radar domain. This confirms the preexisting concept (Davies-Jones, 2015) that in mesocyclonic storms, the onset of the mesocyclone indicates the following onset of hail, or an increase in hail intensity, even in our observational area, where we see a large fraction of storms forming severe hail without being associated with rotation.
Contrary to other studies, most SHS in the Prealpine regions are not associated with a SC. Figure 5.6 b) shows the 0-6 km shear from soundings in Payerne and Milano for all SHS, all SC and only those SHS when no SC were present. Soundings associated with SHS, but not SC, show lower deep-layer shear, indicating that the atmospheric profile did not support the development of significant rotation on these days.

5.4.2 Intensity Comparison of Storm Types in Different Regions

In this section we focus on the regional differences between the different storm types. The separation into region of different orographic complexity and dominant weather regimes allows to investigate the influence of topography from an observational point of view. We look at the distribution of each variable throughout the entire life cycle of the severe storm categories (see Fig. 5.7). We consider 68'000 measurement points along the respective tracks for OR, 109'000 RS, 59'000 SRS, 97'000 HS, 36'000 SHS and 16'000 SC. The weaker storm categories do not show clear signals throughout the topographic regions and are represented with a summarizing boxplot each. In all boxplots the median is marked with a line and the 25th and 75th percentiles are shown at the edges of the boxes. The whiskers extend to the 5th and 95th percentiles.

Figure 5.7 shows the regional distribution of the variables RANK, A, LTG and MESHS. As a first order trend, we can observe that the more intense storm types all show higher distributions for the intensity variables than the weaker storm types. Within the severe storm types the upper

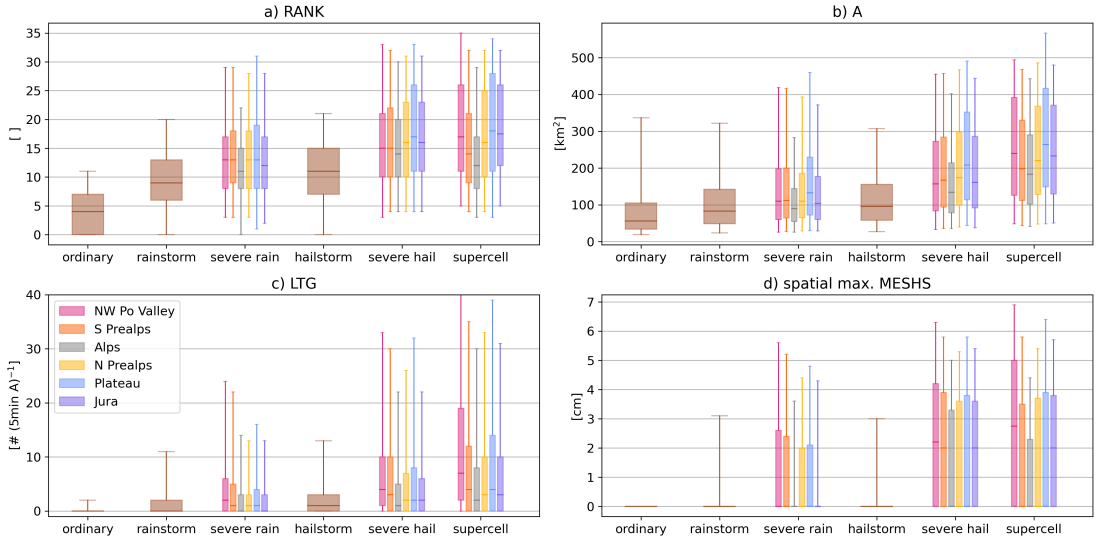

Figure 5.7: Distribution of four variables for the different thunderstorm types in each topographic region

percentiles of all variables show a regional dependency, being weakest over the main Alpine ridge and increasing towards both the NW Po valley and the Swiss plateau. Particularly LTG and MESHS are stronger to the Southern side of the Alps, where hail occurs more frequently (Nisi et al., 2018). The predominantly Mediterranean climate favors higher temperatures, CAPE and moisture content, leading to more convective activity in general (Taszarek et al., 2021a).

The regional intensity differences are most pronounced for SC, indicating that topography has a strong impact on a SC's ability to intensify. SC exhibiting lower RANK, A, LTG and MESHS can occur in all regions. The more complex orography introduces an upper limit to the maximum possible strength of SC, and to a lesser extent SRS and SHS. The top 50 percentiles of the intensity variables consistently follow the regional pattern for SC. The bulk of the distributions overlaps, but the upper percentiles are consistently higher in regions of less topographic complexity. While the Prealpine regions show the highest concentration of SC tracks (see Fig. 5.4 b), the highest severity storms on each Alpine side occur in the NW Po Valley for the South and the Swiss plateau for the North, indicating that less complex terrain favors the co-occurrence of SC ingredients and hence the intensification of the storm (Feldmann et al., 2021; Taszarek et al., 2020). Contrarily, the presence of moderately complex terrain in the Prealps supports the general presence of SC, even if not of the highest severity ones.

5.4.3 Radio Sounding Data of Different Storm Types

In Fig. 5.8 we investigate the atmospheric profile associated with the different storm categories. The variables CAPE, precipitable water, surface and 6 km wind speed, as well as directional and speed shear are derived from the radio soundings in Payerne and Milano. They each

represent the storm categories on the Northern and Southern side of the Alps, respectively. The Southern side of the Alps shows higher values of CAPE and, most notably, precipitable water throughout all storm categories. In addition, OR are associated with distinctly lower CAPE and precipitable water values than all other storm types. As discussed in Fig. 5.5 c), we can see in Fig. 5.8 c) and d) that all storm categories are associated with very low surface wind speeds and significantly higher flow aloft at 6 km. SRS have a tendency to lower wind speeds at 6 km, which is a contributing factor to their low translational speed (and hence high accumulation). The 6 km wind speed is highest for the SC, confirming the elevated wind shear seen in Fig. 5.6 b).

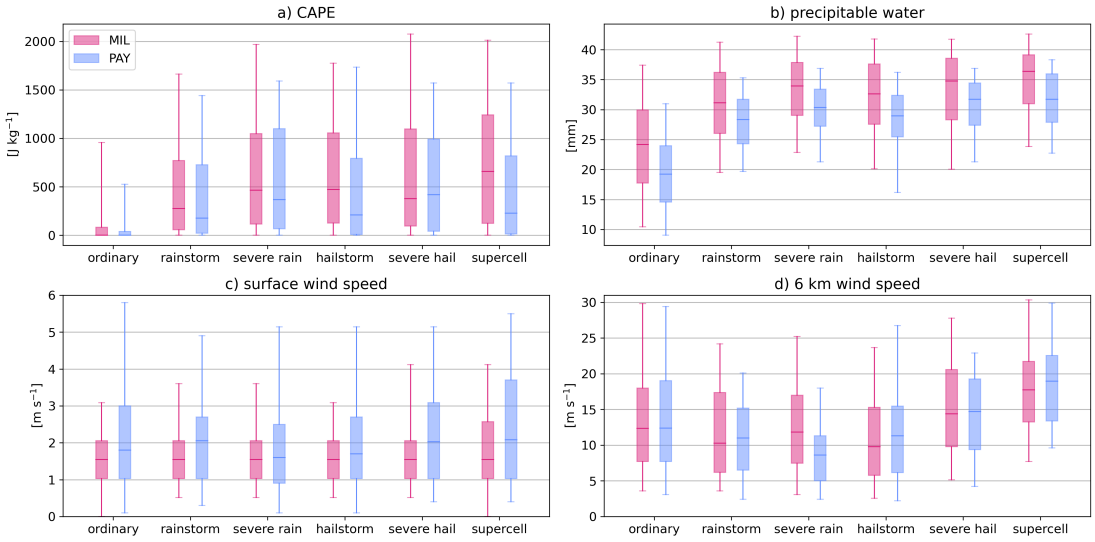

Figure 5.8: Distribution of six sounding variables for the Northern and Southern Alpine regions. Thunderstorms from the NW Po valley and S Prealps are assigned to the MIL sounding, while thunderstorms from the Jura, Swiss plateau and N Prealps are assigned to the PAY sounding.

5.4.4 Discussion of Data Quality and Sensitivity

To investigate the influence of radar data quality, we duplicated the regional intensity analysis from Section 5.4.2 and removed all datapoints below a QI of 0.5 and above a QI of 0.8, which reduced the overall data set by approximately 50 %. This results in 35'000 measurement points for OR, 50'000 RS, 26'000 SRS, 45'000 HS, 16'000 SHS and 9'000 SC. With this selection, the data quality in all regions is much more homogeneous and should not influence the evaluation of storm intensity. The observed trends of the upper quantiles of severe storms being limited in areas of high topographical complexity persist in this data selection (see Fig. 5.9). This indicates that the regional differences in maximum potential intensity are indeed a physical pattern and not owed to observational constraints.

Moreover, severe thunderstorms present with tall vertical extent and metrics such as MESHS

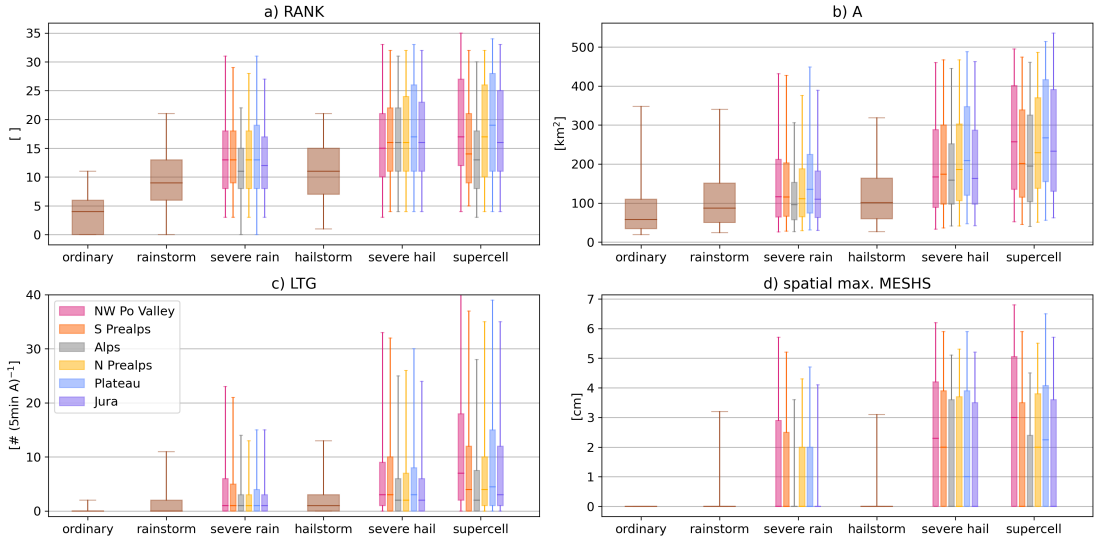

Figure 5.9: Regional intensity distribution with a narrower interval of data quality

are calculated in the upper portion of the observed radar domain. Thus, beam blockage at lower levels in the mountains do not affect these variables.

We also tested the sensitivity to our region assignment. When assigning an entire thunderstorm life cycle to the region of its highest intensity, we avoid splitting up the life cycle into several parts corresponding to the crossed regions. We also performed the same analysis, when simply using all datapoints inside a region towards this region. The qualitative results remain the same (not shown), with the regional peak intensity differences clearly visible. Hence the decision whether to pursue an analysis based on entire storm tracks or point detections does not make a difference in the outcome of the analysis.

For the radiosoundings we assume representativity for all storms in each the Northern and Southern part of the domain, respectively. To test, whether this area selection influences our results, we duplicated the same analysis with a reduced storm selection radius of 50 km. I.e. instead of assigning all thunderstorms within the NW Po valley polygon and S Prealps polygon to the MIL sounding, we only assign those within 50 km of the sounding site to the sounding. As seen in Fig. 5.10, the observed differences between storm types and domain halves are still represented. This indicates that the radiosoundings from Payerne and Milano are indeed representative of the Northern and Southern domain halves, respectively, and not just for their immediate spatial surroundings.

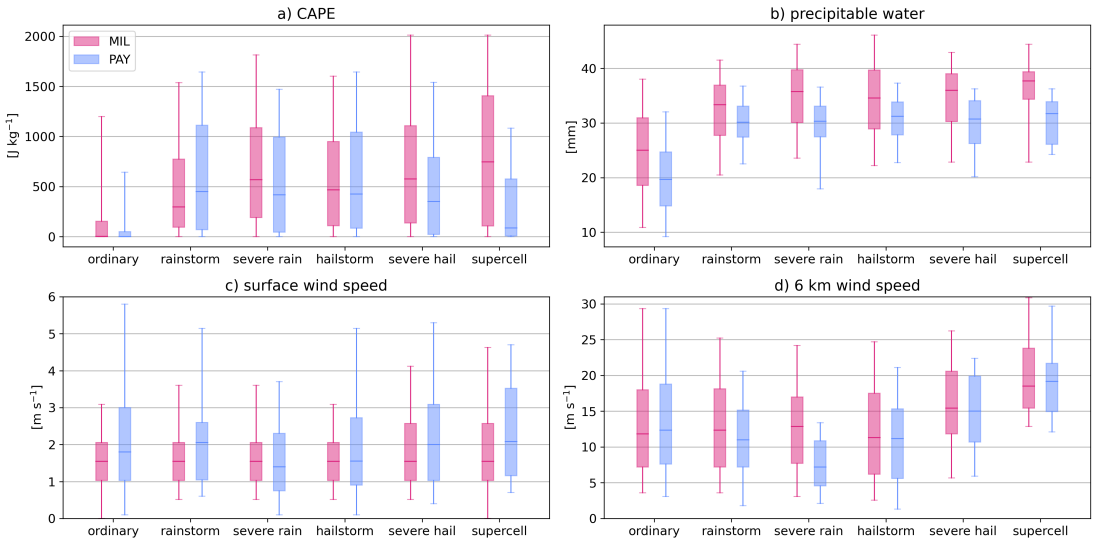

Figure 5.10: Distribution of sounding parameters, when only considering a 50 km radius around the sounding sites MIL and PAY each.

In addition, sensitivity tests were performed on the choice of time window within which to associate thunderstorms to a sounding. These ranged from +- 12 h to +- 2 h and all showed robustness in the observed results (not shown).

5.5 Conclusion

This analysis investigates the behavior of different convective storm types in the Alpine region. Making use of 6 years of high-quality operational radar data from a network of 5 radars, a systematic data set of ordinary, intense rain, hail and supercell thunderstorms is produced for the convective season of the years 2016-2021. Although six years is a limited timeline particularly for events as infrequent as SC, having a homogeneous data set for all storm types allows for a direct comparison of their regional intensity and life cycles. The limitations of the radar network apply to all storm categories equally, therefore not creating biases through different observation methods. This study offers a first-time comprehensive comparison of convective storm types in different orographic regions, with an emphasis of investigating the behavior of SC thunderstorms in complex terrain.

SC represent the most severe storm type and show considerable overlap with both RS and HS. Generally, OR show the weakest values in intensity variables, whose values increase steadily over RS and HS to SC. SC are generally associated with multiple convective hazards, their impact is compounded by the simultaneous occurrence of several severe weather phenomena, such as hail and intense rain. In contrast to previous research (Wapler, 2017; Tuovinen et al., 2015), the majority of HS (97 %) and SHS (76 %) in the Alpine region do not develop a mesocyclone during their life cycle, however the vast majority of storms with a mesocyclone produce hail (88 %). Most SHS in the observational domain form in conditions of lower deep

shear, which is unfavorable for the evolution of a sustained, rotating updraft. The discrepancy may additionally partially be owed to differences in the storm classification, as we here use purely radar-based HS and SC detection algorithms, whereas Wapler (2017) use a selection of hailstorms based on ground reports. Especially SC detection can be less reliable in complex terrain and underestimate the occurrence of shallow, low-lying rotation due to low-level beam blockage.

An initial investigation of the frequency distribution of each storm type shows that the South of the Alps is more convectively active than the North. To the South the convectively more favorable Mediterranean climate dominates. In addition, on each side of the Alps, the Prealpine areas show the highest density of convection for each storm type, indicating that moderately complex topography is beneficial to the overall presence of convection, e.g. by facilitating convective initiation.

A further analysis of the regional intensity differences shows that more complex orography usually leads to less severe storms. The peak intensities for each storm type are generally found in the Swiss plateau for the Northern half of the domain and the NW Po valley for the Southern half. Overall, the strongest storms are prevalent in the NW Po valley, where we also find a systematically higher precipitable water content. In contrast, the most frequent occurrence to either Alpine side is in the Prealpine areas, the Southern Prealps having a higher occurrence than the Northern. The lowest intensities and frequencies occur over the main Alpine ridge.

To understand the evolution of convective hazards in the storm life cycles, we examine the intensity evolution of the different thunderstorm types with respect to their life cycle center. This allows us to identify temporal relationships and potential predictors for convective hazards and intensification. As RS are defined by hourly accumulation, the processes leading up to the exceeded threshold are relevant. Thus the peak intensity of the storm generally is in the 30 minutes before the threshold is crossed. HS, however, are a more instantaneous reflection of convective severity. The intensity sharply increases with the onset of hail (Nisi et al., 2018). For the majority of storms hail is a briefly lasting phenomenon, the intensity increase peaks briefly together with the hail occurrence, before decaying again. SC on the other hand develop a mesocyclone during the formation of the updraft, before the main intensification of the storm. So we see a steady increase in intensity around the onset of rotation that peaks 15-30 minutes later and remains elevated for a prolonged amount of time. The longer intensity peak also reflects the typically longer lifetime of SC, as their internal storm dynamic prolongs the expected life cycle. SC in this region are also often associated with prolonged hail swaths.

While the intensity and life cycle of SC has been studied extensively in flat terrain, it is important to establish, whether these relationships also hold true in complex terrain. The Prealpine areas, where SC are most prevalent, already present with considerable topographical complexity. In contrast to expectations by regional forecasters, SC occur regularly and exhibit many of the established behaviors such as rotation preceding hail formation, and the prolonged intensity maximum.

6 Supercell Thunderstorms in Complex Topography - How Mountain Valleys With Lakes Can Increase Occurrence Frequency

This chapter is based on the preprint version of the manuscript "Supercell Thunderstorms in Complex Topography - How Mountain Valleys With Lakes Can Increase Occurrence Frequency", which is under review at Monthly Weather Review. The modeling experiments and analyses were performed by Monika Feldmann. Dr. Richard Rotunno supported the development of the scenarios and provided valuable insights in the interpretation of the results. Dr. Urs Germann and Prof. Alexis Berne organized the research project and supervised the progress.

Exploiting the observational insights from the previous chapters, we here seek to find the topography-related meteorological drivers behind the identified supercell occurrence clusters in steep prealpine valleys with lakes. By setting up modeling scenarios we can successively add characteristic topographic components to understand their separate impacts on supercell development.

6.1 Introduction

The behavior of supercell thunderstorms in complex terrain is still poorly understood. Considering the high-impact nature of these storms (Hoeppe, 2015; Ward et al., 2020) and the recent focus of field campaigns on areas of more complex topography (NSSL, 2021; Nesbitt et al., 2021), we aim here to improve the understanding of how high-altitude terrain and topographic features such as lakes can affect a supercell's life cycle. Our focus lies on a localized supercell hotspot in the southern Prealps in central Europe (Feldmann et al., 2021, 2022). By reproducing key topographic features in a generalized manner in the idealized model CM1, we aim to provide a conceptual model that details the general impacts of slopes and moisture sources.

The general processes behind supercell formation and the development of a mesocyclone are well known (Davies-Jones, 2015; Markowski and Richardson, 2010; Houze, 2014). The tilting of horizontal vorticity in the atmospheric wind profile is one of the key contributors to the formation of a mid-level mesocyclone, in addition to a sufficient amount of convective available potential energy (CAPE), to generate a strong updraft.
Previous idealized studies focused on case studies (Homar et al., 2003), generalized idealized shapes (Markowski and Dotzek, 2011; Ćurić et al., 2007) and the effects in climatological observations (Soderholm et al., 2014; Reeves and Lin, 2007). More recent research has focused on the impact of terrain on convective environments (Katona et al., 2016; Katona and Markowski, 2021). Even fewer studies target the influence of water bodies and moisture sources on convective storms. Wu and Lombardo (2021) investigated the impact of the marine boundary layer on quasi-linear convective systems in orographic coastal regions, but focus on the effects of the system encountering a stable boundary layer.
Most of these studies focus on severe storms in the United States, where supercells are most prevalent and tend to reach the highest intensities (Zipser et al., 2006). In contrast, Serafin et al. (2020) explored the effects of small-scale terrain features on a supercell in the Swiss and Austrian Alps with a case study, highlighting how small-scale terrain features play a key role in the maintenance of a favorable storm environment.
In this study we aim to investigate the processes leading to supercell frequency clusters in the southern Prealps in a modeling framework. This area was also of key interest during the Mesoscale Alpine Programme (MAP) in 1999, where in the scope of an international field campaign, the importance of orographic precipitation enhancement in convection was investigated (Rotunno and Ferretti, 2003; Medina and Houze, 2003; Rotunno and Houze, 2007; Seity et al., 2003; Richard et al., 2003). Previous studies (Feldmann et al., 2021, 2022) have shown the occurrence of hotspots in valleys with large lakes. The storm-intensity distribution in these areas is, however, lower, than in the neighboring, flat, NW Po valley, where fewer, but stronger supercells were observed (Feldmann et al., 2022). To investigate these findings, we derive modeling scenarios, where the influential factors can be modified. This allows the identification of causal relationships. We pursue an idealized approach, where we derive a simplified representation of the key conditions in the idealized mesoscale model CM1 (Bryan and Fritsch, 2002). CM1 has been used for a number of supercell studies and is highly adaptable to the specific goals of a study. It has been used to study the effects of surface friction on tornadogenesis (Markowski, 2016), high-resolution modeling of tornadoes (Orf et al., 2017), the effects of realistic terrain on supercell environments (Katona and Markowski, 2021), the impact of idealized terrain features on supercell intensity (Markowski and Dotzek, 2011), and, in combination with hail-trajectory-models (Adams-Selin and Ziegler, 2016; Kumjian and Lombardo, 2020), the evolution of large and gargantuan hail in supercell life cycles (Kumjian et al., 2021) and environmental impact on storm severity (Lin and Kumjian, 2022; Dennis and Kumjian, 2017). Our setup differs from previous studies in the magnitude and arrangement of the terrain features and the inclusion of moisture sources. With a generalized setting the study is not limited to a single-case understanding. The present simplified approach also facilitates the identification of the underlying meteorological processes.

6.2 Model Setup

In this section we present the observational data used to derive the idealized model setup, as well as the model setup itself.
Previous studies in the Alpine region (Feldmann et al., 2020, 2021, 2022) have shown the occurrence of hotspots of supercells above the lakes of the southern Prealps, most notably in the northern portion of Lago Maggiore. Figure 6.1a shows a topographical map of the Southern Prealps and Fig. 6.1b the corresponding annual average supercell frequency, observed by the Swiss radar network. This convectively active area is also evident in Manzato et al. (2022); Nisi et al. (2018, 2016); Punge et al. (2017). We aim here to identify the key environmental characteristics describing the region and then translating them into a generalized model setup.

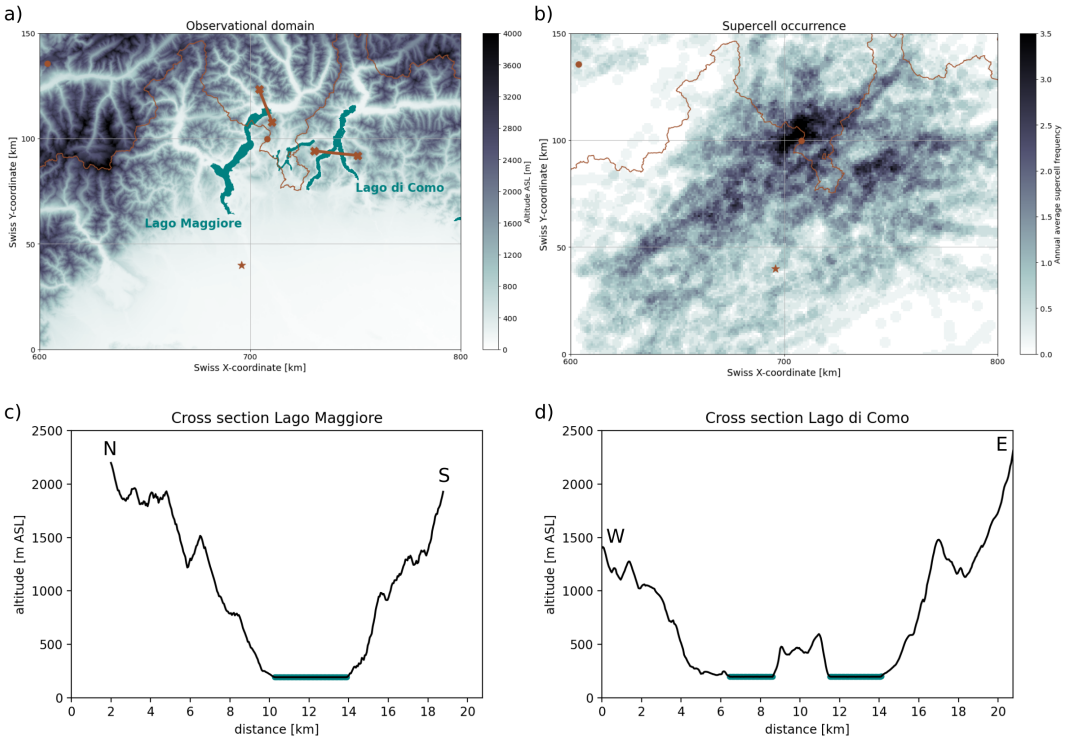

Figure 6.1: a) Topography of observational domain (©swisstopo, 2005; Jarvis et al., 2008), radar locations indicated with circles, sounding location with star, and Swiss borders b) supercell occurrence in a), c)-d) vertical cross-sections respectively of Lago Maggiore and Lago di Como, lake marked in teal (indicated by the lines in a)

The scenarios are simulated using the idealized mesoscale model Cloud Model 1 (CM1) (Bryan and Fritsch, 2002). The domain is 200x300x20 km^3 (x, y and z dimensions) with a horizontal resolution of 1x1 km^2 and 40 evenly spaced, terrain-following vertical levels. The lateral (E/W) boundaries are periodic, while an open-radiative condition is applied to the N/S boundaries to minimize wave reflection (Klemp and Wilhelmson, 1978). The top of the domain has Rayleigh dampening towards the base state, while the lower boundary is free slip. The model is operated in large eddy simulation mode, subgridscale turbulence is modeled using the turbulent kinetic energy scheme (Deardorff, 1980) and vertical turbulence tendencies are calculated implicitly via the Crank-Nicholson scheme. We use the Klemp-Wilhelmsson compressible pressure solver (Klemp and Wilhelmson, 1978) and the Morrison double-moment moisture scheme (Morrison et al., 2005). Since simulations are limited to a few hours and the domain is relatively small, we do not consider the Coriolis force.
Following sounding analyses in Feldmann et al. (2022) and severe convective environments (Bagaglini et al., 2021) and case studies (Kopp et al., 2022; Avolio et al., 2020; Trefalt et al., 2018; Peyraud, 2013), we follow the steps of Markowski and Dotzek (2011) to set up a slightly drier Weisman-Klemp sounding (Weisman and Klemp, 1982) by changing the exponent of the moisture function from 1.25 to 0.75. This results in a CAPE of 1974 J kg^{-1}, which represents the upper tail of the distribution of observed CAPE values in soundings associated with supercells, and a CIN of 25 J kg^{-1}. Considering the lack of directional shear, we transform the quarter-circle hodograph (Rotunno and Klemp, 1982) by using the overall magnitude of wind speed in only the v-direction. We hence maintain the magnitude of the vertical wind shear at 31 m s^{-1} for 0-6 km shear, but eliminate the directional component. Figure 6.2a shows an example radio sounding from Cameri in the northwestern Po valley at 12 UTC on July 8th 2021. The sounding reveals a CAPE of 1935 J kg^{-1} and a CIN of 11 J kg^{-1} and is associated with a severe hail-bearing supercell on the same day (Kopp et al., 2022). Figure 6.2b depicts the analytical sounding used for model initiation. The thunderstorms in the simulation are initialized with a warm bubble (Markowski and Dotzek, 2011).

The valleys in the southern Prealps are characterized by valley floors at a width of 10-20 km with the adjoining peaks rising 1500-2000m above the valley floor. The key supercell hotspots also present with lakes of considerable size. E.g. Lago Maggiore is 65 km long and up to 10 km wide, Lago di Garda 50 x 17 km^2, Lago di Como 50 x 5 km^2 and Lago di Lugano 20 x 3 km^2. Cross-sections of Lago Maggiore and Lago di Como in Figs. 6.1c and 6.1d highlight the steep topography immediately surrounding the lakes.

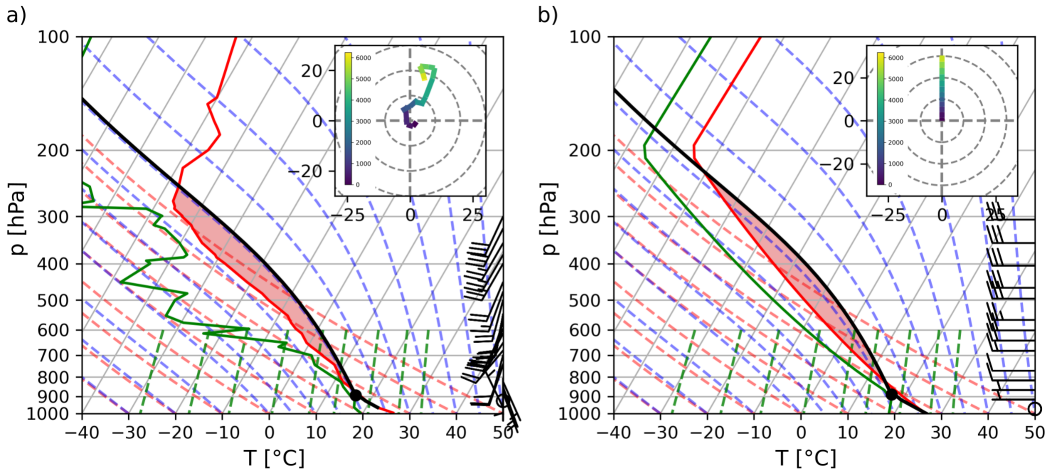

Figure 6.2: Radio sounding from a) Cameri on July 8th, 2021, 12 UTC and b) initial sounding in the CM1 model, for illustrative purposes the model wind barbs are rotated 90°

In the model setup we introduce a slope with a $\cos^2$ function up to 1500 and 2000m, respectively, rising over a length of 50 km before plateauing in the center of the model domain (see Eq. 6.1). We perform experiments with both altitudes to see the influence of differing steepness and altitude. Following Lilly and Klemp (1979) the topography is brought back down to 0 m in the second half of the domain, to avoid producing a singularity in the wind field. In a second step, we introduce long, channel-shaped valleys into the slope. The valleys themselves also have slopes determined by a $\cos^2$ function and have a valley-floor width of 6.7 km and a peak-to-peak distance of 20 km.
The function of the slope is given by:

$$h_{slope}(y) = h_{max} \cdot cos^2\left[\pi \cdot \frac{(y - y_0)}{2y_1}\right], \tag{6.1}$$

where h_{max} is the peak altitude, y_0 the offset of the peak and y_1 the length of the slope.
Within the valleys, we superimpose a function sloping down from $h_{slope}(y)$:

$$h_{valley}(x, y) = h_{slope}(y) \cdot cos^2\left[\pi \cdot \frac{(x - x_0)}{2x_1}\right], \tag{6.2}$$

where x_0 is the edge of the slope before descending into the valley and x_1 the width of the slope leading down to the valley floor.
Focusing on Lago Maggiore, we introduce a moisture ellipsoid the size of 60 x 10 x 1 km^3. The height of the moisture perturbation (1000 m) is oriented on the height of the surrounding terrain, as indicated in Laiti et al. (2014). The magnitude of the moisture perturbation is also determined by the measurements taken in Laiti et al. (2014) over Lago di Garda. We reduce the undersaturation in the perturbed area by the same fraction as the measurements indicate (10%). Moreover, the moisture perturbation is maintained over the course of the simulation

via a nudging term, representing the continuous evaporation over the lake.
The perimeter of the moisture perturbation is given by an ellipse:

$$\frac{x^2}{a^2} + \frac{y^2}{b^2} + \frac{z^2}{c^2} = 1 \tag{6.3}$$

For the inner core of the lake (ell_1<1) a, b and c are defined as follows: a_1=3500 m, b_1=20000 m, c_1=500 m. In a second, larger ellipse (ell_2<1, $ell_1 \geq 1$), the moisture perturbation decays linearly towards the background: a_2=5000 m, b_2=30000 m, c_2=1000 m.
The perturbation in the initial conditions is confined to ell_2<1:

$$Q_v(x,y,z) = Q_v(x,y,z) + \alpha(x,y,z) \cdot \Delta Q_v \tag{6.4}$$

Where ell_1<1, α=1. However, in between the two ellipses, where $ell_1 \geq 1$ and ell_2<1, α is defined as the following:

$$\alpha(x,y,z) = 1 - \frac{ell_2(x,y,z) - ell_2(a_1,b_1,c_1)}{ell_2(a_2,b_2,c_2) - ell_2(a_1,b_1,c_1)} \tag{6.5}$$

The nudging then maintains this perturbation where ell_2 <1:

$$\Delta Q_v(x,y,z,t) = Q_v(x,y,z,t=0) - Q_v(x,y,z,t) \tag{6.6}$$

$$Q_v(x,y,z,t) = Q_v(x,y,z,t) + 0.8 \cdot \Delta Q_v \tag{6.7}$$

Figure 6.3 shows the final topographical setup in the full model domain including the slope up to 2000 m, the two valleys and the moisture source in the western valley. Comparing to Fig. 6.1, the dimensions of the topography in the model are also observed in the area. The results are shown in the reduced area of the red box in panel (a).

In addition to the topographical scenarios, the initial conditions of the atmospheric profile are varied. We reduce CAPE to approximately 1500 and 1000 J kg^{-1}, by reducing the temperature in the boundary layer by 1 K each and adjusting the moisture to maintain the relative humidity. Additionally, we reduce the 0-6 km shear to 25 and 20 m s^{-1}. An overview of all tested scenarios is given in Table 6.1.

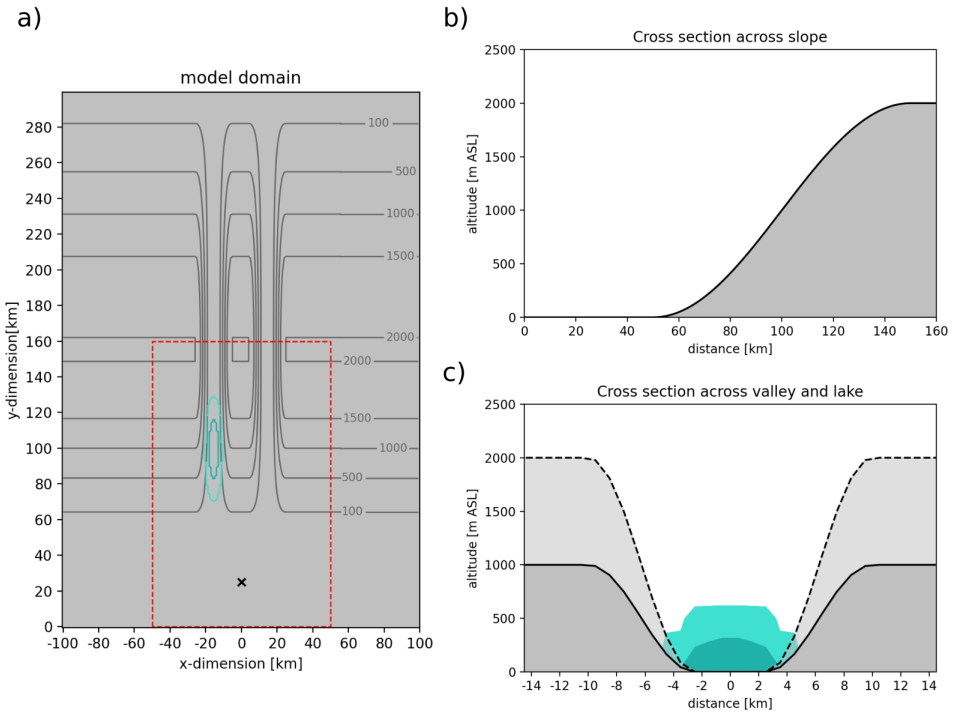

Figure 6.3: Modeled topography for a) full domain with key area for analyses shown in the red box, b) cross-section across the slope and c) cross-section across the valley with the lake at y=100 km (solid line and teal shading) and y=150 km (dashed line), moisture perturbation shown in teal.

Table 6.1: Scenario descriptions; scenarios highlighted in results noted with asterisk and numbered in order

Scenario name	topography	lake	CAPE [J kg^{-1}]	0-6 km windshear [m s^{-1}]
control* [1]	none	none	2000	31
slope_1500	slope to 1500 m	none	2000	31
slope_2000* [2]	slope to 2000 m	none	2000	31
valley_1500	1500 m valleys	none	2000	31
valley_2000	2000 m valleys	none	2000	31
lake	none	lake	2000	31
lake_valley_1500	1500 m valleys	lake	2000	31
lake_valley_2000* [3]	2000 m valleys	lake	2000	31
med_cape	none	none	1500	31
low_cape* [4]	none	none	1000	31
med_shear	none	none	2000	25
low_shear* [5]	none	none	2000	20
med_cape_shear* [6]	none	none	1500	25
low_cape_shear	none	none	1000	20
valley_med_cape	2000 m valleys	lake	1500	31
valley_low_cape* [7]	2000 m valleys	lake	1000	31
valley_med_shear	2000 m valleys	lake	2000	25
valley_low_shear* [8]	2000 m valleys	lake	2000	20
valley_med_cape_shear* [9]	2000 m valleys	lake	1500	25
valley_low_cape_shear	2000 m valleys	lake	1000	20

To investigate the meteorological processes behind the different outcomes in the scenarios, we also produce all scenarios without initializing storms with the warm bubble.

6.3 Analysis Methods

To analyze the model output, we process the scenarios containing an initialized thunderstorm with the thunderstorm detection and tracking algorithm T-DaTing (Feldmann et al., 2021; PySteps developers, 2021). By ingesting the composite reflectivity from the model output, the algorithm identifies reflectivity peaks above a certain thresholds and identifies the contours at a lower reflectivity threshold using an inverse watershed algorithm (Beucher and Lantuejoul, 1979; van der Walt et al., 2014). Utilizing optical flow (Lucas and Takeo, 1981) computed over three previous time steps, the cell motion is estimated. Between time steps detected cells are advected with their estimated motion and the overlap with cells detected in the next time step is computed to re-identify the same cells (Feldmann et al., 2021).
Since most thunderstorm-tracking algorithms struggle with cell splits [see also TRT (Hering et al., 2004), KONRAD3D (DWD, 2022) or TITAN (NCAR, 2022)], and we are working here with symmetrically splitting supercells, we simplify the tracking problem by splitting the domain in half and running T-DaTing independently in each half. This yields reliable tracking results for all tested scenarios by using the default thunderstorm-tracking thresholds of this algorithm.

6.4 Results

In this first section we investigate the influence of terrain features on a supercell's life cycle, as shown in Fig. 6.4. The control run using flat topography serves as a baseline. With unidirectional shear and in the absence of the Coriolis force, the control run produces two mirror-symmetric, long-lived supercells - a left- and a right-mover (see Figs. 6.4a, 6.4d and 6.4g). First looking at *slope_2000* we can see that the symmetry is maintained, as expected (see Figs. 6.4b, 6.4e and 6.4h). The supercells' life cycles are shortened, as conditions at higher altitudes are unfavorable, with lower CAPE and less moisture present. Over the upslope portion around the 500 m contour at t = 120, there is an area, where the supercells are locally enhanced. The updraft is stronger over the slope (Fig. 6.4e), with the environmental flow adding to the vertical motion. In addition, the most-unstable CAPE is based on parcels originating from slightly higher altitudes, so particularly the beginning of the slope presents with more favorable conditions and higher CAPE. The tracks of both cells appear slightly wider, and the translational speed decreases along the slope, allowing for a stronger deviation along the track. In comparison to *slope_1500* (not shown here), steeper slopes and higher altitudes lead to more pronounced changes, so the enhancement and decay are to a lesser degree in this scenario.
Moving towards the simulations including valleys, we can see in *valley_2000* that the supercells behave very similarly to *control* as long as they are within the valley. The eastern valley of the *valley_lake_2000* scenario behaves very similarly to the scenario *valley_2000*, we therefore only show the results of *valley_lake_2000* in Figs. 6.4c, f and i and discuss *valley_2000* by focusing on the eastern valley. Upon encountering the steep upslope portion at the valley walls (t=150 min), vorticity, updraft and precipitation rate are strongly enhanced in this portion. Once the storms fully reach the plateau portion, they rapidly decay in the less favorable environment (t>=150). The increased storm intensity is confined to the favorable, upslope portion of the storm track. Over the total storm life cycle, intensity is on average lower than in the *control* scenario. Also here, *valley_1500* shows the same responses (not shown here), but to a lesser extent. Slope steepness and altitude influence the magnitude of the response.

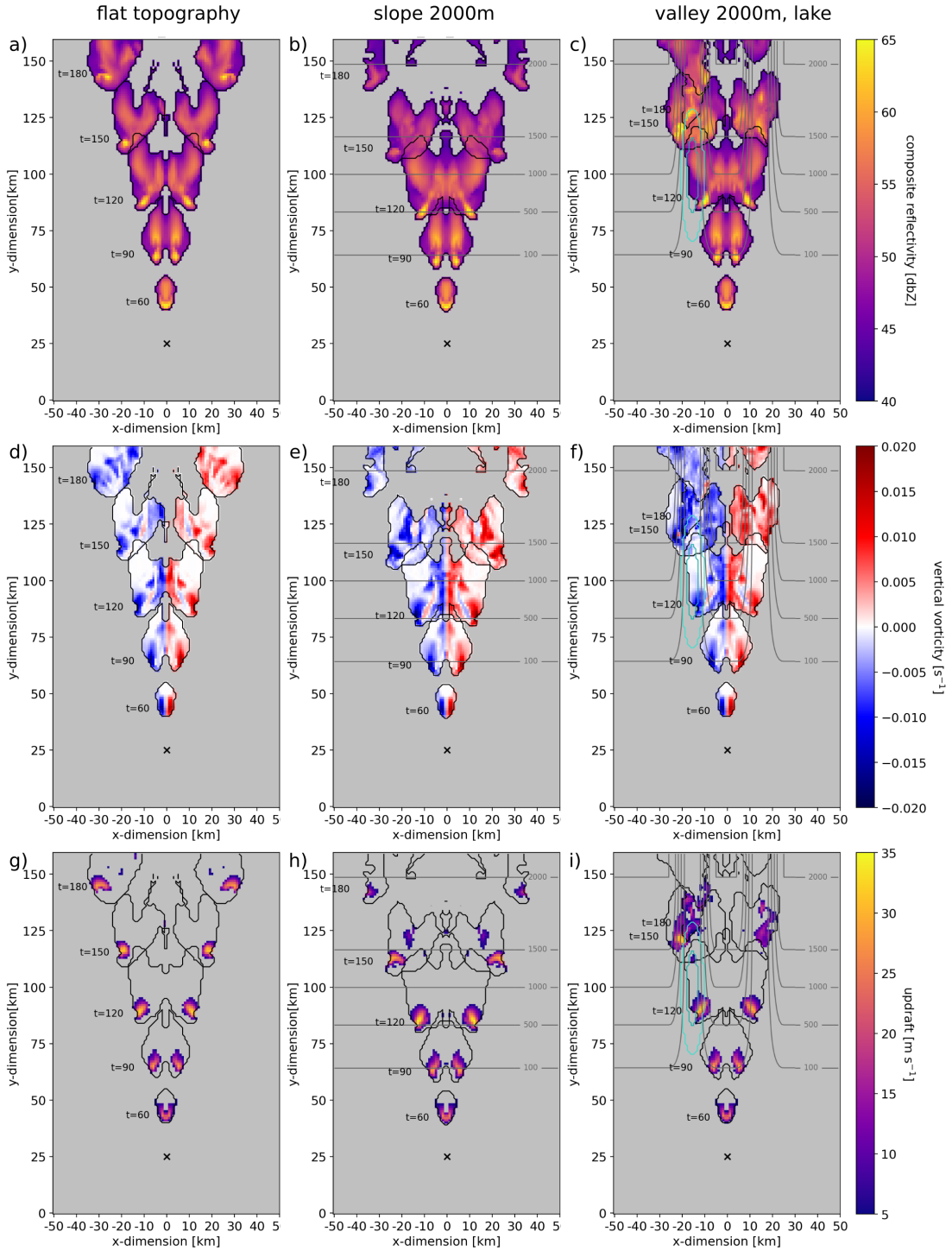

Figure 6.4: Evolution of a)-c) reflectivity, d)-f) 0-5 km vertical vorticity and g)-i) 0-5 km updraft >5 m s^{-1} within thunderstorm contours every 30 min for the respective scenarios *control*, *slope_2000* and *valley_lake_2000*. Isohypses indicated in gray, lake contour in teal, initiation location with a cross.

In this second section we examine the influence of a lake on the storm evolution. We look here at the comparison between the western valley with the lake and the eastern one without it in Fig. 6.4c, 6.4f and 6.4i. In addition, Fig. 6.5 shows the perturbations of valleys and lake on the initial thermodynamic conditions at the surface, as well as the background flow between 0 and 2500 m. CAPE and moisture content are elevated in the area of the moisture perturbation (see Fig. 6.5a). Comparing both valleys in Fig. 6.5b, we see that the lake in itself only causes a minor circulation to occur, orders of magnitude smaller than the circulatory effects of topography. The topography causes convergence of the horizontal flow at the valley entrances and divergence around the peak of the slope. In addition, the flow accelerates in the valleys. The flow going up the principal slope experiences enhanced vertical motion. Where it converges into the valley, it first slopes downward. Further into the valley, where the flow diverges back onto the principal slope, the average motion is upslope. The heterogeneity in the flow field results in additional horizontal vorticity. The formulas for x-, y-, and z-vorticity (ξ, η and ζ) are shown here:

$$\vec{\omega} = \nabla \times \vec{v} \tag{6.8}$$

$$(a)\ \xi = \frac{\partial w}{\partial y} - \frac{\partial v}{\partial z}\ ;\ (b)\ \eta = \frac{\partial u}{\partial z} - \frac{\partial w}{\partial x}\ ;\ (c)\ \zeta = \frac{\partial v}{\partial x} - \frac{\partial u}{\partial y} \tag{6.9}$$

As shown in Fig. 6.5b from a Eulerian viewpoint, the magnitude ξ increases over the principal slope due to the increased vertical gradient of v (see Eq. 6.9a). This is visible in the increased v-velocity in the 1000-2500 m layer upon encountering the slope. Moreover, the valley walls have higher values of η, due to the convergence phenomena that introduce a u-component into the flow and hence heterogeneity in the vertical gradient of u (see Eq. 6.9b). The changes in the vertical wind are much smaller than those in the horizontal flow, hence the horizontal flow modification dominates the vorticity distribution in the background state.
For a Lagrangian perspective, we inspect the frictionless governing equations of vorticity:

$$\frac{D\xi}{Dt} = \xi u_x + \eta u_y + \zeta u_z + B_y \tag{6.10}$$

$$\frac{D\eta}{Dt} = \xi v_x + \eta v_y + \zeta v_z - B_x \tag{6.11}$$

$$\frac{D\zeta}{Dt} = \xi w_x + \eta w_y + \zeta w_z\,, \tag{6.12}$$

where B_x and B_y correspond to the horizontal baroclinicity.

To explain the vorticity distribution, first follow a parcel in the y-direction up the principal slope; the isentropes begin to rise with the parcel ascent. This deformation in isentropes increases the horizontal vorticity ξ through baroclinicity; at constant altitude (in Fig. 6.5c at 3000 m), $B_y < 0$ corresponding to ξ becoming more negative (see Fig. 6.5c and Eq. 6.10). On the principal slope there is no u-component to the velocity field, therefore the increasingly negative values of ξ stem mainly from the baroclinic term. Also note that all the terms in (6.11) vanish on the principle slope, so that η remains zero there.

Next consider a parcel flowing up the valley. In this case $B_y = 0$ along the mid-line and there is no further contribution to ξ. However as the isentropes are lower in the valleys, than above the elevated topography the buoyancy gradient B_x has two signs: positive on the the west and negative on the east side of the valley; thus by (6.11), $-B_x$ creates $\eta < 0$ on the west and $\eta > 0$ on the east side of the valley entrance. Further up the valley the flow switches to upslope (on the east side) which reverses B_x and creates $\eta < 0$ there. In addition, the gradient v_x follows the same pattern as B_x, increasing in magnitude when entering into the valleys and decreasing with distance up the valley. With both ξ and the contribution of $-B_x$ being negative, the terms ξv_x and $-B_x$ contribute with the same sign on both sides of the valley (see Eq. 6.11). The gradient v_y is positive over the slopes and inside the valley, with an acceleration occurring in both cases. This further increases the magnitude of η through the term ηv_y (see Fig. 6.5d), leading to an increased magnitude of η at the valley walls.
The vertical vorticity increases over time, when each of the vorticity components encounters gradients in vertical wind (see Eq. 6.12). Once the updraft of the supercell enters the valleys, the greater horizontal vorticity there becomes available for tilting. Moreover, with the overpass of the supercell, the additional moisture and buoyancy increase the area of the updraft and precipitation rate (see Fig. 6.4c and 6.4i). The additional moisture content provides a greater reservoir for latent heat release and condensation when rising within the updraft of the storm. The larger updraft area results in a larger amount of horizontal vorticity available for tilting, leading to amplified vertical vorticity in the storm after passing over the lake (see Fig. 6.4f, t=150 min). This also increases the overall vertical gradient in vertical velocity, leading to additional vorticity stretching. The upslope enhancement of the updraft further increases the amount of vertical vorticity generated from stretching.
In addition, the modified flow in the valleys leads to a change in the vertical wind profile, which previously consisted in a linear increase with altitude. In Fig. 6.5e selected vertical profiles within the valleys along the supercells' tracks are shown. The further the tracks proceed into the valleys, the greater the curvature in the vertical profile becomes. Where previously only crosswise vorticity was present, there is now an increasing component of streamwise vorticity. The clockwise rotation of the flow with height for the right-mover (profiles shown in red) is beneficial for its evolution. Likewise, the counterclockwise rotation (blue profiles) along the track of the left-mover supports its development.

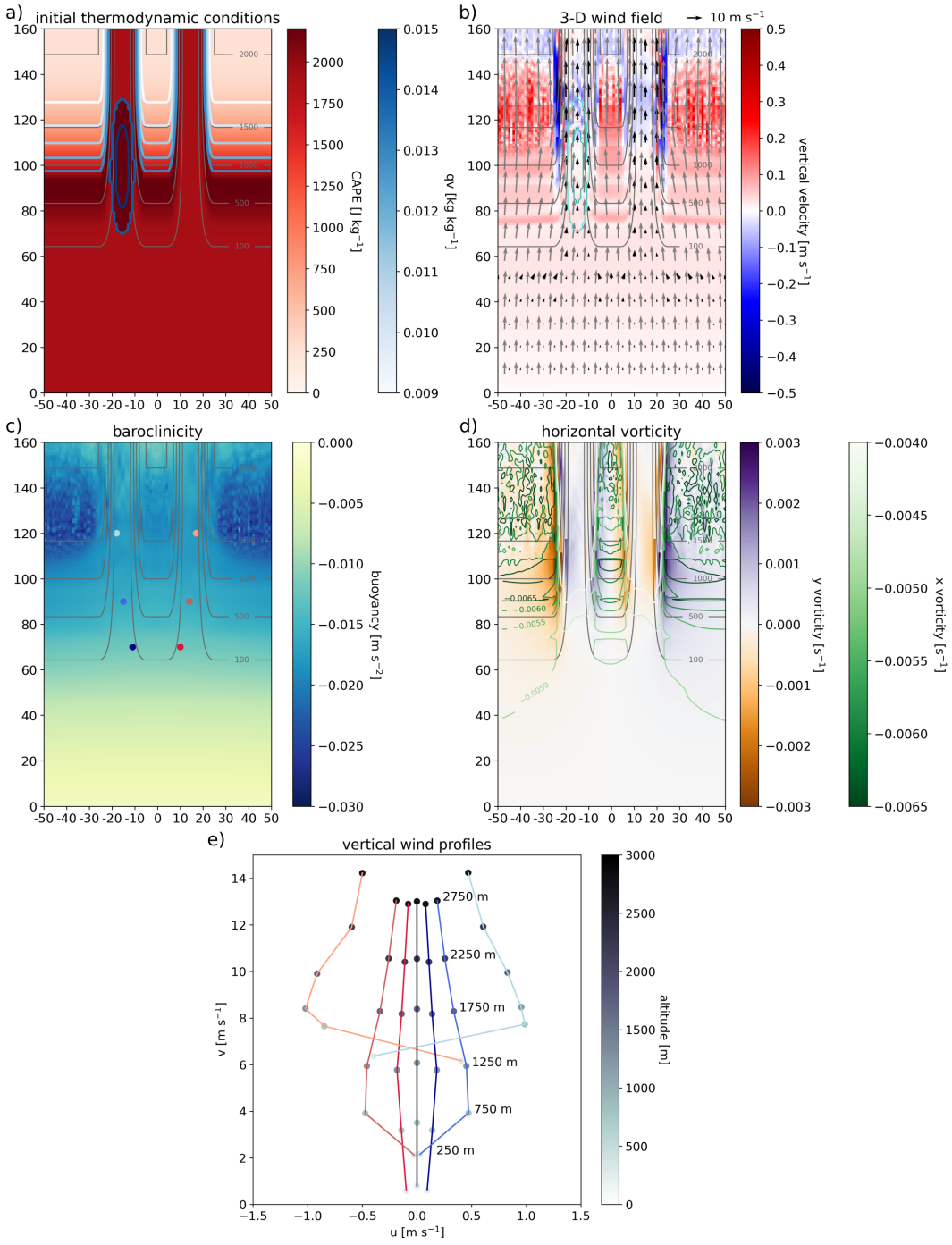

Figure 6.5: Perturbations in the *valley_lake_2000* scenario; a) surface CAPE and water vapor mixing ratio; b) average vertical velocity from 0-2500m in background, black arrows indicate horizontal flow 0-1000m, gray arrows horizontal flow 1000-2500m; c) average buoyancy at 3000 m in background, locations of vertical profiles from e) marked with dots; d) average x-vorticity from 0-2500m in green contours, average y-vorticity in background; e) vertical wind profiles along the valley sides as indicated in c), initial conditions in black profile. On panels a) - d) isohypses are indicated in gray.

Lower terrain as seen in *Lake_valley_1500* shows the same tendencies, but with a weaker perturbation with respect to the *control* scenario (not shown here). The experiments with the lake were also performed without valleys (*lake* scenario). In this case the effects are limited to the thermodynamic perturbation, with higher CAPE and moisture content increasing the updraft area and precipitation rate (not shown here).

Following the topographical and lake experiments, we conduct a series of tests changing the initial atmospheric profile. First, we investigate how this affects the *control* scenario. We modify the initial sounding to lower the CAPE values to 1500 and 1000 J kg^{-1}, respectively. In *med_cape* and *low_cape* the storm intensity is reduced overall due to the reduced CAPE. *Low_CAPE* shows the stronger decrease in intensity, however the supercells still form as split storms and present with significantly rotating updrafts, as shown in Figs. 6.6a, 6.6d and 6.6g. The deviation from the mean flow for the right- and left-mover is less pronounced than before. The next series of tests utilizes the initial CAPE, but reduced deep shear to 25 and 20 m s^{-1}, respectively. In *med_shear* and *low_shear* (Figs. 6.6b, 6.6e and 6.6h) we can see the effects of a lower vertical shear profile on the evolution of the *control* scenario. With the mid-level flow being lower, the overall translational speed is reduced. Moreover the lower shear results in a less pronounced pressure perturbation deviating the storm from the mean flow, which narrows the tracks (Davies-Jones, 2015; Bunkers et al., 2000). With decreasing shear, the overall intensity also decreases and the lifetime shortens. The tracks are also narrower, with the *low_shear* case barely separating the two storm cells before they decay. Overall, the supercells react more sensitively to the change in deep shear than to the change in CAPE previously described. Fig. 6.6c, 6.6f and 6.6i show the combination of both effects, with moderately reduced CAPE and shear (1500 J kg^{-1} and 25 m s^{-1}, *med_cape_shear*). In this case the cells form, split and are persistent. The translational speed is lower than in the *control* case, but not as low as in the *low_shear* case. The deviation from the mean flow is also less pronounced than in the *control* scenario. The overall intensity of the storms is still strongly reduced, with peak updraft and updraft area smaller than in the *control* case. When strongly reducing both CAPE and deep shear (1000 J kg^{-1} and 20 m s^{-1}, *low_cape_shear*), the cells no longer fully form and the environment no longer supports deep convection (not shown here).

We now investigate the same modifications for the *valley_lake* scenario. When adding topography and a lake, *valley_med_cape* and *valley_low_cape* (Figs. 6.7a, 6.7d and 6.7g) also show according intensity reductions. In these cases, the supercells form and split into symmetrical pairs (aside from the influence of the lake). Since the *low_cape* scenarios present with a weaker updraft, the pressure perturbation responsible for the track deviation is also less pronounced. The presence of the lake does enhance the magnitude and area of the updraft subsequently, but does not compensate for the overall reduction in CAPE.

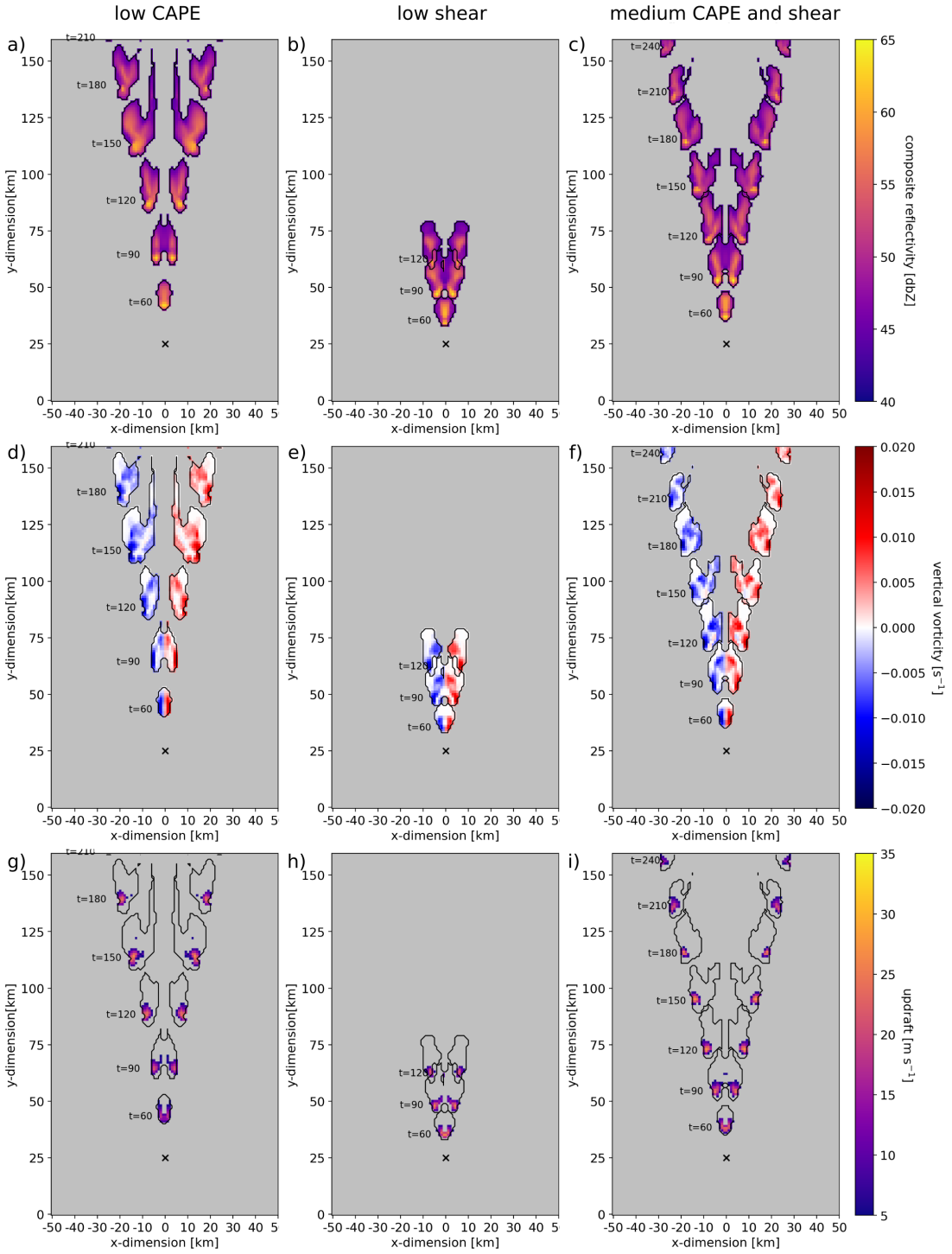

Figure 6.6: Evolution of a)-c) reflectivity, d)-f) 0-5 km vertical vorticity and g)-i) 0-5 km updraft >5 m s^{-1} within thunderstorm contours every 30 min for the respective scenarios *low_cape*, *low_shear* and *med_cape_shear*. Isohypses indicated in gray, lake contour in teal, initiation location with a cross.

The reduced shear scenarios *valley_med_shear* and *valley_low_shear* (Figs. 6.7b, 6.7e and 6.7h) are also able to produce deep convection with significant rotation, however in the *valley_low_shear* scenario the storms immediately decay on the ridge. The evolution is significantly stronger than in the *control* scenarios with lower shear, with longer lifetime, higher reflectivity values, a larger spatial extent of the storm, a more pronounced split and higher vorticity values. This concerns both the valley with and without a lake. Considering Fig. 6.5, the topography of the valleys is key for the generation of additional horizontal vorticity.
When combining both modifications here into the *valley_med_cape_shear* scenario, we can see the importance of both the thermodynamic and dynamic modifications of lake and valley (Figs. 6.7c, 6.7f and 6.7i). The case *valley_med_cape_shear* shows distinctly stronger cells both with the lake and without it, but the eastern cell no longer reaches the plateau due to the narrower track. It hence does not fully encounter the upslope portion of the valleyside. The western cell intensifies after crossing the lake, presenting with stronger updraft and higher precipitation rates. It still reaches the plateau and later decays. The combination of both increased vorticity and CAPE in the western valley leads to a storm that locally intensifies to vorticity, updraft and precipitation values similar to the *valley_lake* scenario. The case *valley_low_cape_shear* also does not support a full storm evolution, but the weak convection forming is longer-lasting than in the *low_cape_shear* case (not shown here). The tracks here no longer deviate from the flow and do not move towards the valley sides. The convective cells hence only encounter the prolonged slope in the center of the domain, where the x-component of vorticity is increased and the updraft is supported by the slope.

The comparison of weaker convective environments with and without terrain has shown that supercell thunderstorms are able to persist in less conducive environments in topography, even if their intensity is not as high as in the *control* case. Particularly the lower shear environments are of interest here. In the simulations without initiated storms, we can identify areas of increased horizontal vorticity along the valley sides. These stem from converging flow that channels into the valleys instead of ascending up the principal slope. This convergence also leads to an increased horizontal wind speed further up the valley. The convergence flow presents with additional vertical shear that is not present in the *control* simulation. The increased horizontal vorticity yields a greater net amount of vorticity to tilt in the updraft of the supercell. This additional vorticity compensates the lack of vorticity in a low-shear environment without topography. While the presence of the lake in these simulations does not cause an inherent circulation, the equivalent potential temperature (Θ_e) is greater through the higher moisture content. So air stemming from the lake entering the storm has a greater potential to rise, increasing the strength and size of the updraft, thus enabling the tilt of a greater portion of the horizontal vorticity. In addition, higher peak updraft velocities enable a larger degree of vorticity stretching, further increasing the amount of vertical vorticity in the storm. This indicates that especially valleys with lakes are able to sustain supercell thunderstorms in conditions that no longer support their full development without topography, which is in agreement with the findings of Feldmann et al. (2021, 2022).

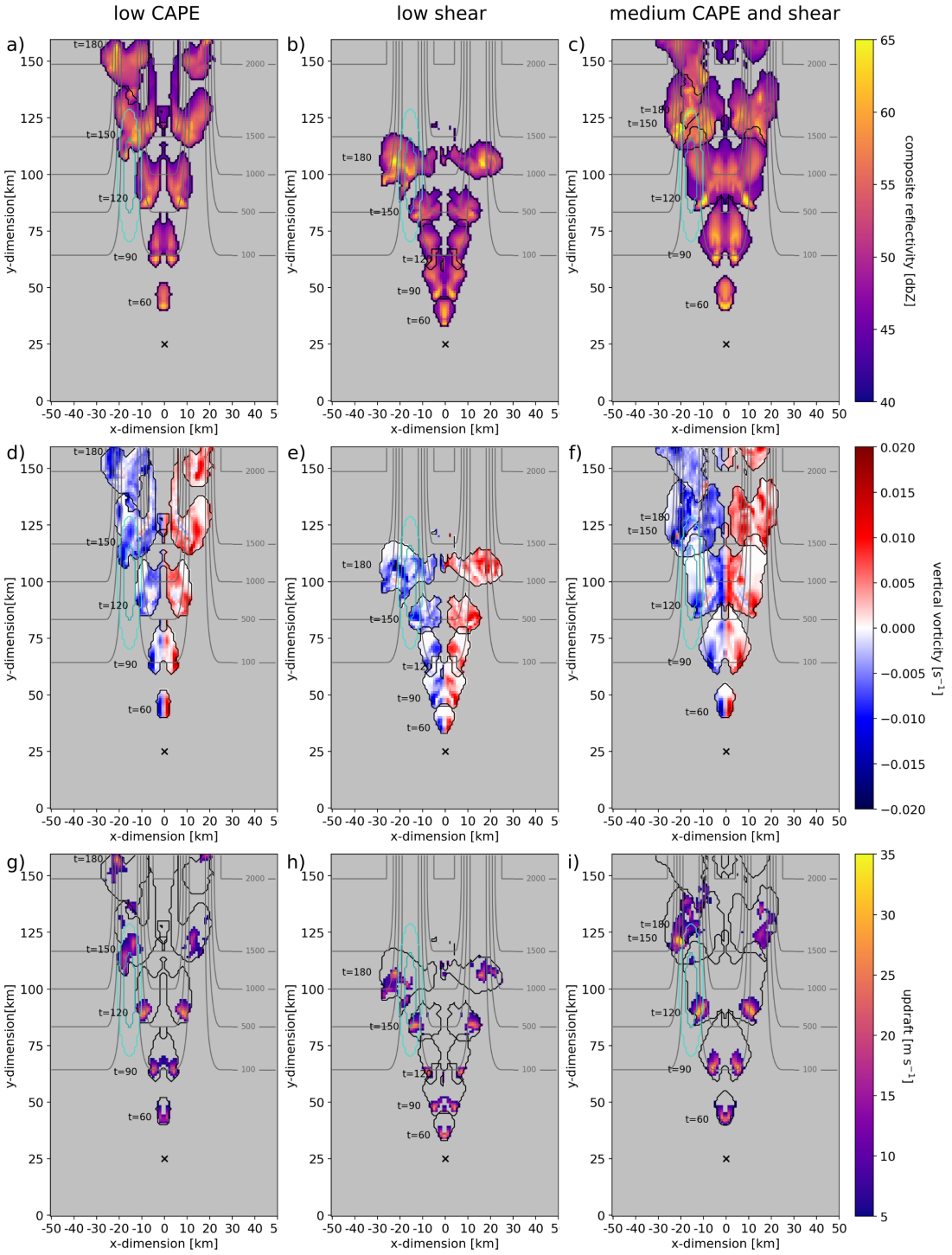

Figure 6.7: Evolution of a)-c) reflectivity, d)-f) 0-5 km vertical vorticity and g)-i) 0-5 km updraft >5 m s^{-1} within thunderstorm contours every 30 min for the respective scenarios *valley_low_cape*, *valley_low_shear* and *valley_med_cape_shear*. Isohypses indicated in gray, lake contour in teal, initiation location with a cross.

To explore the limits of supercell occurrence in the modeled scenarios, we further reduce CAPE down to 300 J kg^{-1} and 0-6 km shear to 10 m s^{-1}. Table 6.2 shows a summary of CAPE, surface temperature, lifting condensation level (LCL), level of free convection (LFC) and convective inhibition (CIN) in the differing CAPE environments. In comparison to the change in CAPE, the corresponding changes in LCL, LFC and CIN are marginal. In flat terrain at 31 m s^{-1} deep shear, supercells stop occurring at CAPE levels below 800 J kg^{-1}. In valleys with lakes, supercells only stop occurring at CAPE values below 400 J kg^{-1}. As shown in Fig. 6.6, in flat terrain at 2000 J kg^{-1} CAPE, supercells no longer form at 20 m s^{-1} deep shear. Supercells in valleys with lake persist in environments with deep shear as low as 15 m s^{-1}.

Table 6.2: Environmental characteristics of varying CAPE scenarios

CAPE [J kg^{-1}]	surface temperature [K]	LCL [m]	LFC [m]	CIN [J kg^{-1}]
2000	300	1076	1538	28.5
1500	299	1076	1573	30
1000	298	1065	1618	32.25
650	296	1009	1623	31.5
300	294	990	1700	34

The importance of topography for vorticity generation was also found in Markowski and Dotzek (2011); Ćurić et al. (2007); Homar et al. (2003). Especially small-scale features have an important role in maintaining a favorable environment, as found in case studies (Scheffknecht et al., 2017; Homar et al., 2003; LeBel et al., 2021). Markowski and Dotzek (2011) also highlights the upslope enhancement of convection and how topography induces heterogeneity in the atmospheric environment. The effect of the lake is mainly represented by increased CAPE and Θ_e in the environment. The impact of CAPE on the storm intensity and updraft is also discussed in Lin and Kumjian (2022); Peters et al. (2020); Markowski and Dotzek (2011); Weisman and Klemp (1982). The role of topography in maintaining higher Θ_e environments is also discussed in Scheffknecht et al. (2017); LeBel et al. (2021); Mulholland et al. (2019). The key combination is here the higher Θ_e environment from the lake inside the topographic setting with the valley. The valley walls channel the flow, reducing the source of inflow air to the valley, where the lake is located. The subsequent higher moisture content in the storm increases the precipitation rate, which is further enhanced orographically when encountering the slope (Houze, 2014).
Overall, we here combine several aspects of topographic influence, where both dynamic and thermodynamic perturbations play a role. The findings agree with previous studies that also reflect on these aspects.

6.4.1 Sensitivity Tests

A number of sensitivity tests were performed on the valley shape, the width / steepness of the slopes and the size and magnitude of the lake as a moisture source. The tests with different terrain setups revealed that supercell evolution is sensitive to the steepness of a slope, but as long as it is not excessively steep, the upslope vertical motion, increase in horizontal vorticity and locally enhanced CAPE will support the storm's intensification. Valleys narrowing towards the end have a more pronounced convergence effect and a stronger upslope effect at their end. When varying the terrain altitude, strongly nonlinear responses were seen starting from ridge heights around 2500m, likely stemming from the increasingly steep valley walls.
While the size of the lake and strength of its moisture perturbation are taken from observations, we also experimented with larger sizes and modified perturbations. Increasing or decreasing the initial perturbation leads to a proportional response in precipitaton rate. However, changing the size of the lake or the nature of the maintained nudging has a stronger effect on the outcome. Increasing the size increases the overall amount of moisture that is additionally available. This results in a larger volume that is nudged, which further increases the available moisture. The nudging is the most sensitive part of the setup since it affects every computational time step and changes accumulate throughout the simulation. When reducing the nudging to the lowest model layer, the outcome is very similar. However, when turning off the nudging entirely, the initial perturbation is moved with the flow, gets absorbed into an overpassing storm and hence dissipates. The storm will still experience strengthening, but to a much lesser degree, as the additional moisture is much lower. A moisture perturbation that is too strong will provoke a circulation that in itself disturbs the organization of deep convection. In this case, where the perturbation barely produces a circulation, the results are deemed to be realistic.
To assess the robustness of the results with respect to model resolution, a selection of scenarios was repeated with an increased horizontal resolution of 500 m x 500 m and 100 evenly spaced terrain-following vertical levels. The higher resolution allows for more pronounced extremes at smaller scales, leading to some quantitative differences. However, the qualitative differences between the scenarios remain the same, with slopes locally enhancing updraft and storm strength, high altitude being detrimental, the lake increasing updraft area and precipitation rate and the valleys sustaining supercells in lower-shear environments. The main mechanisms discussed before remain the same.

6.5 Conclusion

In this work we analyze the evolution of idealized supercell simulations in different topographic and environmental settings. We aim to explore the meteorological processes leading to observed high frequencies of supercell occurrence in Prealpine valleys with lakes on the southern side of the Swiss Alps. With the scenarios explored here we can isolate the effects stemming from topography from those of the lakes. The topographic experiments show a localized enhancement of the updraft, when the supercell is moving upslope. In addition, the vertical vorticity signature is more pronounced in these areas. At lower altitudes of the slopes, the environment is very favorable with even higher CAPE values than in the absence of topography, supporting the localized enhancement. At higher altitudes, the environment becomes increasingly unfavorable, with decreasing CAPE, decreasing moisture content and a lack of vertical wind shear. In all scenarios the supercells decay once they reach the high altitude plateau of 1500-2000 m.
The presence of valleys leads to a modification of the horizontal flow. On the slopes next to the valleys, the flow converges into the valley with an initial downslope motion. This introduces heterogeneity in the u and v field, that leads to additional horizontal vorticity. Inside the valley, the channeled flow has a higher velocity and presents with an upslope motion at the valley sides, diverging back onto the plateau. The additional horizontal vorticity leads to higher vertical vorticity values once the supercells' updraft tilts the horizontal vorticity. The outflow of the storms induces a strong upslope motion along the valley sides. Likewise, once the storm moves upslope over the steep valley sides, its updraft is strongly enhanced until it reaches the plateau and subsequently decays. The valleys also provide a component of streamwise vorticity that supports each of the split cells, whereas the initial conditions only present with crosswise vorticity.
The presence of a lake provides the supercells with additional moisture and energy. While not perturbing the initial flow, it presents an area of elevated CAPE, leading to a larger and stronger updraft. This also allows the storm to tilt a larger volume of horizontal vorticity, resulting in greater vertical vorticity. The additional moisture increases the precipitation rate. These effects of the lake compound with the effects of topography. Figure 6.8a gives an overview of all identified processes. Figure 6.8b additionally gives an overview of the results, which conditions support supercellular development in flat terrain in contrast to valleys with lakes.

Experiments with modifications of the initial environmental conditions show that overall the supercells react more strongly to modifications of the vertical shear profile, than a reduction in CAPE. The scenarios including topography are less sensitive to a reduction in vertical shear, as the converging flow provides additional horizontal vorticity to compensate for the lack of shear. While not quite reaching the same peak intensity, supercells are able to form and subsist in conditions, where they no longer persist in the experiments without topography. The addition of a lake with the resulting larger updraft further bolsters this robustness.

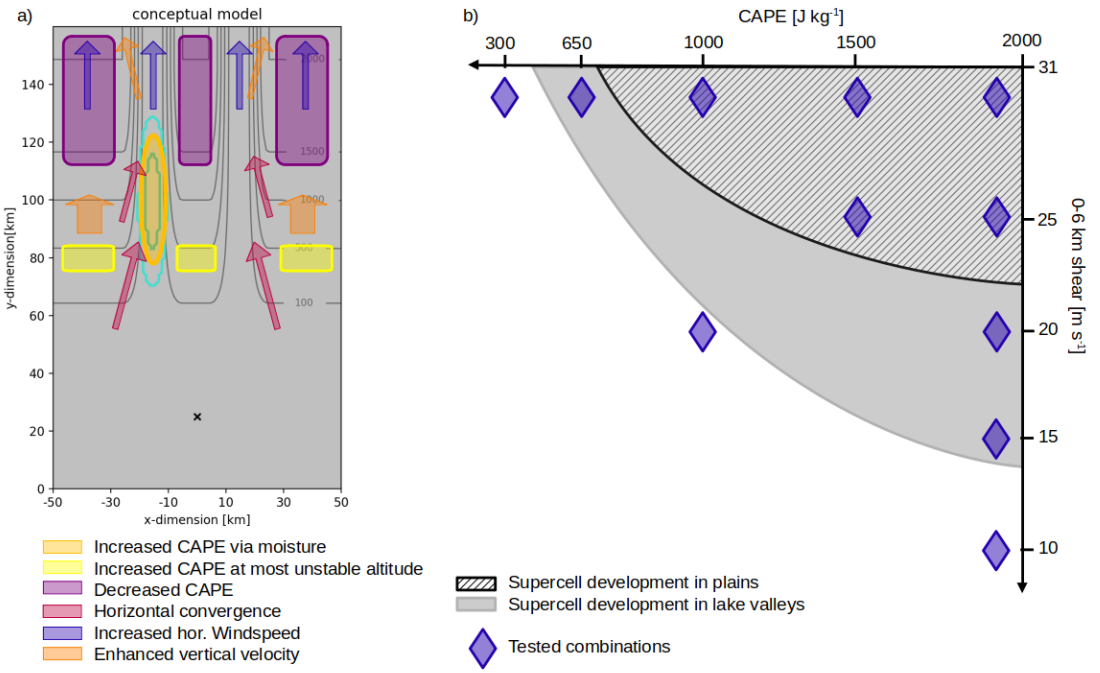

Figure 6.8: a) Conceptual model of the dynamic and thermodynamic effects affecting supercell evolution in valleys with lakes b) CAPE and shear environments leading to supercell development in differing topography

Overall the longest supercell life cycle with the highest persisting intensity is found in the control simulation without topography and high CAPE and shear values. However, the scenarios with topography and lake show localized pronounced intensification of the storms during their passage over upslope portions of the terrain. The life cycles are shortened by the decay on the high-altitude plateau. The influence of terrain and lakes on supercell results in a systematic location dependence of the frequency, intensity and lifetime of supercells. In addition, these scenarios are less sensitive to reductions in vertical shear, indicating that supercells can persist in a wider range of environmental conditions.
Considering the observational background, that supercells in the Southern Prealps are more frequent, but of lesser intensity than those in the flat NW Po Valley, the investigated scenarios support this observation. We conclude that the additional vorticity induced by orographic flow locally provides favorable conditions for supercell persistence, while moisture sources and upslope portions can locally intensify a storm considerably.
By identifying new thresholds for larger-scale environmental shear for foothill regions of mountains, climatological studies may utilize reanalysis data to derive the frequency of severe convective environments. Specifically for the southern Prealps, such an analysis may yield a longer record of supercell occurrence than the current, radar-based data set (Feldmann et al., 2021, 2022).

7 Conclusions

7.1 Summary and Discussion of Results

The initial research questions target establishing a systematic detection and tracking of supercells in Switzerland and utilizing it to investigate the characteristics of supercell thunderstorms within the observational domain. In the following we summarize, how the previous chapters cover the main objectives:

- Systematic supercell tracking
- Characterization of supercell frequency and spatio-temporal occurrence
- Identification of topographic influence
- Comparison with other types of severe convection
- Understanding of processes leading to orographic impact

The objectives cover the full spectrum of data processing and quality control, algorithm development, data analysis and interpretation, as well as numerical modeling.

7.1.1 Doppler Velocity Processing

The revision of the operational Doppler dealiasing algorithm set the foundation for the subsequent steps of establishing a mesocyclone detection algorithm. By combining multiple established approaches and employing an iterative strategy, we exploit all available information in the Doppler velocity field. The region-based recursive Doppler dealiasing algorithm R2D2 begins with region-based dealiasing to identify large, homogeneous areas that lie within the same Nyquist interval. By masking high-shear areas and possible velocity folds, the regions pose a simplified dealiasing problem and can be adjusted into the correct Nyquist interval as a whole. This reduces the probability of errors bleeding through the data. The subsequent pixel-wise dealiasing is constrained to the highest shear areas. While this can solve more complex

dealiasing problems, it is also more prone to error propagation. By repeating the iterations of region-based dealiasing and pixel-wise dealiasing, larger areas are identified as regions and can be dealiased together, finally reducing the pixel-wise dealiasing to only the highest shear regions of the velocity field. Both approaches make use of 4-D continuity constraints, assuming relative constancy in the horizontal, vertical and since the last volume update. A major improvement is also achieved by using numerical weather prediction model data to initialize the algorithm. While the vertical azimuth display provides useful information, when there is widespread precipitation and the flow field is homogeneous, it falls short in situations of scattered precipitation and heterogeneous flow. NWP data provides a fully covered field, no matter where and if there is precipitation. In addition, it represents the spatial heterogeneity of the flow.
This combination of strategies allowed us to greatly improve the quality of the dealiased Doppler velocity data, in spite of the low Nyquist velocities. This provides a degree of reliability that is crucial for further applications, such as mesocyclone detection.

The mesocyclone detection and tracking (M-DaTing) algorithm targets anomalies in the azimuthal shear field, constructing 3-D vertical objects of rotation and tracking them in time. The azimuthal derivative is strongly dependent on the azimuthal resolution, particularly for a relatively small phenomenon like the mesocyclone. To achieve the best possible coverage, we employ range-dependent thresholds that relax with increasing distance to the observing radar. When constructing the 3-D object, we also make use of all available radars, to optimize coverage in the areas lying in between the radars. For the tracking in time we rely on thunderstorm tracking algorithms, such as T-DaTing and TRT. By setting a constraint of at least 4 detections within 10 minutes of one another, we allow for gaps of one time step in the temporal constraint. This permits for a detected rotation to pass through areas of reduced observation quality, without losing its continuity.
In complex orography, Doppler velocity fields tend to be rather heterogeneous and present with numerous small-scale rotations and shear zones that are not related to convection. To constrain the detection algorithm to areas of relevance, it is only employed within or close to the contours of an identified thunderstorm. By dilating the thunderstorm contours with a 5x5km^2 kernel, we ensure that the mesocyclone is included. As it is usually located at the edge of the hook echo, where reflectivity values can sharply drop, expanding the contour encompasses this region reliably.
Due to numerical noise in the azimuthal derivative, the first 5 km around each radar are excluded, however, they are usually within the coverage of another radar in the vicinity, hence not producing a detection gap. Additionally, detected mesocyclones must leave a radius of 20 km of any of the detecting radars, to avoid false alarms due to high azimuthal shear in strong wind situations.
This combination of range-dependent thresholds and a number of quality constraints to avoid false detections yields a detection algorithm, that operates reliably up to, and sometimes exceeding, 100 km range from the closest radar.

Both of these algorithms were developed with the target of expanding the operational product chain at MeteoSwiss. R2D2 was implemented in real-time shortly after its development in 2019 and has been running in parallel with the previous algorithm ever since. This allowed us to monitor its performance in real-time during diverse meteorological situations, coming to the conclusion that it performs particularly well in convective situations with fragmented data and high shear.
M-DaTing was first used to process archived data in the past for the studies discussed in the following sections. In summer 2022, we tailored it for real-time use, adapting it to continuously launch and produce output once the required data is available. Hence we were able to monitor the second half of the convective season in real-time. This revealed a robust performance of the algorithm that reliably identified persistent rotation features in convection.

7.1.2 Supercell Thunderstorm Occurrence in the Alpine Region

Utilizing the newly developed mesocyclone detection algorithm, the MeteoSwiss radar archive since 2016 is exploited to establish a database of supercell thunderstorms in the past. Comparisons with overall thunderstorm occurrence show that only a minute fraction (<1 %) of thunderstorms produce a mesocyclone. The spatial distribution shows similar patterns, with the absolute maximum of convective activity occurring in the Southern Prealps and a secondary maximum in the Northern Prealps. The diurnal cycle shows a distinct maximum in the late afternoon, with convective activity dropping to a minimum in the early morning hours. The few supercells that do occur at this time, however, are among the longest and largest overall. This was also shown for hailstorms (Nisi et al., 2018), indicating that severe convection occurring during an overall unfavorable time of day, is among the most severe that we observe in Switzerland. As for other severe convection (Nisi et al., 2018; Mohr et al., 2020; Wapler et al., 2016), a large-scale Southwesterly flow is the most frequent synoptic flow associated with supercells, with a smaller fraction occurring during Westerly and Southerly flow. Southwesterly situations advect warm, moist air stemming from the Mediterranean towards Switzerland. Particularly to the South of the Alps, a Southerly flow can lead to a similar situation. The synoptic flow is also the predominant factor influencing the track direction of a supercell. Within the spread owing to the track deviation from the mean flow due to the pressure perturbation at the storm flank, the tracks broadly follow the direction of their synoptic flow class. With the Alps situated in the center of the domain, the influence of orography is one of the most prominent questions regarding supercell behavior. The maximum possible rotation intensity decreases with increasing altitude and orographic complexity. With CAPE being related to altitude, weaker updrafts in lower CAPE environments can lead to lower rotation due to less stretching of vorticity. Moreover, supercell dynamics depend on the generation of vorticity at the surface through the gust front and its advection into the storm through the low-level inflow. In increasingly complex terrain, this process is perturbed, particularly once the terrain features reach the cloud base.

While this study establishes a first, fundamental characterization of supercell behavior in the Swiss radar domain, it is still based on a relatively short observational period. The quality index helps with the interpretation thereof, by differentiating areas of low occurrence frequency from underobserved areas.

7.1.3 Supercell Thunderstorms in Comparison with Severe Hail- and Rainstorms

With supercells being a new, systematic classification category for thunderstorms at MeteoSwiss, we compare them to the established classes of severe hail and rainstorms. This provides the necessary context to understand supercell behavior in comparison. The spatial distribution of all classes reveals the same patterns established before, with the primary activity hotspot in the Southern Prealps and a secondary maximum in the Northern Prealps. These also agree with past studies including this region. A lower frequency of thunderstorms of all categories is found in the flat areas of the Swiss Plateau and the NW portion of the Po valley. In contrast, the intensity distribution shows the highest intensity storms occurring in the flat areas, while both sides of the Prealps experience lower intensity storms, albeit more frequently. This concurs with the previous observation that rotation intensity decreases with increasing topographic complexity. Overall, thunderstorm intensity and frequency are lowest over the main Alpine ridge, where the highest altitudes and most complex terrain occur.
While these patterns hold true for all storm classes, it is also evident that supercell thunderstorms represent the rarest and most severe fraction of storms. Severe hailstorms as the second rarest category can reach similar intensities. In addition, supercells present with the longest intensity peaks and lifetimes overall, with a mesocyclone usually being followed by an hour of high intensity.
Another notable component is the large number of hailstorms that present without detected mesocyclone. This contradicts studies in Germany, where the majority of severe hailstorms were found to have a mesocyclone. An analysis of radiosoundings showed that severe hailstorms without rotation occur on days with lower wind shear than those with mesocyclone. The presence of a certain amount of wind shear is crucial for the formation of a mesocyclone, indicating that the atmospheric profile on these days did not support the formation of a consistent rotation.

7.1.4 Investigating the Influences of Topography

With the spatial distribution of supercell showing a clear clustering in the moderately complex Prealps, we investigate these clusters by deriving idealized modeling scenarios that represent a simplified, generalized model of the key areas. Within the Southern Prealps, the local frequency peaks are within or close to prealpine valleys with large lakes, most notably Lago Maggiore and Lago di Como.

The investigated scenarios contain no topography, a slope up to 2000 m and valleys embedded in the slope, with one valley containing a moisture source. The initial conditions are set with a modified Weisman-Klemp sounding and a straightline shear hodograph, which represent CAPE and shear values that have been observed for supercells in the region. In a high CAPE, high shear environment, a right- and left-mover supercell form and persist in all cases. The longevity is most pronounced in the absence of topography, with the high altitude terrain presenting with an unfavorable storm environment and causing the cells to decay. During the upslope portion and increase in the updraft area, peak updraft velocity and vertical vorticity are visible. This leads to a heterogeneous intensity life cycle, with an intensification on the upslope and a subsequent weakening and decay at high altitudes. In the scenario with the lake in the valley, the lake additionally causes an enhancement of updraft area, vertical vorticity and precipitation rate, with the additional moisture locally increasing CAPE and precipitable water. The long, sustained life cycle of the flat case results in an overall higher intensity, than the shorter, more heterogeneous life cycles in the slope and valley cases, which aligns well with the observed patterns.
We additionally performed experiments, varying the initial conditions to lower values of CAPE and vertical wind shear. These experiments showed, that supercells no longer form in flat terrain, once shear values drop below a certain threshold. In the valley-lake scenario, however, they persist at these lower shear values, albeit at a lower overall intensity. The channeling of flow at the valley entrance increases the amount of horizontal vorticity available for tilting. In reduced CAPE scenarios the lake additionally replaces some of the lacking environmental energy. The ability to sustain supercells in an atmospheric environment that no longer supports them in the absence of terrain, may explain the higher occurrence frequency in prealpine valleys with lakes. The local modification of flow increases the shear, while lakes present as an energy reservoir.
Where the previous chapters establish an observational understanding of supercell behavior, we here translate the findings into generalized initial conditions in modeling scenarios. This enables the results to be more generally applicable, outside of the analyzed area. Modeling also gives us control of the single elements, allowing a separation of effects. Hence we are able to disentangle a general slope from valleys and additionally single out the effect of a lake.

7.2 Conclusions and Relevance

The previous chapters have covered the questions posed in the beginning of the thesis, providing insights into detection and tracking techniques, spatio-temporal occurrence, orographic patterns and their underlying meteorological drivers. Figure 7.1 provides an overview of the relations between the separate research projects and how they contributed to the main outcomes.

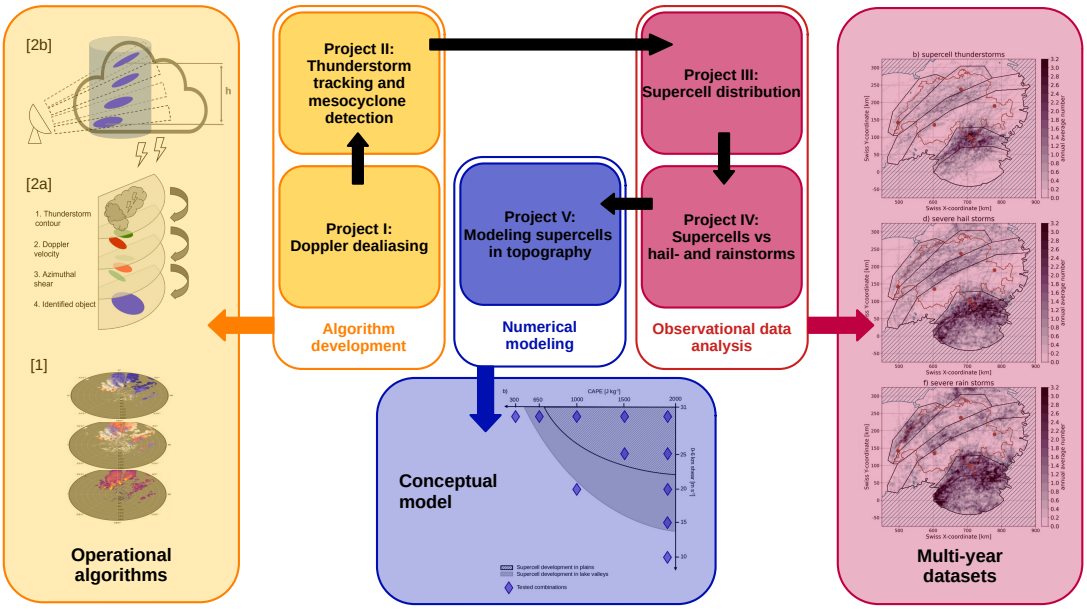

Figure 7.1: Overview of research projects and outcomes, black arrows denote information flow from one project to the next, colored arrows show contributions to the main outcomes.

Chapters 2 and 3 focus on algorithm development and lay the methodological foundation for chapters 4 and 5. The developed algorithms directly contribute to the operational data processing at MeteoSwiss. Chapters 4 and 5 establish multi-year data sets of supercells in the domain of the Swiss radar network, exploiting them to identify characteristics of severe convection in complex terrain. These findings are transferred to idealized modeling scenarios in chapter 6. This allows the investigation of underlying meteorological processes that lead to the observed characteristics.

The main findings are summarized in the following:

- While only <1 % of the thunderstorm population, supercells occur regularly within the Swiss radar domain, with peak annual occurrence frequencies of >3 yr^{-1} in the Southern Prealps, and present the most severe category of severe convection with the longest intensity maxima

- The diurnal and synoptic weather dependency of supercells reveal activity peaks in the late afternoon and during southwesterly flow
- The Prealpine areas have the highest frequencies of supercells on each Alpine side, whereas the adjoining plains experience the highest severity of supercells on each Alpine side
- After mesocyclone initiation, supercells have a prolonged period of high intensity and usually begin producing hail
- Valleys with lakes modify CAPE and horizontal vorticity in a manner that allows supercellular development to occur in a wider range of atmospheric profiles than in their absence
- Slopes and moisture sources lead to localized enhancement of convection, whereas high altitudes are detrimental, leading heterogeneous intensity life cycles that are on average weaker than in the absence of terrain

This first-time systematic evaluation of supercell characteristics in Switzerland advances our understanding of severe convection in complex orography. Comprehensive data sets of severe convection in mountainous regions are rare, making this a substantial contribution to severe storms research. Spanning the range from algorithm development over observational data analysis and interpretation to process understanding yields a thorough discussion of the subject of supercells in the Alpine region, reflecting it from the technical, analytical and theoretical standpoint. The main conclusions from the regional observational studies are key to understanding supercell behavior in the region, but their representativeness is confined to this area. Due to the high-impact nature of supercell thunderstorms, a regional understanding is important to assess the risk of severe weather hazards to the population and enact adaptation measures. However, by taking the observational results into generalized idealized modeling scenarios, the derived conceptual model is applicable to other regions featuring similar characteristics.

In addition to the scientific findings, the algorithms developed in chapters 2 and 3 have been implemented in the pre-operational, real-time chain of MeteoSwiss. This work contributes to the continuous improvement of radar data processing and the real-time warning chain. The new quality of the Doppler velocity data allows for more research projects and applications to rely on it, opening new possibilities for the operational processing chain. By providing forecasters with the highest possible quality of data and new automated products, severe weather warnings continue to improve. Considering the tendency of supercell thunderstorms to have significantly prolonged periods of peak intensity and a long lifetime, leading to a long track, real-time information about a persistent mesocyclone allows forecasters to identify impactful storms.

7.3 Remaining Scientific Questions and Perspectives

As these studies are among the first targeting supercell thunderstorms in Switzerland, both the observational and modeling analyses only scratch the surface of possible research on this in the Alpine region.

One of the biggest shortcomings of the supercell archive in its current state is the relatively short span of observations. It is limited by the availability of latest generation radar data, which yields a high enough quality that reprocessing the raw velocity data with R2D2 was possible. The database begins in 2016 and has been periodically updated throughout the duration of this thesis. This database should be kept up-to-date in future. In several years time, the observation period will be long enough to pursue studies that still suffer from sampling issues at the current stage. Such analyses may focus on the seasonal cycle, establishing the interannual variability and investigating whether trends emerge over time. With severe convective environments expected to increase in frequency in central Europe with climate change, it may be possible to observe such an increase in supercell occurrence as well.

In most other regions, severe hailstorms are linked to significant rotation. In contrast, we here show a certain disconnection between the two. Since the majority of severe hailstorms form on days, when the environment does not support supercellular development, this poses the question of how severe hailstorms can still be sustained and how they develop. One of the main differences of the Alpine region to hailstorms in Germany or the Great Plains is the prevalence of orography. A detailed observational case study of severe hailstorms with and without mesocyclone may yield insights into the differing storm dynamics and characteristics. Hailstorms are dependent on an even, wide, moderately strong and longlived updraft, so the mechanisms leading to a stable, sustained updraft are of key importance. Informed by case studies, modeling studies can help to identify key environmental and topographical factors influencing storm dynamics.

Another question is posed by supercell thunderstorms presenting without hail. Severe hailstorms have an occurrence maximum further to the South than supercell thunderstorms. While the vast majority of supercells does produce hail, a number of supercells in their occurrence maximum at the Northern end of Lago Maggiore were not associated with hail. A study of the microphysical processes and updraft properties making use of the polarimetric radar data of Monte Lema radar may shed light on the reasons for this.

The final chapter 6 aims to explain the frequency clusters in the Southern Prealps, however, it does not target the Northern Prealps. The configuration of flow and terrain are different there, as well as the pre-storm environmental conditions. Similar modeling experiments with a modified setup representing the regional conditions may provide insights into the factors enhancing supercell occurrence there.
In addition to the idealized modeling approach, a case-study based reproduction of examples for either location can further support the conceptual models resulting from the idealized scenarios. By running a more complex model and reducing complexity in subsequent experiments, the conceptual model can be approached from the opposite direction. In idealized modeling we start with the simplest setup and add complexity. In case-study based NWP model experiments, we start with the most complex scenario with all available information for a specific case and then reduce complexity to identify key necessary components. When both strategies yield the same results, the conceptual model can be deemed robust.

A more general future subject is the additional use of the new, higher-quality Doppler velocity data at MeteoSwiss. Robust Doppler velocity data can be used for 3-D flow studies employing multi-Doppler analyses, turbulence studies, especially with regard to air traffic safety, analyses targeting divergence signatures, Doppler velocity assimilation in numerical weather prediction models, and many more applications.

"The projected greater increases in hazards than in lightning over many regions imply that a greater fraction of thunderstorms will produce severe weather. Indeed, the severe weather efficiency of storms is predicted to increase in all regions and in all climate scenarios until 2100."
—Rädler, Groenemeijer, Faust, Sausen, and Púčik (2019)

Monika Feldmann, March 2021, scarf with climate change stripes of Switzerland, mean annual temperature 1864 - 2020, ©Showyourstripes

A Appendix A - Derivatives for Polar Data

Computing derivatives in polar data is not trivial, as the range-dependent resolution of the data conveys different scales of information. The approach of linear-least squares derivatives (LLSD) aims to provide a more homogeneous result, by merging a similar area of data for all ranges of the derivative. This results in a smoothing effect at close ranges, where a centered-difference approach tends to be very noisy and hard to interpret.
The equations presented here were initially published in Mahalik et al. (2019), but contained several errors. By repeating the derivation of the final formula, the equations below were obtained. These were subsequently also published in a correction by the original authors (Smith et al., 2021).
We experimented with the use of LLSD in the context of the mesocyclone detection. However, due to the possibility of residual aliasing in the velocity data, this yielded unsatisfying results. While the centered-difference approach is harder to interpret visually, it is easier to add error-removal techniques and process it numerically. The smoothing nature of the LLSD also requires a re-tuning of all established rotation and vorticity thresholds, as the true peak values are no longer preserved.
The following variables are used in the derivation:
k - index for each kernel grid point, m and n - number of grid points in the LLSD kernel in $x(m)$ and $y(n)$, Δr_k - radial distance from the kernel center, $\Delta\Theta_k$ - azimuthal distance from kernel center, u_k - radar variable measurement at kernel grid point k, and w_k - local weight at kernel grid point k.

Modified Matrix M

$$M = \begin{pmatrix} \sum w_k \Delta r_k \Delta\Theta_k & \sum w_k \Delta r_k^2 & \sum w_l \Delta r_k \\ \sum w_k \Delta\Theta_k^2 & \sum w_k \Delta r_k \Delta\Theta_k & \sum w_k \Delta\Theta_k \\ \sum w_k \Delta\Theta_k & \sum w_k \Delta r_k & \sum w_k \end{pmatrix} \tag{A.1}$$

Modified Azimuthal and Radial Derivatives

$$
\begin{aligned}
u_\Theta = &\Big[\sum w_k \Delta r_k \Delta\Theta_k \cdot \sum w_k \Delta r_k \Delta\Theta_k \cdot \sum w_k \\
&+ \sum w_k \Delta\Theta_k^2 \cdot \sum w_k \Delta r_k \cdot \sum w_k \Delta r_k \\
&+ \sum w_k \Delta\Theta_k \cdot \sum w_k \Delta r_k^2 \cdot \sum w_k \Delta\Theta_k \\
&- 2 \cdot \sum w_k \Delta r_k \Delta\Theta_k \cdot \sum w_k \Delta r_k \cdot \sum w_k \Delta\Theta_k \\
&- \sum w_k \Delta\Theta_k^2 \cdot \sum w_k \Delta r_k^2 \cdot \sum w_k \Big]^{-1} \\
&\cdot \Big(\sum w_k \Delta r_k u_k \cdot \Big(\sum w_k \Delta r_k \Delta\Theta_k \cdot \sum w_k - \sum w_k \Delta\Theta_k \cdot \sum w_k \Delta r_k \Big) \\
&+ \sum w_k \Delta\Theta_k u_k \cdot \Big(- \sum w_k \Delta r_k^2 \cdot \sum w_k + \sum w_k \Delta r_k \cdot \sum w_k \Delta r_k \Big) \\
&+ \sum w_k u_k \cdot \Big(\sum w_k \Delta r_k^2 \cdot \sum w_k \Delta\Theta_k - \sum w_k \Delta r_k \cdot \sum w_k \Delta r_k \Delta\Theta_k \Big) \Big)
\end{aligned}
\tag{A.2}
$$

$$
\begin{aligned}
u_r = &\Big[\sum w_k \Delta r_k \Delta\Theta_k \cdot \sum w_k \Delta r_k \Delta\Theta_k \cdot \sum w_k \\
&+ \sum w_k \Delta\Theta_k^2 \cdot \sum w_k \Delta r_k \cdot \sum w_k \Delta r_k \\
&+ \sum w_k \Delta\Theta_k \cdot \sum w_k \Delta r_k^2 \cdot \sum w_k \Delta\Theta_k \\
&- 2 \cdot \sum w_k \Delta r_k \Delta\Theta_k \cdot \sum w_k \Delta r_k \cdot \sum w_k \Delta\Theta_k \\
&- \sum w_k \Delta\Theta_k^2 \cdot \sum w_k \Delta r_k^2 \cdot \sum w_k \Big]^{-1} \\
&\cdot \Big(\sum w_k \Delta r_k u_k \cdot \Big(- \sum w_k \Delta\Theta_k^2 \cdot \sum w_k + \sum w_k \Delta\Theta_k \cdot \sum w_k \Delta\Theta_k \Big) \\
&+ \sum w_k \Delta\Theta_k u_k \cdot \Big(\sum w_k \Delta r_k \Delta\Theta_k \cdot \sum w_k - \sum w_k \Delta\Theta_k \cdot \sum w_k \Delta r_k \Big) \\
&+ \sum w_k u_k \cdot \Big(- \sum w_k \Delta r_k \Delta\Theta_k \cdot \sum w_k \Delta\Theta_k + \sum w_k \Delta r_k \cdot \sum w_k \Delta\Theta_k^2 \Big) \Big)
\end{aligned}
\tag{A.3}
$$

B Appendix B - Operationalizing Supercell Tracking at MeteoSwiss

Both the dealiasing and mesocyclone detection algorithm are novel algorithms that were added to the operational processing chain of MeteoSwiss. R2D2 was developed as a real-time applicable algorithm from the beginning, being based off of the previous operational algorithm 4DD. It runs in real-time with the velocity azimuth display as initialization. The quality achieved here is lower than when using COSMO-1, but, especially in convective situations, higher than with 4DD. R2D2 has been operating since December 2019 and is routinely monitored to assess its performance. It outperforms 4DD particularly in convective situations and frontal passages with high wind speeds and strong shears along the front. R2D2 is set to replace 4DD soon and become the new official dealiasing algorithm at MeteoSwiss.

M-DaTing was initially developed for past analyses. To operate in real-time, adjustments in the code were necessary. The algorithm now produces a tracking result every 5 minutes and conveys tracking information from one time step to the next. It launches once the required data is available. With the temporal constraint on mesocyclones, a real-time detection can only be confirmed by the algorithm after at least 20 minutes.
M-DaTing ingests the operationally available data from R2D2 and uses the contours of TRT to identify areas of interest. After assessing its robustness and functionality with the past archive, it was deployed into real-time operations in August 2022. Since then it has been monitored during convective situations to assess its performance and reliability.

Operationalizing an algorithm comes with additional constraints that are not required for archival analyses. Robustness against missing data is key to maintain operations when there is a partial data outage. It is crucial to know and account for as many artifacts as possible, to ensure low rates of false alarm and missing detections. Computational efficiency is also essential, as the analyses of one time step must at least be faster than the update rate of the data, to ensure temporal continuity. In addition, the available data is reduced in real-time, as many products are produced with a delay.

Bibliography

Adams-Selin, R. D. and Ziegler, C. L.: Forecasting Hail Using a One-Dimensional Hail Growth Model within WRF, Monthly Weather Review, 144, 4919 – 4939, doi: 10.1175/MWR-D-16-0027.1, URL https://journals.ametsoc.org/view/journals/mwre/144/12/mwr-d-16-0027.1.xml, 2016.

Allen, J. T.: Climate Change and Severe Thunderstorms, January, Oxford Research Encyclopedia of Climate Science, doi: 10.1093/acrefore/9780190228620.013.62, 2018.

Allen, J. T. and Tippett, M. K.: The characteristics of United States hail reports, Electronic J. Severe Storms Meteor., 10, 1–31, doi: https://doi.org/10.55599/ejssm.v10i3.60, 2015.

Allen, J. T., Tippett, M. K., Sobel, A. H., and Lepore, C.: Understanding the Drivers of Variability in Severe Convection: Bringing Together the Scientific and Insurance Communities, Bulletin of the American Meteorological Society, 97, ES221 – ES223, doi: 10.1175/BAMS-D-16-0208.1, URL https://journals.ametsoc.org/view/journals/bams/97/11/bams-d-16-0208.1.xml, 2016.

Allen, J. T., Giammanco, I. M., Kumjian, M. R., Jurgen Punge, H., Zhang, Q., Groenemeijer, P., Kunz, M., and Ortega, K.: Understanding Hail in the Earth System, Reviews of Geophysics, 58, e2019RG000 665, doi: 10.1029/2019RG000665, URL https://agupubs.onlinelibrary.wiley.com/doi/abs/10.1029/2019RG000665, 2020.

Altube, P., Bech, J., Argemi, O., Rigo, T., Pineda, N., Collis, S., and Helmus, J.: Correction of Dual-PRF Doppler Velocity Outliers in the Presence of Aliasing, Journal of Atmospheric and Oceanic Technology, pp. 1529–1543, doi: 10.1175/JTECH-D-16-0065.1, 2017.

AMS Glossary of Meteorology: Effective earth radius model, accessed on 2021-10-04, URL https://glossary.ametsoc.org/wiki/Effective_earth_radius, 2012.

Anderson, G. and Klugmann, D.: A European lightning density analysis using 5 years of ATDnet data, Natural Hazards and Earth System Sciences, 14, 815–829, doi: 10.5194/nhess-14-815-2014, URL https://nhess.copernicus.org/articles/14/815/2014/, 2014.

Aregger, M. P.: Stationary and slow-moving convection over Switzerland: A 14-year radar-based climatology, last accessed: 7-3-2022, URL https://occrdata.unibe.ch/students/theses/msc/326.pdf, 2021.

Ashley, W. S., Haberlie, A. M., and Strohm, J.: A Climatology of Quasi-Linear Convective Systems and Their Hazards in the United States, Weather and Forecasting, 34, 1605 – 1631, doi: 10.1175/WAF-D-19-0014.1, URL https://journals.ametsoc.org/view/journals/wefo/34/6/waf-d-19-0014_1.xml, 2019.

Avolio, E., Nisi, L., Panziera, L., Peyraud, L., and Miglietta, M. M.: A multi-sensor and modeling analysis of a severe convective storm in Lake Maggiore area (northwestern Italy), Atmospheric Research, 242, 105 008, doi: 10.1016/j.atmosres.2020.105008, 2020.

Azadifar, M., Rachidi, F., Rubinstein, M., Paolone, M., Diendorfer, G., Pichler, H., Schulz, W., Pavanello, D., and Romero, C.: Evaluation of the performance characteristics of the European Lightning Detection Network EUCLID in the Alps region for upward negative flashes using direct measurements at the instrumented Säntis Tower, Journal of Geophysical Research: Atmospheres, 121, 595–606, doi: https://doi.org/10.1002/2015JD024259, URL https://agupubs.onlinelibrary.wiley.com/doi/abs/10.1002/2015JD024259, 2016.

Bagaglini, L., Ingrosso, R., and Miglietta, M. M.: Synoptic patterns and mesoscale precursors of Italian tornadoes, Atmospheric Research, 253, 105 503, doi: https://doi.org/10.1016/j.atmosres.2021.105503, URL https://www.sciencedirect.com/science/article/pii/S0169809521000557, 2021.

Barras, H., Hering, A., Martynov, A., Noti, P. A., Germann, U., and Martius, O.: Experiences with >50,000 crowdsourced hail reports in Switzerland, Bulletin of the American Meteorological Society, 100, 1429–1440, doi: 10.1175/BAMS-D-18-0090.1, 2019.

Barras, H., Martius, O., Nisi, L., Schroeer, K., Hering, A., and Germann, U.: Multi-day hail clusters and isolated hail days in Switzerland – large-scale flow conditions and precursors, Weather and Climate Dynamics Discussions, 2021, 1–32, doi: 10.5194/wcd-2021-25, 2021.

Barthlott, C. and Kirshbaum, D. J.: Sensitivity of deep convection to terrain forcing over Mediterranean islands, Quarterly Journal of the Royal Meteorological Society, 139, 1762–1779, doi: https://doi.org/10.1002/qj.2089, URL https://rmets.onlinelibrary.wiley.com/doi/abs/10.1002/qj.2089, 2013.

Bergen, W. R. and Albers, S. C.: Two- and Three-Dimensional De-aliasing of Doppler Radar Velocities, Journal of Atmospheric and Oceanic Technology, 5, 305–319, doi: 10.1175/1520-0426(1988)005<0305:TATDDA>2.0.CO;2, 1988.

Betschart, M. and Hering, A.: Automatic Hail Detection at MeteoSwiss – Verification of the radar-based hail detection algorithms POH, MESHS and HAIL, Arbeitsberichte der MeteoSchweiz, p. 59pp, URL https://www.meteoswiss.admin.ch/content/dam/meteoswiss/en/Ungebundene-Seiten/Publikationen/Fachberichte/doc/ab238.pdf, 2012.

Beucher, S. and Lantuejoul, C.: Use of watersheds in contour detection, International workshop on image processing: Real-time Edge and Motion Detection/Estimation, URL https://people.cmm.minesparis.psl.eu/users/beucher/publi/watershed.pdf, 1979.

Blair, S. F., Laflin, J. M., Cavanaugh, D. E., Sanders, K. J., Currens, S. R., Pullin, J. I., Cooper, D. T., Deroche, D. R., Leighton, J. W., Fritchie, R. V., II, M. J. M., Goudeau, B. T., Kreller, S. J., Bosco, J. J., Kelly, C. M., and Mallinson, H. M.: High-Resolution Hail Observations: Implications for NWS Warning Operations, Weather and Forecasting, 32, 1101 – 1119, doi: 10.1175/WAF-D-16-0203.1, 2017.

Bluestein, H. B.: A History of Severe-Storm-Intercept Field Programs, Weather and Forecasting, 14, 558–577, doi: 10.1175/1520-0434(1999)014<0558:AHOSSI>2.0.CO;2, publisher: American Meteorological Society, 1999.

Bluestein, H. B.: A Tornadic Supercell over Elevated, Complex Terrain: The Divide, Colorado, Storm of 12 July 1996, Monthly Weather Review, 128, 15, 2000.

Bryan, G. H. and Fritsch, J. M.: A Benchmark Simulation for Moist Nonhydrostatic Numerical Models, Monthly Weather Review, 130, 2917 – 2928, doi: 10.1175/1520-0493(2002)130<2917:ABSFMN>2.0.CO;2, URL https://journals.ametsoc.org/view/journals/mwre/130/12/1520-0493_2002_130_2917_absfmn_2.0.co_2.xml, 2002.

Bundesamt für Meteorologie und Klimatologie MeteoSchweiz: Gewitter- und Blitzhäufigkeit in der Schweiz, last accessed on 2022-04-18, URL https://www.meteoschweiz.admin.ch/home/wetter/wetterbegriffe/gewitter/gewitter-und-blitzhaeufigkeit-in-der-schweiz.html, 2017.

Bundesamt für Meteorologie und Klimatologie MeteoSchweiz: Beschreibung zu den Gefahrenstufen, last accessed: 08-03-2022, URL https://www.meteoschweiz.admin.ch/content/dam/meteoswiss/de/Wetter/doc/beschreibungenzudengefahrenstufen.pdf, 2021.

Bundesamt für Meteorologie und Klimatologie MeteoSchweiz: Normwert-Karten, last accessed on 2022-03-12, URL https://www.meteoschweiz.admin.ch/home/klima/schweizer-klima-im-detail/klima-normwerte/normwert-karten.html?filters=temp_9120_09, 2022.

Bundesamt für Meteorologie und Klimatologie MeteoSchweiz: Das Schweizer Wetterradarnetz, accessed on 2019-12-12, URL https://www.meteoswiss.admin.ch/content/dam/meteoswiss/de/Mess-und-Prognosesysteme/Atmosphaere/Radarnetz/doc/20170830_Radarnetz_DE_einzeln.pdf, 2018.

Bunkers, M. J., Klimowski, B. A., Zeitler, J. W., Thompson, R. L., and Weisman, M. L.: Predicting Supercell Motion Using a New Hodograph Technique, Weather and Forecasting, 15, 61 – 79, doi: 10.1175/1520-0434(2000)015<0061:PSMUAN>2.0.CO;2, URL https://journals.ametsoc.org/view/journals/wefo/15/1/1520-0434_2000_015_0061_psmuan_2_0_co_2.xml, 2000.

Chang, P.-L., Fang, W.-T., Lin, P.-F., and Yang, M.-J.: A Vortex-Based Doppler Velocity Dealiasing Algorithm for Tropical Cyclones, Journal of Atmospheric and Oceanic Technology, 36, 1521–1545, doi: 10.1175/jtech-d-18-0139.1, 2019.

Consortium for Small Scale Modelling: MeteoSwiss Operational Applications within COSMO, accessed on 2020-01-20, URL http://www.cosmo-model.org/content/tasks/operational/meteoSwiss/default.htm#cosmo-1, 2018.

Ćurić, M., Janc, D., and Vučković, V.: Numerical simulation of Cb cloud vorticity, Atmospheric Research, 83, 427–434, doi: https://doi.org/10.1016/j.atmosres.2005.10.024, URL https://www.sciencedirect.com/science/article/pii/S016980950600113X, 2007.

Davies-Jones, R.: A review of supercell and tornado dynamics, Atmospheric Research, 158-159, 274–291, doi: https://doi.org/10.1016/j.atmosres.2014.04.007, URL https://www.sciencedirect.com/science/article/pii/S0169809514001756, 2015.

de Morsier, G., Fuhrer, O., and Arpagaus, M.: Challenges for a new 1 km non-hydrostatic model over the Alpine area, accessed on 2020-04-01, in: AMS 15th International Conference on Mountain Meteorology, American Meteorological Society, 2012.

Deardorff, J. W.: Stratocumulus-capped mixed layers derived from a three-dimensional model, Boundary-Layer Meteorology, 18, 495–527, doi: 10.1007/BF00119502, 1980.

Dennis, E. J. and Kumjian, M. R.: The Impact of Vertical Wind Shear on Hail Growth in Simulated Supercells, Journal of the Atmospheric Sciences, 74, 641 – 663, doi: 10.1175/JAS-D-16-0066.1, URL https://journals.ametsoc.org/view/journals/atsc/74/3/jas-d-16-0066.1.xml, 2017.

Diffenbaugh, N. S., Scherer, M., and Trapp, R. J.: Robust increases in severe thunderstorm environments in response to greenhouse forcing, Proceedings of the National Academy of Sciences, 110, 16 361–16 366, doi: 10.1073/pnas.1307758110, 2013.

DWD: Thunderstorm Detection and Tracking with KONRAD, accessed on 2022-10-24, URL https://www.dwd.de/EN/research/weatherforecasting/met_applications/nowcasting/konrad_en_node.html, 2022.

Eilts, M. D. and Smith, S. D.: Efficient Dealiasing of Doppler Velocities Using Local Environment Constraints, Journal of Atmospheric and Oceanic Technology, 7, doi: 10.1175/1520-0426(1990)007<0118:EDODVU>2.0.CO;2, 1990.

Enno, S.-E., Sugier, J., Alber, R., and Seltzer, M.: Lightning flash density in Europe based on 10 years of ATDnet data, Atmospheric Research, 235, 104 769, doi: 10.1016/j.atmosres.2019.104769, 2020.

Fabry, F.: Radar Meteorology, Cambridge University Press, doi: 10.1017/CBO9781107707405, 2015.

Feldmann, M., James, C. N., Boscacci, M., Leuenberger, D., Gabella, M., Germann, U., Wolfensberger, D., and Berne, A.: R2D2: A Region-Based Recursive Doppler Dealiasing Algorithm for Operational Weather Radar, Journal of Atmospheric and Oceanic Technology, 37, 2341–2356, doi: 10.1175/JTECH-D-20-0054.1, 2020.

Feldmann, M., Germann, U., Gabella, M., and Berne, A.: A characterisation of Alpine mesocyclone occurrence, Weather and Climate Dynamics, 2, 1225–1244, doi: 10.5194/wcd-2-1225-2021, URL https://wcd.copernicus.org/articles/2/1225/2021/, 2021.

Feldmann, M., Hering, A., Gabella, M., and Berne, A.: Hailstorms and rainstorms versus supercells - a regional analysis of convective storm types in the Alpine region, PREPRINT (Version 1) available at Research Square; npj Climate and Atmospheric Science, doi: https://doi.org/10.21203/rs.3.rs-1666457/v1, 2022.

Feudale, L. and Manzato, A.: Cloud-to-Ground Lightning Distribution and Its Relationship with Orography and Anthropogenic Emissions in the Po Valley, Journal of Applied Meteorology and Climatology, 53, 2651 – 2670, doi: 10.1175/JAMC-D-14-0037.1, URL https://journals.ametsoc.org/view/journals/apme/53/12/jamc-d-14-0037.1.xml, 2014.

Figueras i Ventura, J., Pineda, N., Besic, N., Grazioli, J., Hering, A., Van Der Velde, O. A., Romero, D., Sunjerga, A., Mostajabi, A., Azadifar, M., Rubinstein, M., Montanyà, J., Germann, U., and Rachidi, F.: Analysis of the lightning production of convective cells, Atmospheric Measurement Techniques, 12, 5573–5591, doi: 10.5194/amt-12-5573-2019, 2019.

Foote, G. B., Krauss, T. W., and Makitov, V.: Hail metrics using convectional radar, vol. 1.5, Amer. Meteor. Soc., 2005.

Foresti, L., Sideris, I. V., Panziera, L., Nerini, D., and Germann, U.: A 10-year radar-based analysis of orographic precipitation growth and decay patterns over the Swiss Alpine region, Quarterly Journal of the Royal Meteorological Society, 144, 2277–2301, doi: 10.1002/qj.3364, 2018.

Foresti, L., Sideris, I. V., Nerini, D., Beusch, L., and Germann, U.: Using a 10-Year Radar Archive for Nowcasting Precipitation Growth and Decay: A Probabilistic Machine Learning Approach, Weather and Forecasting, 34, 1547 – 1569, doi: 10.1175/WAF-D-18-0206.1, URL https://journals.ametsoc.org/view/journals/wefo/34/5/waf-d-18-0206_1.xml, 2019.

Frew, E. W., Argrow, B., Borenstein, S., Swenson, S., Hirst, C. A., Havenga, H., and Houston, A.: Field observation of tornadic supercells by multiple autonomous fixed-wing unmanned aircraft, Journal of Field Robotics, 37, 1077–1093, doi: 10.1002/rob.21947, 2020.

Gaál, L., Molnar, P., and Szolgay, J.: Selection of intense rainfall events based on intensity thresholds and lightning data in Switzerland, Hydrology and Earth System Sciences, 18, 1561–1573, doi: 10.5194/hess-18-1561-2014, URL https://hess.copernicus.org/articles/18/1561/2014/, 2014.

Gabella, M., Speirs, P., Hamann, U., Germann, U., and Berne, A.: Measurement of Precipitation in the Alps Using Dual-Polarization C-Band Ground-Based Radars, the GPM Spaceborne Ku-Band Radar, and Rain Gauges, Remote Sensing, doi: https://doi.org/10.3390/rs9111147, 2017.

Garcia de Jesus, E. I.: Tornado scientists send drone fleet into violent thunderstorms, Nature, doi: 10.1038/d41586-019-01486-y, 2019.

Gensini, V. A. and Brooks, H. E.: Spatial trends in United States tornado frequency, npj Climate and Atmospheric Science, 1, 2397–3722, doi: 10.1038/s41612-018-0048-2, URL https://doi.org/10.1038/s41612-018-0048-2, 2018.

Germann, U.: Vertical wind profile by Doppler radars, MAP Newsletters, pp. 6–7, 1999.

Germann, U. and Joss, J.: Operational measurement of precipitation in mountainous terrain. In Weather Radar: Principles and advanced applications; Meischner, P. (Ed.), Springer: Berlin, 2004.

Germann, U., Galli, G., Boscacci, M., and Bolliger, M.: Radar precipitation measurement in a mountainous region, Quarterly Journal of the Royal Meteorological Society, 132, 1669–1692, doi: https://doi.org/10.1256/qj.05.190, URL https://rmets.onlinelibrary.wiley.com/doi/abs/10.1256/qj.05.190, 2006.

Germann, U., Boscacci, M., Gabella, M., and Sartori, M.: Peak Performance - Radar design for prediction in the Swiss Alps, Meteorological Technology International, pp. 42–45, 2015.

Germann, U., Boscacci, M., Gabella, M., and Schneebeli, M.: Weather radar in Switzerland, in: From weather observations to atmospheric and climate sciences in Switzerland, edited by Willemse S. and Furger M., vdf, 2016a.

Germann, U., Boscacci, M., Gabella, M., and Schneebelie, M.: Weather radar in Switzerland - in "From weather observations to atmospheric and climate sciences in Switzerland", edited by S. Willemse and M. Furger, vdf, doi: 10.3218/3746-3, 2016b.

Germann, U., Figueras i Ventura, J., Gabella, M., Hering, A. M., Sideris, I., and Calpini, B.: Triggering Innovation, Meteorological Technology International, pp. 63–64, 2016c.

Germann, U., Boscacci, M., Clementi, L., Gabella, M., Hering, A., Sartori, M., Sideris, I. V., and Calpini, B.: Weather Radar in Complex Orography, Remote Sensing, 14, doi: 10.3390/rs14030503, URL https://www.mdpi.com/2072-4292/14/3/503, 2022.

Grazioli, J., Leuenberger, A., Peyraud, L., Figueras, J., Gabella, M., Hering, A., and Germann, U.: Adaptive thunderstorm measurements using C-band and X-band radar data, IEEE Geoscience and Remote Sensing Letters, 16, 1673–1677, doi: 10.1109/LGRS.2019.2909970, 2019.

Gunn, R. and Kinzer, G. D.: THE TERMINAL VELOCITY OF FALL FOR WATER DROPLETS IN STAGNANT AIR, Journal of Atmospheric Sciences, 6, 243 – 248, doi: 10.1175/1520-0469(1949)006<0243:TTVOFF>2.0.CO;2, URL https://journals.ametsoc.org/view/journals/atsc/6/4/1520-0469_1949_006_0243_ttvoff_2_0_co_2.xml, 1949.

Gutierrez, R. E. and Kumjian, M. R.: Environmental and Radar Characteristics of Gargantuan Hail–Producing Storms, Monthly Weather Review, 149, 2523 – 2538, doi: 10.1175/MWR-D-20-0298.1, URL https://journals.ametsoc.org/view/journals/mwre/149/8/MWR-D-20-0298.1.xml, 2021.

Haberlie, A. M. and Ashley, W. S.: A Radar-Based Climatology of Mesoscale Convective Systems in the United States, Journal of Climate, 32, 1591 – 1606, doi: 10.1175/JCLI-D-18-0559.1, URL https://journals.ametsoc.org/view/journals/clim/32/5/jcli-d-18-0559.1.xml, 2019.

He, G., Li, G., Zou, X., and Ray, P. S.: Applications of a Velocity Dealiasing Scheme to Data from the China New Generation Weather Radar System (CINRAD), Weather and Forecasting, pp. 218–230, doi: 10.1175/WAF-D-11-00054.1, 2011.

Helmus, J. J. and Collis, S. M.: The Python ARM Radar Toolkit (Py-ART), a Library for Working with Weather Radar Data in the Python Programming Language, Journal of Open Research Software, doi: http://doi.org/10.5334/jors.119, URL https://arm-doe.github.io/pyart/API/generated/pyart.correct.dealias_region_based.html, 2016.

Hengstebeck, T., Wapler, K., Heizenreder, D., and Joe, P.: Radar Network – Based Detection of Mesocyclones at the German Weather Service, Journal of Atmospheric and Oceanic Technology, 35, 299–321, doi: 10.1175/JTECH-D-16-0230.1, 2018.

Hering, A., Germann, U., Boscacci, M., and Senesi, S.: Operational nowcasting of thunderstorms in the Alps during MAP D-PHASE, Proc. ERAD Conference 2008, URL https://www.researchgate.net/profile/Urs-Germann/publication/237123756_Operational_nowcasting_of_thunderstorms_in_the_Alps_during_MAP_D-PHASE/links/54d3c17c0cf246475802d28d/Operational-nowcasting-of-thunderstorms-in-the-Alps-during-MAP-D-PHASE.pdf, 2008.

Hering, A. M., Morel, C., Galli, G., Ambrosetti, P., and Boscacci, M.: Nowcasting thunderstorms in the Alpine Region using a radar based adaptive thresholding scheme, Proc. ERAD Conference 2004, pp. 206–211, URL https://www.copernicus.org/erad/2004/online/ERAD04_P_206.pdf, 2004.

Hoeppe, P.: Trends in weather related disasters – Consequences for insurers and society, Weather and Climate Extremes, pp. 70–79, doi: http://dx.doi.org/10.1016/j.wace.2015.10.002, 2015.

Hoeppe, P.: Trends in weather related disasters - Consequences for insurers and society, Weather and Climate Extremes, 11, 70–79, doi: 10.1016/j.wace.2015.10.002, URL http://dx.doi.org/10.1016/j.wace.2015.10.002, 2016.

Homar, V., Gayà, M., Romero, R., Ramis, C., and Alonso, S.: Tornadoes over complex terrain: an analysis of the 28th August 1999 tornadic event in eastern Spain, Atmospheric Research, 67-68, 301–317, doi: https://doi.org/10.1016/S0169-8095(03)00064-4, URL https://www.sciencedirect.com/science/article/pii/S0169809503000644, 2003.

Houze, R. A.: Chapter 12 - Clouds and Precipitation Associated with Hills and Mountains, in: Cloud Dynamics, edited by Houze, R. A., vol. 104 of *International Geophysics*, pp. 369–402, Academic Press, doi: https://doi.org/10.1016/B978-0-12-374266-7.00012-3, URL https://www.sciencedirect.com/science/article/pii/B9780123742667000123, 2014.

Houze, R. A., Schmid, W., Fovell, R. G., and Schiesser, H.-H.: Hailstorms in Switzerland: Left Movers, Right Movers, and False Hooks, Monthly Weather Review, 121, 3345–3370, doi: 10.1175/1520-0493(1993)121<3345:hislmr>2.0.co;2, 1993.

Huntrieser, H., Schiesser, H. H., Schmid, W., and Waldvogel, A.: Comparison of Traditional and Newly Developed Thunderstorm Indices for Switzerland, Weather and Forecasting, 12, 108 – 125, doi: 10.1175/1520-0434(1997)012<0108:COTAND>2.0.CO;2, URL https://journals.ametsoc.org/view/journals/wefo/12/1/1520-0434_1997_012_0108_cotand_2_0_co_2.xml, 1997.

Isotta, F. A., Frei, C., Weilguni, V., Perčec Tadić, M., Lassègues, P., Rudolf, B., Pavan, V., Cacciamani, C., Antolini, G., Ratto, S. M., Munari, M., Micheletti, S., Bonati, V., Lussana, C., Ronchi, C., Panettieri, E., Marigo, G., and Vertačnik, G.: The climate of daily precipitation in the Alps: development and analysis of a high-resolution grid dataset from pan-Alpine rain-gauge data, International Journal of Climatology, 34, 1657–1675, doi: https://doi.org/10.1002/joc.3794, URL https://rmets.onlinelibrary.wiley.com/doi/abs/10.1002/joc.3794, 2014.

James, C. N. and Houze, R. A. J.: A Real-Time Four-Dimensional Doppler Dealiasing Scheme, Journal of Atmospheric and Oceanic Technology, 18, 1674–1683, doi: 10.1175/1520-0426(2001)018<1674:ARTFDD>2.0.CO;2, 2001.

Jarvis, A., Reuter, H., Nelson, A., and Guevara, E.: Hole-filled SRTM for the globe Version 4, available from the CGIAR-CSI SRTM 90m Database, URL http://srtm.csi.cgiar.org, 2008.

Jiang, Y. and Xu, Q.: Adaptive Dealiasing for Doppler Velocities Scanned from Hurricanes and Typhoons, Journal of Atmospheric and Oceanic Technology, 33, 1931–1947, doi: 10.1175/JTECH-D-15-0146.1, 2016.

Joss, J. and Waldvogel, A.: Ein Spektrograph für Niederschlagstropfen mit automatischer Auswertung, Pure and Applied Geophysics, 68, 240 – 246, doi: 10.1007/BF00874898, URL https://doi.org/10.1007/BF00874898, 1967.

Joss, J., Schädler, B., Galli, G., Cavalli, R., Boscacci, M., Held, E., Della Bruna, G., Kappenberger, G., Nespor, V., and Spiess, R.: Operational use of radar for precipitation measurements in Switzerland, vdf Hochschulverlag AG, ETH Zürich, Switzerland, doi: 10.1.1.625.1278, URL https://citeseerx.ist.psu.edu/viewdoc/download?doi=10.1.1.625.1278&rep=rep1&type=pdf, 1998.

Kaltenboeck, R. and Steinheimer, M.: Radar-based severe storm climatology for Austrian complex orography related to vertical wind shear and atmospheric instability, Atmospheric Research, 158-159, 216–230, doi: https://doi.org/10.1016/j.atmosres.2014.08.006, URL https://www.sciencedirect.com/science/article/pii/S0169809514003330, 2015.

Katona, B. and Markowski, P.: Assessing the Influence of Complex Terrain on Severe Convective Environments in Northeastern Alabama, Weather and Forecasting, 36, 1003 – 1029, doi: 10.1175/WAF-D-20-0136.1, URL https://journals.ametsoc.org/view/journals/wefo/36/3/WAF-D-20-0136.1.xml, 2021.

Katona, B., Markowski, P., Alexander, C., and Benjamin, S.: The Influence of Topography on Convective Storm Environments in the Eastern United States as Deduced from the HRRR, Weather and Forecasting, 31, 1481 – 1490, doi: 10.1175/WAF-D-16-0038.1, URL https://journals.ametsoc.org/view/journals/wefo/31/5/waf-d-16-0038_1.xml, 2016.

Klemp, J. B. and Wilhelmson, R. B.: The Simulation of Three-Dimensional Convective Storm Dynamics, Journal of Atmospheric Sciences, 35, 1070 – 1096, doi: 10.1175/1520-0469(1978)035<1070:TSOTDC>2.0.CO;2, URL https://journals.ametsoc.org/view/journals/atsc/35/6/1520-0469_1978_035_1070_tsotdc_2_0_co_2.xml, 1978.

Kopp, J., Schröer, K., Schwierz, C., Hering, A., Germann, U., and Martius, O.: The summer 2021 Switzerland hailstorms: weather situation, major impacts and unique observational data, Weather, n/a, doi: https://doi.org/10.1002/wea.4306, URL https://rmets.onlinelibrary.wiley.com/doi/abs/10.1002/wea.4306, 2022.

Kron, W., Löw, P., and Kundzewicz, Z. W.: Changes in risk of extreme weather events in Europe, Environmental Science & Policy, 100, 74–83, doi: 10.1016/j.envsci.2019.06.007, 2019.

Kukulies, J., Chen, D., and Curio, J.: The Role of Mesoscale Convective Systems in Precipitation in the Tibetan Plateau Region, Journal of Geophysical Research: Atmospheres, 126, e2021JD035 279, doi: https://doi.org/10.1029/2021JD035279, URL https://agupubs.onlinelibrary.wiley.com/doi/abs/10.1029/2021JD035279, 2021.

Kumjian, M. R. and Lombardo, K.: A Hail Growth Trajectory Model for Exploring the Environmental Controls on Hail Size: Model Physics and Idealized Tests, Journal of the Atmospheric Sciences, 77, 2765 – 2791, doi: 10.1175/JAS-D-20-0016.1, URL https://journals.ametsoc.org/view/journals/atsc/77/8/jasD200016.xml, 2020.

Kumjian, M. R. and Ryzhkov, A. V.: Polarimetric Signatures in Supercell Thunderstorms, Journal of Applied Meteorology and Climatology, 47, 1940 – 1961, doi: 10.1175/2007JAMC1874.1, 2008.

Kumjian, M. R., Lombardo, K., and Loeffler, S.: The Evolution of Hail Production in Simulated Supercell Storms, Journal of the Atmospheric Sciences, 78, 3417 – 3440, doi: 10.1175/JAS-D-21-0034.1, URL https://journals.ametsoc.org/view/journals/atsc/78/11/JAS-D-21-0034.1.xml, 2021.

Kunz, M., Wandel, J., Fluck, E., Baumstark, S., Mohr, S., and Schemm, S.: Ambient conditions prevailing during hail events in central Europe, Natural Hazards and Earth System Sciences, 20, 1867–1887, doi: 10.5194/nhess-20-1867-2020, URL https://nhess.copernicus.org/articles/20/1867/2020/, 2020.

Laiti, L., Zardi, D., de Franceschi, M., Rampanelli, G., and Giovannini, L.: Analysis of the diurnal development of a lake-valley circulation in the Alps based on airborne and surface measurements, Atmospheric Chemistry and Physics, 14, 9771–9786, doi: 10.5194/acp-14-9771-2014, URL https://acp.copernicus.org/articles/14/9771/2014/, 2014.

LeBel, L. J., Tang, B. H., and Lazear, R. A.: Examining Terrain Effects on an Upstate New York Tornado Event Utilizing a High-Resolution Model Simulation, Weather and Forecasting, 36, 2001 – 2020, doi: 10.1175/WAF-D-21-0018.1, URL https://journals.ametsoc.org/view/journals/wefo/36/6/WAF-D-21-0018.1.xml, 2021.

Liang, X., Xie, Y., Yin, J., Luo, Y., Yao, D., and Li, F.: An IVAP-Based Dealiasing Method for Radar Velocity Data Quality Control, Journal of Atmospheric and Oceanic Technology, doi: 10.1175/JTECH-D-18-0216.1., 2019.

Lilly, D. K. and Klemp, J. B.: The effects of terrain shape on nonlinear hydrostatic mountain waves, Journal of Fluid Mechanics, 95, 241–261, doi: 10.1017/S0022112079001452, 1979.

Lim, E. and Sun, J.: A Velocity Dealiasing Technique Using Rapidly Updated Analysis from a Four-Dimensional Variational Doppler Radar Data Assimilation System, Journal of Atmospheric and Oceanic Technology, 27, 1140–1152, doi: 10.1175/2010JTECHA1300.1, URL https://doi.org/10.1175/2010JTECHA1300.1, 2010.

Lin, Y. and Kumjian, M. R.: Influences of CAPE on Hail Production in Simulated Supercell Storms, Journal of the Atmospheric Sciences, 79, 179 – 204, doi: 10.1175/JAS-D-21-0054.1, URL https://journals.ametsoc.org/view/journals/atsc/79/1/JAS-D-21-0054.1.xml, 2022.

Linder, W., Schmid, W., and Schiesser, H.-H.: Surface Winds and Development of Thunderstorms along Southwest–Northeast Oriented Mountain Chains, Weather and Forecasting, 14, 758 – 770, doi: 10.1175/1520-0434(1999)014<0758:SWADOT>2.0.CO;2, 1999.

Lohmann, U., Lüönd, F., and Maahrt, F.: An Introduction to Clouds - From the Microscale to Climate, Cambridge University Press, 2016.

Lombardo, K. and Kumjian, M. R.: Observations of the Discrete Propagation of a Mesoscale Convective System during RELAMPAGO–CACTI, Monthly Weather Review, 150, 2111 – 2138, doi: 10.1175/MWR-D-21-0265.1, URL https://journals.ametsoc.org/view/journals/mwre/150/8/MWR-D-21-0265.1.xml, 2022.

Louf, V., Protat, A., Jackson, R. C., Collis, S. M., and Helmus, J.: UNRAVEL: A Robust Modular Velocity Dealiasing Technique for Doppler Radar, Journal of Atmospheric and Oceanic Technology, 37, 741–758, doi: 10.1175/JTECH-D-19-0020.1, 2020.

Lucas, B. D. and Takeo, K.: An Iterative Image Registration Technique with an Application to Stereo Vision, in: Proceedings of 7th International Joint Conference on Artificial Intelligence (IJCAI '81), vol. 2, pp. 674 – 679, 1981.

Mahalik, M. C., Smith, B. R., Elmore, K. L., Kingfield, D. M., Ortega, K. L., and Smith, T. M.: Estimates of Gradients in Radar Moments Using a Linear Least Squares Derivative Technique, Weather and Forecasting, 34, 415–434, doi: 10.1175/waf-d-18-0095.1, 2019.

Manzato, A., Davolio, S., Miglietta, M. M., Pucillo, A., and Setvák, M.: 12 September 2012: A supercell outbreak in NE Italy?, Atmospheric Research, 153, 98–118, doi: https://doi.org/10.1016/j.atmosres.2014.07.019, URL https://www.sciencedirect.com/science/article/pii/S0169809514002828, 2015.

Manzato, A., Serafin, S., Miglietta, M. M., Kirshbaum, D., and Schulz, W.: A pan–Alpine climatology of lightning and convective initiation, Monthly Weather Review, doi: 10.1175/MWR-D-21-0149.1, URL https://journals.ametsoc.org/view/journals/mwre/aop/MWR-D-21-0149.1/MWR-D-21-0149.1.xml, 2022.

Markowski, P. and Richardson, Y.: Mesoscale Meteorology in Midlatitudes, Wiley-Blackwell, doi: 10.1002/9780470682104, 2010.

Markowski, P. M.: Hook Echoes and Rear-Flank Downdrafts: A Review, Monthly Weather Review, 130, 852 – 876, doi: 10.1175/1520-0493(2002)130<0852:HEARFD>2.0.CO;2, 2002.

Markowski, P. M.: An Idealized Numerical Simulation Investigation of the Effects of Surface Drag on the Development of Near-Surface Vertical Vorticity in Supercell Thunderstorms, Journal of the Atmospheric Sciences, 73, 4349 – 4385, doi: 10.1175/JAS-D-16-0150.1, URL https://journals.ametsoc.org/view/journals/atsc/73/11/jas-d-16-0150.1.xml, 2016.

Markowski, P. M. and Dotzek, N.: A numerical study of the effects of orography on supercells, Atmospheric Research, 100, 457–478, doi: https://doi.org/10.1016/j.atmosres.2010.12.027, URL https://www.sciencedirect.com/science/article/pii/S0169809511000044, 5th European Conference on Severe Storms, 2011.

Martius, O., Hering, A., Kunz, M., Manzato, A., Mohr, S., Nisi, L., and Trefalt, S.: Challenges and Recent Advances in Hail Research, Bulletin of the American Meteorological Society, 99, ES51 – ES54, doi: 10.1175/BAMS-D-17-0207.1, URL https://journals.ametsoc.org/view/journals/bams/99/3/bams-d-17-0207.1.xml, 2018.

Medina, S. and Houze, R. A.: Air motions and precipitation growth in Alpine storms, Quarterly Journal of the Royal Meteorological Society, 129, 345–371, doi: https://doi.org/10.1256/qj.02.13, URL https://rmets.onlinelibrary.wiley.com/doi/abs/10.1256/qj.02.13, 2003.

Meteorage: Publications and Technical Notes, accessed on 2022-09-29, URL https://www.meteorage.com/resources/publications-and-technical-notes, 2022.

MeteoSwiss: Climatologie des éclairs, accessed on 2021-10-08, URL https://www.meteosuisse.admin.ch/home/actualite/meteosuisse-blog/meteosuisse-blog-recherche.subpage.html/fr/data/blogs/2016/5/climatologie-des-eclairs.html, 2016.

MeteoSwiss: Stabilisierung nach nächtlichem Rekordgewitter, accessed on 2021-10-08, URL https://www.meteoschweiz.admin.ch/home/aktuell/meteoschweiz-blog/meteoschweiz-blog-suche.subpage.html/de/data/blogs/2017/8/stabiliserung-nach-naechtlichem-rekordgewitter-.html, 2017.

MeteoSwiss: The climate of Switzerland - accessed on 2021-09-27, URL https://www.meteoswiss.admin.ch/home/climate/the-climate-of-switzerland.html, 2018.

MeteoSwiss: Orage supercellulaire en Valais, accessed on 2021-10-08, URL https://www.meteosuisse.admin.ch/home/actualite/meteosuisse-blog/meteosuisse-blog-recherche.subpage.html/fr/data/blogs/2019/8/orage-supercellulaire-en-valais.html, 2019.

MeteoSwiss: Clutter in der Wetterradartechnik, accessed on 2020-07-14, URL https://www.meteoschweiz.admin.ch/home/aktuell/meteoschweiz-blog/meteoschweiz-blog.subpage.html/de/data/blogs/2020/6/clutter_in_der_wetterradartechnik.html, 2020.

Miglietta, M. M. and Davolio, S.: Dynamical forcings in heavy precipitation events over Italy: lessons from the HyMeX SOP1 campaign, Hydrology and Earth System Sciences, 26, 627–646, doi: 10.5194/hess-26-627-2022, URL https://hess.copernicus.org/articles/26/627/2022/, 2022.

Miglietta, M. M., Manzato, A., and Rotunno, R.: Characteristics and predictability of a supercell during HyMeX SOP1, Quarterly Journal of the Royal Meteorological Society, 142, 2839–2853, doi: https://doi.org/10.1002/qj.2872, URL https://rmets.onlinelibrary.wiley.com/doi/abs/10.1002/qj.2872, 2016.

Miglietta, M. M., Mazon, J., and Rotunno, R.: Numerical Simulations of a Tornadic Supercell over the Mediterranean, Weather and Forecasting, 32, 1209 – 1226, doi: 10.1175/WAF-D-16-0223.1, URL https://journals.ametsoc.org/view/journals/wefo/32/3/waf-d-16-0223_1.xml, 2017.

Miller, M. L., Lakshmanan, V., and Smith, T. M.: An Automated Method for Depicting Mesocyclone Paths and Intensities, Weather and Forecasting, 28, 570–585, doi: 10.1175/WAF-D-12-00065.1, 2013.

Milrad, S. M., Lombardo, K., Atallah, E. H., and Gyakum, J. R.: Numerical Simulations of the 2013 Alberta Flood: Dynamics, Thermodynamics, and the Role of Orography, Monthly Weather Review, 145, 3049 – 3072, doi: 10.1175/MWR-D-16-0336.1, URL https://journals.ametsoc.org/view/journals/mwre/145/8/mwr-d-16-0336.1.xml, 2017.

Mohr, S. and Kunz, M.: Recent trends and variabilities of convective parameters relevant for hail events in Germany and Europe, Atmospheric Research, 123, 211–228, doi: 10.1016/j.atmosres.2012.05.016, 2013.

Mohr, S., Wandel, J., Lenggenhager, S., and Martius, O.: Relationship between atmospheric blocking and warm-season thunderstorms over western and central Europe, Quarterly Journal of the Royal Meteorological Society, 145, 3040–3056, doi: 10.1002/qj.3603, 2019.

Mohr, S., Wilhelm, J., Wandel, J., Kunz, M., Portmann, R., Punge, H. J., Schmidberger, M., Quinting, J. F., and Grams, C. M.: The role of large-scale dynamics in an exceptional sequence of severe thunderstorms in Europe May–June 2018, Weather and Climate Dynamics, 1, 325–348, doi: 10.5194/wcd-1-325-2020, 2020.

Morris, S. M.: The Spanish plume - testing the forecaster's nerve, Meteorological Magazine, 115, 349 – 357, 1986.

Morrison, H., Curry, J. A., and Khvorostyanov, V. I.: A New Double-Moment Microphysics Parameterization for Application in Cloud and Climate Models. Part I: Description, Journal of the Atmospheric Sciences, 62, 1665 – 1677, doi: 10.1175/JAS3446.1, URL https://journals.ametsoc.org/view/journals/atsc/62/6/jas3446.1.xml, 2005.

Mulholland, J. P., Nesbitt, S. W., Trapp, R. J., Rasmussen, K. L., and Salio, P. V.: Convective Storm Life Cycle and Environments near the Sierras de Córdoba, Argentina, Monthly Weather Review, 146, 2541 – 2557, doi: 10.1175/MWR-D-18-0081.1, URL https://journals.ametsoc.org/view/journals/mwre/146/8/mwr-d-18-0081.1.xml, 2018.

Mulholland, J. P., Nesbitt, S. W., and Trapp, R. J.: A Case Study of Terrain Influences on Upscale Convective Growth of a Supercell, Monthly Weather Review, 147, 4305–4324, doi: 10.1175/MWR-D-19-0099.1, URL http://journals.ametsoc.org/doi/10.1175/MWR-D-19-0099.1, 2019.

Mulholland, J. P., Nesbitt, S. W., Trapp, R. J., and Peters, J. M.: The Influence of Terrain on the Convective Environment and Associated Convective Morphology from an Idealized Modeling Perspective, Journal of the Atmospheric Sciences, 77, 3929–3949, doi: 10.1175/JAS-D-19-0190.1, 2020.

Murillo, E. M. and Homeyer, C. R.: Severe Hail Fall and Hailstorm Detection Using Remote Sensing Observations, Journal of Applied Meteorology and Climatology, 58, 947–970, doi: 10.1175/JAMC-D-18-0247.1, URL http://journals.ametsoc.org/doi/10.1175/JAMC-D-18-0247.1, 2019.

Murillo, E. M., Homeyer, C. R., and Allen, J. T.: A 23-Year Severe Hail Climatology Using GridRad MESH Observations, Monthly Weather Review, 149, 945 – 958, doi: 10.1175/MWR-D-20-0178.1, URL https://journals.ametsoc.org/view/journals/mwre/149/4/MWR-D-20-0178.1.xml, 2021.

NCAR: Thunderstorm Identification, Tracking, Analysis, and Nowcasting (TITAN), accessed on 2022-10-24, URL https://ral.ucar.edu/solutions/products/thunderstorm-identification-tracking-analysis-and-nowcasting-titan, 2022.

NCCS: Hail Climate Switzerland - National hail hazard maps, National Centre for Climate Services, URL www.hailclimatology.ch, 2021.

Nesbitt, S. W., Salio, P. V., Ávila, E., Bitzer, P., Carey, L., Chandrasekar, V., Deierling, W., Dominguez, F., Dillon, M. E., Garcia, C. M., Gochis, D., Goodman, S., Hence, D. A., Kosiba,

K. A., Kumjian, M. R., Lang, T., Luna, L. M., Marquis, J., Marshall, R., McMurdie, L. A., Nascimento, E. L., Rasmussen, K. L., Roberts, R., Rowe, A. K., Ruiz, J. J., São Sabbas, E. F., Saulo, A. C., Schumacher, R. S., Skabar, Y. G., Machado, L. A. T., Trapp, R. J., Varble, A., Wilson, J., Wurman, J., Zipser, E. J., Arias, I., Bechis, H., and Grover, M. A.: A storm safari in Subtropical South America: proyecto RELAMPAGO, Bulletin of the American Meteorological Society, pp. 1–64, doi: 10.1175/BAMS-D-20-0029.1, 2021.

Nisi, L., Ambrosetti, P., and Clementi, L.: Nowcasting severe convection in the Alpine region: the COALITION approach, Quarterly Journal of the Royal Meteorological Society, 140, 1684–1699, doi: https://doi.org/10.1002/qj.2249, URL https://rmets.onlinelibrary.wiley.com/doi/abs/10.1002/qj.2249, 2014.

Nisi, L., Martius, O., Hering, A., Kunz, M., and Germann, U.: Spatial and temporal distribution of hailstorms in the Alpine region: A long-term, high resolution, radar-based analysis, Quarterly Journal of the Royal Meteorological Society, 142, 1590–1604, doi: 10.1002/qj.2771, 2016.

Nisi, L., Hering, A., Germann, U., and Martius, O.: A 15-year hail streak climatology for the Alpine region, Quarterly Journal of the Royal Meteorological Society, 144, 1429–1449, doi: 10.1002/qj.3286, 2018.

Nisi, L., Hering, A., Germann, U., Schroeer, K., Barras, H., Kunz, M., and Martius, O.: Hailstorms in the Alpine region: Diurnal cycle, 4D-characteristics, and the nowcasting potential of lightning properties, Quarterly Journal of the Royal Meteorological Society, 146, 4170–4194, doi: 10.1002/qj.3897, 2020.

NSSL: VORTEX @ NSSL, accessed on 2021-05-17, URL https://www.nssl.noaa.gov/projects/vortex/, 2019.

NSSL: VORTEX SOUTHEAST - accessed on 2021-09-23, URL https://www.nssl.noaa.gov/projects/vortexse/, 2021.

Orf, L., Wilhelmson, R., Lee, B., Finley, C., and Houston, A.: Evolution of a Long-Track Violent Tornado within a Simulated Supercell, Bulletin of the American Meteorological Society, 98, 45 – 68, doi: 10.1175/BAMS-D-15-00073.1, URL https://journals.ametsoc.org/view/journals/bams/98/1/bams-d-15-00073.1.xml, 2017.

Panziera, L. and Germann, U.: The relation between airflow and orographic precipitation on the southern side of the Alps as revealed by weather radar, Quarterly Journal of the Royal Meteorological Society, 136, 222–238, doi: https://doi.org/10.1002/qj.544, URL https://rmets.onlinelibrary.wiley.com/doi/abs/10.1002/qj.544, 2010.

Panziera, L., Germann, U., Gabella, M., and Mandapaka, P. V.: NORA–Nowcasting of Orographic Rainfall by means of Analogues, Quarterly Journal of the Royal Meteorological Society, 137, 2106–2123, doi: https://doi.org/10.1002/qj.878, URL https://rmets.onlinelibrary.wiley.com/doi/abs/10.1002/qj.878, 2011.

Panziera, L., Gabella, M., Zanini, S., Hering, A., Germann, U., and Berne, A.: A radar-based regional extreme rainfall analysis to derive the thresholds for a novel automatic alert system in Switzerland, Hydrology and Earth System Sciences, 20, 2317–2332, doi: 10.5194/hess-20-2317-2016, URL https://hess.copernicus.org/articles/20/2317/2016/, 2016.

Peters, J. M., Morrison, H., Nowotarski, C. J., Mulholland, J. P., and Thompson, R. L.: A Formula for the Maximum Vertical Velocity in Supercell Updrafts, Journal of the Atmospheric Sciences, 77, 3747 – 3757, doi: 10.1175/JAS-D-20-0103.1, URL https://journals.ametsoc.org/view/journals/atsc/77/11/JAS-D-20-0103.1.xml, 2020.

Peyraud, L.: Analysis of the 18 July 2005 Tornadic Supercell over the Lake Geneva Region, Weather and Forecasting, 28, 1524–1551, doi: 10.1175/waf-d-13-00022.1, 2013.

Piper, D., Kunz, M., Ehmele, F., Mohr, S., Mühr, B., Kron, A., and Daniell, J.: Exceptional sequence of severe thunderstorms and related flash floods in May and June 2016 in Germany – Part 1: Meteorological background, Natural Hazards and Earth System Sciences, 16, 2835–2850, doi: 10.5194/nhess-16-2835-2016, URL https://nhess.copernicus.org/articles/16/2835/2016/, 2016.

Piper, D. A., Kunz, M., Allen, J. T., and Mohr, S.: Investigation of the temporal variability of thunderstorms in central and western Europe and the relation to large-scale flow and teleconnection patterns, Quarterly Journal of the Royal Meteorological Society, 145, 3644–3666, doi: 10.1002/qj.3647, 2019.

Púčik, T., Groenemeijer, P., Rädler, A. T., Tijssen, L., Nikulin, G., Prein, A. F., van Meijgaard, E., Fealy, R., Jacob, D., and Teichmann, C.: Future Changes in European Severe Convection Environments in a Regional Climate Model Ensemble, Journal of Climate, 30, 6771 – 6794, doi: 10.1175/JCLI-D-16-0777.1, 2017.

Púčik, T., Castellano, C., Groenemeijer, P., Kühne, T., Rädler, A. T., Antonescu, B., and Faust, E.: Large Hail Incidence and Its Economic and Societal Impacts across Europe, Monthly Weather Review, 147, 3901 – 3916, doi: 10.1175/MWR-D-19-0204.1, 2019.

Pulkkinen, S., Nerini, D., Pérez Hortal, A. A., Velasco-Forero, C., Seed, A., Germann, U., and Foresti, L.: Pysteps: an open-source Python library for probabilistic precipitation nowcasting (v1.0), Geoscientific Model Development, 12, 4185–4219, doi: 10.5194/gmd-12-4185-2019, 2019.

Punge, H. and Kunz, M.: Hail observations and hailstorm characteristics in Europe: A review, Atmospheric Research, 176-177, 159–184, doi: https://doi.org/10.1016/j.atmosres.2016.02.012, URL https://www.sciencedirect.com/science/article/pii/S0169809516300291, 2016.

Punge, H. J., Bedka, K. M., Kunz, M., and Reinbold, A.: Hail frequency estimation across Europe based on a combination of overshooting top detections and the ERA-INTERIM reanalysis, Atmospheric Research, 198, 34–43, doi: 10.1016/j.atmosres.2017.07.025, URL http://dx.doi.org/10.1016/j.atmosres.2017.07.025, 2017.

PySteps developers: pySTEPS – The nowcasting initiative, accessed on 2021-05-17, URL https://pysteps.readthedocs.io/en/latest/, 2021.

Rädler, A. T., Groenemeijer, P. H., Faust, E., Sausen, R., and Púčik, T.: Frequency of severe thunderstorms across Europe expected to increase in the 21st century due to rising instability, npj Climate and Atmospheric Science, 2, 3–7, doi: 10.1038/s41612-019-0083-7, 2019.

Rampanelli, G., Zardi, D., and Rotunno, R.: Mechanisms of Up-Valley Winds, Journal of the Atmospheric Sciences, 61, 3097 – 3111, doi: 10.1175/JAS-3354.1, 2004.

Raupach, T. H., Martius, O., Allen, J. T., Kunz, M., Lasher-Trapp, S., Mohr, S., Rasmussen, K. L., Trapp, R., and Zhang, Q.: The effects of climate change on hailstorms, Nature reviews earth & environment, pp. 213–226, doi: 1https://doi.org/10.1038/s43017-020-00133-9, URL https://www.nature.com/articles/s43017-020-00133-9, 2021a.

Raupach, T. H., Martynov, A., Nisi, L., Hering, A., Barton, Y., and Martius, O.: Object-based analysis of simulated thunderstorms in Switzerland: application and validation of automated thunderstorm tracking with simulation data, Geoscientific Model Development, 14, 6495–6514, doi: 10.5194/gmd-14-6495-2021, URL https://gmd.copernicus.org/articles/14/6495/2021/, 2021b.

Reeves, H. D. and Lin, Y.-L.: The Effects of a Mountain on the Propagation of a Preexisting Convective System for Blocked and Unblocked Flow Regimes, Journal of the Atmospheric Sciences, 64, 2401 – 2421, doi: 10.1175/JAS3959.1, URL https://journals.ametsoc.org/view/journals/atsc/64/7/jas3959.1.xml, 2007.

Richard, E., Cosma, S., Tabary, P., Pinty, J.-p., and Hagen, M.: High-resolution numerical simulations of the convective system observed in the Lago Maggiore area on 17 September 1999 (MAP IOP 2a), Quarterly Journal of the Royal Meteorological Society, 129, 543–563, doi: https://doi.org/10.1256/qj.02.50, URL https://rmets.onlinelibrary.wiley.com/doi/abs/10.1256/qj.02.50, 2003.

Rotunno, R. and Ferretti, R.: Orographic effects on rainfall in MAP cases IOP 2b and IOP 8, Quarterly Journal of the Royal Meteorological Society, 129, 373–390, doi: https://doi.org/10.1256/qj.02.20, URL https://rmets.onlinelibrary.wiley.com/doi/abs/10.1256/qj.02.20, 2003.

Rotunno, R. and Houze, R. A.: Lessons on orographic precipitation from the Mesoscale Alpine Programme, Quarterly Journal of the Royal Meteorological Society, 133, 811–830, doi: https://doi.org/10.1002/qj.67, URL https://rmets.onlinelibrary.wiley.com/doi/abs/10.1002/qj.67, 2007.

Rotunno, R. and Klemp, J. B.: The Influence of the Shear-Induced Pressure Gradient on Thunderstorm Motion, Monthly Weather Review, 110, 136 – 151, doi: 10.1175/1520-0493(1982)110<0136:TIOTSI>2.0.CO;2, URL https://journals.ametsoc.org/view/journals/mwre/110/2/1520-0493_1982_110_0136_tiotsi_2_0_co_2.xml, 1982.

Ryzhkov, A. V. and Zrnic, D. S.: Radar Polymetry for Weather Observations, Springer Atmospheric Sciences, 2019.

Scheffknecht, P., Serafin, S., and Grubišić, V.: A long-lived supercell over mountainous terrain, Quarterly Journal of the Royal Meteorological Society, 143, 2973–2986, doi: https://doi.org/10.1002/qj.3127, URL https://rmets.onlinelibrary.wiley.com/doi/abs/10.1002/qj.3127, 2017.

Schemm, S., Nisi, L., Martinov, A., Leuenberger, D., and Martius, O.: On the link between cold fronts and hail in Switzerland, Atmospheric Science Letters, 17, 315–325, doi: 10.1002/asl.660, 2016.

Schulz, W., Diendorfer, G., Pedeboy, S., and Poelman, D. R.: The European lightning location system EUCLID – Part 1: Performance analysis and validation, Natural Hazards and Earth System Sciences, 16, 595–605, doi: 10.5194/nhess-16-595-2016, URL https://nhess.copernicus.org/articles/16/595/2016/, 2016.

Seity, Y., Soula, S., Tabary, P., and Scialom, G.: The convective storm system during IOP 2a of MAP: Cloud-to-ground lightning flash production in relation to dynamics and microphysics, Quarterly Journal of the Royal Meteorological Society, 129, 523–542, doi: https://doi.org/10.1256/qj.02.03, URL https://rmets.onlinelibrary.wiley.com/doi/abs/10.1256/qj.02.03, 2003.

Serafin, S., Rotach, M. W., Arpagaus, M., Colfescu, I., Cuxart, J., De Wekker, S. F. J., Evans, M., Grubišić, V., Kalthoff, N., Karl, T., Kirshbaum, D. J., Lehner, M., Mobbs, S., Paci, A., Palazzi, E., Raudzens Bailey, A., Schmidli, J., Wohlfahrt, G., and Zardi, D.: Multi-scale transport and exchange processes in the atmosphere over mountains, innsbruck university press, 1 edn., doi: 10.15203/99106-003-1, 2020.

Sideris, I. V., Foresti, L., Nerini, D., and Germann, U.: NowPrecip: localized precipitation nowcasting in the complex terrain of Switzerland, Quarterly Journal of the Royal Meteorological Society, 146, 1768–1800, doi: https://doi.org/10.1002/qj.3766, URL https://rmets.onlinelibrary.wiley.com/doi/abs/10.1002/qj.3766, 2020.

Smith, B. R., Sandmæl, T., Mahalik, M. C., Elmore, K. L., Kingfield, D. M., Ortega, K. L., and Smith, T. M.: Corrigendum, Weather and Forecasting, 36, 1131 – 1133, doi: 10.1175/WAF-D-20-0125.1, URL https://journals.ametsoc.org/view/journals/wefo/36/3/WAF-D-20-0125.1.xml, 2021.

Soderholm, B., Ronalds, B., and Kirshbaum, D. J.: The Evolution of Convective Storms Initiated by an Isolated Mountain Ridge, Monthly Weather Review, 142, 1430 – 1451, doi: 10.1175/MWR-D-13-00280.1, URL https://journals.ametsoc.org/view/journals/mwre/142/4/mwr-d-13-00280.1.xml, 2014.

Stumpf, G. J., Witt, A., Mitchell, E. D., Spencer, P. L., Johnson, J. T., Eilts, M. D., Thomas, K. W., and Burgess, D. W.: The National Severe Storms Laboratory Mesocyclone Detection Algorithm for the WSR-88D, Weather and Forecasting, 13, 304–326, doi: 10.1175/1520-0434(1998)013<0304:TNSSLM>2.0.CO;2, 1998.

Sturmarchiv Schweiz: Sturmarchiv Schweiz - Tornados, accessed on 2021-05-15, URL https://www.sturmarchiv.ch/index.php?title=Tornados, 2021.

©swisstopo: DHM25 / 200m, URL https://www.swisstopo.admin.ch/de/geodata/height/dhm25200.html, 2005.

Tabary, P., Scialom, G., and Germann, U.: Real-Time Retrieval of the Wind from Aliased Velocities Measured by Doppler Radars Real-Time Retrieval of the Wind from Aliased Velocities Measured by Doppler Radars, Journal of Atmospheric and Oceanic Technology, 0426, doi: 10.1175/1520-0426(2001)018<0875, 2001.

Tang, B. H., Gensini, V. A., and Homeyer, C. R.: Trends in United States large hail environments and observations, npj Climate and Atmospheric Science, 2, doi: 10.1038/s41612-019-0103-7, URL https://doi.org/10.1038/s41612-019-0103-7, 2019.

Taszarek, M.: Long-term changes in thunderstorm environments over Europe and United States as the response to a globally warming climate, accessed on 2019-12-12, URL https://meetingorganizer.copernicus.org/ECSS2019/ECSS2019-145-2.pdf, 2019.

Taszarek, M., Allen, J., Púčik, T., Groenemeijer, P., Czernecki, B., Kolendowicz, L., Lagouvardos, K., Kotroni, V., and Schulz, W.: A Climatology of Thunderstorms across Europe from a Synthesis of Multiple Data Sources, Journal of Climate, 32, 1813 – 1837, doi: 10.1175/JCLI-D-18-0372.1, 2019.

Taszarek, M., Allen, J. T., Groenemeijer, P., Edwards, R., Brooks, H. E., Chmielewski, V., and Enno, S.-E.: Severe Convective Storms across Europe and the United States. Part I: Climatology of Lightning, Large Hail, Severe Wind, and Tornadoes, Journal of Climate, 33, 10 239 – 10 261, doi: 10.1175/JCLI-D-20-0345.1, URL https://journals.ametsoc.org/view/journals/clim/33/23/jcliD200345.xml, 2020.

Taszarek, M., Allen, J. T., Brooks, H. E., Pilguj, N., and Czernecki, B.: Differing Trends in United States and European Severe Thunderstorm Environments in a Warming Climate, Bulletin of the American Meteorological Society, 102, E296 – E322, doi: 10.1175/BAMS-D-20-0004.1, URL https://journals.ametsoc.org/view/journals/bams/102/2/BAMS-D-20-0004.1.xml, 2021a.

Taszarek, M., Allen, J. T., Marchio, M., and Brooks, H. E.: Global climatology and trends in convective environments from ERA5 and rawinsonde data, npj Climate and Atmospheric Science, 4, 2397–3722, doi: 10.1038/s41612-021-00190-x, URL https://doi.org/10.1038/s41612-021-00190-x, 2021b.

Trefalt, S., Martynov, A., Barras, H., Besic, N., Hering, A. M., Lenggenhager, S., Noti, P., Röthlisberger, M., Schemm, S., Germann, U., and Martius, O.: A severe hail storm in complex topography in Switzerland - Observations and processes, Atmospheric Research, 209, 76–94, doi: 10.1016/j.atmosres.2018.03.007, 2018.

Treloar, A. B.: Vertically integrated radar reflectivity as an indicator of hail size in the greater Sydney region of Australia, Amer. Meteor. Soc., 1998.

Tuovinen, J.-P., Rauhala, J., and Schultz, D. M.: Significant-Hail-Producing Storms in Finland: Convective-Storm Environment and Mode, Weather and Forecasting, 30, 1064 – 1076, doi: 10.1175/WAF-D-14-00159.1, URL https://journals.ametsoc.org/view/journals/wefo/30/4/waf-d-14-00159_1.xml, 2015.

University of Wyoming: Upper Air Data - Soundings, accessed on 02-08-2022, URL https://weather.uwyo.edu/upperair/sounding.html, 2022.

van der Walt, S., Schönberger, J. L., Nunez-Iglesias, J., Boulogne, F., Warner, J. D., Yager, N., Gouillart, E., Yu, T., and the scikit-image contributors: scikit-image: image processing in Python, PeerJ, 2, e453, doi: 10.7717/peerj.453, 2014.

Varble, A. C., Nesbitt, S. W., Salio, P., Hardin, J. C., Bharadwaj, N., Borque, P., DeMott, P. J., Feng, Z., Hill, T. C. J., Marquis, J. N., Matthews, A., Mei, F., Öktem, R., Castro, V., Goldberger, L., Hunzinger, A., Barry, K. R., Kreidenweis, S. M., McFarquhar, G. M., McMurdie, L. A., Pekour, M., Powers, H., Romps, D. M., Saulo, C., Schmid, B., Tomlinson, J. M., van den Heever, S. C., Zelenyuk, A., Zhang, Z., and Zipser, E. J.: Utilizing a Storm-Generating Hotspot to Study Convective Cloud Transitions: The CACTI Experiment, Bulletin of the American Meteorological Society, pp. 1–67, doi: 10.1175/BAMS-D-20-0030.1, 2021.

Waldvogel, A., Federer, B., and Grimm, P.: Criteria for the Detection of Hail Cells, Journal of Applied Meteorology (1962-1982), 18, 1521–1525, URL http://www.jstor.org/stable/26179076, 1979.

Wapler, K.: The life-cycle of hailstorms : Lightning , radar reflectivity and rotation characteristics, Atmospheric Research, 193, 60–72, doi: 10.1016/j.atmosres.2017.04.009, 2017.

Wapler, K.: Mesocyclonic and non-mesocyclonic convective storms in Germany: Storm characteristics and life-cycle, Atmospheric Research, 248, 105 186, doi: 10.1016/j.atmosres.2020.105186, 2021.

Wapler, K. and James, P.: Thunderstorm occurrence and characteristics in Central Europe under different synoptic conditions, Atmospheric Research, 158-159, 231–244, doi: 10.1016/j.atmosres.2014.07.011, 2014.

Wapler, K., Hengstebeck, T., and Groenemeijer, P.: Mesocyclones in Central Europe as seen by radar, Atmospheric Research, 168, 112–120, doi: 10.1016/j.atmosres.2015.08.023, 2016.

Ward, P. J., Blauhut, V., Bloemendaal, N., Daniell, J. E., de Ruiter, M. C., Duncan, M. J., Emberson, R., Jenkins, S. F., Kirschbaum, D., Kunz, M., Mohr, S., Muis, S., Riddell, G. A., Schäfer, A., Stanley, T., Veldkamp, T. I. E., and Winsemius, H. C.: Review article: Natural hazard risk assessments at the global scale, Natural Hazards and Earth System Sciences, 20, 1069–1096, doi: 10.5194/nhess-20-1069-2020, URL https://nhess.copernicus.org/articles/20/1069/2020/, 2020.

Weisman, M. L. and Klemp, J. B.: The Dependence of Numerically Simulated Convective Storms on Vertical Wind Shear and Buoyancy, Monthly Weather Review, 110, 504 – 520, doi: 10.1175/1520-0493(1982)110<0504:TDONSC>2.0.CO;2, URL https://journals.ametsoc.org/view/journals/mwre/110/6/1520-0493_1982_110_0504_tdonsc_2_0_co_2.xml, 1982.

Weusthoff, T.: Weather Type Classification at MeteoSwiss, Arbeitsberichte der MeteoSchweiz, p. 46pp, 2011.

Wilhelm, J., Mohr, S., Punge, H. J., Mühr, B., Schmidberger, M., Daniell, J. E., Bedka, K. M., and Kunz, M.: Severe thunderstorms with large hail across Germany in June 2019, Weather, 76, 228–237, doi: https://doi.org/10.1002/wea.3886, URL https://rmets.onlinelibrary.wiley.com/doi/abs/10.1002/wea.3886, 2021.

Witt, A. and Brown, R. A.: PERFORMANCE OF A NEW VELOCITY DEALIASING ALGORITHM FOR THE WSR-88D, in: 34th Conference on Radar Meteorology, URL https://ams.confex.com/ams/pdfpapers/155951.pdf, 2009.

Witt, A., Burgess, D. W., Seimon, A., Allen, J. T., Snyder, J. C., and Bluestein, H. B.: Rapid-Scan Radar Observations of an Oklahoma Tornadic Hailstorm Producing Giant Hail, Weather and Forecasting, 33, 1263 – 1282, doi: 10.1175/WAF-D-18-0003.1, 2018.

Wolfensberger, D. and Berne, A.: From model to radar variables: a new forward polarimetric radar operator for COSMO, Atmospheric Measurement Techniques, 11, 3883–3916, doi: 10.5194/amt-11-3883-2018, URL https://www.atmos-meas-tech.net/11/3883/2018/, 2018.

Wu, F. and Lombardo, K.: Precipitation Enhancement in Squall Lines Moving over Mountainous Coastal Regions, Journal of the Atmospheric Sciences, 78, 3089 – 3113, doi: 10.1175/JAS-D-20-0222.1, URL https://journals.ametsoc.org/view/journals/atsc/78/10/JAS-D-20-0222.1.xml, 2021.

Wüest, M., Germann, U., and Schmid, W.: A Variational De-Aliasing Technique, Phys. Chem. Earth, 25, 1179–1183, doi: 10.1016/S1464-1909(00)00175-1, 2000.

Xu, Q. and Nai, K.: Mesocyclone-targeted Doppler velocity dealiasing, Journal of Atmospheric and Oceanic Technology, 34, 841–853, doi: 10.1175/JTECH-D-16-0170.1, 2017.

Xu, Q., Nai, K., and Wei, L.: Fitting VAD winds to aliased doppler radial-velocity observations: A global minimization problem in the presence of multiple local minima, Quarterly Journal of the Royal Meteorological Society, 136, 451–461, doi: 10.1002/qj.589, 2010.

Xu, Q., Nai, K., Wei, L., Zhang, P., Liu, S., and Parrish, D.: A VAD-based dealiasing method for radar velocity data quality control, Journal of Atmospheric and Oceanic Technology, 28, 50–62, doi: 10.1175/2010JTECHA1444.1, 2011.

Xu, Q., Nai, K., Karstens, C., Smith, T., and Zhao, Q.: Improved Doppler Velocity Dealiasing for Radar Data Assimilation and Storm-Scale Vortex Detection, Advances in Meteorology, 2013, 10, doi: 10.1155/2013/562386, 2013.

Yuan, Y., Wang, P., Wang, D., and Shi, J.: A Velocity Dealiasing Scheme Based on Minimization of Velocity Differences between Regions, Advances in Meteorology, 2020, doi: 10.1155/2020/6157636, 2020.

Zhang, J. and Wang, S.: An automated 2D multipass Doppler radar velocity dealiasing scheme, Journal of Atmospheric and Oceanic Technology, 23, 1239–1248, doi: 10.1175/JTECH1910.1, 2006.

Zipser, E. J., Cecil, D. J., Liu, C., Nesbitt, S. W., and Yorty, D. P.: WHERE ARE THE MOST INTENSE THUNDERSTORMS ON EARTH?, Bulletin of the American Meteorological Society, 87, 1057 – 1072, doi: 10.1175/BAMS-87-8-1057, URL https://journals.ametsoc.org/view/journals/bams/87/8/bams-87-8-1057.xml, 2006.

Zöbisch, I.: Thunderstorms: Life cycle analyses and nowcasting based on multi-source data, Ph.D. thesis, Ludwig-Maximilians-Universität München, doi: 10.5282/edoc.25680, URL http://nbn-resolving.de/urn:nbn:de:bvb:19-256804, 2020.

Zrnić, D. S., Burgess, D. W., and Hennington, L. D.: Automatic Detection of Mesocyclonic Shear with Doppler Radar, Journal of Atmospheric and Oceanic Technology, 2, 425–438, doi: 10.1175/1520-0426(1985)002<0425:adomsw>2.0.co;2, 1985.

Name	Monika Feldmann	Telephone	+41/76 701 9056
Address	Via Borghese 17 6600 Locarno (CH)	E-mail	monika.feldmann@epfl.ch

Curriculum Vitæ

Personal Data

Name	Monika Feldmann	Address	Via Borghese 17
Date of birth	1. May 1994, Laufenburg (CH)		6600 Locarno (CH)
Marital status	unmarried	Telephone	+41/76 701 9056
Nationality	German (D)	E-mail	monika.feldmann@epfl.ch

Education

2022	Graduate Visitor Program, NCAR (USA)
2019-2023	Doctoral studies, environmental remote sensing, EPFL (CH) and MeteoSwiss (CH)
2018	MSc thesis, atmosphere and climate science, MIT (USA)
2016-2018	Master of environmental sciences, ETH Zurich (CH) Major in atmosphere and climate science, Minor in sustainable energy use
2013-2016	Bachelor of environmental sciences, ETH Zurich (CH)

Internships and Jobs

2019-2023	PhD candidate, environmental remote sensing, EPFL (CH) and MeteoSwiss (CH)
2018	Postgraduate researcher at ETH Zurich and Sorbonne (Paris)
2017-2018	Communications assistant in global EHS (Environment, Health & Safety) at Givaudan
2016-2017	Internship in atmospheric dispersion modelling in global EHS at Givaudan
2014-2017	Assistant at ETH Zurich

Volunteer Work

2022	Organization of online poster sessions at ERAD 2022
2019-2022	Organization and moderation of EPFL weather club
2018	Communications of the visiting student association MIT VISTA
2016-2018	Student representative of the ”Schweizerische Gesellschaft für Meteorologie”
2015-2016	Actuary of the “Umwelt und Forstfachverein der ETH Zurich“

Languages

German	native language
English	native level
French	fluent
Italian	conversational
Mandarin	basic knowledge
Spanish	basic knowledge

Name	Monika Feldmann	Telephone	+41/76 701 9056
Address	Via Borghese 17 6600 Locarno (CH)	E-mail	monika.feldmann@epfl.ch

Stays abroad

2022	Graduate Visitor Program at NCAR / Boulder, USA
2018	Visiting student at MIT / Cambridge, USA
2016	Chinese language courses in Singapore and Beijing, China
2012-2013	Au Pair in Auckland, New Zealand
1997-2001	Residence in Mobile, USA

Technical skills

Programming languages	Python and Matlab (advanced) C, Fortran, Bash and R (basics)
Operating systems	Windows, Linux
Office	LaTeX, MS Office, LibreOffice
various	version control and collaboration with Git environment management with Anaconda server management with slurm

Publications

Feldmann, M., Rotunno, R., Germann, U., Berne, A. (under review). Supercell thunderstorms in complex topography - how mountain valleys with lakes can increase occurrence frequency. Under review at Monthly Weather Review

Feldmann, M., Hering, A., Gabella, M., Berne, A. (accepted 2023). Hailstorms and Rainstorms Versus Supercells - A Regional Analysis of Convective Storm Types in the Alpine Region. Accepted at npj Climate and Atmospheric Science, preprint doi:10.21203/rs.3.rs-1666457/v1

Feldmann, M., Germann, U., Gabella, M., Berne, A. (2021). A Characterisation of Alpine Mesocyclone Occurrence. Weather and Climate Dynamics, 2(4), 1225-1244, doi:10.5194/wcd-2-1225-2021

Feldmann, M. and James, C. N., Boscacci, M., Leuenberger, D., Gabella, M., Germann, U., Wolfensberger, D., Berne, A. (2020). R2D2 - A Region-based Recursive Doppler Dealiasing Algorithm for Operational Weather Radar. Journal of Atmospheric and Oceanic Technology, 37(12), 2341-2356, doi:10.1175/JTECH-D-20-0054.1

Feldmann, M., Emanuel, K., Zhu, L., and Lohmann, U. (2019). Estimation of Atlantic tropical cyclone rainfall frequency in the United States. Journal of Applied Meteorology and Climatology, 58(8), 1853–1866, doi:10.1175/JAMC-D-19-0011.1

Name	Monika Feldmann	Telephone	+41/76 701 9056
Address	Via Borghese 17 6600 Locarno (CH)	E-mail	monika.feldmann@epfl.ch

Publications

Sarhadi, A., Rousseau-Rizzi, R., Mandli, K., Neal, J., Wiper, M. P., Feldmann, M., Emanuel, K. (submitted). Climate change intensifies compound flooding risk of tropical and extratropical cyclones in New York City. Submitted to Bulletin of the American Meteorological Society.

Gasparini, B., Münch, S., Poncet, L., Feldmann, M., and Lohmann, U. (2017).
Is increasing ice crystal sedimentation velocity in geoengineering simulations a good proxy for cirrus cloud seeding?, Atmospheric Chemistry and Physics, 17, 4871-4885, doi:10.5194/acp-17-4871-2017

Datasets

Feldmann, M., Hering, A., Gabella, M., Berne, A. (2022).
Radar-based severe thunderstorm classification in Switzerland from 2016-2021 [Data set]. Zenodo.
doi:10.5281/zenodo.6534510

Feldmann, M., Germann, U., Gabella, M., Berne, A. (2021).
Radar-based mesocyclone detections in Switzerland from 2016-2020 [Data set]. Zenodo.
doi:10.5281/zenodo.5122519

Feldmann, M. (2019). Climatology of rainfall from Atlantic hurricanes in the USA from radar data [Data set]. Zenodo. doi:10.5281/zenodo.1745239

Peer Review

2022-2023	Atmospheric Measurement Techniques
2021	npj Climate and Atmospheric Science
2020	JGR Atmospheres

Name	Monika Feldmann	Telephone	+41/76 701 9056
Address	Via Borghese 17 6600 Locarno (CH)	E-mail	monika.feldmann@epfl.ch

Conferences and Presentations

Feldmann, M., Gabella, M., Hering, A., Berne, A. (2022). Hailstorms and Rainstorms vs. Supercells - A Comparison of Severe Thunderstorms in the Alpine Region. 2nd North American Hail Workshop

Feldmann, M., Gabella, M., Berne, A. (2022). Supercells vs. Hailstorms and Rainstorms - A Radar-based Comparison of Severe Thunderstorms in the Alpine Region. 11th European Conference on Radar in Meteorology and Hydrology

Feldmann, M., Gabella, M., Berne, A. (2022). Hailstorms and Rainstorms vs. Supercells - A Comparison of Severe Thunderstorms in the Alpine Region. 20th Conference on Mountain Meteorology, AMS

Feldmann, M. (2022). Orographic Convection. Summer School Embry Riddle Aeronautical University

Feldmann, M., Gabella, M., Berne, A. (2022). Hailstorms vs. Supercells - A Comparison of Severe Thunderstorms in the Alpine Region. EGU General Assembly 2022

Feldmann, M. (2022). Supercells in the Alpine Region - From Observations to Idealized Modeling. NCAR MMM Seminar

Feldmann, M. (2022). Superzellengewitter im Schweizer Radarnetzwerk. Kundeninformationstag, MeteoSchweiz im Sicherheitsverbund Schweiz

Feldmann, M. (2021). Numerical Differentiation and Thunderstorm Research. Summer Course MIT

Feldmann, M. (2021). Doppler Velocity Products in Convection – Mesocyclone Detection. MetObs Forecaster Training, MeteoSwiss

Feldmann, M., Emanuel, K., Zhu, L., Lohmann, U. (2021). Estimating Long-Term Tropical Cyclone Rainfall Frequency - A Physics-Based Approach. 34th Conference on Hurricanes and Tropical Meteorology, AMS

Feldmann, M., Germann, U., Gabella, M., Berne, A. (2021). Characterization of Rotation in Severe Convection. 3rd European Hail Workshop

Feldmann, M., Gabella, M., Berne, A. (2021). Characterization of Mesocyclonic Rotation in Severe Convection Over the Swiss Alps. EGU General Assembly 2021

Locarno, February 15, 2023